KING'S
College
LONDON

Development of Patient-Specific Diastolic Models for the study of Dilated Cardiomyopathy

Hadjicharalambous, Myrianthi

Awarding institution:
King's College London

King's College London

Development of patient-specific diastolic models for the study of dilated cardiomyopathy

DOCTORAL THESIS

Author:
Myrianthi Hadjicharalambous

Supervisors:
David Nordsletten, PhD
Nicolas Smith, PhD

A thesis submitted in fulfillment of the requirements for the degree of Doctor of Philosophy in the

Division of Imaging Sciences and Biomedical Engineering
School of Medicine
King's College London

January, 2016

Abstract

The main objective of this thesis is the development of personalised diastolic cardiac mechanics models for the study of dilated cardiomyopathy. A model personalisation pipeline is developed, which deals with two core challenges in patient-specific modelling, namely data integration and parameter identifiability. Important modelling aspects of the pipeline are selected based on the potential and limitations of the data at hand, following systematic investigation using *in silico* and *in vivo* tests.

To assist in the model development process, numerical schemes for dealing with incompressibility / near incompresibility in the heart are compared in terms of accuracy and efficiency. *In silico* testing is extended to a parameter identifiability study, where commonly used passive constitutive laws are compared in terms of identifiability and model fidelity, using synthetic 3D tagged MRI.

The model personalisation pipeline is developed based on these modelling considerations, with a focus on optimising the use of the available data to improve model fidelity. The proposed pipeline is tested on a group of volunteers and patients, enabling an assessment of modelling attributes which can improve model accuracy and parameter identifiability *in vivo*. Finally, the developed patient-specific models are employed for a comparative analysis of diastolic heart function, in patients with dilated cardiomyopathy and healthy volunteers.

Acknowledgements

This thesis is the result of four years of hard work, persistence and devotion, yet its completion would not had been possible without the continuous support of many academics, colleagues, friends and family.

Foremost, I am extremely grateful for the supervision of Dr. David Nordsletten throughout these four years. Through endless discussions he was always willing to help and guide me, while his persistence in constructive feedback and attention to detail made me strive to do my best. His expertise in a wide range of topics has helped me tackle many of the challenges that came along. I am most of all grateful for his patience, support and encouragement, particularly in times of complete frustration on my behalf, which he would somehow turn into optimism and hope that kept me going.

I would also like to express my gratitude to my second supervisor, Prof. Nic Smith, for his guidance and support. Owing to his deep understanding of various engineering aspects, his feedback has helped me look at my work within the context of a bigger picture.

A very special thanks is owed to Liya Asner, my close colleague and friend, who was always there for me, both professionally and personally. Throughout countless "trial and error" attempts – combined with laughs and often frustration – we've developed and tested the *in vivo* pipeline followed in this work. Her guidance and support was invaluable throughout this time. I am of course particularly grateful to her for proofreading my thesis, correcting my commas and my often "Greek adaptation" of the English language.

I would also like to thank Radomir Chabiniok for introducing me to 3D tagged MRI and motion tracking, and guiding me through the use of synthetic tags. A special thanks to both Radomir Chabiniok and Eva Sammut, for providing their expertise on the medical aspect of the project, to Devis Peressutti for a lot of segmentations and meshes and to Jack Lee, for his useful input in several aspects of the project. I am also particularly grateful to Eric Kerfoot, for providing the visualisation software used for viewing models on medical images. Matt, thanks for CMgui tips!

A huge thanks is owed to all my friends in the department who have made my PhD years an unforgettable experience. Lunch breaks with Simone, Matt, Devis, Nika and recent "lunch acquaintances" Lauren and Dan, provided a new topic for conversation every singe day, getting my mind off of work problems. Numerous coffee breaks with Liya, Ross, Sam and Andy kept me going through the day. Snack breaks and long talks with Anastasia or Lucas reminded me of home. And of course, Friday drinks with many old and new friends, Sara, Yolanda, Fabrizio, Andrew, Bojan, Eoin, Angela, Kirsten, Marcus, Marta and many more. Thanks for all the good times everyone!

Outside of work, I'd like to thank my friends Marianna, Michalis, Vasilis, Yiota, Nayia, Efi and Eleftheria, who have helped me keep sane and let go off work for a while, with cocktails, food, flat sharing, flat moving, movie nights, board games nights and trips. A very special mention goes to Yiannis, for always being there for me, taking good care of me and making me happy.

Finally, this section could not be complete without the biggest and warmest gratitude towards my family. To my parents, who have been supporting me with all means and in all aspects, through my entire life. They have always insisted that I could and I should follow my dreams and carve my own path. Without my dad's pushing to get better and mum's listening to all my complaining, and encouraging me to think that I can achieve anything, I would had never come this far. Everything I've accomplished, I owe to them. A special thanks to my brother, always trying to cheer me up with his – what he thinks is – living on the edge life philosophy. Last but not least, a huge thanks to my sister for supporting me with long talks throughout the PhD and for cheering me up during writing up with photos and videos of the newest family member, Antonis!

Publications

M. Hadjicharalambous, J. Lee, N. Smith, D. Nordsletten (2014). A displacement-based finite element formulation for incompressible and nearly-incompressible cardiac mechanics. *Computer Methods in Applied Mechanics and Engineering*, 274:213-236.

M. Hadjicharalambous, R. Chabiniok, L. Asner, E. Sammut, J. Wong, G. Carr-White, J. Lee, R. Razavi, N. Smith, D. Nordsletten (2015). Analysis of passive cardiac constitutive laws for parameter estimation using 3D tagged MRI. *Biomechanics and Modeling in Mechanobiology*, 14(4):807-828.

L. Asner, M. Hadjicharalambous, J. Lee, D. Nordsletten (2015). Stacom challenge: Simulating left ventricular mechanics in the canine heart. *Lecture Notes in Computer Science*, 8896:123-134. Springer International Publishing.

R. Chabiniok, E. Sammut, M. Hadjicharalambous, L. Asner, D. Nordsletten, R. Razavi, N. Smith (2015). Steps towards quantification of the cardiological stress exam. *Functional Imaging and Modeling of the Heart*, 9126:12-20. Springer International Publishing.

L. Asner, M. Hadjicharalambous, R. Chabiniok, D. Peresutti, E. Sammut, J. Wong, P. Chowienczyk, J. Lee, A. King, N. Smith, R. Razavi, D. Nordsletten, (In print). Estimation of passive and active properties in the human heart using 3D tagged MRI. *Biomechanics and Modeling in Mechanobiology.*

R. Chabiniok, V. Wang, M. Hadjicharalambous, L. Asner, J. Lee, M. Sermesant, E. Kuhl, A. Young, P. Moireau, M. Nash, D. Chapelle, D. Nordsletten, (In print). Multiphysics and Multiscale Modeling, Data-Model Fusion and Integration of Organ Physiology in the Clinic: Cardiac Mechanics. *Interface Focus.*

Contents

List of abbreviations

DCM	Dilated cardiomyopathy
FEM	Finite element method
MRI	Magnetic resonance imaging
LV	Left ventricle
RV	Right ventricle
EDV	End-diastolic volume
ESV	End-systolic volume
SV	Stroke volume
EF	Ejection fraction
HR	Heart rate
LA	Long-axis
SA	Short-axis
EDP$^{\text{est}}$	Estimated end-diastolic pressure
EDPVR	End-diastolic pressure-volume relation
$\mathcal{J}$	Objective function
BC	Boundary condition
LM	Lagrange multiplier
PL	Perturbed Lagrangian
SNR	Shamanskii-Newton-Raphson
NT BC	No-traction epicardial boundary condtion
RV BC	RV-epicardial boundary condtion
PCMRI	Phase contrast MRI

List of Figures

List of Tables

1 Introduction

Dilated cardiomyopathy (DCM) is a cardiac disorder characterised by the progressive deterioration of the heart's pumping efficiency. Associated with poor survival rates (25% mortality rate over one year and 50% mortality rate over five years[54]), DCM has been the focus of significant research interest from both clinical and engineering points of view. The basis of the present research effort is that obtaining a better understanding of the mechanisms responsible for the development and progression of this condition will assist therapeutic planning and improve treatments.

The wealth and quality of medical imaging data available nowadays offers a powerful tool for studying and characterising the human heart in DCM. Capable of providing comprehensive information on cardiac anatomy, blood flow through the heart's chambers and great vessels as well as regional myocardial motion, medical imaging enables an accurate quantification of the kinematics of the heart, identifying potential abnormalities. While medical imaging allows for the assessment of cardiac function and pathology, linking the kinematics of the heart to specific physiological mechanisms that could explain the progression of disease and determining their impact remains a challenge.

Filling this gap, mathematical models of heart function allow for the quantification of important functional metrics related to observed kinematics, which can in turn be linked to underlying mechanisms. By describing heart function based on fundamental laws of physics, a simplified quantifiable representation of the heart behaviour is created. This produces the ideal framework for testing hypotheses, assessing the role of model parameters and quantitatively characterising the heart function in a systematic way.

Over the last few decades, advances in image processing, numerical techniques, and availability of computational power have enabled the joint use of comprehensive medical images and mathematical models of the heart function, for the creation of personalised cardiac models. Incorporating personalised geometries, boundary conditions and model parameters, patient-specific modelling allows for the identification of individual patient characteristics that could be clinically relevant. Furthermore, it enables personalised *in silico* tests of potential treatments or surgical procedures, assisting tailored and ul-

timately effective therapy strategies. Personalised heart models of varying complexity, focus and scale have been developed, to investigate the complex physical phenomena occurring over a heart beat. The focus of this work is on personalised cardiac mechanics models and specifically models covering the diastolic part of the cycle. Due to the significant remodelling observed in myocardial tissue in DCM patients, cardiac mechanics provide a convenient framework for answering questions on the development of the disease.

Developing personalised cardiac models, however, is not an easy task. This is foremost due to the inevitable inability to accurately represent a highly complex organ with a mathematical structure, suggesting the need for a careful consideration of modelling decisions. Moreover, the accuracy of the personalised model will always be restricted by the quantity and quality of the data at hand. For instance, due to the absence of relevant data, important modelling attributes such as the fibre distribution or the reference geometry, are likely to be based on assumptions which need to be thoroughly examined. Additional modelling aspects (degree of compressibility, constitutive law) need to be carefully selected taking into account the available clinical data and acknowledging its limitations.

On other practical aspects, even though image quality is continuously improving, resolution is not always sufficient and noise is present. Furthermore, patient's motion and breathing are likely to introduce inconsistencies between the available imaging sequences. Therefore, a core challenge in model personalisation is integrating the available data in an optimal way, *i.e.* maximising the use of the data at hand without introducing artefacts due to poor quality / incomplete data into the model.

The work presented in this thesis is part of the BHF funded project, *"BHF Integrated mathematical modelling and imaging study"* during which comprehensive imaging data from a group of volunteers and DCM patients were acquired. The main aim of this thesis is the integration of these data into personalised diastolic LV models to be used for the study of DCM. Taking the above-mentioned challenges into account, this involves developing a pipeline for bridging the gap between the available images and models. This pipeline has to be:

1. *efficient*, to allow for the study of multiple cases,

2. *robust*, so that it is applicable to all volunteers and patients with potentially low quality / noisy data,

3. *reliable*, to enable comparisons between cases, and safe conclusions.

The proposed pipeline is developed through careful selection of modelling attributes based on the data at hand. A key objective is to optimise the use of the available data in order to improve model accuracy, while ensuring unique parametrisation. This

fundamental step for reliable model outcomes and model parameters, lays the ground for comparisons between volunteers and DCM patients.

With these goals in mind, the remaining sections of the Introduction provide a brief review of the cardiac anatomy, behaviour and pathophysiology in DCM, along with previous work in cardiac mechanics modelling. Section 1.1 presents an introduction to the basics of heart structure and function, focusing on the aspects that are relevant for modelling studies. A brief overview of DCM and the current state of knowledge on the disease are presented in section 1.2. Subsequently, section 1.3 outlines the significant advances made over the last decades in the fields of tissue mechanics, while section 1.4 focuses on the progress made in personalised cardiac models as well as the challenges the field is currently facing. Finally, section 1.5 provides a short outline of the thesis' structure.

1.1 Review of cardiac anatomy and function

1.1.1 Cardiac anatomy

The heart is a remarkably complex and efficient mechanical pump, designed to deliver blood to the entire body through the circulatory system. Blood provides the body with essential nutrients and oxygen, and transfers metabolic waste products and carbon dioxide from body's tissues and organs to the lungs, where they are expelled. As the heart is responsible for blood circulation it has been deservedly described as *"the beginning and author, the fountain and original of all the things in the body, the primary cause of life"* (William Harvey, 1628).

The human heart has the dual role of circulating both oxygenated and deoxygenated blood, by supplying blood to the two compartments of the cardiovascular system, the systemic and pulmonary networks. The pulmonary arterial network is responsible for carrying deoxygenated blood to the lungs, where carbon dioxide is released from the blood, which is subsequently enriched with oxygen during respiration. The pulmonary venous system carries the oxygenated blood back to the heart, where it is then delivered to the entire body's organs and tissues through the systemic arteries. Systemic veins return deoxygenated blood back to the heart.

Because of this dual function, the human heart is divided into two functional halves (Fig. 1.1), the left and right heart, driving the systemic and pulmonary systems, respectively. Each side is comprised of two chambers, the atrium and the ventricle, which vary significantly in structure and function. The atria are thin-walled reservoirs receiving blood from the venous system, whereas ventricles are thick-walled pumps, ejecting blood to the arterial system. The heart is also equipped with four valves which
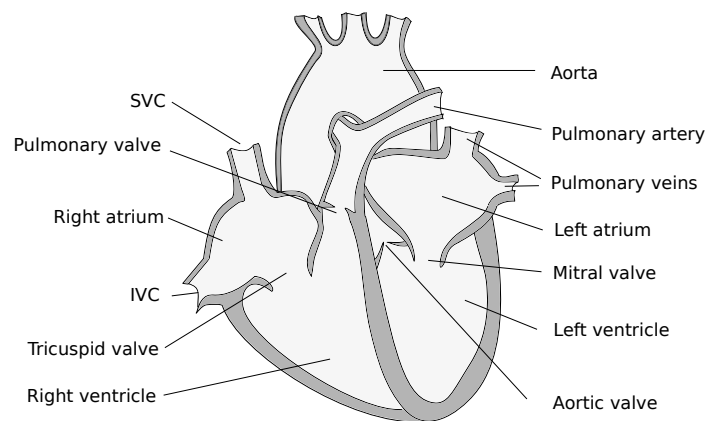
Figure 1.1 Schematic diagram of the heart and main vessels attached to it. IVC and SVC are the inferior and superior vena cava, respectively.

work to promote unidirectional blood flow and prevent back flow.

The right atrium (RA) collects deoxygenated blood coming from the inferior and superior vena cava. Blood is then directed to the right ventricle (RV) through the tricuspid valve, and subsequently to the pulmonary artery and lungs through the pulmonary valve. The now oxygenated blood returns to the heart through the pulmonary veins and enters the left atrium (LA). It then flows to the left ventricle (LV) via the mitral valve, where it is subsequently redirected to the aorta through the aortic valve. Finally, through the aorta and its branches, the blood is delivered to the entire body's tissues and organs. The heart muscle itself receives blood and nutrients through the coronary circulation.

The two sides of the heart differ significantly in function, a distinction which is also reflected in their structure. The LV must develop a high cavity pressure in order to overpass the high aortic pressure (approximately 110mmHg) and effectively pump blood to the entire systemic circulation. In contrast, due to lower pressure in the pulmonary artery (approximately 30mmHg), the RV has significantly lower pressure. This substantial difference in pressure requires increased wall thickness for the LV (approximately two times thicker than the RV). Interestingly, the atria have quite similar blood pressures (approximately 10mmHg for both LA and RA). A lower pressure is required in atria compared to ventricles, as their main function is to act as compliant reservoirs, collecting blood to assist ventricular filling.

1.1.2 Description of the cardiac cycle

The cardiac cycle is the periodic filling and ejection of blood from the ventricles, defined by the time interval between two successive RR peaks (approximate duration of $0.7 - 1s$). It is characterised by four distinct phases: diastole (ventricular filling), isovolumic contraction (IVC), systole (ejection) and isovolumic relaxation (IVR). These phases and changes in volume and pressure are commonly illustrated through Wigger plots (Fig. 1.2). During the cardiac cycle, the tissue and bulk behaviour of the heart vary significantly. The repetition of the cardiac cycle is responsible for the rhythmical pumping function of the myocardium and for delivering blood to the entire body. The cardiac cycle description that follows focuses on the left ventricle, which is of interest in this work.
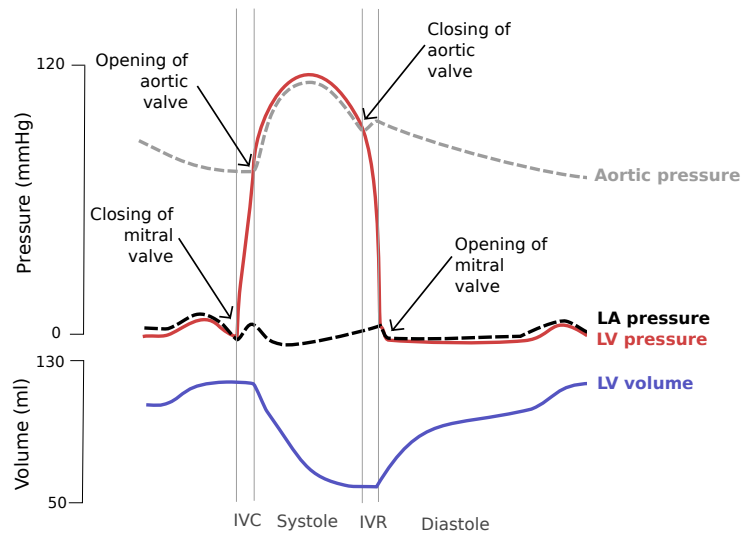
Figure 1.2 Wigger diagram, showing LV, LA and aortic pressures as well as LV volume, through the phases of the cardiac cycle.

Diastole is the portion of the cycle during which blood from the left atrium fills the left ventricle, leading in an increase in ventricular volume. Diastole, covering approximately two thirds of the cycle, is commonly divided into three regimes, early diastole, diastasis and end diastole. During early diastole, rapid active tension decay increases the pressure difference between LA and LV, causing opening of the mitral valve. This phase is characterised by rapid blood flow and accounts for 70% of ventricular filling. As ventricular volume increases, ventricular pressure rises during diastasis, causing a drop in the pressure gradient and thus in blood flow into the LV. Subsequently, atrial systole occurring at end diastole causes a peak in atrial pressure providing an additional 20% of ventricular filling (atrial kick)[84].

Isovolumic contraction is the period during which LV pressure rises without correspond-

ing volume change. Due to active tension development and ventricular contraction, LV pressure increases but is still lower than aortic pressure and thus not sufficiently high to open the aortic valve. The increase in pressure causes the mitral valve to shut, keeping LV volume constant during this period.

Once LV pressure increases sufficiently due to contraction, the aortic valve opens, initiating *systole*. During early systole blood is expelled rapidly out of the LV and into the aorta. Due to contraction, the mitral valve is pulled towards the apex, causing atrial elongation and initiating atrial filling. As the contraction continues, ventricular pressure and aortic flow peak during mid-systole. Once maximal contraction occurs, ventricular pressure and blood velocity start declining, leading to the closure of aortic valve at end systole.

Finally, during *isovolumic relaxation*, the LV starts to relax as active tension decays and contraction ends. As both mitral and aortic valves are closed, the release of potential energy accumulated during contraction is restricted by the constant ventricular volume, leading to a rapid pressure decrease. In parallel, LA pressure becomes higher than LV pressure, causing the opening of the mitral valve and the onset of a new heart cycle.

1.1.3 Myocardial tissue structure

The heart wall is composed of three layers with different functional properties. The inner layer, or *endocardium*, is a thin lining between the wall and the cavities also covering the heart valves. The outer layer, or *epicardium*, is encased by the thin, fibrous pericardium which acts as a protective sac around the heart. The middle layer of the heart wall, called *myocardium*, is the functional part of the wall, responsible for the heart's ability to contract and deliver blood to the entire body.

The architecture of the myocardial tissue is a major determinant of both the passive and active cardiac behaviour. As such, the myocardial structure has been studied extensively over the last century and several theories have been proposed with significant variations. Early qualitative studies by MacCallum[143] and Mall[145] and later Robb[207] suggested that the ventricles are made of distinct fibre bundles, running from apex to base and spiralling near the apex. This theory was questioned by Grant[80], who demonstrated branching of fibres and suggested the presence of a complex helical array.

Further quantitative studies by Streeter[238,239], Greenbaum[81] and Fernandez-Teran[68] suggested that the myocardium can be more appropriately described as a continuous fibrous structure, a theory adapted by the majority of studies for more than two decades. Most importantly, these studies observed the transmural variation of fibre orientation, in porcine, canine and human hearts. They reported a fibre angle (measured

from the base) varying from $+60°$ to $-60°$ from endocardium to epicardium as well as circumferential fibre rings around the heart base.

A series of studies by LeGrice[134,133] offered a more detailed analysis of the rat and canine heart tissue, focusing on the laminar myocardial structure. Their work highlighted that the myocardium should not be considered as a continuous structure, as it is instead composed of discrete sheets of fibres – usually four to six cells thick. The sheets, or laminae, are located across the ventricular wall in an almost radial direction and are separated by cleavage planes. They are loosely bounded by perimysial collagen which allows relative movement between adjacent sheets. Recent advances in confocal microscopy have further enhanced and confirmed our understanding of myocardial structure, by enabling more comprehensive and accurate studies of myocardial tissue[132,216,287]. All these works contributed to establishing a generic modelling framework for incorporating fibre structure into finite element cardiac models[170], where the myocardium is described with respect to a fibre-oriented coordinate system.
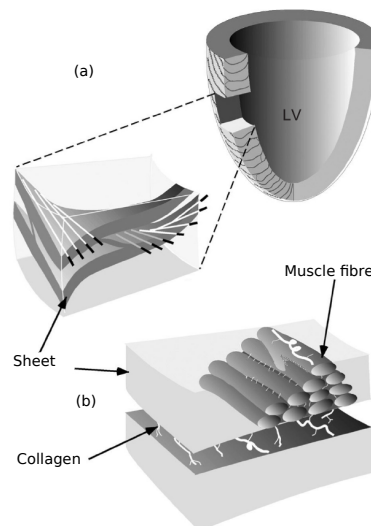
Figure 1.3 Schematic representation of myocardial structure by LeGrice[134,230]. **(a)** Trasmular variation of fibre orientation, and **(b)** close up to the laminar structure of the myocardium in which the sheets are composed of aligned fibres, bound by perimysial and endomysial collagen.

Even though the studies described above provided a comprehensive image of the ventricular architecture, they focused on canine and rat hearts. Early works by Greenbaum[81] and Fernandez-Teran[68] on human hearts provide important information on fibre architecture, yet they are based on gross tissue sections. Recent developments in diffusion tensor magnetic resonance imaging (DTMRI) have enabled the direct quantification of fibre and laminar structure of the human heart. Rohmer[208] *et al.* have performed a comprehensive analysis of ventricular fibre architecture from *ex vivo* human DTMRI data, predicting a transmural distribution similar to experimental animal

studies. Furthermore, preliminary studies of human *in vivo* DTMRI data by Toussaint *et al.* exhibited good agreement with *ex vivo* studies[251]. Although further work is required in order to allow for detailed regional and anatomical information, DTMRI derived fibres have alreal been used within cardiac models[266].

All these works have contributed to a better understanding of the complex tissue structure and its significance on cardiac behaviour. Even though alternative theories have been proposed, the most popular being the band theory by Torrent-Guasp *et al.*[250], the comprehensive data of LeGrice *et al.*[134,133] on the fibre and laminar structure of the heart, along with the fibre distribution proposed by Streeter *et al.*[239] remain the gold standard in most mathematical heart models.

1.1.4 Activation and contraction

Myocardial contraction is due to contractile forces generated by myocytes – or muscle cells – after electrical excitation. This process is initiated by electrical activation waves starting from the self-stimulating cells at the sinoatrial node and propagating through the atria. The waves then travel across the atria, causing atrial contraction, which assists the final stage of ventricular filling. The ventricles are electrically insulated from the atria, except at the atrioventricular (AV) node. Conduction is slow through the AV node, allowing sufficient time for ventricular filling prior to contraction. The depolarisation wave then stimulates the His bundle and the fast conducting Purkinje fibres, which rapidly depolarise the myocardial wall. Individual muscle cells generate contractile forces as the waves travel through them, leading to ventricular contraction.

In the microscopic level, cellular contraction is caused by the depolarisation wave propagating through a myocyte. The depolarisation wave causes a change in the myocyte's electrical potential, which in turn causes release of stored calcium. As the levels of cytosolic calcium rise, they enable compression of the myocyte's contractile unit, composed of actin, myosin, tropomyosin and titin. This initiates the "cross-bridge cycle", responsible for generating contractile force and cellular contraction. The synchronous activation of myocytes across the myocardium creates a contraction wave, generating the force responsible for driving blood flow around the circulatory system.

1.2 Dilated cardiomyopathy (DCM)

1.2.1 Description of DCM

Dilated cardiomyopathy (DCM) is a chronic myocardial disease characterised by the enlargement of the left ventricle and the gradual reduction in the pumping efficiency of the heart, that often leads to heart failure. It is the most common type of non-ischemic cardiomyopathy, occuring in 5-8 cases per 100,000, annually [23] and it affects more men than women. Low survival rates – 25% mortality rate over one year and 50% mortality rate over five years – suggest the need for a better understanding of the disease and the mechanisms underpinning its development and progression.

The currently limited understanding of this condition can be justified by the many heterogeneous diseases of varying etiologies that are associated with DCM. In fact, more than 75 known conditions can present the DCM phenotype [23]. The onset and progression of DCM can be attributed to viral infections [4], alcohol / drug abuse, genetics, thyroid disease, *etc*, but in most cases no specific etiology can be identified (idiopathic DCM). Due to the multi-factorial development of the disease, determination of its origin – and thus appropriate treatment for each patient – is a challenging task.

Numerous treatments have been suggested for DCM, ranging from pharmacological therapies to invasive procedures. DCM patients are commonly administered beta-blockers and ACE inhibitors to control blood pressure and abnormal heart rhythm. Beta-blockers, such as metoprolol, have been found to increase ejection fraction and stroke volume, and in some cases cause reverse remodelling for DCM patients [66]. Positive inotropic agents such as pimobendan have also been reported to have a beneficial effect on DCM patients, by increasing calcium sensitivity of myofilaments and enhancing cardiac contractility [59]. Furthermore, vasodilator drugs, such as nitroprusside, have been shown to decrease pressures and improve ejection fraction [89]. In general, studies report that reverse LV remodelling is possible, provided that the patients receive tailored neurohormonal treatment, and highlight the importance of early diagnosis and frequent individualised follow up [156].

Invasive surgical procedures have also been used to treat DCM patients. Left ventriculoplasty – also known as Batista procedure – is based on the hypothesis that removal of the non-viable part of the myocardial tissue would lead to constructive ventricular reverse remodelling and thus result in a more efficient heart [279]. As the effectiveness of this operation has been questioned, the procedure has been abandoned [201]. Other invasive treatments include pacing devices, applied in either one or both ventricles. Kass *et al.* reported enhancement in cardiac contractile function, especially with single-site pacing at the part of myocardial wall with greatest conduction delay [118], while Nelson *et al.* highlighted the low cardiac energy cost of this process [172], contrary to drug therapies

which tend to increase energy expenditure in an already inefficient heart. Recently, a woven polyester jacket placed around the ventricles has been suggested as a potential mechanism for reversing the progressive remodelling associated with DCM, presenting promising results in heart failure patients[147,272].

1.2.2 The biomechanics of DCM

Recent studies have sought to provide insights into the changes occurring in the heart as DCM develops and progresses, from cellular[3,16,150] to organ level[190,284].

The main characteristic reported by most studies is the enlargement of the left ventricle (Fig. 1.4), with dilation also observed for left atrium and right ventricle[206]. Focusing on the left ventricle, both end-diastolic and end-systolic volumes increase significantly[5,284], often leading to a decrease in the stroke volume[166]. Cardiac dilation is accompanied by moderate wall thinning[116,284], while the shape of the ventricle changes from elliptical to spherical[128,149,87].

Healthy heart   DCM heart
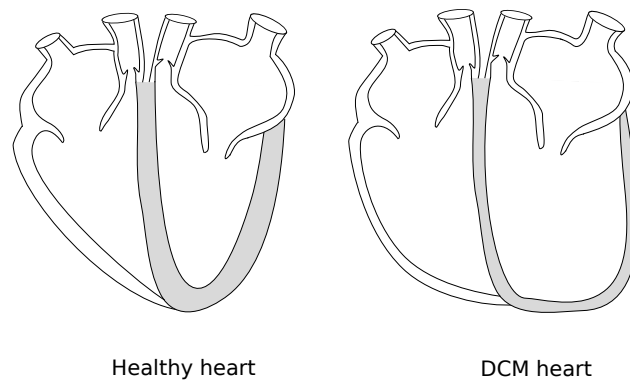
Figure 1.4 The effect of DCM on the geometry of the heart. The LV is significantly dilated and the myocardial wall becomes thinner and weaker. Enlargement is often observed in all cardiac chambers.

Anatomical remodelling occurring in DCM has a strong effect on heart function, during both the diastolic and systolic phases[206] of the cardiac cycle. The mechanical efficiency of the heart is severely impaired with ejection fraction as low as $20 - 25\%$[114]. The systolic phase can be significantly affected, characterised by intraventricular conduction delay[3], reduction in contractility[87], and prolonged relaxation time[89]. Diastolic function is also compromised, associated with abnormalities in LV filling due to low intraventricular pressure gradients[283,138]. Furthermore, both end-systolic and end-diastolic pressures are elevated[128,34], causing a shift to the pressure-volume loop (Fig. 1.5). Significant increase has also been reported for end-systolic and end-diastolic stresses in DCM cases[89,116].

Myocardial wall motion in DCM has been studied extensively based on observations

from various imaging modalities (echocardiography[128], speckle tracking echocardiography[60], MRI[284]). Several studies highlight that the wall is hypokinetic in DCM patients[89], both during systole and diastole[114,42]. Young[284], Joseph[114] and Chuang[42] tracked 2D tagged MRI to better capture the wall motion and reported significant reduction in strains. These studies also highlighted the regional variability in displacements and strains in DCM patients, observing larger deterioration in the septal wall compared to the lateral wall. In fact, Young reported thinning and lengthening on the septal wall during systole. Studies have also highlighted decreased LV torsion in DCM patients[284,42], which might also occur in the opposite direction compared to normals[184].

Heterogeneity appears to be a key feature in DCM, with regional variability reported for myocardial perfusion[116], systolic function[166], asynchrony[89] and myocardial work[279]. In fact, these heterogeneities are likely linked to the increased myocardial oxygen consumption reported in DCM[52,126]. Combined with the reduced external work observed in DCM hearts[5], cardiac mechanoenergetics have been identified as a major determinant of the disease, with studies highlighting that DCM hearts fail to satisfy the increased metabolic demand[126]. Elevated wall stress has also been recognised as an important indicator of DCM related to increased oxygen consumption[52] and regional variations in wall motion abnormalities and contractility[116,279,114].
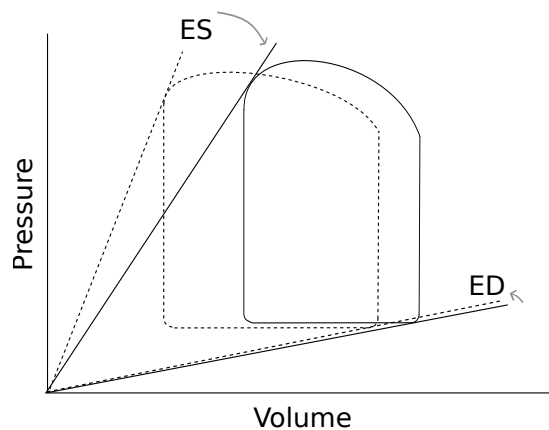
Figure 1.5 The effect of DCM on the pressure-volume loop. Dashed line shows the normal relationship.

Due to the complex structure of the heart and specifically the multifactorial nature of DCM, studies have investigated various aspects of the disease. At the cellular level, lengthening and transverse slippage of myocytes result in ventricular dilation, while interstitial fibrosis occurs in 20% of the tissue[16]. At the same time, a shift in the composition of myosin isoforms has been reported for DCM patients, which also correlated with elevated circumferential stress[95]. From the coronary hemodynamics point of view,

coronary flow is depressed in DCM resulting in reduced myocardial oxygen availability[171]. Particular focus has been given in DCM intraventricular hemodynamics with fluid dynamics models[142] reporting blood vortices of low intensity in DCM cases[19,34]. As diastolic vortices assist LV filling with minimal energetic or pressure cost, weaker vortices significantly damage diastolic function in DCM[148,19]. Finite element models have also been used to study the mechanics of DCM in mice[190,47] and dogs[272,201]. Omens[190] and Costandi[47] used these models to study chamber compliance and tissue stiffness, suggesting that the changes in compliance and stiffness observed in DCM could be in part responsible for the ventricular dysfunction in DCM hearts.

These studies have provided valuable insight into the changes in heart function and anatomy in DCM patients, contributing to a better understanding of the disease. Imaging studies have highlighted the LV dilation, reduction in ejection fraction and hypokinetic wall observed in DCM, yet they lack the mechanistic interpretation of these changes. On the other hand, studies aiming at linking the observed kinematics to specific mechanisms are often based on rough estimates of wall stress[206,89,284] or bulk measures such as pressure-volume loops[240,5], which cannot explain how abnormalities in heart function can affect cardiac performance.

Mathematical modelling can be used to link specific mechanisms to corresponding changes in cardiac function, by isolating the effect of individual parameters. Furthermore, it can provide important metrics which would otherwise require invasive measurements. Existing DCM cardiac models are limited and are usually restricted to animal studies[47,190] or *in silico* cases[13,142]. The development of comprehensive patient-specific models could provide a better understanding of the effect of increased stiffness, heterogeneity and mechanoenergetics, already identified as important features of DCM. Furthermore, recent advances in medical imaging, such as the development of 3D tagged MRI, offer a more detailed description of the heart kinematics, allowing for improved accuracy in model personalisation and thus more reliable model outcomes and interpretation.

1.3   Cardiac models

The cardiac cycle, which occurs 100,000 times per day, is actually based on very complex physical phenomena which occur across various spatial and temporal scales. Therefore, cardiac models of different focus have been developed, aiming to provide an understanding of the individual processes occurring during a heart beat. Spanning from microscopic to macroscopic heart function, these models include descriptions of cellular mechanisms, tissue mechanics, blood flow and coronary flow. All these phenomena are fundamentally interlinked, and thus models of coupled electromechanics and fluid-solid interaction have been developed.

1.3.1   Cardiac mechanics models

The manner in which the heart deforms, the tissue stiffness and the stress developed over the cardiac cycle are all important determinants of heart function and pathology. For instance, increased stiffness and stress, a common characteristic of diastolic dysfunction, are observed in many cardiac conditions (heart failure, DCM, hypertension, *etc*). As a result, models of cardiac mechanics relying on the basic conservation laws and principles of solid mechanics have been extensively employed for the study of heart behaviour in health and disease. Through decades of valuable research effort, cardiac mechanics have evolved drastically to incorporate realistic geometries and physiologically accurate constitutive behaviour. Owing to the development of finite elements for solid mechanics and the increased availability of computational power, as well as a plethora of experimental data on tissue behaviour, state of the art cardiac mechanics models are now a powerful tool for studying heart function.

The work described in this thesis relies on heart mechanics for studying and understanding the mechanisms behind DCM. Due to the significant remodelling observed in myocardial tissue in DCM patients as well as changes in tissue stiffness, cavity pressures and wall stresses, cardiac mechanics provide a convenient framework for an assessment of the disease.

1.3.1.1   Previous work on cardiac mechanics

Quantification of ventricular wall stress has been extensively studied, as stress is considered an important factor in cardiac pathophysiology. First attempts at quantifying stress in cardiac mechanics started with the pioneering work of Woods in 1892[275], who modelled the heart as a thin walled sphere. Even though significantly simplified, Woods' model inspired further applications of Laplace's law on thin walled spherical heart models[136], which identified ventricular size and shape as contributors to myocardial performance[27]. Building on this approach, Sandler[215] and Fry[70] derived analytical expressions for wall stress of a thin walled ellipsoidal heart model, providing a more accurate geometric representation of the LV[56].

Although these early heart models provided important insights into ventricular mechanics, they were unable to capture any transmural wall stress variation. Circumventing this issue, Wong and Rautaharju[273] and Ghista[75] modelled the left ventricle as a thick walled ellipsoid, and estimated nonlinear stress distribution through the myocardial wall. Mirsky[160] extended this work to include transverse shear and bending moments. Thick walled studies provided a notable improvement in describing heart mechanics. Furthermore, they elucidated the importance of accounting for large deformations[162] and nonlinear constitutive laws[161,165] in wall stress estimation, reporting a

10-fold increase in endocardial stress compared to the result predicted by linear elasticity[161].

Increasing experimental data highlighted the material and geometric nonlinearities, heterogeneity and anisotropy of the heart, suggesting the need for an alternative solution-approach. The advent of the finite element method (FEM) enabled more realistic models, by allowing regional variations, more complex geometries and nonlinear constitutive laws. In 1972, Gould *et al*[79] proposed a rotationally symmetric, isotropic 3D finite element model based on a patient-specific geometry, which showed that stresses are affected by variations in wall curvature - a result that could not be predicted by simpler models. Pao *et al.* extended this work to allow for variable wall thickness and reported a nonlinear stress distribution transmurally[194]. In parallel, Janz and colleagues developed a series of finite element models, reporting significant effects of heterogeneity[111], nonlinear constitutive laws[112] and large deformations[113] on myocardial mechanics. More realistic model conditions were considered by Heethaar *et al.*[90], who developed the first biventricular, non-axisymmetric, finite element model and reported compressive stresses at the septal wall. Furthermore, Panda *et al.* examined the influence of fibre orientation on an orthotropic finite element model[193], observing a significant difference in stress distributions. These first FEM studies highlighted the importance of geometry, fibre architecture and constitutive behaviour on cardiac mechanics.

As experimental quantification of stress was deemed unreliable[280], validation of these models and further understanding of cardiac behaviour was sought through experimental and mathematical studies of ventricular strain. A series of studies on biaxial tests[55,153,282] demonstrated the anisotropic behaviour of the tissue, while finite elements and homogeneous strain theory were used to analyse the strain distributions[153,154]. Particular attention was attributed in understanding the relation between fibre architecture and myocardial deformation[261], revealing that maximum epicardial strains are observed in the fibre direction[154] while maximum endocardial strains occur at the cross-fibre direction[189]. Additionally, several studies hypothesised that the fibre distribution is optimised to enable uniform fibre strain and stress distributions[82,6,46] while being energetically efficient[259]. Bovendeerd tested this hypothesis in a finite element model and predicted a fibre configuration to uniformly distribute fibre stresses, which compared well with experimental data[22]. The "optimality" hypothesis[106] was also extended to suggest that the laminar heart architecture facilitates shear and thickening during contraction. Specifically, Arts[6] tested the hypothesis that laminae are aligned with planes of maximum shear – a mechanism that would allow large shear strains without similar increases in shear stress – predicting a sheet distribution matching well with histological data.

Further experimental detail[239,55,282] led to the development of more physiologically ac-

curate finite element models. Several studies focused on the effect of fibre architecture on mechanical response[22], following Nielsen's framework for incorporating the heart's fibrous structure into a finite element model[177]. Within this framework, a number of trasversely isotropic and orthotropic constitutive laws were proposed[82,44,170,98] which significantly improved matching between model and experimental results[188,183]. Further development in numerical methods and computational power allowed for more accurate and efficient finite element models, which used refined[260] or higher order elements[170] and included an accurate representation of both left and right ventricles[236].

Experimental studies also revealed the presence of residual stress and strain in the unloaded myocardium, since a radial cut causes a ring of tissue to open into an arc[187]. Two- and three-dimensional strain measurements suggested the presence of a compressive circumferential endocardial stress[187,45] which could reduce the peak endocardial stresses predicted by nonlinear models[187] and a tensile epicardial stress. Costa *et al.* reported a similar trend for fibre strains, while it has been hypothesised that the residual stresses act to evenly distribute fibre stress across the myocardial wall[82]. Residual stress is typically neglected in models of cardiac mechanics, due to the additional theoretical considerations and assumptions required. Wang *et al.* used a modified constitutive law accounting for residual stress, to investigate its effect, and reported a non-negligible effect on the stress distribution during diastole[263]. This formulation, however, requires an estimation of the reference / unloaded domain, which, in turn, introduces further complexity and requires additional assumptions.

Finally, the latest advances in medical imaging, numerical techniques and cardiac models have made the creation of patient-specific mechanics models possible. Over the last decade, models were significantly improved to include anatomically accurate geometries[127,8,278], and personalised fibre distributions[266]. At the same time, boundary conditions on the base[268,266] and apex[276] were prescribed directly from tagged and cine MRI data, enabling a more accurate representation of individual cases. Furthermore, model parameters were estimated by matching simulation results with data-extracted deformation,[266,265,278,73] providing a marked improvement when contrasted with earlier parametrisation studies relying on bulk measures such as pressure-volume loops or experimental data from excised myocardium.

Despite the remarkable advances made in the cardiac mechanics field since the early work of Woods[275], significant research effort is still required to improve model accuracy and enable safe assessment of cardiac pathologies. Unresolved modelling issues, such as the estimation of the unloaded geometry, the degree of tissue compressibility and the personalised fibre distribution, require further investigation and development to enable improved model accuracy. Moreover, systematic investigation of parameter identifiability complimenting patient-specific applications might be useful in ensuring

reliable – and potentially clinically useful – parameters.

1.3.1.2 Passive constitutive laws

Early finite element cardiac models assumed linear elasticity[111,79], a theory soon deemed inappropriate for ventricular mechanics[280]. Uniaxial[200] and biaxial tests[55] on isolated sections of ventricular myocardium showed a disproportionally rapid increase in stress for large strains. Furthermore, morphological studies on tissue structure[238,239,134] revealed a complex fibre architecture which significantly affects mechanical response[57]. These experimental findings led to the development of a series of nonlinear, hyperelastic constitutive laws, most of them defined with respect to a fibre-aligned coordinate system in order to capture the dependence of strains on fibre orientation. Table 1.1 summarises some of the cardiac constitutive laws proposed and used throughout the cardiac mechanics literature.

One of the first nonlinear constitutive laws used in cardiac models was an exponential law proposed by Fung to model biological tissues[71]. Several transversely isotropic laws were then developed which accounted for the fibrous structure of the myocardium[282]. Humphrey proposed a transversely isotropic exponential law composed of matrix and fibre terms[104]. Horowitz proposed a similar strain energy function incorporating further structural detail[100]. The material parameters of Humphrey and Horowitz's constitutive laws were estimated based on data from biaxial tests. Experimental data were also used to tune a transversely isotropic Fung type law proposed by Guccione[82], which was expressed with respect to strains in the fibre coordinate system.

Model	Structure	Par No	Data	Ref	Year
Humphrey & Yin	TISO	4	BA[282]	[104]	1987
Horowitz	TISO	8	BA[282]	[100]	1988
Humphrey	TISO	5	BA[183]	[103]	1990
Guccione	TISO	5	ES[154]	[82]	1991
Lin & Yin	TISO	4	MA	[137]	1998
Criscione	TISO	–	–	[49]	2001
Costa	ORTH	7	–	[44]	2001
Pole-zero	ORTH	18	LV, BA[229]	[169]	2001
Kerckhoffs*	TISO	4	BA[183], PV[178]	[119]	2003
Holzapfel & Ogden	ORTH	8	SH[57], BA[282]	[98]	2009

Table 1.1 Table of sample of cardiac constitutive equations published and used in the literature (Chabiniok *et al.*[32]). Abbrv: ISO=isotropic, TISO=transversely isotropic, ORTH=orthotropic, UA=uni-axial, BA=bi-axial, MA=multi-axial, SH=shear, PV=pressure-volume, ES=epicardial strains, LV=various literature values
*law also contains additional parameters for modelling tissue compressibility not included in the table

As more complete experimental data on myocardial tissue became available, models

were able to better capture the complex constitutive behaviour of the heart. Transversely isotropic models were replaced by structurally more accurate orthotropic models, as Dokos and LeGrice demonstrated that the orthotropy assumption is more suitable for the myocardial tissue[134,57]. The orthotropic extension of the Guccione law by Costa *et al.* has been widely used to model the myocardial tissue[44]. Although characterised as the more appropriate and robust constitutive law for the myocardial tissue by Schmid *et al.*[219], it is known to present parameter coupling due to its functional form[278].

Nash and Hunter circumvented this parameter coupling by introducing the orthotropic pole-zero law which expresses the strain energy function as a sum of its individual strain contributions[170]. In this formulation, the strain energy grows rapidly as the strain approaches the limit in each axis, and the constitutive parameters are fitted from uniaxial and biaxial data.

An alternative approach was to express the strain energy as a function of strain invariants. This approach was used by Humphrey who proposed a polynomial function of two strain invariants and tuned the five material parameters based on biaxial tests data[103]. Kerckhoffs *et al.* introduced a model involving invariants' dependence as well as a fibre strain dependence to account for the increased material stiffness in the fibre direction[119]. Holzapfel and Ogden proposed a structurally based orthotropic law based on invariants, which has been used extensively in models of cardiac mechanics. The parameters were tuned based on existing data on shear and biaxial deformation[98], while parameter coupling is limited, due to its structural form as a sum of individual strain contributions.

With a range of proposed cardiac constitutive laws, varying notably in structure, complexity and function (as indicated in table 1.1), the choice of an appropriate constitutive law is determined by the scope of each application.

1.3.1.3   Active constitutive laws

While the focus of this thesis is on the passive behaviour of the heart, the active component is equally important, characterising ventricular contraction which drives the cardiac cycle. Early models of myocardial contraction were based on the skeletal muscle model by Hill[94] and Huxley[108]. As more accurate experimental data and detailed calcium models became available[246], complex, biophysically based contraction models were developed. Models of varying complexity are used nowadays, depending on the needs of specific applications. Simple active tension models such as those proposed by Kerckhoffs[119] and Niederer[175], aim to capture the basic characteristics of the mechanics of active contraction, namely the nonlinear development of active tension and its dependence on sarcomere length and rate of extension. The comparatively small

number of parameters, makes these models attractive for patient-specific applications where limited data are available.

More complex models include a more detailed description of the cellular mechanisms responsible for contraction[258,269,182], by modelling the calcium concentration through an ODE system. Active tension development is then related to fibre length and activation level. The HTM model proposed by Hunter *et al.*[105] has also been used in patient-specific applications[267,277]. In the majority of these models, the active tension is incorporated into the three-dimensional heart model through the addition of an active stress component along the fibre direction. Usyk[254,255] also included transverse components of the active stress tensor, following conclusions drawn from biaxial experimental data.

1.3.1.4   Incompressibility/near incompressibility in cardiac mechanics

The myocardial tissue – like other muscle tissues – is traditionally considered incompressible. The various components of the solid myocardium, along with the blood flowing through it, are in fact incompressible materials[281]. At the same time, studies have shown that the volume of the myocardium changes through the cycle due to the extensive perfusion of blood through myocardial tissue. Based on their findings, the vascular network – constituting $10 - 15\%$ of the myocardial volume – is squeezed or extended[96,141] depending on the cardiac phase, leading to changes up to $5 - 10\%$ in the total myocardial volume[64,110,115]. Additionally, studies performed by Taber *et al.*[244] suggest that assuming compressibility can better approximate the results from torsion experiments in the myocardium.

As the degree and influence of compressibility on heart mechanics remains unclear, this ongoing debate concerning the incompressibility of the myocardium is commonly discussed[78,281]. Indeed, models representing the myocardial tissue as both compressible[119,254,255,78,88] and incompressible[231,236,170,44,188] are found throughout the literature.

While the choice of modelling the cardiac tissue using incompressible or nearly incompressible formulations is inherently based on tissue behaviour, it also relies on numerical considerations concerning the scheme employed for enforcing incompressibility / near incompressibility. A range of numerical schemes have been applied in heart models, one of the most popular being the penalty method, which, however, is linked to locking phenomena. Mixed formulations such as the Lagrange multiplier (LM) and the Perturbed Lagrangian (PL) methods are also commonly used in models of cardiac mechanics, however, they incur larger computational cost due to the introduction of additional variables. Nevertheless, the LM method is commonly employed to enforce incompressibility in heart mechanics, as it provides an accurate and efficient option for

the solution of moderate size problems.

1.3.2 Other types of cardiac models

1.3.2.1 Electromechanics models

An important component of the heart function is the electrical activation, responsible for the myocardial contraction which drives the cardiac cycle. As electrical activation and tension generation are interlinked[130,176] (tension depends on the current state of deformation, and can alter calcium buffering which, in turn, affects tension generation), coupled electromechanics models have been developed which allow feedback mechanisms between the electrophysiological and mechanical functions of the heart. Tension is commonly expressed as a function of strain, strain rate, calcium concentration and electrophysiology state variables (see section 1.3.1.3), whose dynamics are in turn expressed as ODE systems depending on transmembrane potential[120,182].

Coupled electromechanics models are mainly categorised by their level of coupling. In weakly coupled models[256,221], the electrical activation is computed separately using Eikonal mapping[248] or the solution of mono- or bi- domain equations[74]. The electrical activation time is then passed to an active tension model, which is used within the finite element framework to provide tissue deformation. In strongly coupled models[233,173], the active tension, tissue deformation and electrical activation are solved simultaneously, thus implicitly capturing feedback mechanisms between deformation and electrophysiology, which weakly coupled models may neglect. This of course comes at an increased computational cost for the strongly coupled models. Nevertheless, recent advances in parallel implementation of finite element electromechanical models[257,2] and increased available computational power alleviate this issue.

1.3.2.2 Models of blood flow and fluid-solid interaction

The flow of blood through the heart is typically modelled using the Navier-Stokes equations, assuming that, at the macro-scale, the blood is a Newtonian fluid. Several models of blood flow have been proposed, using the finite difference[58,197], finite volume[212] or finite element[53] solution methods and showing similar qualitative behaviour to experimental data[213,218]. Recent advances have also enabled patient-specific blood flow models[53]. These models however are limited, as increased interest in understanding the interplay of mechanical energy between blood and tissue led to the development of several fluid-solid coupled cardiac models.

Coupling blood flow and ventricular mechanics usually requires enforcement of kinematic and traction compatibility conditions on the endocardial boundary of the wall

and cavity domains[182]. One of the first coupled fluid-solid heart models was the pioneering work of Peskin and McQueen who used an immersed boundary method and included both left and right ventricles and heart valves[155,198]. Following this approach, Lemmon and Yoganathan created an idealised left heart model to study the blood flow behaviour between left atrium and ventricle[135]. A series of finite element coupled fluid-solid models were also developed, one of the first being the two-dimensional model by Chahboune[33]. More detailed constitutive laws were used by Watanabe[269], while Cheng[40] developed a more numerically rigorous fluid-solid LV model. Further advances were introduced by Nordsletten[181,182] and McCormick[152] who incorporated patient-specific geometries and anisotropic tissue constitutive laws on resolved non-conforming computational grids. Recently, Gao *et al.* used the immersed boundary method to develop a diseased LV finite element model which considered heterogeneous material parameters[72].

Fluid-solid interaction models provide quantitative information on blood flow patterns within the LV cavity, assisting the study of valve-related cardiac conditions. Due to low blood viscosity, shear stresses on the endocardial wall are small, hence traction is predominately affected by intraventricular blood pressure. As spatial variation of intraventricular pressure is small over the cardiac cycle[62], ventricular mechanics are not significantly affected by the blood flow distribution.

1.3.2.3 Coronary blood flow models

Coronary vasculature is intimately integrated into myocardial structure and function. Recent advances in computational methods and medical imaging of coronary vasculature[91,235] have encouraged the creation of several models studying the mechanical interaction between coronary flow and the myocardial wall. These include continuum mechanics models, where the Navier-Stokes equations are solved on coronary vascular meshes[232,249]. One-dimensional approximations[107,234,232] are currently the preferred approach, as they are able to capture the basic features while remaining computationally tractable[131]. 3D models have also been developed and applied in patient-specific applications[249,271], but they are limited due to their high computational demands. Finally, the poroelastic modelling approach was employed in order to capture phenomena in the micro-circulation scale[109,43,37,151]. Replacing wall and fluid domains with one complex structure, this approach can capture basic flow features and investigate fluid-solid interaction without the need to consider individual vessels.

Coronary blood flow models provide valuable insight into the factors contributing to coronary heart disease, the leading cause of death worldwide. While accounting for the contribution of coronary blood flow might elucidate important aspects of transport processes, in particular transport of metabolites, the impact of perfusion on ventricular

mechanics is not yet well characterised.

1.4 Patient-specific models of cardiac mechanics

Recent advances in medical imaging, image analysis and computational methods have driven the development of patient-specific cardiac mechanics models. Patient-specific geometries, loading and boundary conditions are combined to provide a mathematical representation of individual hearts. Patient-specific models hence allow the transition from population-based theoretical studies to more physiologically accurate, personalised investigations. This enables the estimation of clinically relevant metrics, otherwise inaccessible *in vivo*, and provides a framework for personalised *in silico* tests of potential treatments and outcomes.

1.4.1 Available clinical data

A variety of cardiac imaging techniques have been developed and evolved over the last four decades. Offering detailed quantitative and qualitative information on the heart's structure and behaviour, cardiac imaging creates a reliable basis for patient-specific modelling.

Echocardiography (simply referred to as echo) has been extensively used to capture myocardial motion and hemodynamics. It is the most common diagnostic tool in cardiology, providing a wealth of information on heart's morphology, efficiency and potential damage or pathology. Due to its nonivasive, risk-free nature combined with its low cost compared to CT or MRI, echocardiography is routinely used in clinical practice, despite its low signal-to-noise ratio and limited image quality. Multiple studies have used echo data to study heart function, personalise geometries[1] and compute cavity volumes throughout the cycle[124]. Furthermore, the development of speckle tracking echocardiography[157,48] has enabled quantification of regional cardiac motion and tissue deformation.

Cardiac CT has also been used to provide detailed, high resolution images of the heart. In several cases, an iodine-based contrast dye is used to highlight blood flow, resulting in accurate images of the heart morphology. Cardiac CT is often recommended to assist the diagnosis of coronary heart disease, pulmonary embolism, or general problems with heart function. CT images have been used to provide personalised geometries for patient-specific models[159,124], while automatic tracking algorithms have been applied to provide the endocardial and epicardial motion throughout the cardiac cycle[199]. The use of CT for research purposes and wider use in the clinic is restricted by the radiation risks associated with this modality.

Cardiac MRI is increasingly used in research and clinical practice to acquire high resolution and accurate images of the heart. Combined with ECG synchronisation, it provides detailed static and dynamic images of the heart throughout the cardiac cycle. More sophisticated techniques such as cine MRI[253], steady-state free precession (SSFP) cine sequences[217] offer more detailed dynamical and morphological characteristics. Due to the sufficient contrast between tissues, cine MRI provides information on tissue characteristics such as scar and fibrosis. Used together with automatic tracking algorithms which accurately extract the motion of myocardial surfaces during the cardiac cycle, cardiac MRI has gained significant popularity in cardiology and cardiac mechanics community[266,276]. As opposed to CT, it is not harmful, yet it requires long acquisition times and is more expensive than echo and CT.

Although cardiac MRI and tracking algorithms can provide detailed information of the endocardial and epicardial motion, limited information is available on through-wall motion, torsion or shear effects. The development of tagged MRI (SPAtial Modulation of Magnetisation, SPAMM)[289,11,205] has addressed these issues. Enabling the detailed assessment of regional cardiac motion *in vivo*, tagged MRI reveals local characteristics such as wall thickening, torsion and shear. The technique is based on a periodic saturation of magnetisation within the heart wall resulting in a set of dark lines (signal void) which deform with the myocardial wall. The motion and deformation of the heart wall can then be reconstructed through tracking of the tag grid using mainly harmonic phase analysis (HARP)[191,192,7], or image registration methods[285,225]. The translation from 2D to 3D tagging techniques[211] has enabled a direct extraction of full 3D displacement field of the myocardium leading to simultaneous quantification of radial, circumferential and longitudinal motion[225,192]. This technique, along with cine MRI will be discussed further in the following chapters, as the personalised models developed in this thesis are based on cine and tagged MRI data.

Another MRI technique is Diffusion Tensor MRI (DTMRI). DTMRI relies on the different diffusion properties of water into different structures (tissue, bone, *etc*) to reveal the fibrous and laminar structure of the heart. This non-invasive technique has started to gain popularity after exhibiting good matching with experimental data, both *ex vivo*[208] and *in vivo*[251].

Additionally, MRI can provide a detailed quantification of blood flow through the valves and ventricles. Recent advances in 3D velocity encoding and 4D Phase Contrast MRI (4D PCMRI)[252,14] have enabled a comprehensive characterisation of blood flow patterns and potential abnormalities. 2D PCMRI has also been used to provide a quick characterisation of unidimensional flow through mitral and aortic valves and the main vessels.

Complimenting the wide variety of imaging data, ventricular pressure is a critical determinant of cardiac function and as such is often recorded through catheters. Due to

the invasiveness of this procedure, alternative techniques have been devised such as empirical curves which provide estimates of the end-diastolic pressure[122] or the pressure trace throughout the cycle[210]. End-diastolic pressure can also be estimated through measurements of the early diastolic velocity of the flow through the mitral valve and velocity measures in the mitral valve plane[167]. 4D PCMRI data have been combined with modelling to provide intraventricular pressure gradients[125]. Relative pressure can also be assessed through microbubble-based ultrasound contrast agent[51]. Moreover, transformation functions applied on radial artery pressure provide estimates of central blood pressure[117], which in turn provides an estimate for systolic intraventricular pressure.

1.4.2 Model personalisation

1.4.2.1 Personalised geometry

The wide range of clinical data has served as a basis for the creation of patient-specific finite element LV models. The most common use of imaging data in modelling studies is towards the personalisation of the model geometry. Echocardiography[60], CT[159] and MRI[9] images have been used in many patient-specific models. Commonly, manual or automatic segmentation[63,290] of the end-diastolic frame provides a mask which is then processed in meshing software[127] to provide the final patient-specific mesh. Incorporating personalised geometries is crucial for accuracy, as wall curvature[79], thickness[194] and cavity volume have a significant effect on cardiac behaviour and pathophysiology. The recent advent of DTMRI has also enabled the construction of personalised fibre distributions which have been incorporated in patient-specific meshes[266]. An alternative approach is the use of statistical atlases for both the geometry[99] and fibre distributions[76], for the creation of personalised geometries.

1.4.2.2 Personalised boundary conditions

Clinical data also assist in model personalisation by providing appropriate boundary conditions for the finite element model. The choice of boundary conditions is a crucial but challenging step in model development, as the heart is not isolated in the human body but instead constrained by the surrounding organs, diaphragm and large vessels. Boundary conditions are usually applied on the endocardial, epicardial and basal boundaries of the LV model.

Traditionally, endocardial boundary conditions are responsible for driving diastolic simulations. Most commonly, pressure measurements are applied on the endocardial boundary to simulate diastolic filling[266,276]. Data-derived volume trace has also been used as an endocardial boundary condition to drive the LV simulation through the whole

cycle[9,85]. Volume and flow data are also used as boundary conditions on Windkessel models, which provide a representation of the systemic and pulmonary circulations and in turn can act as boundary conditions for the LV model[269,121].

Epicardial and basal boundary conditions have been used to incorporate data-derived motion into the model. These can be applied through Dirichlet boundary conditions, however, strict enforcement of the boundary condition might yield hydrostatic pressure singularities or unphysiological stresses. Recently proposed basal boundary conditions which are based on weak enforcement of data constraints through Lagrange multipliers have provided promising results, restricting localised stress and pressures peaks[9].

1.4.2.3 Parameter estimation

A critical step in model personalisation is the estimation of model parameters based on the available clinical data. This process is essential as it enables the best match between the model and the data, making the model a more accurate representation of the data and thus more reliable. Moreover, it allows the quantification of model parameters which are often linked to cardiac behaviour and can be used as clinical biomarkers of health or disease.

The main idea is retrieving the parameter set that minimises a metric of "difference" or "distance" between the model-predicted outcome and the available data. Different approaches have been used, depending on the data available in each application. Wang *et al.* estimated passive parameters by matching end-diastolic volume between model and data[268], while Asner *et al.* used the cavity pressure to estimate passive and active parameters throughout the cardiac cycle[9]. The transition from bulk metrics, such as cavity pressure and volume, to more detailed metrics, such as tissue displacement and strain, allowed for more accurate parameter estimation. Gao *et al.* estimated passive parameters combining information from volume measurements and circumferential strains from short-axis cine MRI[73]. Chabiniok *et al.* estimated tissue contractility in multiple regions based on the extracted motion of the endocardial and epicardial surfaces from cine images[30]. 2D tagged MRI were also used in parameter estimation applications, offering detailed information on regional motion[221,266]. The transition to 3D tagged MRI has enabled an accurate whole-heart 3D deformation field, creating an ideal setting for estimation of model-based parameters using tissue displacement observations[278,277,8].

Various methodologies have been proposed for parameter estimation, including variational[186,241,276] approaches which usually involve iterative processes such as SQP[10,266], adjoint methods[223], or similar nonlinear least square methods[262]. Filtering assimilation approaches have also been used in cardiac mechanics. These incorporate information regarding measurement noise and model error in the estimation pro-

cess[163,164,276,274,140].

1.4.3   Challenges of patient-specific modelling

Patient-specific cardiac models have evolved dramatically in the last few decades, and are now able to incorporate accurate geometries, data-derived boundary conditions and personalised model parameters. Nevertheless, particular modelling aspects remain unclear and require further investigation and improvement.

1.4.3.1   Parameter identifiability

Naturally, the main difficulties of patient-specific modelling stem from the complexity of the cardiac motion. The nonlinear behaviour of the tissue, combined with the highly interlinked complex processes occurring during a cardiac cycle, make an accurate representation of the heart behaviour a challenging task. The detailed experimental data available today have enabled the development of several passive and active constitutive laws that are able to capture the basic characteristics of the heart behaviour. Furthermore, in order to decrease the inevitable error between model and data, more complex constitutive laws need to be employed which naturally increase the computational cost of the problem.

The choice of constitutive laws becomes more elaborate when model parameters are also of interest. These are often related to physical properties of the heart, such as stiffness or contractility, and can therefore be used as clinical biomarkers of disease[264,30]. As a result, there is a strong need for reliable parameter estimates, an issue which depends on both the underlying cardiac constitutive model as well as the available clinical data. Clearly, as the model complexity and number of parameters increase to better approximate tissue behaviour, estimating model parameters uniquely and accurately becomes an increasingly challenging task[278]. This raises the important question of *structural identifiability* for the various constitutive laws, *i.e.* whether it is possible to uniquely determine parameter values, given infinite well-defined noise-free data[41,203]. Structural identifiability is a property of the model itself and does not depend on the available data. It can be compromised by coupling between model parameters and nonlinear dependence of the model on the parameters. Lack of structural identifiability hinders the ability of any data assimilation method to accurately estimate parameter values.

In a clinical setting, the estimation process is further compromised by limited data resolution and quality, leading to the issue of *practical identifiability, i.e.* whether we can determine unique parameter estimates given a particular type of data[214]. The absence of structural or practical identifiability in a cardiac law given a set of data

leads to unreliable parameter estimates which can no longer provide clinically relevant information. The choice of an appropriate cardiac constitutive law should therefore balance the need for *model fidelity, i.e.* the ability of the model to accurately represent cardiac function, with the requirement for reliable, identifiable parameters.

1.4.3.2 Reference configuration

Another challenging aspect in building personalised heart models is the choice of the reference domain. Even though no stress-free state of the heart exists during the cardiac cycle, a common approach is to assume one from the observed motion states[266,278]. Attempts have been made to estimate the reference state – or unloaded geometry – usually based on assumptions regarding the constitutive law, parameters, boundary conditions, end-diastolic pressure, *etc*[277,124,263]. The estimated reference domain is therefore dependent on the assumptions which might in turn affect the estimated model parameters, model deformation and response. Through consideration of different data frames as reference domain, the effect of this assumption on the parameter identifiability and estimates can be assessed.

1.4.3.3 Data integration

The available clinical data provide the opportunity for model personalisation, yet their integration into cardiac models requires careful consideration and processing. A difficulty arises from potential inconsistencies between available imaging modalities, introducing the need for their spatio-temporal registration. Additionally, data often suffer from noise or artefacts due to patient's motion or breathing and are likely to be further compromised by processing artefacts. Incorporating incomplete / noisy data into the model using commonly employed boundary conditions often results in non-physiological outcomes. This issue can be alleviated through the use of appropriate boundary conditions[9], essentially relaxing the data constraint and avoiding strict adherence to non-physiological data.

1.5 Thesis outline

This thesis is divided into two main parts. Part I deals with theoretical considerations and *in silico* tests, performed to assist the choice and development of a patient-specific cardiac mechanics model, which can be customised in an optimal way using the available medical data. Part II extends the developed personalised model to *in vivo* applications, where the proposed pipeline is tested.

Chapter 2: The objective of this chapter is to briefly present the fundamental mathematical and engineering background necessary for the derivation of the mechanical heart model. The basics of finite elasticity – within which cardiac mechanics are studied – are presented, along with the Galerkin finite element method, employed for the solution of all mechanical tests throughout this thesis.

Chapter 3: The degree of compressibility as well as the solution approach for enforcing it are unresolved issues in heart modelling. This chapter aims to analyse and compare solution approaches for enforcing incompressibility / near-incompressibility in cardiac mechanics. Commonly used methods (penalty and Lagrange multiplier methods) along with a modified displacement-only formulation are compared in terms of accuracy and efficiency. The modifications introduced in the latter approach to enhance its efficiency are also presented.

Chapter 4: The choice of a suitable constitutive law is of particular importance for personalised cardiac mechanics. Focusing on the need for a constitutive law which provides a balance between model fidelity and parameter identifiability, this chapter compares the identifiability of various cardiac constitutive laws, when the available data source is 3D tagged MRI. The considered models are also compared with respect to their ability to accurately capture heart behaviour, resulting in identifying a model that combines these basic requirements.

Chapter 5: Applying the modelling considerations investigated in previous chapters, this chapter describes the pipeline followed for the development of personalised models for the study of DCM. Emphasis in this chapter is placed on optimising the use of the available data through the choice of appropriate boundary conditions while ensuring reliable estimation of passive parameters.

Chapter 6: The aim of this chapter is to test and validate the proposed pipeline. Of interest are modelling attributes that can improve model accuracy and parameter identifiability *in vivo*, mainly the assumed fibre distribution and the employed boundary conditions. Systematic investigation of these modelling aspects over several volunteers and patients enables an accurate assessment of their effect, and examines the robustness of the pipeline.

Chapter 7: This chapter focuses on comparisons between DCM patients and normals. Initially, data-derived metrics are compared over the two groups. Of particular importance are model passive parameters, and their variation in patients and normals. Additional insight is obtained through examination of regional strain distributions.

Chapter 8: The work presented in this thesis is summarised in the last chapter, where directions for future research are discussed. Emphasis is on utility of the personalised models considered in improving our understanding of DCM.

Part I

Model Development

2 Finite element cardiac models

Mathematical modelling is a powerful tool for studying and understanding the complex biological processes occurring during the cardiac cycle. Based on fundamental laws of physics as well as empirical knowledge of myocardial behaviour, mathematical cardiac models provide a simplified – yet quantifiable – representation of heart function. The framework in which models of cardiac mechanics models are developed and studied is continuum mechanics, where continuum representations of fundamental quantities and conservation laws are used to characterise myocardial function.

This chapter presents the derivation of a continuum mechanics cardiac model – solved using the Galerkin finite element method – which will be used throughout the thesis as a basis for studying the behaviour of the heart. Building on the generic framework presented in this chapter, personalised cardiac mechanics models will be used to analyse the differences in function and behaviour between DCM patients and healthy volunteers.

Initially, a description of a model problem is presented (section 2.1), to assist the derivation of the equations governing cardiac mechanics. Section 2.2 provides a brief overview of important kinematic quantities, which are utilised in the definition of conservation laws, governing the behaviour of the mechanical system (section 2.3). Deformation and strain metrics are also essential for the characterisation of the passive myocardial behaviour, through hyperelastic constitutive laws (section 2.4). Owing to the material and geometrical nonlinearities of the cardiac mechanics problems considered throughout this work, the finite element method is employed for the their solution. Within the finite element framework, the governing equations are recast in their weak forms (section 2.5), while geometry and primary variables are approximated by their finite-dimensional variants (section 2.6). The mechanics problems considered in this thesis are solved using the software package, $\mathcal{C}$**Heart** (section 2.7).

2.1 Preliminaries

In this section, we consider the motion of a body, under the action of certain loading constraints (Fig. 2.1). The description of this model problem will be used throughout the chapter for the study of kinematics, and conservation principles.
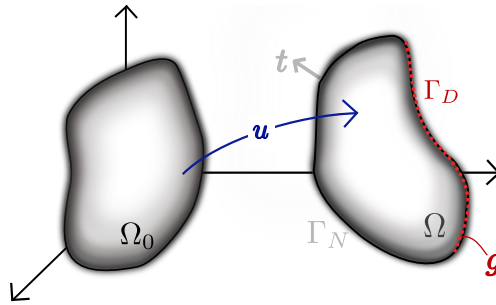
Figure 2.1 The reference (Ω_0) and deformed (Ω) domains under consideration. $\Gamma = \Gamma_D \cup \Gamma_N$ represent the boundaries in the deformed domain, subject to Dirichlet ($\boldsymbol{g}$) and Neumann (traction $\boldsymbol{t}$) conditions, respectively.

The body under consideration is initially defined by the reference domain Ω_0, and initial coordinates $\boldsymbol{X} \in \Omega_0$. At time t, as the body deforms, it can be described by its physical domain $\Omega(t)$, using the coordinates of its current position $\boldsymbol{x}$. The displacement or deformation of the body can then be obtained as $\boldsymbol{u} = \boldsymbol{x} - \boldsymbol{X}$. The motion of the body through the time interval $I = [0, T]$ can be expressed mathematically through a bijective mapping ϕ,

$$\phi : \Omega_0 \to \Omega(t), \quad \boldsymbol{x} = \phi(\boldsymbol{X}, t), \quad \forall \boldsymbol{X} \in \Omega_0, \ \forall t \in I, \tag{2.1}$$

which maps points in the undeformed domain to their position in the deformed domain. Additionally, the mapping is defined so that regions on the reference boundary ($\Gamma_0 = \Gamma_0^D \cup \Gamma_0^N$) are mapped to regions on the physical boundary ($\Gamma = \Gamma_D \cup \Gamma_N$).

The body deforms under the action of a body force $\boldsymbol{f} : \Omega \to \mathbb{R}^d, d \geq 1$, per unit volume, some boundary traction $\boldsymbol{t} : \Gamma_N \to \mathbb{R}^d$, per unit area and a Dirichlet boundary condition, such that $\boldsymbol{u} = \boldsymbol{g}|_{\Gamma_D}$. Here, d is the spatial dimension of the body, which for the remaining chapter is assumed $d = 3$, as mainly 3-dimensional problems are considered throughout this thesis.

Most quantities in models throughout the work presented are described with respect to the undeformed domain $\boldsymbol{X}$, although in certain cases – where convenient – quantities are expressed with respect to the physical domain. A function $f : \Omega_0 \to \mathbb{R}$, can be

represented on the deformed domain $\Omega(t)$ as:

$$\hat{f} : \Omega(t) \to \mathbb{R}, \quad \hat{f}(\boldsymbol{x}, t) := f(\boldsymbol{X}, t) = f(\phi^{-1}(\boldsymbol{x}), t), \quad \forall \boldsymbol{x} \in \Omega, \ \forall t \in I. \tag{2.2}$$

For convenience, functions in the deformed domain are denoted by their notation in the undeformed domain (*i.e.* f instead of $\hat{f}$).

The standard mathematical notation is used throughout the thesis to describe vectors, vector spaces, tensors and operations[21,202,25]. For example the usual definitions are used for the L^p and Sobolev function spaces[38,202], where for $\boldsymbol{x} \in \Omega$ the L^p function space is defined as:

$$L^p(\Omega) = \left\{ h : \int_\Omega |h(\boldsymbol{x})|^p \, dv < \infty \right\}, \quad 1 \le p < \infty, \tag{2.3}$$

and the Sobolev space is defined as:

$$W^{1,p}(\Omega) = \left\{ h \in L^p(\Omega) : \frac{\partial h}{\partial x_i} \in L^p(\Omega), \ 1 \le i \le 3 \right\}. \tag{2.4}$$

Furthermore, considering two column vectors $\boldsymbol{a} \in \mathbb{R}^3$ and $\boldsymbol{b} \in \mathbb{R}^3$, the dyadic[21] or outer product $\boldsymbol{a} \otimes \boldsymbol{b}$ which transforms the vectors to a tensor field, is written as:

$$\boldsymbol{a} \otimes \boldsymbol{b} = \boldsymbol{b}\boldsymbol{a}^T, \quad (\boldsymbol{a} \otimes \boldsymbol{b})_{ij} = a_j b_i, \ i, j \in [1, 3]. \tag{2.5}$$

Similarly, the Hadamard product or double contraction[21] of two tensors $\boldsymbol{A} \in \mathbb{R}^{3\times3}$ and $\boldsymbol{B} \in \mathbb{R}^{3\times3}$ which transforms tensors to a scalar value, can be expressed as:

$$\boldsymbol{A} : \boldsymbol{B} = tr(\boldsymbol{A}^T \boldsymbol{B}) = tr(\boldsymbol{A}\boldsymbol{B}^T) = \sum_{i,j=1}^{3} A_{ij} B_{ij}. \tag{2.6}$$

2.2 Kinematics

Continuum mechanics can be used to characterise the motion of the body in section 2.1, through time and space. Mathematical characterisation of motion through different deformation and strain metrics is essential for cardiac mechanics, as kinematics are utilised in conservation laws and stress characterisation.

In order to quantify deformation, it is important to consider the change in infinitesimal vectors, which can be obtained using the deformation gradient $\boldsymbol{F}$. The deformation gradient[21] is the spatial gradient of mapping ϕ, and is defined as:

$$\boldsymbol{F} = \frac{\partial \phi}{\partial \boldsymbol{X}} = \frac{\partial \boldsymbol{x}}{\partial \boldsymbol{X}} = \nabla_{\boldsymbol{X}} \boldsymbol{u} + \boldsymbol{I}, \tag{2.7}$$

where $\nabla_{\boldsymbol{X}}$ denotes differentiation with respect to the undeformed domain. The deformation gradient can map infinitesimal vectors in the reference domain into infinitesimal vectors in the physical space ($d\boldsymbol{x} = \boldsymbol{F} d\boldsymbol{X}$), characterising the change in their length and direction.

$\boldsymbol{F}$ can also be used to relate infinitesimal areas and volumes in the undeformed domain to their deformed equivalents, since infinitesimal areas and volumes may be expressed by operations on infinitesimal vectors. Accordingly, undeformed area $d\boldsymbol{A} = dA \, \boldsymbol{N}$ can be related to the deformed area $d\boldsymbol{a} = da \, \boldsymbol{n}$, using Nanson's formula[168]:

$$da = J\boldsymbol{F}^{-T}d\boldsymbol{A}, \tag{2.8}$$

where $\boldsymbol{N}$ and $\boldsymbol{n}$ are the undeformed and deformed normal vectors to the surface, respectively. Similarly, local volumes before and after deformation can be related using the determinant of the deformation gradient ($J = \det \boldsymbol{F}$):

$$dv = J \, dV, \tag{2.9}$$

where dV and dv are infinitesimal volumes in the reference and deformed domain, respectively. Based on this expression, if the mapping ϕ conserves volume (*i.e.* $dv = dV$) it follows that $J = 1$. Therefore, the constraint $J = 1$ needs to be satisfied in incompressible materials.

In order to determine strain, it is essential to consider the change in length of an infinitesimal vector. The length of the deformed vector $d\boldsymbol{x}$ can by obtained by:

$$||d\boldsymbol{x}||^2 = d\boldsymbol{x}^T d\boldsymbol{x} = (\boldsymbol{F}d\boldsymbol{X})^T(\boldsymbol{F}d\boldsymbol{X}) = d\boldsymbol{X}^T \boldsymbol{F}^T \boldsymbol{F} d\boldsymbol{X} = d\boldsymbol{X}^T \boldsymbol{C} d\boldsymbol{X} \tag{2.10}$$

where $\boldsymbol{C}$ is the right Cauchy-Green deformation tensor, relating squared lengths before and after deformation. Similarly, the left Cauchy-Green deformation tensor is defined as $\boldsymbol{B} = \boldsymbol{F}\boldsymbol{F}^T$.

Strain can then be expressed as the change in squared lengths:

$$\frac{1}{2}(d\boldsymbol{x} \cdot d\boldsymbol{x} - d\boldsymbol{X} \cdot d\boldsymbol{X}) = d\boldsymbol{X} \cdot \boldsymbol{E} d\boldsymbol{X}, \quad \boldsymbol{E} = \frac{1}{2}(\boldsymbol{C} - \boldsymbol{I}), \tag{2.11}$$

where $\boldsymbol{E}$ is the Lagrangian or Green strain tensor.

The internal forces in a body are assumed to be dependent on the distance between particles. Therefore, deformation and strain metrics form the basis for the development of several constitutive laws describing the relation between stresses and internal kinematics in solid mechanics[21,168].

2.2.1 Invariants

When considering constitutive laws (introduced in section 2.4.2), it is often convenient to express their functional form with respect to principle invariants of deformation and strain metrics, which do not change under coordinate rotation (objectivity). The first three invariants of a general matrix $\boldsymbol{A} \in \mathbb{R}^{3 \times 3}$ are defined as:

$$I_A \;:=\; \boldsymbol{A} : \boldsymbol{I} = tr(\boldsymbol{A}) \tag{2.12}$$

$$II_A \;:=\; \boldsymbol{A} : \boldsymbol{A} = tr(\boldsymbol{A}^T \boldsymbol{A}) \tag{2.13}$$

$$III_A \;:=\; \det(\boldsymbol{A}) \tag{2.14}$$

For isotropic hyperelastic materials, constitutive laws can be expressed solely as a function of invariants[21]. Invariants can also be used for the formulation of constitutive laws for anisotropic materials such as the cardiac tissue (as will be discussed in section 2.4.2), even though additional information is usually incorporated to include the effect of the tissue microstructure.

2.2.2 Isochoric variants

When dealing with incompressible and nearly incompressible materials, it is advisable to separate the volumetric and distortional / isochoric components of deformations, as this decoupling facilitates characterisation of constitutive behaviour. It is therefore common, to express constitutive laws as a function of the isochoric definitions of the deformation gradient and the right Cauchy-Green deformation tensor:

$$\hat{\boldsymbol{F}} = III_F^{-1/3} \boldsymbol{F} = J^{-1/3} \boldsymbol{F}, \quad \hat{\boldsymbol{C}} = III_C^{-1/3} \boldsymbol{C} = J^{-2/3} \boldsymbol{C}. \tag{2.15}$$

which ensure that the isochoric components $\hat{\boldsymbol{F}}$ and $\hat{\boldsymbol{C}}$ are invariant to volume change (*i.e.* $\det(\hat{\boldsymbol{F}}) = 1$). The invariants of $\hat{\boldsymbol{F}}$ and $\hat{\boldsymbol{C}}$ can consequently be expressed as:

$$I_{\hat{F}} = J^{-1/3} I_F, \quad II_{\hat{F}} = J^{-2/3} II_F, \quad III_{\hat{F}} = 1, \tag{2.16}$$

$$I_{\hat{C}} = J^{-2/3} I_C, \quad II_{\hat{C}} = J^{-4/3} II_C, \quad III_{\hat{C}} = 1. \tag{2.17}$$

2.3 Stress equilibrium and conservation laws

Having defined the kinematic framework, necessary for finite deformation analysis, the next step is to consider the fundamental physical principles governing the behaviour of material bodies. Conservation laws provide a mathematical description of physical

laws, enabling quantitative analysis of material behaviour. For instance, the continuum equations describing the deformation of a body are based on the conservation of mass and momentum. Before considering these equations, it is essential to define stress tensors and their importance in governing equations.

2.3.1 Stress tensors

A central concept in solid mechanics is the Cauchy stress tensor, a key component in conservation laws of linear and angular momentum. The Cauchy stress tensor, $\boldsymbol{\sigma}$, describes the force per unit deformed area acting on an infinitesimal surface in the deformed domain. The Cauchy stress tensor transforms a normal to a surface vector $\boldsymbol{n}$ into the traction $\boldsymbol{t}$ applied on that surface[21]:

$$\boldsymbol{t} = \boldsymbol{\sigma} \cdot \boldsymbol{n}, \tag{2.18}$$

where $\boldsymbol{\sigma}$, $\boldsymbol{t}$ and $\boldsymbol{n}$ are defined with respect to the current configuration. As will be discussed in section 2.3.4, $\boldsymbol{\sigma}$ is required to be a symmetric tensor, to enable conservation of angular momentum. Unlike the kinematic quantities introduced in the previous sections, the Cauchy stress tensor is dependent on the material and is commonly expressed through constitutive relations which are empirically driven.

However, the determination of the Cauchy stress tensor using experimental data is a challenging task as it involves knowledge of the exact geometry of the deformed domain. To circumvent this issue, alternative stress measures have been introduced to allow for characterisation of the material behaviour with respect to its undeformed geometry. These mainly include the first and second Piola-Kirchhoff stress tensors, defined respectively as:

$$\boldsymbol{P} = J\boldsymbol{\sigma}\boldsymbol{F}^{-T}, \quad \boldsymbol{S} = J\boldsymbol{F}^{-1}\boldsymbol{\sigma}\boldsymbol{F}^{-T}. \tag{2.19}$$

The first Piola-Kirchhoff stress tensor relates area vectors in the undeformed domain to their corresponding force vectors after deformation. On the other hand, the second Piola-Kirchhoff stress is a purely material tensor, representing the force per unit undeformed area, acting on an infinitesimal surface in the undeformed domain. Note that, due to the dependence of $\boldsymbol{P}$ on $\boldsymbol{F}$, symmetry of $\boldsymbol{\sigma}$ does not guarantee that $\boldsymbol{P}$ is symmetric, while $\boldsymbol{S}$ maintains the symmetry of the Cauchy stress tensor. Similarly, defining $\boldsymbol{S}$ to be symmetric ensures symmetry of the Cauchy stress tensor, whereas if $\boldsymbol{P}$ is symmetric, careful consideration is required to ensure symmetry of $\boldsymbol{\sigma}$[146,21].

2.3.2 Mass conservation

The conservation of mass is a balance law for the mass density, ρ. For problems of continuum mechanics assuming incompressibility, mass can neither be created nor destroyed while the body deforms:

$$\int_{\Omega_0} \rho_0 \ dV = \int_{\Omega} \rho \ dv = \int_{\Omega_0} J\rho \ dV, \tag{2.20}$$

where ρ_0 and ρ are the densities of the undeformed and deformed bodies, respectively[168]. Therefore, assuming ρ is a spatiotemporal constant ($\rho = \rho_0$), the mass conservation can be expressed simply by the incompressibility constraint, *i.e.*:

$$J - 1 = 0, \quad \forall \boldsymbol{X} \in \Omega_0. \tag{2.21}$$

2.3.3 Conservation of linear momentum

Conservation of linear momentum is a generalisation of Newtonian mechanics. Considering an arbitrary volume Ω' in the body in Fig. 2.1, the sum of all forces acting on the body should equal the rate of change of the total linear momentum:

$$\int_{\Gamma'} \boldsymbol{t} \ da + \int_{\Omega'} \boldsymbol{f} \ dv = \frac{\partial}{\partial t} \int_{\Omega'} \rho \boldsymbol{v} \ dv, \tag{2.22}$$

where $\boldsymbol{v}$ is the velocity vector and Γ' is the boundary of the domain Ω'. Models of cardiac mechanics commonly assume quasi-static elasticity[231,276,266]. The assumption of quasi-static elasticity, also employed here, neglects momentum effects based on the fact that inertial effects are small relative to stress and body force terms. Hence, assuming the body is under static equilibrium, using Cauchy's formula (Eq. 2.18) and Gauss theorem,

$$\int_{\Gamma'} \boldsymbol{t} \ da + \int_{\Omega'} \boldsymbol{f} \ dv = 0 \Leftrightarrow \int_{\Gamma'} \boldsymbol{\sigma} \cdot \boldsymbol{n} \ da + \int_{\Omega'} \boldsymbol{f} \ dv = 0 \Leftrightarrow$$
$$\int_{\Omega'} \left(\nabla_{\boldsymbol{x}} \cdot \boldsymbol{\sigma} + \boldsymbol{f} \right) dv = 0. \tag{2.23}$$

Taking the limit of the volume of Ω' to zero, Eq. 2.23 should hold point-wise:

$$\nabla_{\boldsymbol{x}} \cdot \boldsymbol{\sigma} + \boldsymbol{f} = 0, \quad \forall \boldsymbol{x} \in \Omega. \tag{2.24}$$

This expression, also known as the conservation of linear momentum under static equilibrium, or Cauchy's first law of motion, governs most systems in continuum mechanics.

2.3.4 Conservation of angular momentum

Another important conservation law governing the behaviour of mechanical systems is the conservation of angular momentum. For any closed system, the sum of moments of all body and traction forces about any arbitrary origin must be zero. It can be shown[21] that as long as linear momentum is conserved, rotational equilibrium depends only on the symmetry of the Cauchy stress tensor,

$$\boldsymbol{\sigma} = \boldsymbol{\sigma}^T. \tag{2.25}$$

Even though the form of the Cauchy stress tensor is commonly experimentally determined, its functional form is typically restricted to guarantee symmetry. Consequently, conservation of angular momentum is satisfied simply through satisfaction of the linear momentum conservation and symmetry of the constitutive law.

2.4 Constitutive laws and hyperelasticity

The myocardial tissue is most often modeled as an anisotropic hyperelastic material. The choice of anisotropic consitutive laws, is based on experimental data showing a different tissue response in different material axes[55,282]. Furthermore, the assumption of hyperelasticity is based on the strong elastic response of the tissue[112]. It should be noted that, although the myocardial tissue also exhibits viscoelastic behaviour[55], this effect is not accounted by the models in this work, due to modelling challenges and absence of accurate experimental data.

This section deals with hyperelastic solids and presents the constitutive laws used throughout this thesis.

2.4.1 Hyperelastic solids

Hyperelastic materials are a special case of elastic materials, in which the material response can be represented by a stored strain energy function[146], $\Psi : \mathbb{R}^{3\times3} \to \mathbb{R}$. The second Piola-Kirchhoff stress tensor is then derived from the strain energy function, as[21,146]:

$$\boldsymbol{S} = 2\frac{\partial \Psi}{\partial \boldsymbol{C}} = \frac{\partial \Psi}{\partial \boldsymbol{E}}. \tag{2.26}$$

The strain energy function Ψ is usually expressed as a function of basic deformation and strain tensors ($\boldsymbol{F}$, $\boldsymbol{C}$, $\boldsymbol{B}$, $\boldsymbol{E}$) to account for the tendency of the material to return to its undeformed state after applied loading is removed. As the strain energy function represents the amount of energy needed to deform the material to a given state, it

is restricted to positive values ($\Psi \geq 0$). Further, under no loading the body should be stress-free, implying that $\Psi = 0$ at the undeformed geometry. In practice, this condition is not always satisfied due to residual stresses observed in several biological tissues including the myocardium[187].

For the case of incompressible or nearly incompressible materials, the strain energy function is often expressed as a sum of a deviatoric (Ψ_d) and a volumetric energy U component. As will be discussed in chapter 3, different approaches have been proposed to deal with incompressible and nearly incompressible materials. For the remaining of this chapter, the myocardial tissue is assumed to be incompressible and the incompressibility constraint is enforced through a Lagrange multiplier, p:

$$\Psi = \Psi_d + U = \Psi_d + p(J - 1), \tag{2.27}$$

where the multiplier p is referred to as the hydrostatic pressure. The Cauchy stress tensor in this case can be expressed as[21]:

$$\boldsymbol{\sigma} = \boldsymbol{\sigma}_d + p\boldsymbol{I} = 2J^{-1}\boldsymbol{F}\frac{\partial \Psi_d}{\partial \boldsymbol{C}}\boldsymbol{F}^T + p\boldsymbol{I}, \tag{2.28}$$

where $\boldsymbol{\sigma}_d$ is the deviatoric Cauchy stress component, $\boldsymbol{S}_d = 2\frac{\partial \Psi_d}{\partial \boldsymbol{C}}$, and $\boldsymbol{\sigma}_d$ was derived using Eq. 2.19.

Details on the Lagrange multiplier method and other formulations for enforcing incompressibility / near incompressibility can be found in chapter 3.

2.4.2 Cardiac constitutive laws

The majority of the mechanics problems considered in this work are heart models, thus, only three-dimensional hyperelastic constitutive laws are presented in this section. The hyperelastic constitutive laws are presented through their deviatoric strain energy functions and stresses, as discussed in section 2.4.1. It should be noted, however, that some of the constitutive laws presented in this section are not defined as functions of isochoric quantities and are thus not fully deviatoric (though often the introduction of a hydrostatic pressure is still applied).

Perhaps the simplest hyperelastic law is the neo-Hookean law, an extension of Hooke's law in finite elasticity. This well-known isotropic law has also been employed in cardiac models[40]. The deviatoric strain energy function Ψ_d for an incompressible neo-Hookean material is defined as:

$$\Psi_d = \frac{\mu}{2}(I_{\hat{C}} - 3), \tag{2.29}$$

where μ is the stiffness of the material, analogous to the shear modulus of linear elasticity and $I_{\hat{C}}$ is the first invariant of $\hat{C}$ (Eq. 2.17). The deviatoric Cauchy stress can

then be expressed as:

$$\boldsymbol{\sigma}_d = \frac{\mu}{J}(\hat{\boldsymbol{B}} - \frac{I_{\hat{C}}}{3}\boldsymbol{I}). \tag{2.30}$$

Despite the simplicity of the neo-Hookean law which makes it an attractive option, it is rarely used in cardiac mechanics. The majority of cardiac constitutive laws are defined with respect to myocardial architecture to account for the anisotropic nature of the heart tissue. This is commonly achieved by defining the continuous fibre, sheet and sheet-normal fields throughout the heart[177]. The constitutive laws can then be written with respect to strains and deformation in the fibre-oriented coordinate system which is aligned with the fibre $\mathbf{f_0}$, sheet $\mathbf{s_0}$ and sheet-normal $\mathbf{n_0}$ unit vectors. Introducing the orthonormal transformation matrix,

$$\boldsymbol{Q} = (\mathbf{f_0}, \mathbf{s_0}, \mathbf{n_0}), \tag{2.31}$$

and its inverse, enables transformation of quantities defined in the local microstructure directions to their equivalent quantities in the Cartesian coordinate system and vice versa. The introduction of the fibre-oriented system and transformation matrix provides a convenient way for defining constitutive laws based on the observed deformations with respect to myocardial architecture.

Following this approach, the well-known transversely isotropic exponential law by Guccione[82] *et al.* is defined with respect to a fibre-oriented Green-Lagrange strain tensor $\boldsymbol{E}_F$:

$$\boldsymbol{E}_F = \boldsymbol{Q}^T\boldsymbol{E}\boldsymbol{Q} = \begin{pmatrix} E_{ff} & E_{fs} & E_{fn} \\ E_{sf} & E_{ss} & E_{sn} \\ E_{nf} & E_{ns} & E_{nn} \end{pmatrix}. \tag{2.32}$$

The strain energy function is then defined as:

$$\Psi_d = \frac{1}{2}C(e^Q - 1), \quad Q = (\boldsymbol{a} \circ \boldsymbol{E}_F) : \boldsymbol{E}_F = \sum_{i,j \in [1,3]} (a_{ij}E_{ij})E_{ij}, \tag{2.33}$$

where $\boldsymbol{a}$ is a matrix of constants describing the degree of anisotropy in each component:

$$\boldsymbol{a} = \begin{pmatrix} b_f & b_{fs} & b_{fs} \\ b_{fs} & b_t & b_t \\ b_{fs} & b_t & b_t \end{pmatrix}.$$

The deviatoric Cauchy stress tensor can then be derived as described in Appendix B, as:

$$\boldsymbol{\sigma}_d = \frac{Ce^Q}{J}\boldsymbol{F}\boldsymbol{Q}(\boldsymbol{a} \circ \boldsymbol{E}_F)\boldsymbol{Q}^T\boldsymbol{F}^T. \tag{2.34}$$

The Guccione law has been used extensively in models of cardiac mechanics, due to its relatively small number of parameters and its ability to reproduce cardiac behaviour.

However, due to its functional form, the parameters are strongly coupled.

An alternative approach is the structurally-based orthotropic model proposed by Holzapfel and Ogden[98]. Its functional form as a sum of individual strain invariants' contributions, leads to less coupling between the passive parameters. The deviatoric form of the strain energy function is defined as:

$$
\begin{aligned}
\Psi_d =& \frac{a}{2b}\{\exp[b(I_C - 3)] - 1\} + \frac{a_f}{2b_f}\{\exp[b_f(I_{C_f} - 1)^2] - 1\} \\
&+ \frac{a_s}{2b_s}\{\exp[b_s(I_{C_s} - 1)^2] - 1\} + \frac{a_{fs}}{2b_{fs}}[\exp(b_{fs}I_{C_{fs}}^2) - 1],
\end{aligned}
\tag{2.35}
$$

where a, b, a_f, b_f, a_s, b_s, a_{fs} and b_{fs} are positive material parameters, associated with the tissue bulk (a and b) and microstructural (a_f, b_f, a_s, b_s, a_{fs} and b_{fs}) behaviour. In this definition $I_{C_f} = \boldsymbol{C} : \mathbf{f_0} \otimes \mathbf{f_0} = \mathbf{f_0} \cdot (\boldsymbol{C}\mathbf{f_0})$, $I_{C_s} = \boldsymbol{C} : \mathbf{s_0} \otimes \mathbf{s_0} = \mathbf{s_0} \cdot (\boldsymbol{C}\mathbf{s_0})$ and $I_{C_{fs}} = \boldsymbol{C} : \mathbf{f_0} \otimes \mathbf{s_0} = \mathbf{f_0} \cdot (\boldsymbol{C}\mathbf{s_0})$ denote invariants associated with the fibre, sheet and cross-fibre directions, respectively. It should be noted that the invariants I_{C_f} and I_{C_s} are only included in the computation of the strain energy if they are larger than 1 (*i.e.* if $I_{C_f} > 1$ and $I_{C_s} > 1$). This adjustment, suggested in the definition of the constitutive law[98], accounts for the fact that fibres do not support compressive loads.

The deviatoric stress is described by[98]:

$$
\begin{aligned}
\boldsymbol{\sigma}_d =& \ a\exp[b(I_C - 3)]\boldsymbol{B} + \ 2a_f(I_{C_f} - 1)\exp[b_f(I_{C_f} - 1)^2]\mathbf{f} \otimes \mathbf{f} \\
&+ \ 2a_s(I_{C_s} - 1)\exp[b_s(I_{C_s} - 1)^2]\mathbf{s} \otimes \mathbf{s} + \ a_{fs}I_{C_{fs}}\exp(b_{fs}I_{C_{fs}}^2)(\mathbf{f} \otimes \mathbf{s} + \mathbf{s} \otimes \mathbf{f}),
\end{aligned}
\tag{2.36}
$$

where $\mathbf{f} = \boldsymbol{F}\mathbf{f_0}$ and $\mathbf{s} = \boldsymbol{F}\mathbf{s_0}$ denote the deformed fibre and sheet vectors, respectively.

Following the invariants' approach, the isotropic neo-Hookean law can be augmented with a fibre-dependent component. The enhanced version, which will be refer to as the *neo-fibre* law, is a transversely isotropic model which can present different response over the fibre direction. The strain energy function for the neo-fibre model is defined as:

$$
\Psi_d = \frac{1}{2(a+1)}(C_1 - C_2)(I_{\hat{C}_f} - 1)^{a+1} + \frac{C_2}{2}(I_{\hat{C}} - 3),
\tag{2.37}
$$

where $a = 1$ or 2. In this definition $I_{\hat{C}_f}$ represents the first invariant of $\hat{\boldsymbol{C}}$ in the fibre direction, defined as

$$
I_{\hat{C}_f} = J^{-2/3}I_{C_f},
\tag{2.38}
$$

and C_1, C_2 are material parameters, with C_2 being equivalent to neo-Hookean stiffness

μ. The deviatoric Cauchy stress for the neo-fibre law is then expressed as:

$$\boldsymbol{\sigma}_d = J^{-\frac{5}{3}}\left[C_2\boldsymbol{B} + (C_1 - C_2)(I_{\hat{C}_f} - 1)^a\mathbf{f}\otimes\mathbf{f} - \frac{1}{3}\big(C_2 I_C + (C_1 - C_2)(I_{\hat{C}_f} - 1)^a I_{\hat{C}_f}\big)\boldsymbol{I}\right].$$

$$(2.39)$$

The derivation of the deviatoric stress tensor is shown in Appendix B.

The considered constitutive laws are employed in *in silico* and *in vivo* applications throughout this thesis. We note, however, that several other constitutive laws have been proposed and used for modelling the myocardial tissue varying significantly in functional form, anisotropy assumptions and complexity, as discussed in section 1.3.1.2.

2.5 Principle of stationary potential energy

Having introduced hyperelastic solids and their strain energy functions, we can derive the weak form of the equilibrium equation (Eq. 2.24), using the principle of stationary potential energy. This approach, which is equivalent to the principle of virtual work, provides a framework for conveniently introducing additional model components – such as different volumetric energies or boundary constraints – into the mechanical problem, as will be shown in sections 3.1.1 and 5.3.2. The reformulation of the equilibrium equation into its variational or weak form, is an essential step in the finite element method, which will be outlined in section 2.6.

Following the principle of stationary potential energy, the deformation $\boldsymbol{u}$ and pressure p solutions of the body under consideration in section 2.1 and Fig. 2.1, can be obtained by considering the functional, $\Pi : (\boldsymbol{U_D}\times W) \to \mathbb{R}$, describing the total potential energy of the body. The deformation and hydrostatic pressure of the body are sought in function spaces $\boldsymbol{U}_D = \{\boldsymbol{v}\in\boldsymbol{U}|\boldsymbol{v}_{|\Gamma_D} = \boldsymbol{g}\}$ and W, respectively, where $\boldsymbol{U}$ and W are selected to ensure that the strain energy function (and its directional derivatives) are bounded, *i.e.*

$$\boldsymbol{U} = \{\boldsymbol{v}\in[W^{1,4}(\Omega_0)]^{3\times 3} \mid \Psi_d(\boldsymbol{v})\in L^1(\Omega_0),\ \frac{\partial\Psi_d(\boldsymbol{v})}{\partial\boldsymbol{F}}\in[L^2(\Omega_0)]^{3\times 3},$$
$$J\in L^2(\Omega_0),\ \frac{\partial J}{\partial\boldsymbol{F}}\in[L^4(\Omega_0)]^{3\times 3}\},$$
$$W = L^2(\Omega_0),$$

$$(2.40)$$

where $L^p(\Omega_0)$ and $W^{1,4}(\Omega_0)$ denote the usual Banach and Sobolev spaces, respectively[25,38], defined in Eq. 2.3 and 2.4.

The body force $\boldsymbol{f_0} = J\boldsymbol{f}$ and traction vector $\boldsymbol{t_0} = \boldsymbol{t}J\sqrt{\boldsymbol{N}\cdot\boldsymbol{C}^{-1}\boldsymbol{N}}$ are now expressed with respect to the undeformed domain[21], where $\boldsymbol{N}$ is the normal vector in the undeformed domain. Assuming that the traction and body forces are not functions of the

displacement, then under static equilibrium, the total potential energy for a hyperelastic body may be expressed as a sum of the internal and external potential energy as,

$$\Pi(\boldsymbol{v}, \lambda) = \Pi_{int}(\boldsymbol{v}, \lambda) + \Pi_{ext}(\boldsymbol{v}) \tag{2.41}$$

$$\Pi_{int}(\boldsymbol{v}, \lambda) = \int_{\Omega_0} (\Psi_d(\boldsymbol{v}) + \lambda(J - 1)) \ dV, \quad \Pi_{ext}(\boldsymbol{v}) = -\int_{\Omega_0} \boldsymbol{f_0} \cdot \boldsymbol{v} \ dV - \int_{\Gamma_0} \boldsymbol{t_0} \cdot \boldsymbol{v} \ dA, \tag{2.42}$$

where $\boldsymbol{v}$ and λ denote the displacement and pressure variables, respectively, and Ψ_d represents the deviatoric strain energy function defined in section 2.4.1. According to the principle of stationary potential energy, the body will deform in a way that minimises its total potential energy Π, over the space of incompressible displacements. The displacement $\boldsymbol{u}$ and pressure p solutions are then obtained as the saddle-point of the energy functional:

$$\Pi(\boldsymbol{u}, p) = \inf_{\boldsymbol{v} \in \boldsymbol{U}_D} \sup_{\lambda \in W} \Pi(\boldsymbol{v}, \lambda). \tag{2.43}$$

The derivation of the weak form can be regarded as equivalent to obtaining the directional derivatives of the functional $\Pi(\boldsymbol{v}, \lambda)$ with respect to displacement and pressure, and requiring that they vanish, for all arbitrary increments $\delta\boldsymbol{u}$ and δp. These arbitrary increments can be regarded as the test functions of the weak form. The directional derivative of the total potential energy functional $\Pi(\boldsymbol{v}, \lambda)$ with respect to the displacement $\boldsymbol{u}$ in an arbitrary direction $\delta\boldsymbol{u}$ can be expressed as[21],

$$D\Pi(\boldsymbol{v}, \lambda)[\delta\boldsymbol{u}] = \lim_{\epsilon \to 0^+} \frac{\Pi(\boldsymbol{v} + \epsilon\delta\boldsymbol{u}, \lambda) - \Pi(\boldsymbol{v}, \lambda)}{\epsilon}, \tag{2.44}$$

with ϵ being an arbitrarily small positive parameter. Analysing each contribution, the directional derivative with respect to displacement can be written as:

$$\begin{aligned}
D\Pi(\boldsymbol{v}, \lambda)[\delta\boldsymbol{u}] =& \frac{\partial}{\partial \epsilon}\Pi(\boldsymbol{v} + \epsilon\delta\boldsymbol{u}, \lambda)|_{\epsilon=0} = \frac{\partial}{\partial \epsilon} \Big[\int_{\Omega_0} \Psi_d(\boldsymbol{F}(\boldsymbol{v} + \epsilon\delta\boldsymbol{u})) + \lambda(J(\boldsymbol{v} + \epsilon\delta\boldsymbol{u}) - 1) \ dV \\
& - \int_{\Omega_0} \boldsymbol{f_0} \cdot (\boldsymbol{v} + \epsilon\delta\boldsymbol{u}) \ dV - \int_{\Gamma_0} \boldsymbol{t_0} \cdot (\boldsymbol{v} + \epsilon\delta\boldsymbol{u}) \ dA \Big]|_{\epsilon=0} = \\
& \int_{\Omega_0} \frac{\partial \Psi_d}{\partial \boldsymbol{F}} : D\boldsymbol{F}[\delta\boldsymbol{u}] + \lambda DJ[\delta\boldsymbol{u}] \ dV - \int_{\Omega_0} \boldsymbol{f_0} \cdot \delta\boldsymbol{u} \ dV - \int_{\Gamma_0} \boldsymbol{t_0} \cdot \delta\boldsymbol{u} \ dA = \\
& \int_{\Omega_0} \boldsymbol{P}_d : \nabla_{\boldsymbol{X}}\delta\boldsymbol{u} + \lambda DJ[\delta\boldsymbol{u}] \ dV - \int_{\Omega_0} \boldsymbol{f_0} \cdot \delta\boldsymbol{u} \ dV - \int_{\Gamma_0} \boldsymbol{t_0} \cdot \delta\boldsymbol{u} \ dA,
\end{aligned}$$

where $\boldsymbol{P}_d$ is the deviatoric first Piola-Kirchhoff stress tensor. Noting that $DJ[\delta\boldsymbol{u}] = J\boldsymbol{F}^{-T} : \nabla_{\boldsymbol{X}}\delta\boldsymbol{u}$ [21] and requiring that the directional derivative vanishes in all arbitrary directions $\delta\boldsymbol{u} \in \boldsymbol{U}_0$ [97]:

$$\int_{\Omega_0} (\boldsymbol{P}_d + \lambda J\boldsymbol{F}^{-T}) : \nabla_{\boldsymbol{X}}\delta\boldsymbol{u} \ dV - \int_{\Omega_0} \boldsymbol{f_0} \cdot \delta\boldsymbol{u} \ dV - \int_{\Gamma_0} \boldsymbol{t_0} \cdot \delta\boldsymbol{u} \ dA = 0 \quad \forall \delta\boldsymbol{u} \in \boldsymbol{U}_0. \tag{2.45}$$

Note that the previous relation can also be expressed in the deformed domain Ω using

Eq. 2.19 as:

$$\int_\Omega (\boldsymbol{\sigma}_d + \lambda \boldsymbol{I}) : \nabla \delta \boldsymbol{u} \ dv - \int_\Omega \boldsymbol{f} \cdot \delta \boldsymbol{u} \ dv - \int_\Gamma \boldsymbol{t} \cdot \delta \boldsymbol{u} \ da = 0, \quad \forall \ \delta \boldsymbol{u} \in \boldsymbol{U}_0. \qquad (2.46)$$

Similarly, requiring that the directional derivative of the energy functional vanishes for any arbitrary direction $\delta p \in W$:

$$D\Pi(\boldsymbol{v}, \lambda)[\delta p] = \int_{\Omega_0} \delta p (J - 1) dV = 0, \quad \forall \delta p \in W. \qquad (2.47)$$

Combining the directional derivatives of the energy functional with respect to the displacement and pressure variables (Eq. 2.45 and 2.47) the solution to the saddle-point problem in Eq. 2.43 can be expressed as:

$$\int_{\Omega_0} (\boldsymbol{P}_d + \lambda J \boldsymbol{F}^{-T}) : \nabla_{\boldsymbol{X}} \delta \boldsymbol{u} + \delta p (J - 1) \ dV - \int_{\Omega_0} \boldsymbol{f_0} \cdot \delta \boldsymbol{u} \ dV - \int_{\Gamma_0} \boldsymbol{t_0} \cdot \delta \boldsymbol{u} \ dA = 0,$$
$$\forall \ (\delta \boldsymbol{u}, \delta p) \in (\boldsymbol{U}_0, W). \qquad (2.48)$$

2.6 Finite element method

In order to obtain the displacement and hydrostatic pressure for the problem described in section 2.1, the weak form introduced in section 2.5 must be solved. Following an analytic approach might be possible for simplified problems of nonlinear mechanics with regular geometries and known deformation modes (see for example, Appendix D). However, for the more practical applications considered in this work with irregular domains, or more complex loading and boundary conditions, a numerical approach is essential. For cardiac mechanics, this numerical approach is typically the finite element method.

Accordingly, the nonlinear weak formulation of the finite elasticity equation presented in section 2.5 can then be solved within the finite element framework. An essential component of the FEM procedure is the discretisation of the domain and function spaces, resulting in a finite-dimensional system of equations which are then solved using a Newton-Raphson iterative method.

The methodology presented in this section involves displacement and hydrostatic pressure as primary variables, providing the process for solving problems considered in chapters 3 and 4. Even though, more complex applications with additional variables (usually additional Lagrange multipliers) are used in chapters 5 - 7, the presented approach can be easily extended to the solution of problems with additional primary variables, as illustrated in section 5.3.2.
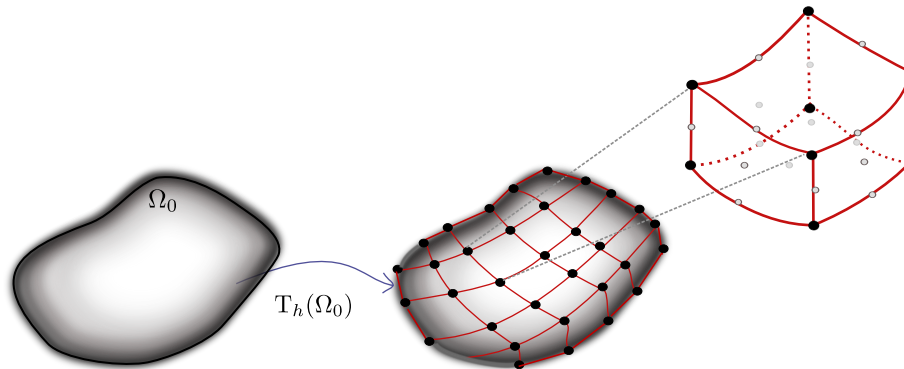
Figure 2.2 Discretisation $T_h(\Omega_0)$ of domain Ω_0 into a hexahedral mesh. Nodes are denoted by black and grey dots for the linear and quadratic hexahedral element, respectively.

2.6.1 Discretisation

In the FEM framework, the undeformed domain Ω_0 in Fig. 2.2 is subdivided into a finite number of non-overlapping elements (τ) which form the mesh or discretisation $T_h(\Omega_0) \subset \mathbb{R}^3$,

$$T_h(\Omega_0) = \{\tau_1, \tau_2, ..., \tau_n\}, \tag{2.49}$$

where h is the mesh size and n is the number of elements forming the mesh. Different definitions can be used for the mesh size depending on element type, and these will be given in relevant sections.

For convenience, we define the approximation of the state variables of the problem (displacement $\boldsymbol{u}$ and hydrostatic pressure p are considered here) over a basic reference element, τ_M (triangular, tetrahedral, quadrilateral and hexahedral master elements were used throughout this thesis). Let $\mathbb{P}^k(\tau_M)$ and $\mathbb{Q}^k(\tau_M)$ denote the standard nodal Lagrange basis functions of degree k on the triangular / tetrahedral and quadrilateral / hexahedral master elements, respectively. Each basis function on the reference element is then parametrically mapped into elements τ_m of the mesh, through a mapping ϕ_m : $\tau_M \to \tau_m, \tau_m \in T_h$. The mapping ϕ_m is actually a function (usually in $\mathbb{P}^k(\tau_M)$ or $\mathbb{Q}^k(\tau_M)$), defining how the master element is mapped into reference domain Ω_0. ϕ_m can be a linear transformation (as in the cases of tetrahedral meshes in chapters 5 - 7) or a non-linear transformation leading to curvilinear elements in the mesh (as in hexahedral meshes in section 3.2.1.2 and chapter 4). The basis functions on any element τ_m on the mesh are given by $\mathbb{P}^k(\tau_m) = \mathbb{P}^k(\phi_m^{-1}(\tau_M))$ or $\mathbb{Q}^k(\tau_m) = \mathbb{Q}^k(\phi_m^{-1}(\tau_M))$.

The displacement and pressure variables in the weak formulation (section 2.5) can now be interpolated with functions in $\boldsymbol{U^h} \subset \boldsymbol{U_D}$ and $W^h \subset W$, respectively, assuming conformity of the discretised and continuous boundaries. The discrete function spaces

U^h and W^h consist of a set of piecewise polynomial functions defined over the mesh, *i.e.*:

$$U^h := \{v^h \in \mathcal{C}(\Omega_0) | \ v^h|_\tau \in \mathbb{P}^{k_u}(\tau), \ \forall \tau \in \mathcal{T}(\Omega_0)\}, \tag{2.50}$$

$$W^h := \{\lambda^h \in \mathcal{C}(\Omega_0) | \ \lambda^h|_\tau \in \mathbb{P}^{k_p}(\tau), \ \forall \tau \in \mathcal{T}(\Omega_0)\}, \tag{2.51}$$

where k_u and k_p denote the order of interpolation used for the displacement and pressure variables, respectively, and $\mathbb{P}$ can be replaced with $\mathbb{Q}$, depending on the discretisation selected.

The displacement and pressure variables can then be expressed as a weighted sum of the variables' nodal values and basis functions,

$$u^h(X) = \sum_{i=1}^{3} \sum_{k=1}^{N_u} e_i u_i^k \phi_u^k(X), \quad X \in \mathrm{T}_h(\Omega_0), \tag{2.52}$$

$$p^h(X) = \sum_{k=1}^{N_p} p^k \phi_p^k(X), \quad X \in \mathrm{T}_h(\Omega_0), \tag{2.53}$$

where $\{e_1, e_2, e_3,\}$ denote the standard unit basis of $\mathbb{R}^3$ and N_u and N_p denote the number of nodes used for the displacement and pressure approximations, respectively. Additionally, u_i^k is the nodal value of the displacement component i for the kth basis, p^k is the nodal value of the pressure for the kth basis and ϕ_u^k and ϕ_p^k are the kth basis functions of the interpolation used for the displacement and pressure variables, respectively.

Rearranging the vector coefficients,

$$\boldsymbol{\mathcal{U}} = \left(u_1^1, u_2^1, u_3^1, ..., u_1^{N_u}, u_2^{N_u}, u_3^{N_u}\right)^T, \quad \boldsymbol{\Phi}_u = \left(\phi_u^1, \phi_u^1, \phi_u^1, ..., \phi_u^{N_u}, \phi_u^{N_u}, \phi_u^{N_u}\right)^T, \tag{2.54}$$

$$\boldsymbol{P} = \left(p^1, ..., p^{N_p}\right)^T, \quad \boldsymbol{\Phi}_w = \left(\phi_p^1, ..., \phi_p^{N_p}\right)^T, \tag{2.55}$$

the resulting displacement and pressure variables can more conveniently be represented as $u^h(X) = \boldsymbol{\mathcal{U}} \cdot \boldsymbol{\Phi}_u(X)$ and $p^h(X) = \boldsymbol{P} \cdot \boldsymbol{\Phi}_w(X)$, respectively.

Finally, in the Galerkin finite element method employed, the basis functions are also chosen as test functions. Therefore, using the finite element approximation of the displacement and pressure variables, the weak formulation in Eq. 2.48 can be written in its discrete form as:

$$\int_{\Omega_0} (P^h + p^h J^h F^{h-T}) : \nabla_X \delta u^h + \delta p^h (J^h - 1) \ dV - \int_{\Omega_0} f_0 \cdot \delta u^h \ dV$$

$$- \int_{\Gamma_0} t_0 \cdot \delta u^h \ dA = 0, \quad \forall \ (\delta u^h, \delta p^h) \in (X^h, W^h). \tag{2.56}$$

where $\boldsymbol{F}^h$ and $\boldsymbol{P}^h$ are distinguished from their continuous forms simply because they are computed using the interpolated function $\boldsymbol{u}^h$.

2.6.2 Global System

The discrete weak form presented in section 2.6.1 can be conveniently rewritten in terms of a functional $\boldsymbol{s}$ as:

$$\boldsymbol{s}(\boldsymbol{u}^h, p^h, \delta\boldsymbol{u}^h, \delta p^h) = \int_{\Omega_0} (\boldsymbol{P}^h + p^h J^h \boldsymbol{F}^{h-T}) : \nabla_{\boldsymbol{X}} \delta\boldsymbol{u}^h + \delta p^h (J^h - 1)\ dV$$
$$- \int_{\Omega_0} \boldsymbol{f_0} \cdot \delta\boldsymbol{u}^h\ dV - \int_{\Gamma_0} \boldsymbol{t_0} \cdot \delta\boldsymbol{u}^h\ dA = 0, \quad \forall\ (\delta\boldsymbol{u}^h, \delta p^h) \in (\boldsymbol{X}^h, W^h). \tag{2.57}$$

This equation can be reformulated by defining $\boldsymbol{z}$ to represent the interpolated displacement and pressure variables, as $\boldsymbol{z} = [\boldsymbol{u}^h, p^h]$, $\boldsymbol{Z} = [\boldsymbol{\mathcal{U}}; \boldsymbol{P}]$ and $\boldsymbol{\Phi} = [\boldsymbol{\Phi}_u; \boldsymbol{\Phi}_w]$. As Eq. 2.57 should hold for all test functions $\delta\boldsymbol{Y} = \boldsymbol{Y} \cdot \boldsymbol{\Phi}$, and noting the linear dependence of $\boldsymbol{s}$ on the test functions,

$$\boldsymbol{s}(\boldsymbol{z}, \delta\boldsymbol{Y}) = \boldsymbol{s}(\boldsymbol{z}, \boldsymbol{Y} \cdot \boldsymbol{\Phi}) = \boldsymbol{Y} \cdot \boldsymbol{R}(\boldsymbol{z}) = 0, \tag{2.58}$$

where $\boldsymbol{R}$ is the residual vector. As the last relation must hold for every choice of $\boldsymbol{Y}$, the residual vector $\boldsymbol{R}$ must vanish in all components.

$$\boldsymbol{R}(\boldsymbol{z}) = 0. \tag{2.59}$$

The use of the finite dimensional approximation space $\boldsymbol{U}^h$ allows the infinite constraints on $\boldsymbol{s}$ in Eq. 2.57 to be replaced by a finite number of constraints, thus simplifying the problem. The displacement and pressure solutions are the root of the residual vector $\boldsymbol{R}$ in Eq. 2.59 and can be iteratively computed using the Newton-Raphson method, as discussed in the following sections. Additionally, it is often convenient to consider $\boldsymbol{R} = \boldsymbol{R}(\boldsymbol{Z})$. The Newton-Raphson solution for the coefficient vector $\boldsymbol{Z} = [\boldsymbol{\mathcal{U}}; \boldsymbol{P}]$ must then be dotted with $\boldsymbol{\Phi}$ to provide the approximation to the state variables.

2.6.3 Solution with Newton-Raphson Method

Given the finite dimensional system in Eq. 2.59, the displacement and pressure coefficient vector $\boldsymbol{Z}$ can be iteratively obtained, using the Newton-Rapson method. Assuming an initial guess $\boldsymbol{Z}_0$ and using Taylor's expansion, the residual vector $\boldsymbol{R}(\boldsymbol{Z})$ can be approximated by:

$$\boldsymbol{R}(\boldsymbol{Z}) = \boldsymbol{R}(\boldsymbol{Z}_0) + \nabla_{\boldsymbol{Z}}\boldsymbol{R}(\boldsymbol{Z}_0) \cdot (\boldsymbol{Z} - \boldsymbol{Z}_0) + \frac{1}{2}\nabla_{\boldsymbol{Z}}\big[\nabla_{\boldsymbol{Z}}\boldsymbol{R}(\boldsymbol{Z}_0) \cdot (\boldsymbol{Z} - \boldsymbol{Z}_0)\big] \cdot (\boldsymbol{Z} - \boldsymbol{Z}_0) + \ ... \tag{2.60}$$

Assuming the initial guess $\boldsymbol{Z}_0$ is sufficiently close to the solution $\boldsymbol{Z}$ so that $(\boldsymbol{Z} - \boldsymbol{Z}_0)$ is small, the third term in the previous equation can be neglected due to its second order dependence on $(\boldsymbol{Z} - \boldsymbol{Z}_0)$. Substituting Eq. 2.59 into Eq. 2.60:

$$\boldsymbol{R}(\boldsymbol{Z}_0) + \nabla_{\boldsymbol{Z}}\boldsymbol{R}(\boldsymbol{Z}_0) \cdot (\boldsymbol{Z} - \boldsymbol{Z}_0) \approx 0. \tag{2.61}$$

This results in the linear matrix system with only $\boldsymbol{Z}$ as the unknown,

$$\boldsymbol{Z} = \boldsymbol{Z}_0 - [\nabla_{\boldsymbol{Z}}\boldsymbol{R}(\boldsymbol{Z}_0)]^{-1} \cdot \boldsymbol{R}(\boldsymbol{Z}_0). \tag{2.62}$$

The last equation can be extended to give the Newton-Raphson iterative process, where given an initial guess $\boldsymbol{Z}_0$ sufficiently close to $\boldsymbol{Z}$, the coefficient vector $\boldsymbol{Z}_n$ can be iteratively updated[67]:

$$\boldsymbol{Z}_n = \boldsymbol{Z}_{n-1} - [\nabla_{\boldsymbol{Z}}\boldsymbol{R}(\boldsymbol{Z}_{n-1})]^{-1} \cdot \boldsymbol{R}(\boldsymbol{Z}_{n-1}), \tag{2.63}$$

to create the sequence $\{\boldsymbol{Z}_n\}_n$ which approximates the coefficient vector $\boldsymbol{Z}$

$$\boldsymbol{Z} = \lim_{n\to\infty} \boldsymbol{Z}_n. \tag{2.64}$$

Here, $\nabla_{\boldsymbol{Z}}\boldsymbol{R}(\boldsymbol{Z}_n)$ denotes the Jacobian matrix at the n-th iteration:

$$\nabla_{\boldsymbol{Z}}\boldsymbol{R}(\boldsymbol{Z}_n) = \nabla_{\boldsymbol{Z}}\boldsymbol{R}(\boldsymbol{Z})|_{\boldsymbol{Z}=\boldsymbol{Z}_n}. \tag{2.65}$$

Derivation of the entries of the Jacobian matrix for the Lagrange multiplier method is presented in Appendix A.

The classic Newton-Raphson iterative process in Eq. 2.63, requires an initial guess $\boldsymbol{Z}_0$ to be sufficiently close to the actual solution to guarantee convergence of the sequence $\{\boldsymbol{Z}_n\}_n$. If the initial guess is not sufficiently close, then $\{\boldsymbol{Z}_n\}_n$ might diverge and not give a finite limit (*i.e.* an approximate solution).

2.6.3.1 Global Newton-Raphson iteration

A variant of the Newton-Raphson method, the global Newton-Raphson, reduces the risk of divergence which is present in the classic Newton-Raphson method (section 2.6.3), by ensuring convergence of the sequence of iterations of the residual vector $\{\boldsymbol{R}(\boldsymbol{Z}_n)\}_n$. Introducing the scaling parameter a_n and following the Newton-Raphson definition in Eq. 2.63, the update coefficient vector $\boldsymbol{Z}_n$ is given by

$$\boldsymbol{Z}_n = \boldsymbol{Z}_{n-1} - a_n[\nabla_{\boldsymbol{Z}}\boldsymbol{R}(\boldsymbol{Z}_{n-1})]^{-1} \cdot \boldsymbol{R}(\boldsymbol{Z}_{n-1}), \tag{2.66}$$

where a_n is chosen at every iteration to ensure that the residual decays, *i.e.*:

$$\max_{a_n \in [0,1]} ||\boldsymbol{R}(\boldsymbol{Z}_n)|| \leq ||\boldsymbol{R}(\boldsymbol{Z}_{n-1})||. \tag{2.67}$$

Eq. 2.67 is usually solved approximately using a line search algorithm. Even though this method presents improved convergence properties over the classic Newton-Raphson method, convergence of the sequence $\{\boldsymbol{Z}_n\}_n$ is not guaranteed, as the method does not allow for non-monotonic convergence.

2.6.3.2   Shamanskii-Newton-Raphson method

The estimation of the update vector in Eq. 2.63 and 2.66 requires the computation and inversion of the global Jacobian matrix, which are often challenging, due to nonlinear dependence on the primary variables, and computationally expensive. To reduce this computational cost we can employ the Shamanskii-Newton-Raphson approach[224,152] which re-uses the Jacobian matrix computed at previous Newton-Raphson iterations.

Following the process oultined in McCormick *et al.*[152], over successive iterations the update vector

$$\delta\boldsymbol{Z}_n = -a_n[\nabla_{\boldsymbol{Z}}\boldsymbol{R}(\boldsymbol{Z}_{n-1})]^{-1} \cdot \boldsymbol{R}(\boldsymbol{Z}_{n-1}), \tag{2.68}$$

is relatively small compared to the approximate solution $\boldsymbol{Z}_n$, we can therefore deduce that the Jacobian matrix should not change significantly. Exploiting this property, we can compute the updated approximate solution using the Jacobian and its inverse computed at a previous iteration (or timestep) β,

$$\boldsymbol{Z}_n = \boldsymbol{Z}_{n-1} - a_n[\nabla_{\boldsymbol{Z}}\boldsymbol{R}(\boldsymbol{Z}_\beta)]^{-1} \cdot \boldsymbol{R}(\boldsymbol{Z}_{n-1}). \tag{2.69}$$

As will be shown in chapter 3, this re-use can significantly improve the efficiency of the system. This approach can provide a reliable update as long as the previously computed Jacobian is not significantly different to the one corresponding to the current approximate solution. Therefore, an additional convergence criterion is introduced,

$$\frac{||\boldsymbol{R}(\boldsymbol{Z}_n)||}{||\boldsymbol{R}(\boldsymbol{Z}_{n-1})||} \leq K, \quad K \leq 1, \tag{2.70}$$

ensuring decay of the residual for successive iterations, or otherwise requiring computation of the updated Jacobian matrix at the next iteration.

2.7 $\mathcal{C}$Heart

The mechanics problems presented in this thesis are solved following the numerical methods described in the current chapter. The considered problems are solved using **$\mathcal{C}$Heart**, a multi-physics finite element solver developed by Nordsletten[179] and expanded by the **CHeart** team at KCL*. Briefly, **CHeart** supports the finite element solution of a range of mechanical problems, including solid, fluid, fluid-solid interaction, electrophysiology, Windkessel and poro-mechanics. When applicable, combinations of these problems can be coupled and solved together.

CHeart is written in FORTRAN 90 and uses parallel computing to enable the solution of large systems and computationally expensive coupled problems. Specifically, **CHeart** uses Message Passing Interface (MPI) to enable inter-process communication. Mesh decomposition – a determinant of the efficiency of the parallelisation in FEM applications – is performed using graph partitioning, whereby the domain is divided into a number of regions depending on the number of processors used. Graph partitioning in **CHeart** is done using existing library ParMETIS†. The graph partitioning scheme used ensures efficient decomposition across domain and potential surface domains. Moreover, **CHeart** integrates with linear algebra libraries PETSc‡, MUMPS§, SuperLU¶ to effectively solve linearised systems in parallel. Furthermore, it enables coupling between physics problems defined on different topologies, allowing for a diverse range of applications.

A more detailed description of the implementation can be found in Nordsletten[179] and McCormick[152] and Lee *et al.*[129].

---

*http://cheart.co.uk/

†http://glaros.dtc.umn.edu/gkhome/metis/parmetis

‡http://www.mcs.anl.gov/petsc/

§http://mumps.enseeiht.fr/

¶http://crd-legacy.lbl.gov/ xiaoye/SuperLU/

3 Compressibility/incompressibility in cardiac mechanics

An issue commonly discussed in cardiac mechanics is the choice of modelling the myocardium using incompressible or nearly incompressible formulations (section 1.3.1.4). As a possible degree of compressibility remains an unresolved issue in the cardiac mechanics community, both compressible[119,254,88] and incompressible[231,170,188] models have been proposed, showing non-negligible differences in results. Although inherently based on tissue behaviour, the choice of modelling the cardiac tissue using incompressible or nearly incompressible formulations is also dependent on numerical considerations: nearly incompressible formulations are often employed as a simplified approximation to incompressible behaviour.

A range of such numerical schemes has been applied in heart models, one of the most popular being the penalty method[260,254,255,119]. An advantage of this approach is its simplified form, requiring only the solution of the tissue displacement. However, when applied in the FEM framework, displacement-based formulations near the incompressible limit exhibit locking, leading to sub-optimal convergence rates and poor numerical approximations in classic elastic models[25,242,97,69]. Critically, the penalty method lacks monotonic convergence to the incompressible solution as the bulk modulus is increased, making it challenging to employ as an approximate model to an incompressible cardiac material model.

The development of numerical strategies circumventing these issues has been a field of significant research effort in the solid mechanics community. Among others, the B-Bar method introduced by Hughes[101], the reduced or selective integration techniques[292,69,144], and augmented Lagrangian methods[77,227] have all been successfully employed to enforce incompressibility while tackling the numerical difficulties associated with the penalty formulation. An alternative approach used extensively in solid mechanics is the class of multi-field variational principles[93,245,185]. The most common of these mixed formulations is the Lagrange Multiplier (LM) method, a two-field variational approach which has been used widely to enforce incompressibility of the myocardium by introducing a variable to respresent the hydrostatic pressure[188,169,44,231,247]. While the LM method is known to improve numerical conver-

gence[21,270,97,243], the use of an additional variable results in increased computational cost and enhanced complexity in the linear algebra involved, due to the indefinite nature of the resulting stiffness matrix[25,21].

The perturbed Lagrangian (PL) formulation was introduced to address this issue, by augmenting the energy functional of the LM approach with a penalty/compressibility term[38,36,18]. The PL is a two-field variational approach suitable for the solution of nearly incompressible problems, where pressure and displacement are treated as independent variables. Sussman and Bathe[243] introduced a generalised form of the PL approach, the u/p formulation, which has been used extensively in the computational mechanics literature[139,26,38] and has also been applied in the myocardium[247]. Similarly, the well established three-field Hu-Washizu formulation by Simo *et al*[226] extends the PL formulation by introducing pressure and dilatation as independent variables[227,270,139,158]. This approach has also been employed in cardiac mechanics[78] (though this procedure comes with the cost of computing an additional variable). The use of a separate interpolation for the independent variables, allows efficient and accurate approximations, alleviating the numerical difficulties associated with both the penalty and LM methods. The efficiency of these methods was also enhanced with the use of discontinuous interpolation for the pressure and dilatation fields (static condensation)[18,243,228,270] allowing the computation of these fields on element level and leading to a generalised displacement-only formulation.

The objective of this chapter is to compare some of these techniques in terms of their accuracy and numerical efficiency. Specifically, the statically condensed Perturbed Lagrangian formulation of Bercovier[18] and others[38,36] is considered, which may be conveniently thought of as a weakly penalised form with an optional choice of projection operator. In this generalised form, the constraint might be strengthened or weakened, with an appropriate choice of the projection operator, resulting in the PL, LM or penalty formulations. A discontinuous pressure field is used for the weakly penalised approach which enables the solution of the projection problem on an element level, leading to an efficient displacement-only formulation. The weakly penalised approach is further augmented and restructured to improve nonlinear convergence properties, particularly for high values of the bulk modulus.

Initially, the general minimisation problem is illustrated (section 3.1.1) indicating how both penalty and LM formulations may be thought of equivalently as weakly penalised constraints in the continuous setting. The basis for locking is then reviewed in section 3.1.2, motivating the introduction of the weakly penalised approach. Modifications introduced to the mechanical system to enhance convergence behaviour are discussed in section 3.1.3. The numerical convergence of these different methods is then compared, using a 2D model problem and cardiac mechanics problems (section 3.2). The results, which show significant variations between the numerical schemes, are discussed

in section 3.3.

The work presented in this chapter has been published in Hadjicharalambous *et al.*[86].

3.1 Numerical formulations for incompressibility / nearly incompressibility

In order to understand and compare the numerical behaviour of the considered methods, this section shows how in the continuous setting LM and penalty formulations can be viewed uniformly through a weakly penalised form (PL) (section 3.1.1). Subsequently, the discretised forms used within the FEM framework are introduced, illustrating the deviation of the two schemes and the resulting locking phenomena in FEM penalty applications (section 3.1.2). These motivate the use of an alternative discretisation strategy, leading to a displacement-only formulation. The solution to this system is then demonstrated and optimised to accommodate the numerical stiffening due to the weakly penalised terms.

3.1.1 Continuous minimisation problem

Problems of static (or quasi-static) solid mechanics involve finding the deformation, $\boldsymbol{u}$, of a body defined over a domain Ω_0, described in section 2.1. According to the principle of stationary potential energy in section 2.5, the body will deform in a way that minimises its total potential energy Π. This problem can be expressed as,

$$\Pi(\boldsymbol{u}) = \inf_{\boldsymbol{v} \in \boldsymbol{U}} \Pi(\boldsymbol{v}), \tag{3.1}$$

where $\boldsymbol{u}$ is the function producing the minimum potential energy compared to all other functions $\boldsymbol{v}$ in function space $\boldsymbol{U}$. In the case of incompressibility, the deformation is required to preserve the determinant of the deformation gradient[21] $\boldsymbol{F}$, as discussed in section 2.2,

$$J - 1 = 0, \quad J = |\boldsymbol{F}| = |\nabla \boldsymbol{v} + \boldsymbol{I}|.$$

In this case, the solution is found, which satisfies,

$$\Pi(\boldsymbol{u}) = \inf_{\boldsymbol{v} \in \boldsymbol{U}_J} \Pi(\boldsymbol{v}), \tag{3.2}$$

$$\boldsymbol{U}_J = \{\boldsymbol{v} \in \boldsymbol{U} | J - 1 = 0, \text{ a.e. on } \Omega_0\}. \tag{3.3}$$

As it is not, in general, straightforward to construct the space $\boldsymbol{U}_J$, it is often preferable to seek the solution in the entire $\boldsymbol{U}$ space.

3.1.1.1 Weakly penalised form and the penalty / LM / PL methods

For later comparisons, this section introduces a weakly penalised form of the mechanical problem and shows its equivalence with both penalty and LM formulations. Here we introduce the projection operator $\pi_W : L^2(\Omega_0) \to W$ which, for any function $g \in L^2(\Omega_0)$, denotes the orthogonal projection onto W, *i.e.*

$$(g - \pi_W(g), q) := \int_{\Omega_0} [g - \pi_W(g)] \, q \, dV := 0, \quad \forall q \in W, \tag{3.4}$$

where the constraint on π_W is satisfied weakly, through test functions q in function space W. In this way, g may be represented coarsely or finely by adjusting the selection of the space W (as will be discussed further in the following sections). Π_P denotes the weakly penalised total potential energy functional,

$$\Pi_P(\boldsymbol{v}) = \int_{\Omega_0} \Psi_d(\boldsymbol{v}) + \frac{1}{2}k[\pi_W(J-1)]^2 dV + \Pi_{ext}(\boldsymbol{v}), \tag{3.5}$$

where Ψ_d is the deviatoric strain energy function in section 2.4.1. Here, an additional penalty term has been included, representing the growth in energy resulting from material compression, as is typical for many penalty methods. The degree of compressibility is introduced through the penalty parameter k. However, the presence of the projection operator π_W within the penalty term enables the selective weakening or strengthening of the constraint by allowing the constraint to hold weakly through Eq. 3.4. When $J \in W$ for any $\boldsymbol{v} \in \boldsymbol{U}$ (for example, when $W := L^2(\Omega_0)$, as is the case for the continuous mechanical system[38]), then

$$\pi_W(J-1) = J - 1, \tag{3.6}$$

and Eq. 3.5 is reduced to the classic total potential energy functional for the penalty method,

$$\Pi_k(\boldsymbol{v}) = \int_{\Omega_0} \Psi_d(\boldsymbol{v}) + \frac{1}{2}k(J-1)^2 dV + \Pi_{ext}(\boldsymbol{v}), \tag{3.7}$$

where the k-dependent term denotes the volumetric penalty term often used in cardiac mechanics[260,119]. The perturbed Lagrangian formulation may be derived by introducing an additional variable, $\lambda \in W$, such that,

$$\lambda := k\pi_W^v. \tag{3.8}$$

Substituting the orthogonal projection with the added variable, and adding the Galerkin orthogonality condition (Eq. 3.4) the PL functional can be derived [18,243,38,228]:

$$\Pi_\lambda(\boldsymbol{v}, \lambda) = \int_{\Omega_0} \Psi_d(\boldsymbol{v}) + \lambda(J-1) - \frac{\lambda^2}{2k} dV + \Pi_{ext}(\boldsymbol{v}). \tag{3.9}$$

This general purpose formulation has been employed for the solution of nearly incompressible solid mechanics[243,18,38,36] and has also been used in cardiac mechanics[247]. Note that, as $k \to \infty$, the previous formulation becomes the classic LM method[25,97],

$$\Pi_{LM}(\boldsymbol{v}, \lambda) = \int_{\Omega_0} \Psi_d(\boldsymbol{v}) + \lambda(J-1)dV + \Pi_{ext}(\boldsymbol{v}). \tag{3.10}$$

In the continuous setting, the solution $\boldsymbol{u} \in \boldsymbol{U}$ satisfies,

$$\Pi_P(\boldsymbol{u}) := \inf_{\boldsymbol{v} \in \boldsymbol{U}} \Pi_P(\boldsymbol{v}) \tag{3.11}$$

$$\Pi_k(\boldsymbol{u}) := \inf_{\boldsymbol{v} \in \boldsymbol{U}} \Pi_k(\boldsymbol{v}) \tag{3.12}$$

$$\Pi_\lambda(\boldsymbol{u}, \lambda) := \inf_{\boldsymbol{v} \in \boldsymbol{U}} \sup_{q \in W} \Pi_\lambda(\boldsymbol{v}, q) \tag{3.13}$$

for all approaches and all values of k, therefore all methods are equivalent. However, this equivalence is often lost in the discrete setting, as different strategies are applied to discretise the function space, $\boldsymbol{U}$, and the orthogonal projection, π_W.

3.1.2 Finite element approximation

In the FEM framework (see section 2.6), used in the solution of problems in Eq. 3.11-3.13, the domain Ω_0 is subdivided into a finite number of non-overlapping elements[291]. The displacement is then interpolated with functions in $\boldsymbol{U}^h \subset \boldsymbol{U}$ and the displacement solution is then expressed as the weighted sum introduced in Eq. 2.54,

$$\boldsymbol{u}^h = \boldsymbol{\mathcal{U}} \cdot \boldsymbol{\Phi_u}, \quad \boldsymbol{\mathcal{U}} \in \mathbb{R}^{N_{\boldsymbol{u}}}, \tag{3.14}$$

with $\boldsymbol{\Phi_u}$ an $N_{\boldsymbol{u}}$ vector function comprised of basis functions. In all approaches, the minimisation of the total potential energy occurs over $\boldsymbol{U}^h \subset \boldsymbol{U}$.

The primary point of departure between the penalty and PL formulations comes in the choice of orthogonal projection. In the case of the penalty method, the orthogonal projection $\pi_W : L^2(\Omega_0) \to W$ remains on the continuous space $W = L^2(\Omega_0)$, leaving the total potential energy Π_k unchanged. In contrast, the PL approach given in Eq. 3.9 and 3.13 requires a numerical approximation of the pressure variable, λ by λ^h, it is hence natural to introduce the discrete function space $W^h \subset W$, defined in Eq. 2.51.

Numerical approximation of λ is equivalent to introducing the projection operator $\pi_{W^h} : L^2(\Omega_0) \to W^h$, which satisfies the Galerkin orthogonality condition (Eq. 3.4) on W^h. This change means that π_{W^h} projects the incompressibility onto a discrete set of polynomials of degree k_p, effectively relaxing strict satisfaction of the constraint. The

spaces $\boldsymbol{U}^h$ and W^h are often selected to satisfy the inf-sup condition (where we note $k_p < k_u$), which ensures uniqueness in the multiplier for all k [12,25,174,20,202]. Additionally, for appropriately selected spaces W^h – such as $\mathbb{Q}^{k_u} - \mathbb{Q}^{k_p}$ with $k_u = k_p + 1$ – convergence rates in the energy norm are optimal (*i.e.* $\mathcal{O}(h^{k_u})$).

It is well known that penalty and Lagrange multiplier methods need not be equivalent in the discrete setting, as can also be confirmed by the presence of locking phenomena in penalty applications [25,242]. These facts can also be observed through the dependence of the methods on the penalty parameter k. As $k \to \infty$, the PL becomes the classic LM method, and the approximation spaces are reduced to the subsets,

$$\boldsymbol{U}^h_k = \{\boldsymbol{v}^h \in \boldsymbol{U}^h | \pi_W(J^h - 1) = 0\}, \tag{3.15}$$

$$\boldsymbol{U}^h_\lambda = \{\boldsymbol{v}^h \in \boldsymbol{U}^h | \pi_{W^h}(J^h - 1) = 0\}, \tag{3.16}$$

for the penalty and LM methods, respectively. In this case, J^h denotes the discrete J, distinguished from its continuous form because it is computed using the interpolated functions $\boldsymbol{v}^h$. These spaces are nested, *i.e.*

$$\boldsymbol{U}^h_k \subseteq \boldsymbol{U}^h_\lambda \subseteq \boldsymbol{U}^h, \tag{3.17}$$

illustrating the more restrictive subset of functions over which the minimisation problem can be considered. As a consequence, the space $\boldsymbol{U}^h_k$ of the penalty method is typically a small subset of $\boldsymbol{U}^h$ and can be too restrictive. This is because a small violation of the incompressibility constraint can cause a significant increase in the strain energy even though the approximate solution may have a minor degree of error from the true solution.

In contrast, while the LM approach effectively weakens the satisfaction of the constraint, it also has proven optimal convergence rates when $\boldsymbol{U}^h$ and W^h are chosen to satisfy the inf-sup condition [25]. Therefore, the use of the LM approach circumvents over-constraining of the approximation space, but comes at the expense of computing an additional variable.

3.1.3   Discrete weakly penalised form

In the discrete setting, the projection operator $\pi_{W^h} : L^2(\Omega_0) \to W^h$ introduced in Eq. 3.4 can be written in a matrix form as,

$$(g - \pi^h_W(g), q^h) := \boldsymbol{Q}^T(\boldsymbol{R}_g - \boldsymbol{M}\boldsymbol{\pi}) := 0, \quad \forall q^h \in W^h \tag{3.18}$$

where $q^h = \boldsymbol{Q} \cdot \boldsymbol{\Phi}_{\boldsymbol{w}}$ is a test function in W^h and $\pi^h_W(g) = \boldsymbol{\pi} \cdot \boldsymbol{\Phi}_{\boldsymbol{w}}$ denotes the projection of g on W^h, with $\boldsymbol{\Phi}_{\boldsymbol{w}}$ a vector function composed of basis functions as defined in Eq. 2.55

and $\boldsymbol{Q}$ and $\boldsymbol{\pi}$ the nodal values' vectors of the test function and projection, respectively. Moreover, $\boldsymbol{M}$ is the W^h-mass matrix,

$$[\boldsymbol{M}]_{ij} := \int_{\Omega_0} \phi_w^i \, \phi_w^j dV, \quad \phi_w^i, \phi_w^j \in W^h, \tag{3.19}$$

where ϕ_w^i is the $i-$th basis function of W^h and $\boldsymbol{R}_g$ is the weighted function over the test space W^h,

$$[\boldsymbol{R}_g]_j = \int_{\Omega_0} \phi_w^j gdV, \quad \phi_w^j \in W^h. \tag{3.20}$$

Therefore, the introduced term in Eq. 3.5 can be written as

$$\int_{\Omega_0} \frac{1}{2} k[\pi_W(J-1)]^2 dV = \frac{1}{2} k \boldsymbol{\pi}^T \boldsymbol{M} \boldsymbol{\pi}, \tag{3.21}$$

where here $\boldsymbol{\pi} \cdot \boldsymbol{\Phi_w} = \pi(J^h - 1)$. Following from Eq. 3.18 and noting the requirement that the projection holds for $q^h \in W^h$ is equivalent to requiring it holds for all $\boldsymbol{Q} \in \mathbb{R}^{N_w}$ (where N_w is the dimension of the discrete space W^h), $\boldsymbol{\pi}$ can be seen to satisfy the linear system,

$$\boldsymbol{M} \boldsymbol{\pi} = \boldsymbol{R}_J, \tag{3.22}$$

where $\boldsymbol{M}$ is given in equation 3.19 and

$$[\boldsymbol{R}_J]_j = \int_{\Omega_0} \phi_w^j (J^h - 1) dV, \quad \phi_w^j \in W^h. \tag{3.23}$$

Inverting $\boldsymbol{M}$ in Eq. 3.22 and substituting into Eq. 3.21, the weakly penalised system (Eq. 3.5) may be written in discrete form as,

$$\Pi_P(\boldsymbol{v}^h) = \int_{\Omega_0} \Psi_d(\boldsymbol{v}^h) dV + \frac{1}{2} k \boldsymbol{R}_J^T \boldsymbol{M}^{-1} \boldsymbol{R}_J + \Pi_{ext}(\boldsymbol{v}^h). \tag{3.24}$$

This form, also used by Bercovier[18] and others[38,36], reduces the system into a single minimisation problem on $\boldsymbol{U}^h$. However, the presence of $\mathbf{M}^{-1}$ requires the solution of Eq. 3.22, incurring similar computational cost as computing the PL solution. Considering the discrete weak form and its solution (as will be shown later), this weakly penalised term requires matrix-matrix products which are (1) expensive, (2) nonlinearly dependent on the solution and (3) generally of a more dense sparsity than the standard penalty system.

The practical issues presented above, stem from the choice of global orthogonal projection, π_{W^h}, which unfortunately complicates the computation. However, the choice of π_{W^h} is essentially arbitrary and should ideally balance the need for accuracy with ease of computation. An improved alternative approach would be to use a local orthogonal

projection, $\pi_{W_{loc}^h}$, satisfying

$$\boldsymbol{M}_\tau \boldsymbol{\pi}_l = \boldsymbol{R}_{J,\tau}, \quad \forall \tau \in \mathcal{T}, \tag{3.25}$$

where $\boldsymbol{M}_\tau$ and $\boldsymbol{R}_{J,\tau}$ are the mass matrix and the weighted constraint vectors on the element τ. Essentially, the local orthogonal projection, $\pi_{W_{loc}^h}$ satisfies Eq. 3.4 on the piecewise discontinuous space,

$$W_{loc}^h := \{q^h \in L^2(\Omega_0)|\ q^h|_\tau \in \mathbb{P}^{k_\pi}(\tau),\ \forall \tau \in \mathcal{T}(\Omega_0)\}. \tag{3.26}$$

Using this locally continuous, but globally discontinuous interpolation space, the total potential energy for the body becomes,

$$\Pi_P(\boldsymbol{v}^h) \;=\; \int_{\Omega_0} \Psi_d(\boldsymbol{v}^h)dV + \frac{k}{2}\sum_{\tau \in \mathcal{T}} \boldsymbol{R}_{J,\tau}^T \boldsymbol{M}_\tau^{-1} \boldsymbol{R}_{J,\tau} + \Pi_{ext}(\boldsymbol{v}^h), \tag{3.27}$$

which by construction enables the computations of the constraint and mass matrix on each element and then incorporates the contribution of each element in the total potential energy of the system.

This localised projection, also known as static condensation, has been employed by Sussman and Bathe[243], Bercovier[18] and Simo *et al.*[226,227] to enhance the efficiency of the formulation. Indeed, by localising the projection, computations remain on the element level, reducing the computational cost relative to Eq. 3.24. Moreover, localisation of the penalty term preserves sparsity of the penalty system, significantly reducing sparsity to that resulting from Eq. 3.24. These practical improvements come at the cost of restricting the approximation space. Again, as $k \to \infty$, the approximation space of the weakly penalised formulation in equation 3.27 is restricted to the space,

$$\boldsymbol{U}_P^h = \{\boldsymbol{v}^h \in \boldsymbol{U}^h | \pi_{W_{loc}^h}^{v^h} = 0\}. \tag{3.28}$$

which we note is,

$$\boldsymbol{U}_k^h \subseteq \boldsymbol{U}_P^h \subseteq \boldsymbol{U}_\lambda^h. \tag{3.29}$$

Though the weakly penalised form in Eq. 3.27 does not mandate the inf-sup condition, usage of inf-sup stable spaces (such as Nicolaides-Boland[20] or Crouzeix-Raviart[50] elements) with globally discontinuous pressure enables optimal convergence. However, as will be demonstrated, even for some spaces which are not inf-sup stable (for instance $\mathbb{Q}^2 - \mathbb{Q}_{loc}^1$), this weakening of the constraint is sufficient to restore convergence.

3.1.4 Discrete weak form of the weakly penalised formulation

The discrete weak form for the weakly penalised formulation can be obtained as discussed in section 2.5, by requiring that the directional derivative of the total potential energy functional vanishes in all arbitrary directions $\delta\boldsymbol{u}^h \in \boldsymbol{U_0}^h$ at $\boldsymbol{u}^h$, *i.e.*

$$D\Pi_P(\boldsymbol{u}^h)[\delta\boldsymbol{u}^h] = 0, \quad \forall\delta\boldsymbol{u}^h \in \boldsymbol{U_0}^h, \tag{3.30}$$

with $\boldsymbol{U_0}^h$ the homogeneous zero Dirichlet subspace of $\boldsymbol{U}^h$. Following this procedure, the discrete weak form can be written in operator notation as,

$$A(\boldsymbol{u}^h, \delta\boldsymbol{u}^h) + C(\boldsymbol{u}^h, \delta\boldsymbol{u}^h) = F(\delta\boldsymbol{u}^h). \tag{3.31}$$

The residual function R is defined as,

$$R(\boldsymbol{u}^h, \delta\boldsymbol{u}^h) := A(\boldsymbol{u}^h, \delta\boldsymbol{u}^h) + C(\boldsymbol{u}^h, \delta\boldsymbol{u}^h) - F(\delta\boldsymbol{u}^h) = 0, \tag{3.32}$$

where the operators A, F, and C are defined as,

$$A(\boldsymbol{u}^h, \delta\boldsymbol{u}^h) = \int_{\Omega_0} \boldsymbol{F}^h \boldsymbol{S}^h : \nabla_{\boldsymbol{X}}\delta\boldsymbol{u}^h dV,$$

$$F(\delta\boldsymbol{u}^h) = \int_{\Omega_0} \boldsymbol{f}_0 \cdot \delta\boldsymbol{u}^h dV + \int_{\Gamma_0} \boldsymbol{t}_0 \cdot \delta\boldsymbol{u}^h dA,$$

$$C(\boldsymbol{u}^h, \delta\boldsymbol{u}^h) = k \sum_{\tau \in \mathcal{T}} \delta\boldsymbol{U}_\tau^T \boldsymbol{B}_\tau^T \boldsymbol{M}_\tau^{-1} \boldsymbol{R}_{J,\tau},$$

where $\boldsymbol{F}^h = \nabla\boldsymbol{u}^h + \boldsymbol{I}$ and $\boldsymbol{S}^h$ are the discrete deformation gradient and second Piola stress tensors, respectively[21]. Here, $\delta\boldsymbol{U}_\tau$ represents the local basis coefficients for $\delta\boldsymbol{u}^h$ on the element, and the element matrix $\boldsymbol{B}_\tau$ denotes the linearised constraint, derived from the PL functional, *i.e.*

$$[\boldsymbol{B}_\tau]_{ij} = B_\tau(\phi_w^i, \boldsymbol{u}^h, \boldsymbol{\phi}_u^j) = \int_\tau \phi_w^i J^h \boldsymbol{F}^{h-T} : \nabla_{\boldsymbol{X}}\boldsymbol{\phi}_u^j dV \tag{3.33}$$

with $(\phi_w^i, \boldsymbol{\phi}_u^j) \in W_{loc}^h \times \boldsymbol{U}^h$. Note that $\boldsymbol{M}_\tau$ and $\boldsymbol{R}_{J,\tau}$ are identical to those in Eq. 3.19 and 3.23, with $\phi_w^i \in W_{loc}^h$.

The weak forms for the penalty, LM and PL formulations can be similarly derived as outlined in appendix A.

3.1.4.1 Non-linear solution and Jacobian

The global Shamanskii-Newton-Raphson (SNR) method[224], described in section 2.6.3.2 is employed in the solution of the mechanical system introduced in equation 3.32 (as

well as the others discussed in Appendix A). This method has been shown to be effective for problems in fluid-structure interaction[152], enabling faster computation by re-using the Jacobian matrix over multiple time / load steps.

As both penalty and LM formulations have been outlined elsewhere, the focus in this section is on the Jacobian and residual evaluations for the weakly penalised approach. Following the SNR approach, n denotes the current iteration and β denotes a previous iteration at which the Jacobian was computed. Note that $\boldsymbol{J} \in \mathbb{R}^{N_u \times N_u}$ and $\boldsymbol{R} \in \mathbb{R}^{N_u}$ may be written as,

$$\boldsymbol{J}(\boldsymbol{U}^{\beta}) = \mathsf{A}^{\tau} \boldsymbol{A}_{\tau}(\boldsymbol{U}^{\beta}) + \boldsymbol{C}_{\tau}(\boldsymbol{U}^{\beta}), \tag{3.34}$$

$$\boldsymbol{R}(\boldsymbol{U}^{n}) = \mathsf{A}^{\tau} \boldsymbol{R}_{A,\tau}(\boldsymbol{U}^{n}) + \boldsymbol{R}_{P,\tau}(\boldsymbol{U}^{n}), \tag{3.35}$$

where A is the FEM assembly operator, the subscript τ denotes vector, matrices or operators constructed on the element and $\boldsymbol{R}_{P,\tau}$ and $\boldsymbol{R}_{A,\tau}$ are element-level residual contributions, stemming from the projection term and all other terms, respectively. Introducing a short-hand notation, i.e. $\boldsymbol{C}_{\tau}^{\beta} = \boldsymbol{C}_{\tau}(\boldsymbol{U}^{\beta})$, we can express the element-level Jacobian contributions $\boldsymbol{A}_{\tau}$ and $\boldsymbol{C}_{\tau}$ as,

$$[\boldsymbol{A}_{\tau}^{\beta}]_{ij} = \frac{1}{\epsilon}\Big[A_{\tau}(\boldsymbol{u}_{\beta}^{h} + \epsilon\boldsymbol{\phi}_{u}^{j}, \boldsymbol{\phi}_{i}) - F_{\tau}(\boldsymbol{u}_{\beta}^{h} + \epsilon\boldsymbol{\phi}_{u}^{j}, \boldsymbol{\phi}_{i}) - A_{\tau}(\boldsymbol{u}_{\beta}^{h} - \epsilon\boldsymbol{\phi}_{u}^{j}, \boldsymbol{\phi}_{i})$$
$$+ F_{\tau}(\boldsymbol{u}_{\beta}^{h} - \epsilon\boldsymbol{\phi}_{u}^{j}, \boldsymbol{\phi}_{i})\Big],$$
$$\boldsymbol{C}_{\tau}^{\beta} = k[\boldsymbol{B}_{\tau}^{\beta}]^{T}\boldsymbol{M}_{\tau}^{-1}\boldsymbol{B}_{\tau}^{\beta},$$
$$[\boldsymbol{R}_{A,\tau}^{n}]_{j} = A_{\tau}(\boldsymbol{u}_{n}^{h}, \boldsymbol{\phi}_{u}^{j}) - F_{\tau}(\boldsymbol{\phi}_{u}^{j}),$$
$$\boldsymbol{R}_{P,\tau}^{n} = k[\boldsymbol{B}_{\tau}^{n}]^{T}\boldsymbol{M}_{\tau}^{-1}\boldsymbol{R}_{J,\tau}^{n}.$$

The element-level matrix $\boldsymbol{A}_{\tau}$ denotes the terms resulting from the elasticity stress / boundary contributions* and is evaluated using central finite differencing (typically $\epsilon = 10^{-4}h$, where h is the mesh size). $\boldsymbol{C}_{\tau}$ denotes those terms which result from the weakly penalised form. The linearisation of the C operator introduced in section 3.1.4, assumes that $\boldsymbol{B}_{\tau}$, defined in equation 3.33, is independent of $\boldsymbol{u}$. This linearisation does not seem to impact convergence of the Newton scheme and preserves symmetric positive semi-definiteness of the weakly penalised matrix term. $\boldsymbol{C}_{\tau}$ is comprised of the local element mass matrix $\boldsymbol{M}_{\tau}$ and the linearised constraint $\boldsymbol{B}_{\tau}$ introduced in the previous section (Eq. 3.33). It should be noted that as $\boldsymbol{M}_{\tau}$ and its inverse are linear, they may be computed once for the entire simulation. On the other hand, the linearised constraint must be re-computed due to its nonlinear dependence on the solution. However, computing this matrix is quick, as it does not require differencing.

---

*Note that, as the traction $\boldsymbol{t}$ typically depends on the physical domain, the operator F_{τ} often depends on $\boldsymbol{u}$ and is included in the Jacobian.

3.1.4.2 Residual modifications for the nonlinear solution of the weakly penalised system

This section presents modifications introduced in the weakly penalised formulation to improve its nonlinear convergence. As mentioned in section 3.1.1.1, the weakly penalised system can be thought of as a generalised formulation from which the PL, penalty or statically condensed PL formulations can be derived, depending on the choice of the projection operator. The equivalence of these methods under the weakly penalised regime, allows us to combine and take advantage of the good characteristics of each method. For instance, the weakly penalised formulation combines the simplified structure of the penalty method with the convergence characteristics of the PL formulation. However, due to the stiffness of the linear system at high values of the bulk modulus, the penalised formulations (classic penalty / weakly penalised) exhibit deteriorated nonlinear convergence. This stands in stark contrast to the PL method, which (for inf-sup stable schemes) exhibits fast convergence even for high bulk modulus. However, it has been observed that, when the choice of π^h provides equivalence with the discrete PL method, the scheme presents poor nonlinear convergence, although, in principle, the convergence should be similar. Examining the update formulae for both weakly penalised and PL approaches (see Appendix C), we observe that deteriorated convergence stems from: (1) initial residual amplification, and (2) the k-dependence of the residual.

The first factor contributing to poor convergence results from non-monotonicity in the residual. This manifests particularly early during the nonlinear solution after the first iteration. This is particularly evident with Dirichlet conditions on a stiff material, where the norm of the boundary displacement (for example) may be much smaller than the updated residual, due to stiffness in the material. This issue, which is not observed in the PL solution, is circumvented in the Newton-Raphson procedure and the SNR procedure outlined in section 2.69, by enabling an initial amplification of the residual and relaxing strict requirements on monotonicity, through relevant parameters of the scheme.

A less trivial issue to address, is the amplification of the residual of the weakly penalised formulation (Eq. 3.35) resulting from large k, which can lead to poor convergence or stalling in the iterative solve. This increased residual, due to strong dependence on the weakly penalised term, often does not imply divergence but rather results from a k-dependent scaling of the projection problem and its nonlinear dependence on $\boldsymbol{u}^h$, as shown in Appendix C. This issue is, however, not observed in the PL approach, where the projection constraint is not scaled by k.

The weakly penalised residual contribution in Eq. 3.35 can be rewritten in terms of

the linearised guess and a remainder,

$$
\begin{aligned}
\boldsymbol{R}_{P,\tau}^n &= \boldsymbol{R}_{P^*,\tau} + k[\boldsymbol{B}_\tau^n]^T \boldsymbol{R}_{e,\tau}, & (3.36) \\
\boldsymbol{R}_{P^*,\tau} &= k[\boldsymbol{B}_\tau^n]^T \boldsymbol{M}_\tau^{-1}(\boldsymbol{R}_{J,\tau}^{n-1} + \boldsymbol{B}_\tau^{n-1}\delta\boldsymbol{U}_\tau^{n-1}), & (3.37) \\
\boldsymbol{R}_{e,\tau} &= \boldsymbol{M}_\tau^{-1}(\boldsymbol{R}_{J,\tau}^n - \boldsymbol{R}_{J,\tau}^{n-1} - \boldsymbol{B}_\tau^{n-1}\delta\boldsymbol{U}_\tau^{n-1}). & (3.38)
\end{aligned}
$$

where $\boldsymbol{R}_{P^*,\tau}$ and $\boldsymbol{R}_{e,\tau}$ are the element contributions of the terms introduced in the PL linearised system for $\beta = n$ (Eq. C.8).

Here the first term approximates the current linearised guess of the projection, while the second examines how well the current guess satisfies the projection problem. In other words, the first term denotes the hydrostatic contribution to momentum, while the second represents the error remaining in the projection problem amplified by the bulk modulus k. For large k, the latter term can become disproportionately scaled, making nonlinear convergence more challenging. Considering Eq. C.3, the residual terms are actually $\boldsymbol{R}_A + \boldsymbol{R}_{P^*}$ and $\boldsymbol{R}_e$, where the latter term is not scaled by k in this case. Therefore, poor convergence stemming from the hydrostatic constraint is avoided in the PL formulation.

To circumvent this issue, the Newton-Raphson scheme of the weakly penalised formulation is modified to measure convergence of $\|\boldsymbol{R}_A + \boldsymbol{R}_{P^*}\|$ instead of $\|\boldsymbol{R}_A + \boldsymbol{R}_P\|$. Clearly, $\|\boldsymbol{R}_{P^*,\tau}^n - \boldsymbol{R}_{P,\tau}^n\| \to 0$ as $\|\delta\boldsymbol{U}^n\| \to 0$; however, measuring convergence of $\boldsymbol{R}_{P^*}$ avoids issues due to high bulk modulus.

Furthermore, extending this form to the penalty formulation to enable fair comparisons, we must select the projection $\pi^h : L^2(\Omega_0) \to L^2(\Omega_0)$. As, in this case, the rank of $\boldsymbol{M}$ is no longer finite dimensional, the modified penalty form may instead be written in its equivalent integral form, *i.e.*

$$
\begin{aligned}
\boldsymbol{R}_{P,\tau}^n &= \boldsymbol{R}_{P^*,\tau} + \boldsymbol{R}_{e,\tau}, & (3.39) \\
(\boldsymbol{R}_{P^*,\tau})_i &= \int_{\Omega_0} k(J^{n-1} + J^{n-1}(\boldsymbol{F}_h^{n-1})^{-T} : \nabla_{\boldsymbol{X}}\delta\boldsymbol{u}^{h,n-1})J^n(\boldsymbol{F}_h^n)^{-T} : \nabla_{\boldsymbol{X}}\phi_i dV & (3.40) \\
(\boldsymbol{R}_{e,\tau})_i &= \int_{\Omega_0} k(J^n - J^{n-1} - J^{n-1}(\boldsymbol{F}_h^{n-1})^{-T} : \nabla_{\boldsymbol{X}}\delta\boldsymbol{u}^{h,n-1})J^n(\boldsymbol{F}_h^n)^{-T} : \nabla_{\boldsymbol{X}}\phi_i dV.
\end{aligned}
$$

Similarly to the modifications introduced in the weakly penalised approach, in the modified penalty formulation we measure the convergence of $\|\boldsymbol{R} + \boldsymbol{R}_{P^*}\|$ instead of $\|\boldsymbol{R} + \boldsymbol{R}_P\|$. In this way, amplification of the error in the second term of the residual is avoided, allowing better nonlinear convergence of the scheme.

3.1.4.3 Residual modifications for the SNR solution of the weakly penalised system

While the Shamanskii-Newton-Raphson scheme can significantly enhance the performance of the PL scheme, acceleration in the SNR approach for penalised methods is minimal or even worse than standard Global Newton-Raphson. This deterioration in performance is predominantly due to the stiffness of the system for high k and the inevitable inaccuracies introduced in the descent direction by the re-used Jacobian. In contrast, this deterioration in performance is not observed in either PL or LM formulations, which can take significant advantage of matrix re-use (as will be shown in section 3.2). Once more, by examining the equivalence between weakly penalised and PL formulations (section 3.1.4.2), we observe this deterioration may be circumvented using the modified form,

$$
\begin{align}
\boldsymbol{R}_{P,\tau}^n &= \boldsymbol{R}_{P^*,\tau} + k[\boldsymbol{B}_\tau^\beta]^T \boldsymbol{R}_{e,\tau}, \tag{3.41}\\
\boldsymbol{R}_{P^*,\tau} &= k[\boldsymbol{B}_\tau^n]^T \boldsymbol{M}_\tau^{-1}(\boldsymbol{R}_{J,\tau}^{n-1} + \boldsymbol{B}_\tau^\beta \delta \boldsymbol{U}_\tau^{n-1}), \tag{3.42}\\
\boldsymbol{R}_{e,\tau} &= \boldsymbol{M}_\tau^{-1}(\boldsymbol{R}_{J,\tau}^n - \boldsymbol{R}_{J,\tau}^{n-1} - \boldsymbol{B}_\tau^\beta \delta \boldsymbol{U}_\tau^{n-1}). \tag{3.43}
\end{align}
$$

Note that, as $\|\delta \boldsymbol{U}^n\| \to 0$, the difference in the constraint residual $\|\boldsymbol{R}_{J,\tau}^n - \boldsymbol{R}_{J,\tau}^{n-1}\| \to 0$ and, as a result,

$$
\boldsymbol{R}_{P,\tau}^n \to k[\boldsymbol{B}_\tau^n]^T \boldsymbol{M}_\tau^{-1} \boldsymbol{R}_{J,\tau}^n,
$$

which represents the standard residual resulting from equation 3.32. Therefore, as the scheme converges, the modified residual $\boldsymbol{R}_{P,\tau}$ converges to the residual obtained by evaluating C. Furthermore, if $\beta = n$, the first term in the definition $\boldsymbol{R}_{P,\tau}$ drops away, resulting to the expected residual.

The modifications introduced to the residual of the weakly penalised formulation can also be applied in the penalty method to improve its nonlinear convergence behaviour, by once more selecting the projection operator $\pi^h : L^2(\Omega_0) \to L^2(\Omega_0)$, and using the equivalence of the weakly penalised / penalty forms. Expressing these modifications in integral form, the modified penalty form can be expressed by the following residual contributions:

$$
\begin{align}
\boldsymbol{R}_{k,\tau}^n &= \boldsymbol{R}_{k^*,\tau} + \boldsymbol{R}_{ek,\tau}, \tag{3.44}\\
(\boldsymbol{R}_{P^*,\tau})_i &= \int_{\Omega_0} k(J^{n-1} + J^\beta(\boldsymbol{F}_h^\beta)^{-T} : \nabla_{\boldsymbol{X}} \delta \boldsymbol{u}^{h,n-1}) J^n (\boldsymbol{F}_h^n)^{-T} : \nabla_{\boldsymbol{X}} \phi_i dV \tag{3.45}\\
(\boldsymbol{R}_{e,\tau})_i &= \int_{\Omega_0} k(J^n - J^{n-1} - J^\beta(\boldsymbol{F}_h^\beta)^{-T} : \nabla_{\boldsymbol{X}} \delta \boldsymbol{u}^{h,n-1}) J^\beta (\boldsymbol{F}_h^\beta)^{-T} : \nabla_{\boldsymbol{X}} \phi_i dV.
\end{align}
$$

With the introduced modifications in the residual monitored for convergence, the modified penalty method is able to significantly exploit matrix re-use, and substantially

improve its computational efficiency.

3.2 Numerical results

In this section, the various formulations outlined in section 3.1 are compared on a simple two-dimensional problem as well as on cardiac mechanics problems. The convergence behaviour of the LM, PL, penalty and weakly penalised formulations is assessed in the solution of incompressible mechanics problems, for varying values of k. Furthermore, these approaches are compared on nearly-incompressible solid mechanics problems, assuming various values for the bulk modulus. The considered formulations are also examined with respect to their numerical efficiency.

3.2.1 Mechanical tests

3.2.1.1 Elongation of a two-dimensional square domain

The convergence behaviour of the LM, penalty and weakly penalised methods was compared on the simple case of the stretch of a square domain (Fig. 3.1a). The body was assumed to be made of a neo-Hookean material, described by the deviatoric strain energy / Second-Piola stress tensor [21],

$$\Psi_d(\boldsymbol{C}) = \frac{\mu}{2} \left(\frac{I_{\boldsymbol{C}}}{III_{\boldsymbol{C}}^{1/2}} - 2 \right), \quad \boldsymbol{S}_d = \frac{\mu}{III_{\boldsymbol{C}}^{1/2}} \left(\boldsymbol{I} - \frac{I_{\boldsymbol{C}}}{2} \boldsymbol{C}^{-1} \right), \tag{3.46}$$

where the material parameter μ is analogous to the shear modulus of linear elasticity.

Mesh	1	2	3	4	5	6	7
no. elem.	16	64	256	1,024	4,096	16,384	262,144
no. DOFS[†]	187	659	2,467	9,539	37,507	148,739	5,875,363
no. DOFS[‡]	162	578	2,178	8,450	33,282	132,098	4,924,738

(b)

(a)
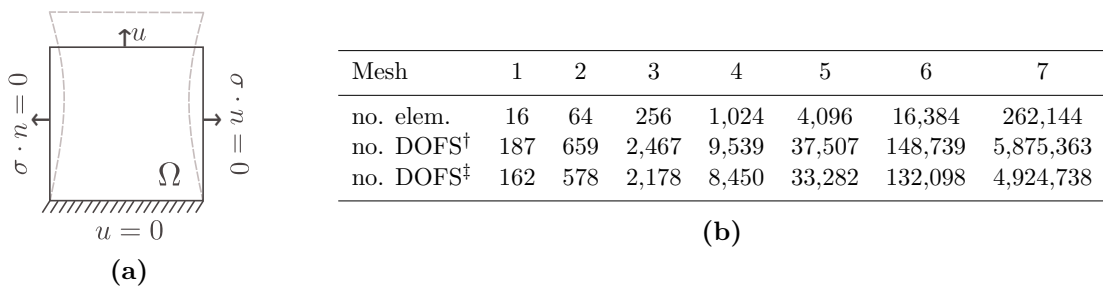
Figure 3.1 Discretisation of the two-dimensional square domain: (**a**) A neo-Hookean material in a square domain (1×1) under no slip (bottom edge), no traction (side walls), and vertical displacement of 20% (top edge). A shear modulus of $\mu = 100 Pa$ was used. (**b**) Number of elements and degrees of freedom (DOFS) in each discretisation for the (†) LM / PL and (‡) weakly penalised / penalty methods.

The domain was discretised using six different meshes of inf-sup stable $\mathbb{Q}^2 - \mathbb{Q}^1$ Taylor-

Hood quadrilateral elements[25]. For the weakly penalised formulation, a quadratic interpolation was used for the displacement field and a discontinuous linear interpolation was used for the pressure. The actual solution was approximated using the LM and PL solution (for the incompressible and nearly-incompressible comparison, respectively) on a finer mesh (mesh$_7$), with a cubic interpolation for the displacement and a quadratic interpolation for the pressure. Fig. 3.1b presents the number of elements in all seven meshes, and the corresponding degrees of freedom when the LM, PL, penalty and weakly penalised methods were used.

3.2.1.2 Cardiac mechanics in the left ventricle

The three methods were also tested on a model of the passive inflation of a left ventricle under diastolic loading conditions. The left ventricle (LV) was modeled as a thick-walled truncated ellipsoid (Fig. 3.2a). A standard generic heterogeneous fibre field was used to represent the structure of the tissue[134], where the fibre angle varied linearly between $60°$ and $-60°$, from endocardium to epicardium[244].

Mesh	1	2	3	4
no. elem.	56	448	3,584	28,672
no. DOFS†	1,914	13,160	97,260	747,092
no. DOFS‡	1,815	12,555	93,075	716,067
Error on mesh	1	2	3	4
PEN*	72.7%	24.7%	12.6%	−
WP*	69.7%	15.9%	7.4%	−
LM*	70.6%	17%	8.1%	−

† LM / PL methods, ‡ weakly penalised / penalty methods
* Error=$\max_t\{||\nabla\boldsymbol{u}(t) - \nabla\boldsymbol{u}_{inc}(t)||/||\nabla\boldsymbol{u}_{inc}(t)||\}$

(a) Idealised LV model

(b)
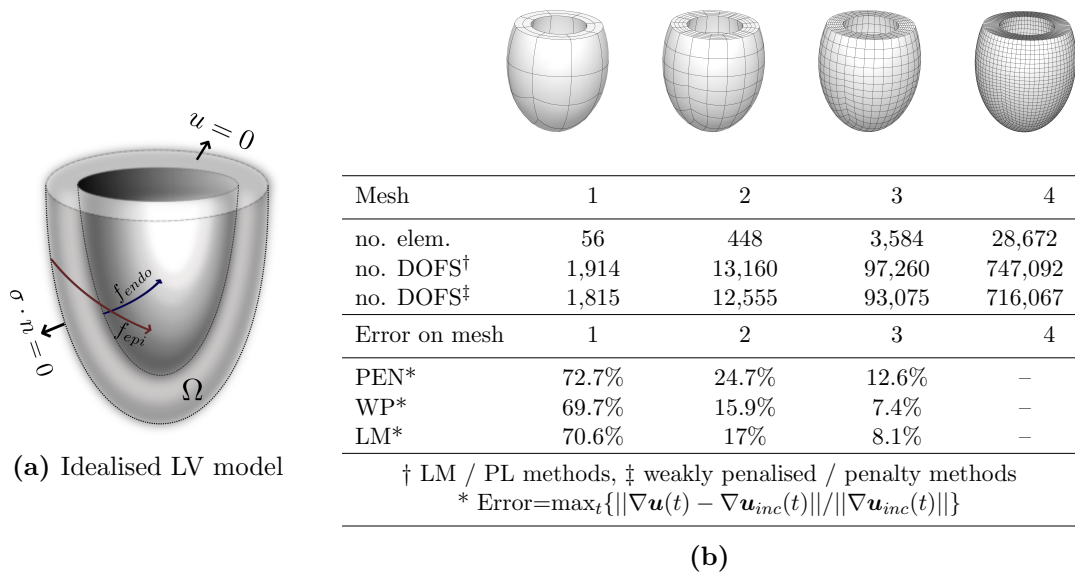
Figure 3.2 Discretisation of the cardiac model: (a) The idealised LV was modeled as a thick-walled ellipsoid truncated at $\frac{3}{4}$ of the total height. Typical cardiac dimensions were used (semi-major axis=$8cm$, semi-minor axis=$5.5cm$, wall thickness= $0.5cm$ at the apex, $1cm$ at the base). The red and blue curves denote the epicardium (f_{epi}) and endocardium (f_{endo}) fibre directions, respectively. Zero traction condition was applied on the epicardial surface, and the base was held fixed. (b) Number of elements and degrees of freedom (DOFS) in each discretisation, and error in displacement solution of the three methods when used in the cardiac cycle test ($k = 10^7$ for the penalty (PEN) and weakly penalised (WP) methods). The error is computed on meshes $1 − 3$ with respect to the incompressible LM solution $\boldsymbol{u}_{inc}(t)$ on mesh$_4$.

The LV was modeled using the transversely isotropic Guccione law[82] as defined in

Eq. 2.33 and the parameters used[260] were $C = 1760Pa$, $b_f = 18.5$, $b_t = 3.58$, $b_{fs} = 1.63$. The endocardial surface of the ventricular model was passively loaded to $3kPa$ ($22.5mmHg$), to describe both normal and pathological LV functions at end diastole. The LV was inflated using 150 equal load steps, by setting the boundary traction equal to the product of the pressure and the deformed surface normal.

In order to simulate a cardiac cycle, the heart model was modified to include myocardial contraction through an active tension generation model[175]. Active tension generation was incorporated into the cardiac model by the addition of the active stress in the fibre direction of the stress tensor. The LV model was also coupled to a Windkessel model representing the systemic circulation, using the parameters given by Korakianitis *et al.* [123]. The coupling was enabled through the use of a Lagrange multiplier which enforced the same rate of change of LV volume in the two models.

The LV was discretised using four different meshes of hexahedral elements (Fig. 3.2b). On the first three discretisations, a quadratic interpolation was used for the displacement. The pressure field was interpolated using linear continuous (for the LM / PL methods) and discontinuous (for the weakly penalised formulation) Lagrange polynomials. In the cardiac tests, the results on the first three meshes were compared with the LM and PL solution on mesh$_4$ (for the incompressible and compressible comparison respectively), where a quadratic-linear interpolation scheme was employed.

3.2.2 Numerical solution

The solid mechanics tests presented in section 3.2.1 were initially used to assess qualitative differences of the methods discussed, and subsequently to test their convergence behaviour. The convergence rate of each method was acquired by observing the change in the error between a high resolution benchmark solution and the approximate solution, with mesh refinement. As compressible methods may be selected as an approximation to incompressible behaviour, we tested the convergence characteristics of the penalty and weakly penalised approaches to the incompressible LM solution (Eq. 3.10). We also examined the ability of these approaches to model compressible behaviour, comparing the results with a fine grid compressible solution(s) (PL solution(s)). The error tolerance for these tests was set to 1×10^{-9}. The problems under consideration were solved in $\mathcal{C}$**Heart** (section 2.7).

(a) $k = 100$ (b) $k = 1000$ (c) $k = 10^7$ (d) LM
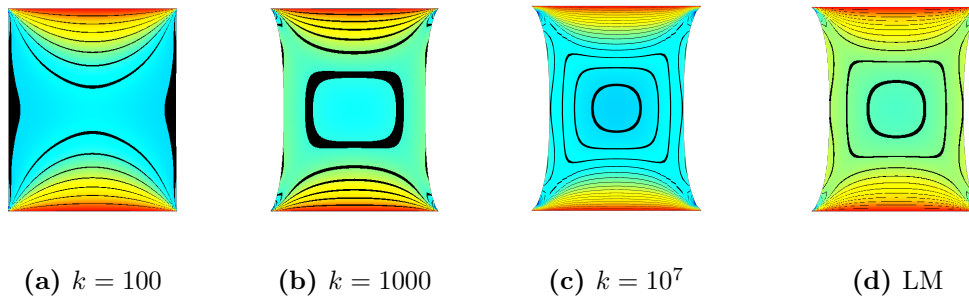
Figure 3.3 Deformation of the two-dimensional domain under elongation, when the penalty ((**a**) $k = 100$, (**b**) $k = 10^3$, (**c**) $k = 10^7$) and (**d**) LM methods are used. Each figure also illustrates the strain in the horizontal direction (E_{xx}) on each point on the domain, ranging between: (**a**) -0.0092 (*blue*) and 0 (*red*), (**b**) -0.24 (*blue*) and 0 (*red*), (**c**) -0.29 (*blue*) and 0 (*red*), (**d**) -0.36 (*blue*) and 0 (*red*). The black contours connect points of the same horizontal strain.

(a) $k = 100$ (b) $k = 1000$ (c) $k = 10^7$ (d) LM
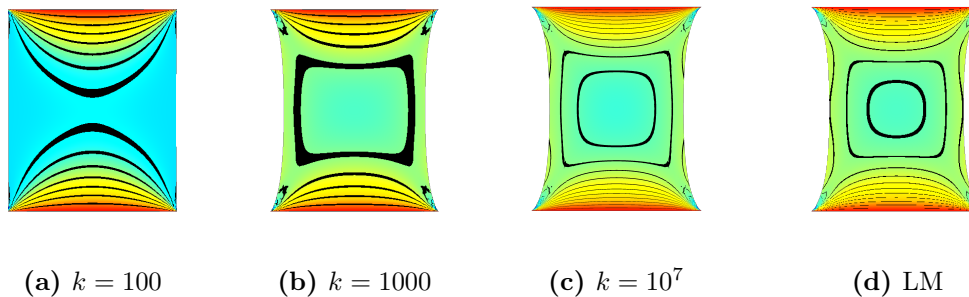
Figure 3.4 Deformation of the two-dimensional domain under elongation, when the weakly penalised ((**a**) $k = 100$, (**b**) $k = 10^3$, (**c**) $k = 10^7$) and (**d**) LM methods are used. Each figure also illustrates the strain in the horizontal direction (E_{xx}) on each point on the domain, ranging between: (**a**) -0.0094 (*blue*) and 0 (*red*), (**b**) -0.28 (*blue*) and 0 (*red*), (**c**) -0.34 (*blue*) and 0 (*red*), (**d**) -0.36 (*blue*) and 0 (*red*). The black contours connect points of the same horizontal strain.

Initially, the methods considered were compared over the solution of the elongation 2D problem, on the same discretisation (mesh 4). Qualitative differences can be deduced through comparisons of strains and deformation in figures 3.3 and 3.4. The behaviour of the methods with increasing values of the penalty parameter is examined. In order to assess the degree of compressibility introduced for the different values of the penalty parameter, figure 3.5 presents the ratio between deformed and undeformed surface area. In this case, a ratio of 1 would imply incompressible deformation.

Similarly, examining the different effects of the methods on cardiac mechanics, we solved each model over a single cardiac cycle, comparing the differences in their behaviour, using the LM method as the point of reference. The cardiac cycle was solved on an intermediate mesh (mesh$_2$), using a quadratic-linear interpolation scheme for the displacement and pressure variables. Fig. 3.6 illustrates the pressure-volume loop derived from the coupled Windkessel-ventricle model as well as the differences between the LM

model and both penalty and weakly penalised methods (with $k = 10^7$) throughout the cycle.
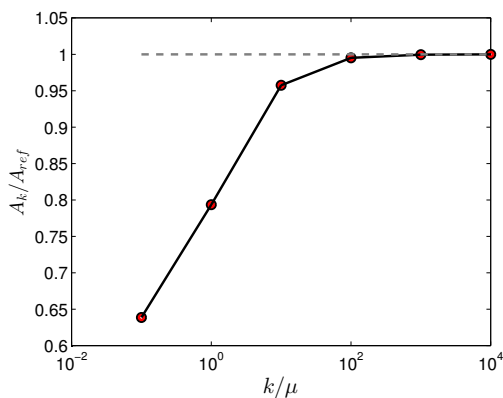
Figure 3.5 Ratio of deformed (A_k) over undeformed (A_{ref}) surface area (degree of compressibility = 1 - A_k/A_{ref}) for the 2D elongation problem, for different values of the penalty parameter k. Penalty (in black) and weakly penalised (in red) approaches are considered here. The ratio for the LM method is presented in grey, although not dependent on k. The ratio is reported over different values of the ratio between penalty parameter k and stiffness value μ.
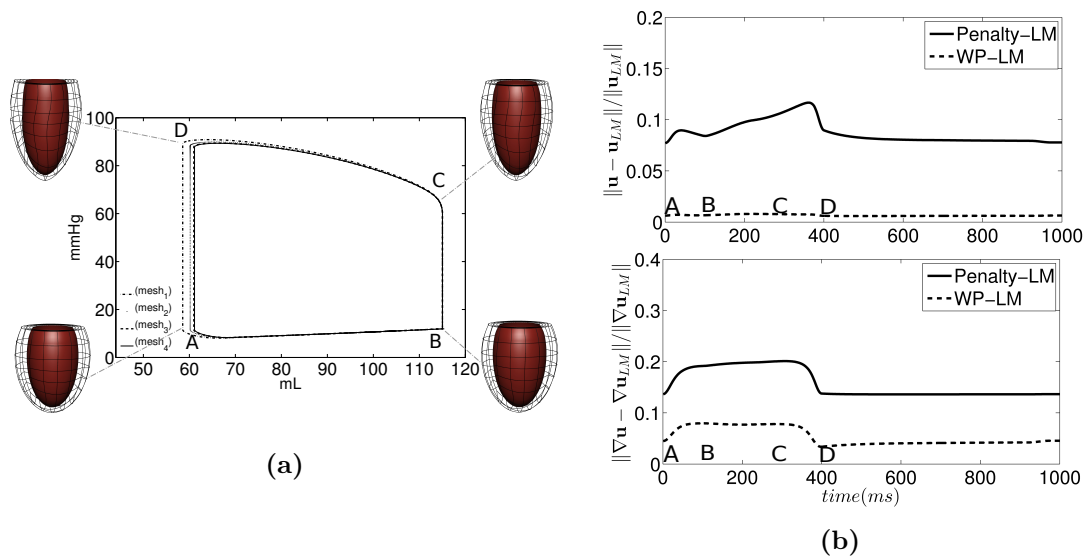
Figure 3.6 Comparison over the cardiac cycle: **(a)** Pressure-volume loops of the weakly penalised solution of the cardiac cycle on the first three meshes. These pressure-volume loops are converging to the pressure-volume loop of the LM solution on mesh$_4$. **(b)** The L^2 norm (*top*) and $\boldsymbol{H}^1$ semi-norm (*bottom*) comparison of the displacement between the penalty and weakly penalised formulations ($k = 10^7$) in different phases of the cardiac cycle on mesh$_2$. Letters A, B, C, D map the time in cycle to cardiac phase on the pressure-volume loop.

3.2.3 Numerical results for the convergence rates

The convergence behaviour of the LM, penalty and weakly penalised formulations was compared using their convergence rates with mesh refinement, over the incompressible formulation of the elongation problem (section 3.2.1.1). Fig. 3.7 compares the error of the penalty and weakly penalised methods in the solution of the incompressible elongation problem, measured over the entire domain as well as a horizontal patch excluding the corners (where singularities in the solution occur). Finally, the importance of interpolation order is highlighted in Fig. 3.8, where linear interpolation was used for both penalty and weakly penalised formulations (where the local orthogonal projection was selected as the set of piecewise-discontinuous constants).

Similar results can be observed in the passive inflation problem detailed in section 3.2.1.2. In this case, convergence of the L^2-norm displacement error in the different methods is shown in Fig. 3.9 for approximation to the fine grid incompressible (for $k \in [10^4, 10^7] Pa$) passive inflation problem. The LM, penalty and weakly penalised methods were also compared using the cardiac cycle model, showing consistent results to those illustrated in the passive inflation test. Representative results of this comparison are illustrated in Fig. 3.2b, while Fig. 3.6a illustrates convergence of the weakly penalised pressure-volume loops with mesh refinement.
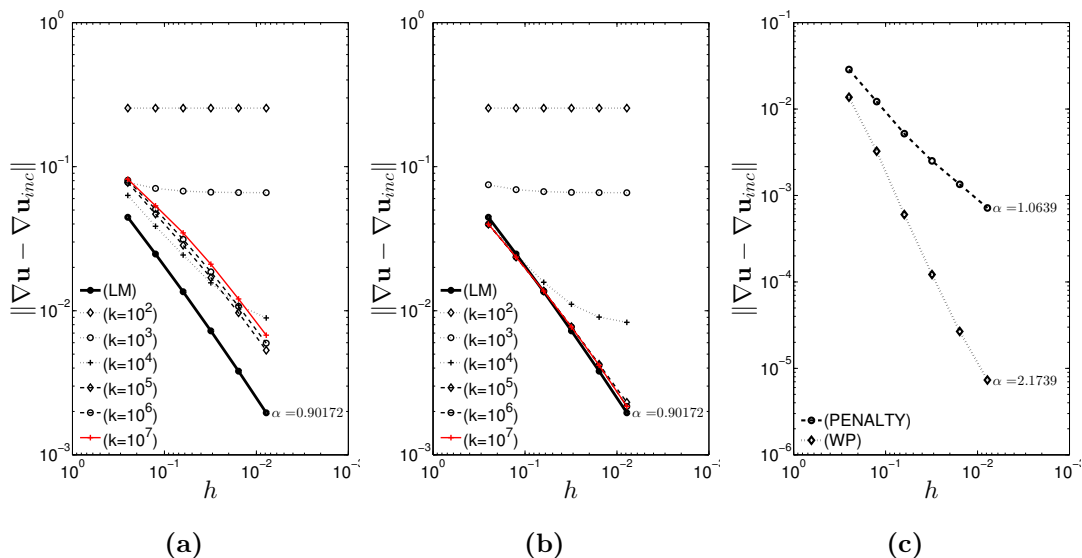
Figure 3.7 Error between the **(a)** penalty and **(b)** weakly penalised approaches ($\boldsymbol{u}$) and the incompressible fine grid solution ($\boldsymbol{u}_{inc}$) for six different values of the bulk modulus k. Convergence of the LM method is shown in black for comparison (the slope of these curves is denoted by a), whereas the red line represents the highest value of k. **(c)** Illustration of the error for the penalty / weakly penalised ($k = 10^7 Pa$) approaches, measured over a subset of the domain, excluding the region around the four corners of the square.
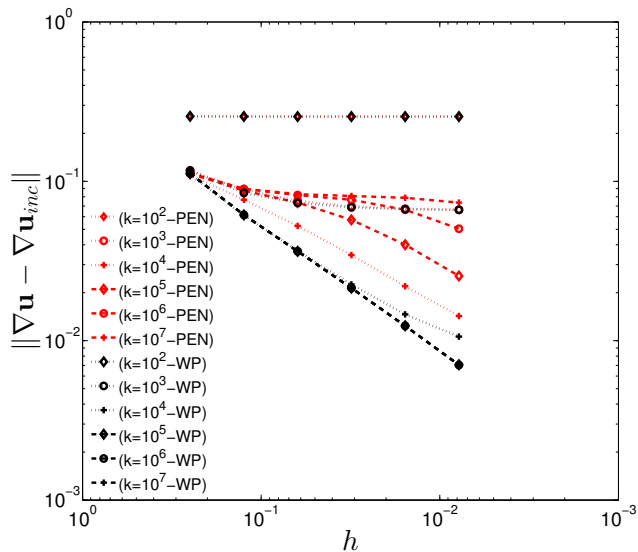
Figure 3.8 Comparison of the convergence behaviour of the penalty and weakly penalised formulations when a lower order interpolation scheme is used: The errors between the penalty (in red) and weakly penalised (in black) forms ($\boldsymbol{u}$) and the fine grid solution to the incompressible ($\boldsymbol{u}_{inc}$) elongation problem using linear interpolations are illustrated.
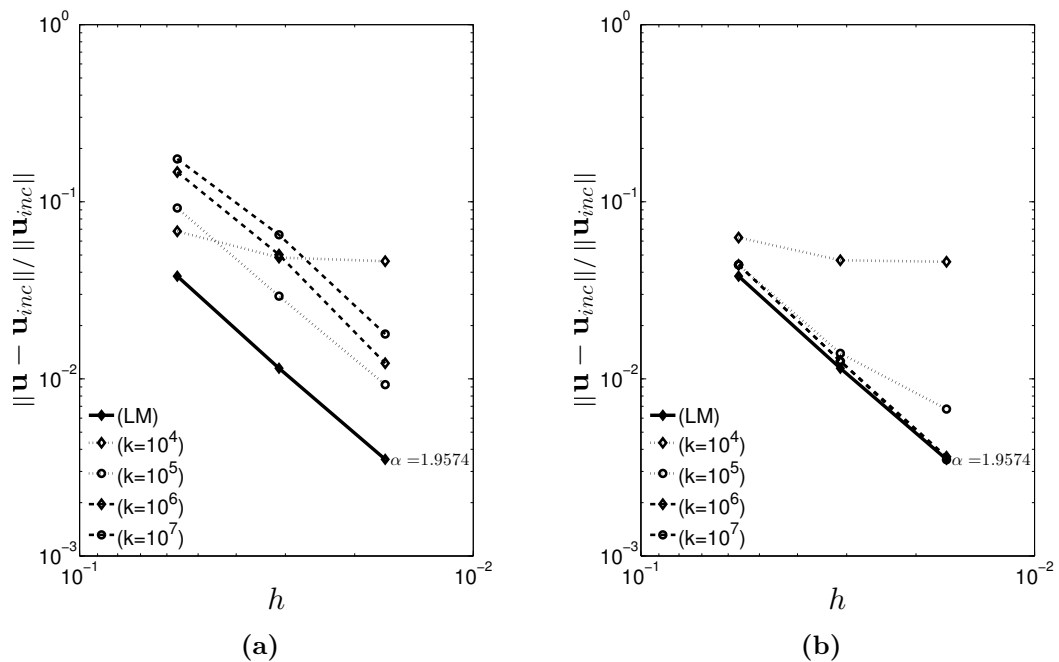
Figure 3.9 Comparison of the L^2-norm displacement error of (**a**) penalty and (**b**) weakly penalised methods as approximation to the incompressible passive inflation problem (LM solution) for different k values. The black line presents the LM convergence rate, while α denotes the slope of the LM curves.

Finally, convergence rates were also used to assess the behaviour of the various formulations in the solution of compressible problems. Both the elongation (Fig. 3.10) and cardiac problems (Fig. 3.11) were considered, and the error was computed with

81

respect to the PL solution on the finest discretisation, for the specific value of the bulk modulus.
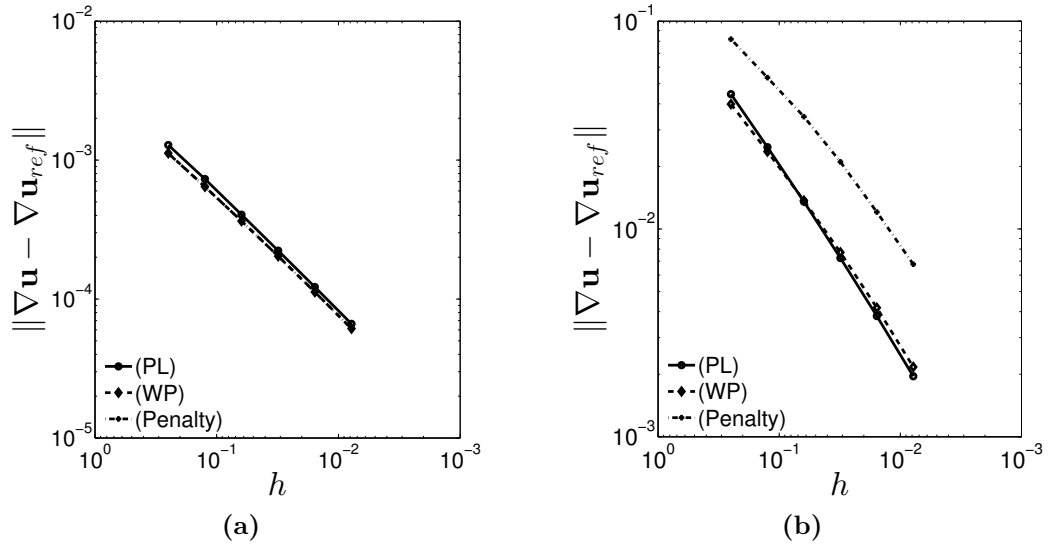
Figure 3.10 Comparison of the convergence behaviour of the 3 methods on the two-dimensional compressible problem: The error between the penalty, weakly penalised and PL approaches ($\boldsymbol{u}$) and the compressible fine grid solutions ($\boldsymbol{u}_{ref}$) for **(a)** $k = 100Pa$ and **(b)** $k = 10^7 Pa$.
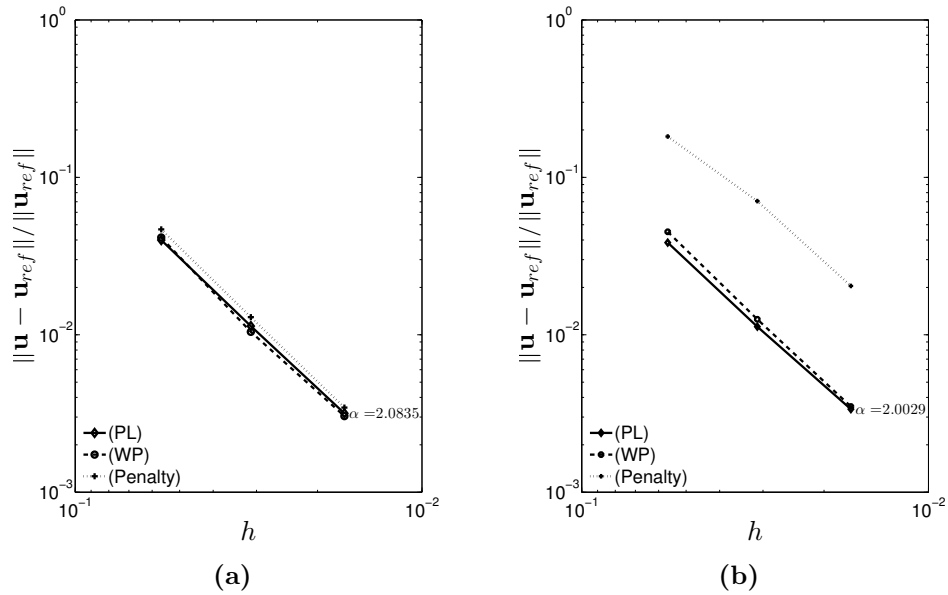
Figure 3.11 Comparison of the L^2-norm displacement error of the different methods when used as an approximation to compressible passive inflation problems (PL solution) for **(a)** $k = 10^4 Pa$ and **(b)** $k = 10^7 Pa$. The black line presents the PL convergence rate, while α denotes the slope of the PL curves.

3.2.4 Numerical results for the efficiency of the different formulations

The PL, penalty and weakly penalised formulations were also compared in terms of their nonlinear convergence behaviour. Representative values for the number of iterations of the Newton-Rapson scheme, the number of Jacobian matrix computations (and their respective times) along with the linear solution time and total time are presented in table 3.1. The change in the efficiency of the different methods when the SNR scheme is applied is presented as well. Finally, the effect of the modifications introduced in the SNR scheme for the penalty method can be deduced as the table compares the application of the SNR scheme to the penalty method with and without the introduced modifications. Note that although not presented here, the nonlinear behaviour of the weakly penalised system when the SNR is applied without the introduced modifications is similar to that of the penalty method without the introduced modifications (PEN). Similar observations can be made using Fig. 3.12, which compares the number of Jacobian and residual computations when the classic Newton-Raphson and the SNR scheme are used for the different methods.

| | Newton-Raphson | | | | | |
	J c. time [s]*	J c/s*	R c. time [s]*	R c/s*	Solve time [s]*	Total time [s]*
PEN	181.55	4	1.93	4	47.51	231.13
WP	242.05	3.81	2.42	3.81	41.46	286.06
PL	246.77	3.88	2.49	3.88	45.36	294.75

| | Shamanskii-Newton-Raphson | | | | | |
	J c. time [s]*	J c/s*	R c. time [s]*	R c/s*	Solve time [s]*	Total time [s]*
PEN	25.80	0.46	11.67	10.82	7.2	44.81
PEN-MOD	10.14	0.113	14.07	9.51	1.76	26.08
WP-MOD	3.95	0.047	13.19	9.79	1.18	18.47
PL	4.66	0.053	13.43	9.88	1.37	19.61

* Times / Iterations given as the average per load step

Table 3.1 Comparison of average number of Newton-Raphson iterations and Jacobian computations (c/s) per load step, as well as their respective average times between Newton-Raphson and Shamanskii-Newton-Raphson schemes. The efficiency of the SNR scheme with (PEN-MOD) and without (PEN) the introduced modifications on the penalty method is presented as well. The computational time (c.time), total solve time per load step and the total time per load step are also illustrated. This comparison was performed on the passive inflation test (section 3.2.1.2) on mesh$_2$ ($k = 10^7$ for the penalty, weakly penalised and PL methods), the simulations were run on a single processor and a direct solver was used.
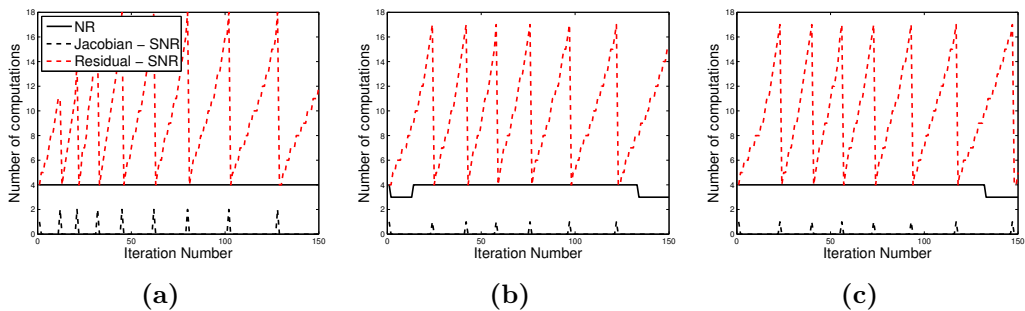
Figure 3.12 Comparison of the number of Jacobian and residual computations for **(a)** the penalty, **(b)** the weakly penalised and **(c)** the PL formulation. The methods are compared over the passive inflation simulation (section 3.2.1.2) on mesh$_2$ ($k = 10^7$ for the penalty, weakly penalised and PL methods). The solid black line represents the number of Jacobian and residual computations for the classic Newton-Raphson scheme and the dotted lines represent the number of Jacobian (black line) and residual (red line) computations when the SNR scheme is applied.

3.3 Discussion

3.3.1 Comparison of the methods for modelling incompressibility

The LM, penalty and weakly penalised formulations were initially compared qualitatively over the incompressible formulation of the elongation problem (section 3.2.1.1), on mesh$_4$. The method used for the solution of the incompressible problem and the values of the penalty parameter chosen have an important impact on the ability of approximating the actual incompressible solution. Fig. 3.3 and 3.4 illustrate the solution of the penalty and weakly penalised formulations, respectively, for increasing values of the penalty parameters, along with the solution of the classic LM method. Based on both figures, the solutions of the weakly penalised formulation appear to converge towards the LM solution as k increases, which is not as clear based on the qualitative behaviour of the penalty method. Furthermore, comparing the values of the horizontal component of strain, for higher values of k, the weak penalisation appears to be closer to the LM solution, compared to the penalty method.

Examining the ability of all approaches to model imcompressibility (section 3.1.1.1), the most straightforward is the incompressible LM method which enforces weak incompressibility. However, we could consider the compressible penalty and weakly penalised approaches as approximations to the incompressible system. With this in mind, from Eq. 3.9, the error for any method should converge to zero with a rate proportional to $1/k$. Based on Fig. 3.7a and Fig. 3.9a the error of the penalty method relative to the incompressible solution was generally higher and increased with increasing k, as a result

of the well-known locking phenomena associated with displacement-only formulations. In the cardiac model, with $k = 10^7$, the error was actually uniformly worse than all other values of the parameter at almost all levels of refinement, making the selection of an appropriate k to model incompressible behaviour non-trivial.

As discussed in section 3.1.2, it was initially hypothesised that issues affiliated with the penalty method could be circumvented by projecting the constraint using an orthogonal projection operator, $\pi_{W_{loc}}$, resulting in the displacement-based formulation suggested by Bercovier[18] and others[38,36]. Indeed, it can be deduced based on Fig. 3.7b and Fig. 3.9b, that as k increased, the error in the approximation decreased proportionally to $1/k$ and became indistinguishable from the convergence of the LM method. The existence of a k-dependent error bound for the weakly penalised approach enables regulation of the error by an appropriate choice of k. Moreover, due to its dependence on the discretisation, the error showed a plateauing behaviour for values of k which incurred an error smaller than the error associated with the discretisation.

The locking behaviour of the penalty method was observed to worsen with lower interpolation order, as shown in Fig. 3.8, where linear elements were used. In this case, as the bulk modulus increased, the rate of convergence observed in the penalty method deteriorated to nearly zero. In contrast, the weakly penalised approach exhibited consistent linear convergence for $k > 10^5$.

An interesting observation stems from the degree of compressibility actually introduced as the penalty parameter varies. Based on Fig. 3.5, near incompressibility can be achieved even with moderate values of the penalty parameter, for the 2D elongation problem. Specifically, a ratio $k/\mu = 10$ is sufficient to introduce less than 5% compressibility. It could therefore be possible to select a moderate value for the penalty parameter in the penalty method, which would produce only a small degree of compressibility while at the same time avoid locking issues associated with larger values. Nevertheless, even though a penalty value offering a balance between the degree of compressibility and numerical accuracy could be possible, its existence and actual value would be dependent on the specific application.

Additionally, for both elongation / cardiac problems, the rates of convergence from all methods were not optimal as would be expected based on the error estimates[202]. Based on the fact that sub-optimal convergence rates appeared in the application of all methods, it can be deduced that this was not a method-dependent issue. It is hypothesised, however, that sub-optimal rates are due to singularities in the two problems which limit convergence. In the elongation problem, singularities occurred at all corners of the domain. Measuring convergence in a horizontal patch excluding corners as shown in Fig. 3.7c, for $k = 10^7$ the rate of convergence in the weakly penalised method was restored to the expected order $\mathcal{O}(h^2)$ (for the $\boldsymbol{H}^1$ semi-norm). In contrast, due to locking, no improvement to the rate of convergence was observed in the penalty approach.

In the cardiac model, sub-optimal convergence likely stemmed from the strict boundary condition on the base plane of the model and the singularity in the fibre field near the apex. Even though the specific boundary condition and fibre field incur singularities, they were chosen because of their frequent use in cardiac models.

3.3.2 Comparison of the methods for modelling compressibility

The application of the PL, penalty and weakly penalised formulations in the solution of compressible problems lead to conclusions similar to the incompressible behaviour. In compressible problems, the three formulations should provide consistent results for low and moderate values of k, as observed in Fig. 3.10a and 3.11a. While for $k = 10^4$, flattening of the convergence behaviour to the incompressible solution was observed for both penalty and weakly penalised methods (and, though not shown, for PL), in the compressible problem, uniform and consistent convergence to the compressible solution was observed.

Increasing k, however, caused deterioration in the convergence of the penalty method as shown in Fig. 3.10b and 3.11b. Here, the error increased significantly (two and almost one order of magnitude increase for the two-dimensional and cardiac problems, respectively), while convergence remained consistent between the PL and weakly penalised methods.

3.3.3 Comparison over the cardiac cycle

In Fig. 3.6b, all methods are compared over a cardiac cycle, by plotting the difference between both penalty and weakly penalised approaches (with $k = 10^7$) and the incompressible LM method on the same discretisation. In this case, the LM and penalty methods differed by up to 20% in the $\boldsymbol{H}^1$ semi-norm (which is indicative of errors we could expect in strain), while the peak difference between weakly penalised and LM approaches remained below 8%. These differences occurred primarily during the systolic phase, with decreased error through the rest of the cardiac cycle.

The influence of these effects is heavily dependent on the k chosen for the model. Considering convergence (*i.e.* mesh$_3$ with fine grid mesh$_4$) of the compressible model over the cardiac cycle (even though not shown here), the maximum error for $k = 10^7$ was $\sim 1\%$ for the weakly penalised and LM methods, and $\sim 10\%$ for the penalty method. However, for $k = 10^5$, the error for weakly penalised and LM methods remained around $\sim 1\%$, while the error observed in the penalty method dropped to $\sim 3\%$. As the bulk modulus represents the tissue's resistance to compression, its value is tied to the other cardiac constitutive parameters. Thus, the influence of locking in the penalty method depends on the level of compressibility which is acceptable in the model. In general,

based on the results presented, as $k/C > 10^3$, where C is the bulk scaling on the strain energy in section 3.2.1.2, locking becomes increasingly more predominant.

3.3.4 Comparison of linearised systems and efficiency of formulations

The solution procedure for the weakly penalised formulation was outlined in section 3.1.4.1, illustrating that the linearised system involves only the body displacement, $\boldsymbol{u}^h$. Considering the Jacobian for the LM ($\boldsymbol{J}_\lambda$) and penalty methods ($\boldsymbol{J}_k$), shown in equation 3.47, the LM formulation has an indefinite saddle point structure, while the penalty method adds to the principle $\boldsymbol{A}-$block,

$$
\boldsymbol{J}_\lambda = \begin{pmatrix} \boldsymbol{A} & \boldsymbol{B} \\ \hat{\boldsymbol{B}} & \boldsymbol{0} \end{pmatrix}, \quad \boldsymbol{J}_k = \boldsymbol{A} + \boldsymbol{P}. \tag{3.47}
$$

Similar to $\boldsymbol{J}_k$, the Jacobian of the weakly penalised formulation shown in Eq. 3.34, also augments the $\boldsymbol{A}-$block with a matrix $\boldsymbol{C}$ which, by construction, is symmetric positive semi-definite. Furthermore, the Jacobian of the PL method augments the zero block matrix with a k-dependent term, avoiding the indefinite nature of the LM Jacobian (the Jacobians of the different formulations are outlined in Appendix A).

The structure of these systems has a significant impact on their solution. While the actual system sizes (shown in Fig. 3.1b and 3.2b) are not substantially different, the indefinite structure of $\boldsymbol{J}_\lambda$ makes it more challenging to solve, requiring direct methods, "sophisticated" preconditioners or splitting schemes[17]. In contrast, the penalty, PL and weakly penalised strategies are more straightforward in structure, making them more amenable to classic preconditioning strategies. However, as the bulk modulus k increases, care must be taken to deal with the conditioning of the linear system.

Based on table 3.1, in addition to having contrasting linear structure, the methods also exhibited differing convergence behaviour in the Newton-Raphson scheme[†]. In general, the non-linear convergence of the weakly penalised formulation averaged ~ 3.81 iterations per load step when the classic Newton-Raphson scheme was employed (table 3.1). The modifications introduced in the weakly penalised form (section 3.1.4.1), enhanced the numerical ability of the scheme, which exhibited marginally better non-linear convergence behaviour than that of the PL method.

Furthermore, the PL and weakly penalised forms were able to exploit the Jacobian re-use strategy (Shamanskii-Newton-Raphson scheme), leading to approximately 93%

[†]We note that in the examples presented in this work, the cost of computing the Jacobian is larger than the Newton-Raphson solution process, due to the quadratic interpolation used for the displacement and the higher order quadrature rule applied

decrease in the computational time of the Jacobian matrix $\boldsymbol{J}$ (build and solution) and a 94% reduction in the total time per loading step (for the weakly penalised form). By modifying the weakly penalised scheme to avoid the high sensitivity to the bulk modulus associated with displacement formulations, the weakly penalised formulation allows efficient re-use of the Jacobian matrix, whereas the performance of the penalty formulation (PEN) is not significantly improved when the SNR scheme is applied. When these modifications were also extended to the penalty method (PEN-MOD), they resulted in significant improvements in both the computational time of the Jacobian matrix $\boldsymbol{J}$ (87% decrease) and the total time per loading step (89% decrease), compared to the classic Newton-Raphson scheme.

Similar conclusions can be deduced from Fig. 3.12, which compares the number of Jacobian and residual computations over the iteration number, with and without the SNR scheme. Based on these results, the SNR scheme significantly reduced the number of Jacobian computations for all methods. Furthermore, the introduced modifications ensured monotonic residual convergence after the first step for all methods, avoiding the non-monotonic convergence observed in penalised formulations (section 3.1.4.2). It is important to note that these observations were consistent in all formulations, indicating that the introduced modifications in the SNR scheme for both the weakly penalised and penalty formulations, were able to significantly improve the performance of the methods.

3.3.5   Weakly penalised formulation

Section 3.1.1.1 illustrated how the energy functional for a hyperelastic solid can be written consistently for both penalty and LM methods, by choosing both an appropriate space of solutions, $\boldsymbol{U}$, and orthogonal projection, π_W. Furthermore, in the finite element context, the LM method required discretisation of both $\boldsymbol{U}$ and π_W as both the displacement and pressure variables need to be computed. In the penalty formulation, however, the orthogonal projection is not necessarily discretised, as the only unknown variable is the displacement (section 3.1.2). As previously discussed, this selection of discretisation of the orthogonal projection can restrict the approximation space $\boldsymbol{U}^h$ for high values of k.

To circumvent this issue while retaining the single field approach, a displacement-only formulation introduced by Bercovier[18] and others[38,36] was applied in section 3.1.3, which uses a localised discrete orthogonal projection operator, $\pi_{W_{loc}}$. Similar to augmented Lagrangian and reduced integration techniques[25], the aim of the discrete projection is to weaken the compressible / incompressible constraint, thereby enhancing the approximation space in the limit as k gets large. Furthermore, by appropriate restructuring of the weakly penalised system, the poor nonlinear convergence for high

bulk modulus associated with displacement-only formulations was avoided. As shown in Figs. 3.7, and 3.9, the weakly penalised formulation restores convergence behaviour while maintaining the simplicity of a single field approach. Finally, viewing the various methods under the same generalised framework enabled the extension of the SNR modifications of the weakly penalised form to the penalty approach, significantly improving the computational performance of the scheme.

A convenient feature of the weakly penalised approach is that it enables more straightforward analysis by tapping into known finite element spaces. Although for uniqueness inf-sup stability is not necessary, this condition ensures optimal convergence in the null space of π_W for linear problems, for appropriately chosen spaces[86]. In the examples presented here, the projection was chosen to be one polynomial order less and piecewise discontinuous. Although this pairing is not inf-sup stable, for the quadrilateral and hexahedral elements considered, this restored convergence. Another convenient choice are Nicolaides-Boland[20] elements, which give consistent results to those presented here.

3.4 Summary

This chapter compared the use of different methods for approximating incompressible and compressible tissue mechanics in the heart. Noting that the choice of model is governed by both model validity and numerical considerations, the use of Lagrange (LM and PL) and penalty methods as models of both incompressible and compressible behaviour was assessed. Motivated by the classic locking phenomena observed for linear mechanics[25,242], an enhancement of the Bercovier[18] formulation was introduced which enables the single field approach while providing similar convergence behaviour to the LM method. Furthermore, the comparison of different approaches for incompressibility / compressibility has not been performed on cardiac mechanics before, and could be useful in indicating the appropriate approach for the specific application.

The convergence behaviour of the methods discussed highlighted the fact that the LM and penalty methods, although often used equivalently in cardiac mechanics, may present significant variations in results. This is due to the deterioration of the convergence behaviour of the penalty method for large values of the bulk modulus. Indeed, in both the 2D elongation problem and the cardiac models, the penalty method generally exhibited a larger error compared to the other two methods, for all values of the bulk modulus. In contrast, the single field weakly penalised approach provided both improved rates of convergence and avoided issues associated with locking phenomena over these test problems. Further modifications introduced in this work enhanced the computational performance of the numerical scheme, by allowing efficient application of the SNR re-use strategy, which significantly reduced the computational time.

Taking all into account, the choice of an appropriate numerical scheme should be based on the specific application under consideration. As all approaches behave similarly for compressible, low bulk modulus problems, the penalty formulation may be an attractive option for such applications, due to its straightforward structure and implementation. For incompressible and nearly-incompressible applications, however, the penalty method should be avoided due to its deteriorated convergence behaviour. Instead, the LM, PL and weakly penalised formulations are all accurate and efficient options which can be reliably employed for incompressible and nearly-incompressible problems. Finally, the simple structure of the weakly penalised approach – compared to the indefinite structure of the LM Jacobian – makes it an appealing alternative for large systems' solutions.

4 Analysis of passive cardiac constitutive laws using synthetic 3D tagged MRI

An important step in the creation of personalised models of cardiac mechanics is the choice of an appropriate passive constitutive law. Although this choice is determined by the scope of the specific application, it is often based on balancing the need for an accurate description of the passive myocardial behaviour with the requirement for uniquely identifiable parameters, tunable from available clinical data. Parameter identifiability is a crucial aspect in patient-specific applications, as passive parameters are important determinants of cardiac function – with the potential of providing clinical biomarkers – and as such, need to be uniquely and accurately estimated. Specifically, the tissue remodelling observed in DCM patients[128,16,190], is expected to be reflected in the passive parameters as well, therefore reliable parameter estimation is of particular importance in this work.

This chapter aims to assist the choice of an appropriate constitutive law when the main data source is 3D tagged MRI – part of the data available through the DCM study. Constitutive laws commonly employed in cardiac mechanics are considered, keeping in mind the basic requirements for capturing passive myocardial behaviour (*model fidelity*) as well as providing unique and accurate parameter estimates (*parameter identifiability*). The analysis is focused on 3D tagged MRI, which offer a framework for estimation of model-based parameters, using tissue-displacement observations. In order to gain insights into the parameter estimation process, synthetic tagged MRI are created directly from simulation results, resembling actual 3D tags. Through *in silico* simulations and parameter sweeps, the behaviour of a minimisation criterion ($\mathcal{J}$) over the parameter space is examined for the constitutive laws considered. The various models are further compared with respect to their ability in representing physiological cardiac deformation and end-diastolic pressure-volume relation (EDPVR), in order to identify a model balancing between practical identifiability and adequate representation of cardiac behaviour.

The following sections describe the approach used for investigating practical identifiabil-

ity and model fidelity for the laws considered. The process for characterising practical identifiability and model fidelity for each one of the considered models, is reviewed in section 4.1. The proposed workflow is employed for *in silico* tests of diastolic filling using an idealised left ventricle (section 4.2).

Large part of the work presented in this chapter, was included in a publication by Hadjicharalambous *et al.*[85].

4.1 Methodology for parameter identifiability study

In this section, the process followed in this work for assessing the practical identifiability of various laws is presented. As described in Fig. 4.1, the process focuses on the creation of synthetic tags, the motion extraction algorithm used and the parameter sweeps performed to retrieve the parameter values over minimisation (section 4.1.1). The cardiac model of LV diastolic filling used is then described, as well as the various cardiac constitutive laws considered (section 4.1.2). Finally, the general theoretical framework for the inverse problem of parameter estimation using 3D tags is presented (section 4.1.3), focusing on the concepts of structural and practical identifiability, and the factors that influence them (data, constitutive laws, objective function).
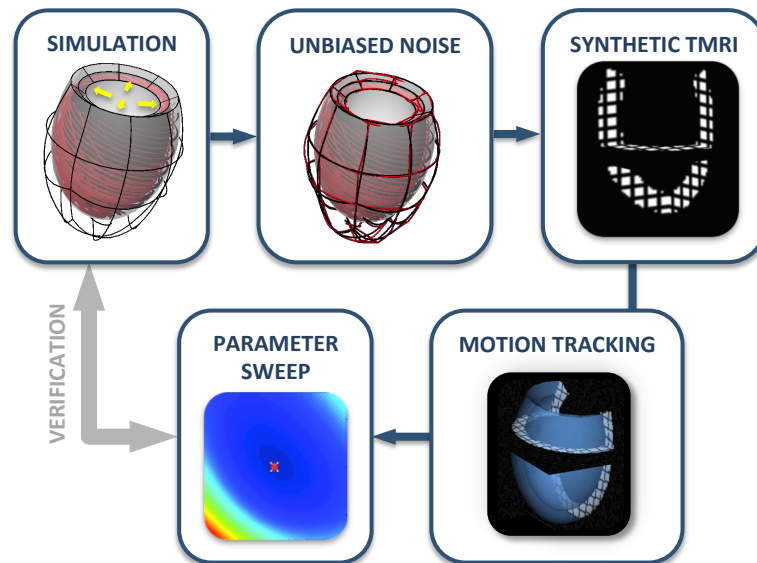
Figure 4.1 Workflow followed for the *in silico* study of practical identifiability using synthetic 3D tags.

4.1.1 *In silico* tagging and assessment protocol

A primary goal of this study is to assess the potential of using 3D tagged MRI in parameter estimation applications. Even though 3D tagged MRI offer a rich dataset for parametrisation, the process may be compromised by low resolution or noisy data
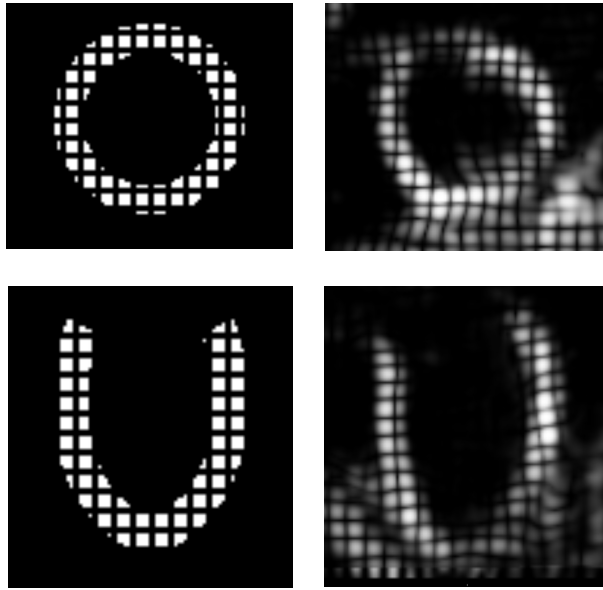
Figure 4.2 Comparison between synthetic (left) and real (right) 3D tags at beginning of diastole, short-axis view on top figures, long-axis view on bottom figures.

and any error introduced during the motion tracking procedure. In order to investigate this issue, synthetic 3D tagged images were generated directly from simulation results. Within this controlled environment, the actual parameters of the heart model are known, allowing for an assessment of the error between actual and estimated parameters. Furthermore, as the synthetic tags approximate real 3D tagged images (Fig. 4.2), within this framework we can quantify the error associated with various aspects of 3D tags such as resolution, noise in the data, and error introduced by the tracking algorithm.

Initially, a simulation of LV diastolic filling was run for each constitutive law, choosing parameters which produced a physiological end-diastolic volume. Synthetic 3D tags were then created from the resulting deformation and the myocardial motion was extracted and propagated on a mesh. These deformed meshes were then treated as data and were used directly for comparisons with simulation results. By performing parameter sweeps, computing and minimising an objective function or minimisation criterion $\mathcal{J}$ over a bounded parameter space, parameter estimates were obtained and the behaviour of $\mathcal{J}$ was quantified.

4.1.1.1 LV diastolic filling

Several constitutive laws (section 4.1.2.2) were employed to model the passive behaviour of the tissue (step "SIMULATION" in Fig. 4.1), and the simulated diastolic deformation in each case was compared with diastolic data to provide parameter estimates. The LV was modeled as a thick-walled truncated ellipsoid of typical cardiac dimensions. The domain was discretised using a mesh composed of 56 hexahedral elements with two elements transmurally, and a quadratic-linear interpolation scheme was employed for the displacement and pressure variables, respectively. A generic heterogeneous fibre field was applied, with the fibre angle varying linearly between $60°$ and $-60°$ from endocardium to epicardium. A zero traction condition was enforced on the epicardial surface, while the base plane was fully fixed. Finally, the endocardial surface of the LV model was passively inflated to a typical end-diastolic pressure of 1.5kPa, using 50 uniform loading steps.

4.1.1.2 *In silico* assessment protocol

As the focus of this chapter is passive cardiac parameters, synthetic tags were generated (step "SYNTHETIC TMRI" in Fig. 4.1) from a passive inflation simulation of a model left ventricle (section 4.1.1.1) using the various constitutive laws which will be described in section 4.1.2.2. Using rasterisation, a binary mask of the mesh was created, and tag planes were generated within the image[222,61], resulting in a final 3D tagged image with a resolution of $1 \times 1 \times 1$ mm. Simulated deformations were then mapped and interpolated within the image, producing a 3D-tagged representation of the passive inflation simulation. For the remaining steps of the parameter estimation study, these synthetic tags served as data and were treated as real 3D tags.

In order to assess the effect of data noise, Gaussian noise was added to the simulation results, prior to the *in silico* tagging (step "UNBIASED NOISE" in Fig. 4.1). The mean value of the added Gaussian noise was zero and the variance was a percentage (usually $5 - 20\%$) of the maximum deformation of the diastolic simulation.

4.1.1.3 Motion extraction of synthetic tagged MRI

Myocardial motion was extracted from *in silico* tagged images (step "MOTION TRACKING" in Fig. 4.1) using the Image Registration Toolkit*. This software uses a non-rigid registration technique proposed by Rueckert *et al.*[209,220] and subsequently extended to tracking of cardiac motion[35,225]. The registration algorithm, which is based on free-form deformations and optimisation of the similarity between two subsequent

---

*http://www.doc.ic.ac.uk/∼dr/software

images, allows tracking any point within the myocardium throughout the cardiac cycle, and provides the deformation field with respect to the beginning of systole. The obtained deformation fields were then applied on an initial mesh and propagated through time, resulting in a set of deformed meshes which were used as the observations within the parameter estimation process.

4.1.1.4 Mechanical simulations and $\mathcal{J}$ characterisation

The parameter estimates for the constitutive laws considered were obtained by parameter sweeps (step "PARAMETER SWEEP" in Fig. 4.1). Specifically, for each law, passive inflation simulations (section 4.1.1.1) were performed for parameter combinations within a neighbourhood of the actual parameters. The parameter estimates were then obtained as the set of values that minimised the objective function $\mathcal{J}$ over the parameter space. Within this process, 10 synthetic tagged frames were used as observations. The objective function employed – defined and discussed in section 4.1.3.2 – is discerning and thus able to provide a unique minimum, assuming that the constitutive law is practically identifiable. Note that, as the same constitutive law is used for both the generated data and simulations, the estimation process does not suffer from model fidelity issues, leading to safe conclusions about practical identifiability.

4.1.2 Cardiac mechanics

4.1.2.1 Finite elasticity

The passive diastolic filling of the LV considered in this work was simulated within the finite elasticity framework (section 2.4.1) due to the large deformation of the myocardium during the cardiac cycle[98].

We consider here a body defined over a reference domain Ω_0 (similarly to Fig. 2.1), which deforms under the action of a traction $\boldsymbol{t}$ (such as the endocardial pressure) on a subset Γ^N of the boundary Γ, with Ω denoting the current configuration. Given a set of parameters $\boldsymbol{\theta}$ related to the employed constitutive law, the mechanics problem can be written as: Find the deformation and hydrostatic pressure pair $x = (\boldsymbol{u}_\theta, p_\theta)$ in $\boldsymbol{W}_0 = \boldsymbol{H}_0^1(\Omega) \times L^2(\Omega)$ such that

$$\mathcal{F}(\boldsymbol{\theta}; x, y) = 0, \quad \forall y \in \boldsymbol{W}_0, \tag{4.1}$$

where

$$\mathcal{F}(\boldsymbol{\theta}; x, y) = \int_\Omega (\boldsymbol{\sigma}_d(\boldsymbol{\theta}; \boldsymbol{u}) + p\boldsymbol{I}) : \nabla \boldsymbol{v} \, dv - \int_{\Gamma^N} \boldsymbol{t} \cdot \boldsymbol{v} \, da + \int_{\Omega_0} q(J - 1) \, dV, \tag{4.2}$$

following the weak form derivation described in section 2.5, and $x = (\boldsymbol{u}, p)$ and $y = (\boldsymbol{v}, q)$ represent the state solutions and test functions, respectively. In this case, the myocardial wall is assumed to be an incompressible material. As the size of the mechanics problems under consideration was relatively small, use of the weakly penalised approach (section 3.1.3) would not have a significant computational benefit over the LM approach, so for simplicity incompressibility is enforced using the classic Lagrange multiplier method (Eq. 3.10).

In the finite elasticity framework considered here, $\boldsymbol{\sigma}_d$ denotes the deviatoric Cauchy stress tensor, which depends on the passive behaviour of the material and the constitutive law chosen to describe it (section 2.3.3). As the myocardium is most typically modeled as a hyperelastic material, the mechanical behaviour is expressed using a strain energy function, whose deviatoric component is denoted here by Ψ_d (as described in section 2.4). The deviatoric component of the Cauchy stress tensor can then be obtained through the expression

$$\boldsymbol{\sigma}_d = \frac{2}{J} \boldsymbol{F} \frac{\partial \Psi_d}{\partial \boldsymbol{C}} \boldsymbol{F}^T. \tag{4.3}$$

The cardiac mechanics problem (4.1) was then solved using the finite element method, which is based on discretisation of the continuous domain and function spaces, as described in section 2.6.

4.1.2.2 Constitutive laws

In order to decide on a suitable constitutive law providing an accurate representation of heart function as well as identifiable parameters, constitutive laws of progressively increased complexity were considered. Initially, the neo-Hookean law was employed, a well-known isotropic hyperelastic law, which has also been used in cardiac models[40]. The strain energy function and deviatoric stress for the neo-Hookean law are given by Eq. 2.29 and 2.30, respectively.

A more structurally accurate model was then examined, by augmenting the neo-Hookean law with a fibre-dependent component[102]. This enhanced version, which will be referred to as the *neo-fibre* law, is defined with respect to a fibre coordinate system (Eq. 2.37, 2.39), and the exponent a was chosen to be 1 or 2.

To better capture the exponential response of the myocardial tissue, the study was then extended to the structurally-based orthotropic law by Holzapfel and Ogden[98], described in Eq. 2.35 and 2.36. Restricting the study to constitutive laws with a small number of parameters to allow for better identifiability, a reduced version of the Holzapfel-Ogden law was used within the tests examined in the current chapter. Specifically, in the reduced Holzapfel-Ogden model, microstructural material parameters a_s and a_{fs} were set to zero and the exponents b and b_f were kept constant. A similar formulation has

previously been applied by Caruel *et al.*[28] in 0-D and 1-D models, demonstrating its ability to fit experimental data and thus reproduce physiological cardiac behaviour. The values of the exponents ($b = 5$ and $b_f = 5$) were chosen so that the model would be able to provide a physiological EDPVR (see section 4.2.3 and Fig. 4.13), as for several combinations of b and b_f a physiological EDPVR could not be produced for any values of the scaling parameters α and α_f. Nevertheless, it should be noted that, there is a range of values that would be appropriate for the choice of exponents, as an interdependence between the exponents and scaling constants can be assumed similar to that of the Guccione law[276]. The added value of this formulation over the Guccione law is that, due to its structure as a sum of individual exponential terms, it can be reduced into a form with uncoupled parameters. For this reduced version, the deviatoric strain energy function is given as:

$$\Psi_d = \frac{a}{2b}\left(\exp[b(I_C - 3)] - 1\right) + \frac{a_f}{2b_f}\left(\exp[b_f(I_{C_f} - 1)^2] - 1\right),$$
(4.4)

where $I_{C_f} = \boldsymbol{C} : \mathbf{f_0} \otimes \mathbf{f_0} = \mathbf{f_0} \cdot (\boldsymbol{C}\mathbf{f_0})$ denotes the invariant associated with the fibre direction. Similarly, the deviatoric Cauchy stress tensor can be derived as:

$$\boldsymbol{\sigma}_d = \left[a \exp[b(I_C - 3)]\boldsymbol{B} + 2a_f(I_{C_f} - 1)\exp[b_f(I_{C_f} - 1)^2]\mathbf{f} \otimes \mathbf{f}.\right.$$
(4.5)

Finally, the well-known transversely isotropic exponential law by Guccione *et al.* was examined, whose strain energy function and Cauchy stress tensor are given by Eq. 2.33 and 2.34, respectively.

4.1.3 Parameter estimation

In patient-specific mechanics simulations, models are often tuned or parametrised based on measurement data (observations). Supposing we have N parameters which govern the material behaviour, a common approach is to try and parametrise based on objective function minimisation. For example, we aim to find a set of N parameters $\boldsymbol{\theta}_{min}$ which satisfies, for an objective function $\mathcal{J}_\theta$,

$$\mathcal{J}_\theta(\boldsymbol{\theta}_{min}) < \min_{\boldsymbol{\theta} \in P\backslash\boldsymbol{\theta}_{min}} \mathcal{J}_\theta(\boldsymbol{\theta})$$
(4.6)

where $P \subseteq \mathbb{R}^N$ is a subset of vectors of real numbers which constitute the admissible parameters for the problem. The behaviour of the model, the observations (or data) over which the behaviour is considered, and the objective function itself, all play an important role in the behaviour of the minimisation problem and uniqueness of the minimiser. This is particularly important in clinical contexts, where the obtained set of parameters $\boldsymbol{\theta}_{min}$ is used to, in some sense, provide an indicator of the health / state of the myocardium. This section examines how these factors – the model, observations

and objective – can influence the identifiability of $\boldsymbol{\theta}_{min}$.

4.1.3.1 Model identifiability

To understand the behaviour of the minimisation problem, it is important to first understand the behaviour of the model and its parameters. Assuming N_s loading conditions are imposed on the model shown in Eq. 4.1, the total model problem can be written using the operator $\mathcal{F}_s$, adding each quasi-static equilibrium state defined in Eq. 4.1,

$$\mathcal{F}_s(\boldsymbol{\theta}; X, Y) = \sum_{k=1}^{N_s} \int_{\Omega_k} \boldsymbol{\sigma}_d(\boldsymbol{\theta}; \boldsymbol{u}_k) : \nabla \boldsymbol{v}_k \, dv + \int_{\Omega_k} p_k \nabla \cdot \boldsymbol{v}_k \, dv$$
$$+ \int_{\Omega_0} q_k(J(\boldsymbol{u}_k) - 1) \, dV - \int_{\Gamma_k^N} \mathbf{t}_k \cdot \boldsymbol{v}_k \, da. \qquad (4.7)$$

In this notation, $\{\mathbf{t}_1, \dots \mathbf{t}_{N_s}\}$ denotes the set of N_s loading conditions (boundary tractions) and

$$X = \{\boldsymbol{u}_1, \dots \boldsymbol{u}_{N_s}\} \times \{p_1, \dots p_{N_s}\}$$

$$Y = \{\boldsymbol{v}_1, \dots \boldsymbol{v}_{N_s}\} \times \{q_1, \dots q_{N_s}\}$$

denote the set of state solutions and test functions for each load state k. Solution spaces can be composed by setting $X, Y \in \boldsymbol{W}_0^s$, where the space $\boldsymbol{W}_0^s = \left[\boldsymbol{H}_0^1(\Omega)\right]^{N_s} \times \left[L^2(\Omega)\right]^{N_s}$ is an extension of space $\boldsymbol{W}_0$ accounting for the multiple loading states.

Using this notation, the quasi-static mechanics problem is (given a set of parameters $\boldsymbol{\theta}$): find an $X_\theta \in \boldsymbol{W}_0^s$ such that,

$$(P1) \quad \mathcal{F}_s(\boldsymbol{\theta}; X_\theta, Y) = 0, \quad \forall Y \in \boldsymbol{W}_0^s.$$

Here, X_θ constitutes the state solution composed of displacements and pressures at each of the N_s loading conditions. Additionally, all solutions to $(P1)$ can be collected to construct a space of solutions $\boldsymbol{\mathcal{V}} \subset \boldsymbol{W}_0^s$, i.e.

$$\boldsymbol{\mathcal{V}} = \{X \in \boldsymbol{W}_0^s | \, \exists \boldsymbol{\theta} \in P \text{ s.t. } (X, \boldsymbol{\theta}) \text{ satisfy } (P1)\}.$$

Based on the definition of $\boldsymbol{\mathcal{V}}$, it is possible to identify pairings between a subset of $P_{\boldsymbol{\mathcal{V}}} \subseteq P$ and the space of state solutions $\boldsymbol{\mathcal{V}}$. These pairings, in general, have no well-defined properties. Indeed, $\boldsymbol{\mathcal{V}}$ and $P_{\boldsymbol{\mathcal{V}}}$ may be empty. Here, it is assumed that $(P1)$ induces a surjective mapping on the parameter space P to the space of state solutions $\boldsymbol{\mathcal{V}}$ (see Fig. 4.3), i.e.

$$\varphi : P \mapsto \boldsymbol{\mathcal{V}}, \qquad \varphi(\boldsymbol{\theta}) = X_\theta, \quad (\boldsymbol{\theta}, X_\theta) \in P \times \boldsymbol{\mathcal{V}}$$
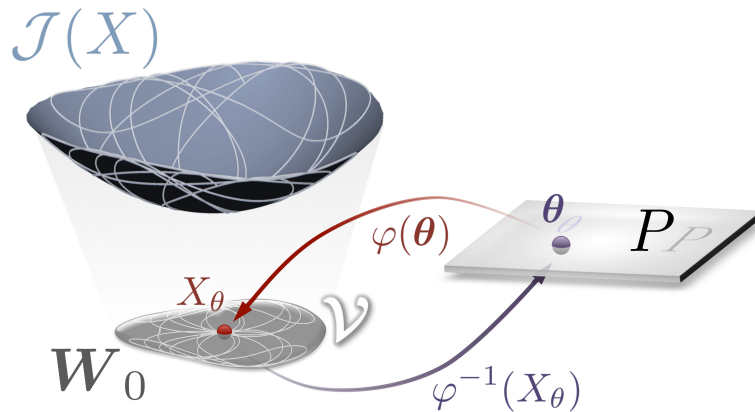
Figure 4.3 Schematic representation of the objective function $\mathcal{J}$ over the solution space W_0 for a given parameter set $\boldsymbol{\theta}$. The bijectivity of mapping φ between parameter space (P) and space of solutions $(\mathcal{V})$ ensures practical identifiability[85].

This assumption is equivalent to assuming that there exists a unique $X_\theta \in \mathcal{V}$ for every $\boldsymbol{\theta} \in P$. If $\varphi : P \mapsto \mathcal{V}$, it implies that for any $\boldsymbol{\theta} \in P$ there is an $X_\theta \in \mathcal{V}$. In other words, it implies there exists a $(X_\theta, \boldsymbol{\theta})$ satisfying (P1). Moreover, non-uniqueness of solutions would imply that for some $\boldsymbol{\theta} \in P$ the mapping φ would be written as:

$$\varphi(\boldsymbol{\theta}) = \{X_\theta^1, X_\theta^2, \ldots\} \subseteq \mathcal{V}.$$

This possibility is precluded, however, by the surjective assumption (implying uniqueness). Though it is not proven for general cardiac mechanics boundary value problems, it is often assumed in these applications that, given the admissible set of loading states and parameters, the solution X_θ to (P1) exists and is unique.

However, this condition is insufficient to guarantee unique parameter identifiability in Eq. 4.6. A stronger condition, which, as will be shown, can ensure unique parameter identifiability, occurs when the mapping φ is in fact bijective, *i.e.* there exists a φ^{-1} where

$$\varphi^{-1} : \mathcal{V} \mapsto P, \qquad \varphi^{-1}(X_\theta) = \boldsymbol{\theta}.$$

In the case of bijectivity of φ we can ensure that the transition from state to parameters is well defined.

Two important determinants of the properties of φ stem from the behaviour of the constitutive law itself and the set of loading states. The parameter dependence of the constitutive law – whether it is linear or nonlinear – can significantly influence a model's ability to uniquely identify parameters. It may also influence the range of loading states (and, as a result, deformations) which must occur to elucidate parameter dependencies. The final set of N_s loading states $\{\mathbf{t}_1, \ldots \mathbf{t}_{N_s}\}$ then defines this scope of deformations.

These considerations lead to a basic property required of a model, referred to as *struc-*

tural identifiability [203,204]. A model is said to be structurally identifiable if there exists an arbitrarily large set of N_T loading states $\{\mathbf{t}_1, \ldots \mathbf{t}_{N_T}\}$ such that the mapping $\varphi : P \mapsto \mathcal{V}$ is bijective. As can be shown (see Theorem 2 and Appendix D), this property is easily demonstrated for constitutive laws with linear parameter dependence, but becomes more complex when this dependence is nonlinear.

However, in most *in vivo* scenarios, model parametrisation is limited to a given set of loading states which cannot be arbitrarily selected, leading to the concept of *practical identifiability*. A model is said to be practically identifiable if, for a given set of N_s loading states $\{\mathbf{t}_1, \ldots \mathbf{t}_{N_s}\}$, the mapping $\varphi : P \mapsto \mathcal{V}$ is bijective. The key difference here is that limited observations comprise a set of loading states that ensure identifiability of all parameters, $\boldsymbol{\theta}$. For personalised cardiac models, these represent the *in vivo* states observed through the cardiac cycle, which must be sufficient to yield practical identifiability of all parameters of the law.

For general nonlinear cardiac models, practical identifiability of passive parameters is difficult to prove *a priori*, as it fundamentally depends on the structural identifiability of the model and the set of loading states and observations provided by the data. However, these considerations dictate the choice of model best-suited for a given set of material deformations.

In general, bijectivity can be ensured by a coercivity assumption, *i.e.*:

Theorem 1. *Suppose $\varphi : P \mapsto \mathcal{V}$ is a surjection (i.e. the solution to (P1) exists and is unique). Then, if for $\alpha > 0$, any $X \in \mathcal{V}$ and a pair of parameter sets $\boldsymbol{\theta}_1, \boldsymbol{\theta}_2 \in P$,*

$$\alpha \|\boldsymbol{\theta}_1 - \boldsymbol{\theta}_2\|_P \leq \sup_{Y \in \boldsymbol{W}_{0,Div}^u} \frac{|\mathcal{F}_s(\boldsymbol{\theta}_1; X, Y) - \mathcal{F}_s(\boldsymbol{\theta}_2; X, Y)|}{\|Y\|_{\boldsymbol{W}_0^u}}$$

then φ is bijective.

Proof. The proof follows from contradiction. Suppose that $\boldsymbol{\theta}_1, \boldsymbol{\theta}_2 \in P$ both happen to satisfy (P1) when paired with the solution states X. Then, by $(P1)$,

$$0 = \mathcal{F}_s(\boldsymbol{\theta}_1; X, Y) - \mathcal{F}_s(\boldsymbol{\theta}_2; X, Y), \quad \forall Y \in \boldsymbol{W}_0^u.$$

Dividing both sides by $\|Y\|_{\boldsymbol{W}_0^u}$ and taking the absolute value and supremum, the coercivity assumption ensures,

$$0 \geq \|\boldsymbol{\theta}_1 - \boldsymbol{\theta}_2\|_P$$

or that the parameters $\boldsymbol{\theta}_1$ and $\boldsymbol{\theta}_2$ are, in fact, the same. Hence, any solution X has a single pair $\boldsymbol{\theta} \in P$. $\square$

A much simpler case occurs when the model depends linearly on N_p parameters, in which case, the properties of φ are easier to decipher. In this case, the model may be

written as:

$$\boldsymbol{\sigma}_d(\boldsymbol{\theta}; \boldsymbol{u}) = \sum_{n=1}^{N_p} \theta_n \boldsymbol{\sigma}_n(\boldsymbol{u}), \tag{4.8}$$

where $\boldsymbol{\sigma}_n$ is the stress tensor (which may nonlinearly depend on $\boldsymbol{u}$) scaled by the nth parameter. In this case, the bijectivity of φ can be ensured by guaranteeing that it is possible to construct N-constraints by using different Y's in $(P1)$. Due to the linear parameter dependence, the constraints may then be written as a matrix system, where the invertibility of the matrix ensures φ is bijective (see Theorem 2).

Theorem 2. *Suppose $\varphi : P \mapsto \mathcal{V}$ is a surjection (i.e. the solution to (P1) exists and is unique). If there exists a set of functions $\{Y_1, \ldots Y_N\}$, $Y_i \in \boldsymbol{W}^u_{0,Div}$ with*

$$Y_i = \{\boldsymbol{v}^i_1, \ldots \boldsymbol{v}^i_{N_s}\}$$

such that the matrix $\boldsymbol{A}$ with entries

$$A_{ij} = \sum_{k=1}^{N_s} \int_{\Omega_k} \boldsymbol{\sigma}_j(\boldsymbol{u}_k) : \nabla \boldsymbol{v}^i_k \, dv$$

is invertible, then φ is bijective.

Proof. The proof may be shown, again, by contradiction. Suppose there are two sets of non-identical parameters $\boldsymbol{\theta}, \boldsymbol{\psi} \in P$ which result in the same state X. Then, by $(P1)$,

$$
\begin{aligned}
0 &= \mathcal{F}_s(\boldsymbol{\theta}; X, Y) - \mathcal{F}_s(\boldsymbol{\psi}; X, Y) \\
&= \sum_{n=1}^{N_p} (\theta_n - \psi_n) \sum_{k=1}^{N_s} \int_{\Omega} \boldsymbol{\sigma}_n(\boldsymbol{u}_k) : \nabla_{\boldsymbol{x}} \boldsymbol{v}_k \, dv
\end{aligned} \tag{4.9}
$$

for any $Y \in \boldsymbol{W}^u_{0,Div} \times (\boldsymbol{W}^p \cap \boldsymbol{0})$. Hence, choosing $\{Y_1, \ldots Y_{N_p}\}$, Equation 4.9 may be re-written as

$$\boldsymbol{A}(\boldsymbol{\theta} - \boldsymbol{\psi}) = 0 \quad \Rightarrow \quad \boldsymbol{\theta} = \boldsymbol{\psi}$$

due to the invertibility of $\boldsymbol{A}$. $\qquad\square$

Theorem 2 depends on a sufficient number of deformation states such that $\boldsymbol{A}$ gains linearly independent rows. Then, *any* test functions in $\boldsymbol{W}^u_{0,Div}$ can further accentuate differences in material response, providing a flexible source from which to select constraints. Using this theorem, the structural identifiability for the neo-Hookean, neo-fibre and reduced Holzapfel-Ogden law which have a linear dependence on their parameters can be demonstrated (see appendix D).

4.1.3.2   Objective function-based minimisation

In data-based parameter estimation procedures, the choice of parameters is often guided by some objective function. Since the parameters are not observed in most cases, parameter estimation instead relies on comparing states with observations. In these cases, it is necessary that the objective function $\mathcal{J} : \boldsymbol{\mathcal{V}} \to \mathbb{R}$ obtains a unique minimum (a *discerning objective*).

Using $3D$ tagged data, where the states are usually displacements, the natural choice of objective function is to use the $\boldsymbol{L}^2$ norm over all states, *i.e.*

$$\mathcal{J}(X) = \frac{|||X - X_d|||}{|||X_d|||} \tag{4.10}$$

where $X_d = \{\boldsymbol{u}_1, \ldots \boldsymbol{u}_{N_s}\}$ are observations on the displacements in the myocardium, divided through by the overall scale of displacements, so that $\mathcal{J}$ gives a percentage error. In this case, $||| \cdot |||$ is a norm on $\boldsymbol{W}_0$ defined as,

$$|||X||| = ((X, X))^{1/2}, \quad ((X, Y)) = \sum_{k=1}^{N_s} (\boldsymbol{u}_k, \boldsymbol{v}_k)$$

where $(\cdot, \cdot)$ is the $\boldsymbol{L}^2-$inner product on the reference domain Ω_0. We then look to minimise the objective, finding $X_{min} \in \boldsymbol{\mathcal{V}}$ where

$$\mathcal{J}(X_{min}) < \min_{X \in \boldsymbol{\mathcal{V}} \backslash X_{min}} \mathcal{J}(X). \tag{4.11}$$

As $||| \cdot |||$ acts as a norm on displacements in $\boldsymbol{\mathcal{V}}$ (and a semi-norm on the entire space), if the observed displacements in the state X_d constitute a set of displacements $\widetilde{X} \in \boldsymbol{\mathcal{V}}$, then $\mathcal{J}$ is automatically a discerning objective, as the norm has a unique zero by definition (and is strictly non-negative).

This is, however, unlikely to occur in a real context due to two dominant factors: (1) data noise and resolution, and (2) model fidelity. The introduction of noise, or degradation in data due to image resolution, introduces offsets which make the likelihood of X_d being a member of $\boldsymbol{\mathcal{V}}$, minimal. In addition, the fidelity of the model can strongly influence whether or not the model can capture the behaviour observed in the data, making it possible that one or more than one minima exist.

Supposing that the model is a good representation of the tissue *in vivo*, then the observed deformation can be expressed as $X_d = \widetilde{X} + \varepsilon$. In this case, assuming that ε is, in fact, some random unbiased noise which satisfies

$$((X, \varepsilon)) \approx 0, \quad \forall X \in \boldsymbol{\mathcal{V}}, \tag{4.12}$$

then we observe that the noise does not bias our minima, but instead introduces a constant offset in $\mathcal{J}$, *i.e.*

$$\mathcal{J}(X) = \frac{|||X - X_d|||}{|||X_d|||} = \frac{\left(|||X - \widetilde{X}|||^2 + |||\varepsilon|||^2\right)^{1/2}}{|||X_d|||}. \tag{4.13}$$

The assumed relation in Eq. 4.12 is a reasonable assumption when the noise fluctuations occur over a small spatial scale compared to the change of the state solutions X near the minima.

The offset in Equation 4.13 does not influence the minimisation on $\mathcal{V}$ and, as a result, $\mathcal{J}$ remains a discerning objective. Obtaining a unique minimum in $\mathcal{V}$ is essential, as, even if a model is practically identifiable based on loading constraints, multiple minima for $\mathcal{J}$ guarantee multiple minima in parameter space. However, with a discerning objective, we then rely on the bijectivity (or practical identifiability) of φ, so that the objective formed through composition,

$$\mathcal{J}_\theta(\boldsymbol{\theta}) = \mathcal{J} \circ \varphi(\boldsymbol{\theta}), \tag{4.14}$$

also obtains a unique minimum

$$\mathcal{J}_\theta(\boldsymbol{\theta}_{min}) < \min_{\boldsymbol{\theta} \in P \backslash \boldsymbol{\theta}_{min}} \mathcal{J}_\theta(\boldsymbol{\theta}). \tag{4.15}$$

In practice, a discerning objective and a set of load states giving practical identifiability are sufficient conditions to ensure that the set of parameters $\boldsymbol{\theta}_{min}$ are uniquely identifiable.

4.1.3.3 Parameter coupling

Characterising the behaviour of the objective function $\mathcal{J}$ over the parameter space is critical for the performance of the parameter estimation process. The behaviour of $\mathcal{J}$ around the minimum value (a distinct localised minimum instead of a wide valley) indicates a discerning objective function, which would allow data assimilation methods to retrieve the parameter estimate. Furthermore, the landscape of $\mathcal{J}$ over the parameter space provides important information regarding the practical identifiability of the constitutive law, revealing the presence of a unique or multiple minima or possible inter-parameter coupling.

Coupling can also be deduced by the Hessian matrix of the objective function at the obtained minimum. Using the Taylor expansion of $\mathcal{J}$ around the obtained minimum $\boldsymbol{\theta}_{min}$,

$$\mathcal{J}(\boldsymbol{\theta}_{min} + \boldsymbol{\epsilon}) = \mathcal{J}(\boldsymbol{\theta}_{min}) + \nabla_{\boldsymbol{\theta}}\mathcal{J}(\boldsymbol{\theta}_{min})^T\boldsymbol{\epsilon} + \frac{1}{2}\boldsymbol{\epsilon}^T\nabla_{\boldsymbol{\theta}}\big(\nabla_{\boldsymbol{\theta}}\mathcal{J}(\boldsymbol{\theta}_{min})\big)\boldsymbol{\epsilon} + \mathcal{O}(||\boldsymbol{\epsilon}||^3).$$

Due to the gradient being zero at the minimum $\boldsymbol{\theta}_{min}$,

$$\mathcal{J}(\boldsymbol{\theta}_{min} + \boldsymbol{\epsilon}) = \mathcal{J}(\boldsymbol{\theta}_{min}) + \frac{1}{2}\boldsymbol{\epsilon}^T \boldsymbol{H}\boldsymbol{\epsilon} + \mathcal{O}(||\boldsymbol{\epsilon}||^3), \tag{4.16}$$

where $\boldsymbol{H}$ denotes the Hessian matrix. As can be deduced by this expression, the Hessian matrix can provide important information as it enables mapping between local growth in $\mathcal{J}$ to local perturbations in the parameters. Further, to allow comparison between laws with varying parameters' scale, a scaled Hessian $\tilde{\boldsymbol{H}}$ was used, defined as:

$$\tilde{H}_{ij} = H_{ij}\theta_i\theta_j, \tag{4.17}$$

where θ_i and θ_j correspond to the $i-th$ and $j-th$ components of $\boldsymbol{\theta}_{min}$. By then using $\boldsymbol{\epsilon} = \tilde{\boldsymbol{\epsilon}} \circ \boldsymbol{\theta_{min}}$, Eq. 4.16 can be expressed as

$$\mathcal{J}(\boldsymbol{\theta}_{min} + \boldsymbol{\epsilon}) = \mathcal{J}(\boldsymbol{\theta}_{min}) + \frac{1}{2}\tilde{\boldsymbol{\epsilon}}^T \tilde{\boldsymbol{H}}\tilde{\boldsymbol{\epsilon}} + \mathcal{O}(||\boldsymbol{\epsilon}||^3),$$

which is now dealing with parameter percentages, enabling comparison between the different laws. The scaled Hessian $\tilde{\boldsymbol{H}}$ can then characterise the sensitivity of $\mathcal{J}$ to the parameters and demonstrate possible inter-parameter coupling. Specifically, the minimum diagonal value of $\tilde{\boldsymbol{H}}$ indicates that $\mathcal{J}$ is least sensitive to the corresponding parameter, as a large error in the parameter can result in an insignificant change in $\mathcal{J}$, suggesting poor sensitivity to the parameter under consideration. Similarly, the minimum eigenvalue of $\tilde{\boldsymbol{H}}$ indicates the parameter combination that $\mathcal{J}$ is least sensitive to. Accordingly, the ratio of the minimum diagonal value of $\tilde{\boldsymbol{H}}$ over the minimum eigenvalue $\lambda(\tilde{\boldsymbol{H}})$

$$R = \frac{\min\{diag(\tilde{\boldsymbol{H}})\}}{\min\{\lambda(\tilde{\boldsymbol{H}})\}} \tag{4.18}$$

represents a metric of the degree of coupling between parameters. Specifically, large values of R indicate that there is a parameter combination whose possible error will cause a smaller change in $\mathcal{J}$ than error in each parameter separately, suggesting inter-parameter coupling. Similarly, coupling ratios close to 1 suggest that there is no significant coupling between parameters.

4.2 Results and discussion

4.2.1 Comparison of practical identifiability using 3D tags

For each of the considered constitutive laws, the behaviour of $\mathcal{J}$ over the parameter space was examined, and the error between actual and estimated parameters was quantified. For each law, a ground truth set of parameters was selected to give physiologically reasonable pressure / volume response, and synthetic 3D tags were generated

from an LV inflation simulation. The extracted myocardial motion applied on meshes was then used as data, and compared with simulations with varying parameter combinations, to provide the landscape of the objective function and an assessment of the error in the parameter estimates. This process enabled the characterisation of the practical identifiability of each law and the assessment of its potential use in patient-specific applications.

4.2.1.1 $\mathcal{J}$ characterisation of the neo-Hookean law

(a)

(b)
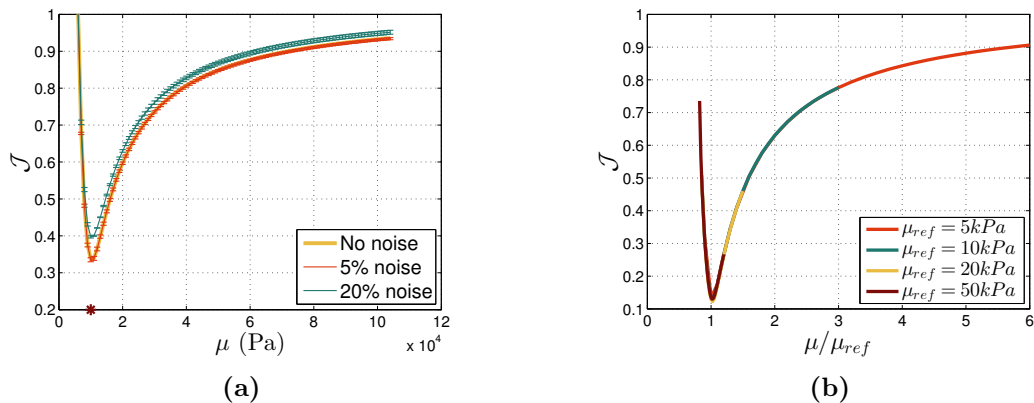
Figure 4.4 a: $\mathcal{J}$ over neo-Hookean stiffness μ, for different data noise levels. The original stiffness value ($\mu = 10kPa$) is marked with a red asterisk. The minimum was obtained among 100 simulations with different stiffness values. **b**: $\mathcal{J}$ over scaled μ for four different original stiffness values. 100 simulations were performed for each parameter sweep, with an average computational time of 20.518 s.

Firstly, the practical identifiability of the neo-Hookean law was investigated by examining the behaviour of $\mathcal{J}$ over a range of stiffness values. Due to the simple structure of the law and its linear parameter dependence, it is expected that, given some deformation, good identifiability characteristics should be possible. Specifically, $\mathcal{J}$ is expected to have a unique and distinct minimum, and it is anticipated that the incorporation of unbiased noise should not affect the behaviour of $\mathcal{J}$ or the estimated parameter, but only cause a shift towards larger $\mathcal{J}$ values.

Indeed, as illustrated in Fig. 4.4a, the objective function $\mathcal{J}$ has a unique and distinct minimum at the initial stiffness value ($\mu = 10kPa$). Furthermore, the actual stiffness value is retrieved even in the case of noisy data (5% and 20% Gaussian noise), and the overall behaviour of $\mathcal{J}$ remains the same, with just a small shift towards larger values. These results suggest that, using 3D tags, the stiffness value can be uniquely and accurately estimated.

The neo-Hookean *in silico* test was extended to study the influence of the actual parameter value on the estimation process. Using the same inflating pressure, increased

stiffness would result in smaller deformation, that might be insufficient to allow for parameter estimation. We therefore performed four passive inflation simulations, where in each case the inflating pressure was adjusted to provide the same end-diastolic volume. We note that, as can be observed in Eq. 4.1 (where the inflating pressure is introduced through traction as the product of pressure and deformed surface normal vector), due to the linear dependence of the law on the parameter, the inflating pressure required to produce the same deformation was simply scaled by the ratio between the stiffness values. Fig. 4.4b presents the behaviour of the objective function $\mathcal{J}$ over scaled stiffness (μ over the initial stiffness for each case), showing consistent behaviour for any initial stiffness value. This fact confirms practical identifiability of the neo-Hookean law using 3D tags for any initial stiffness.

4.2.1.2 $\mathcal{J}$ characterisation of the neo-fibre law
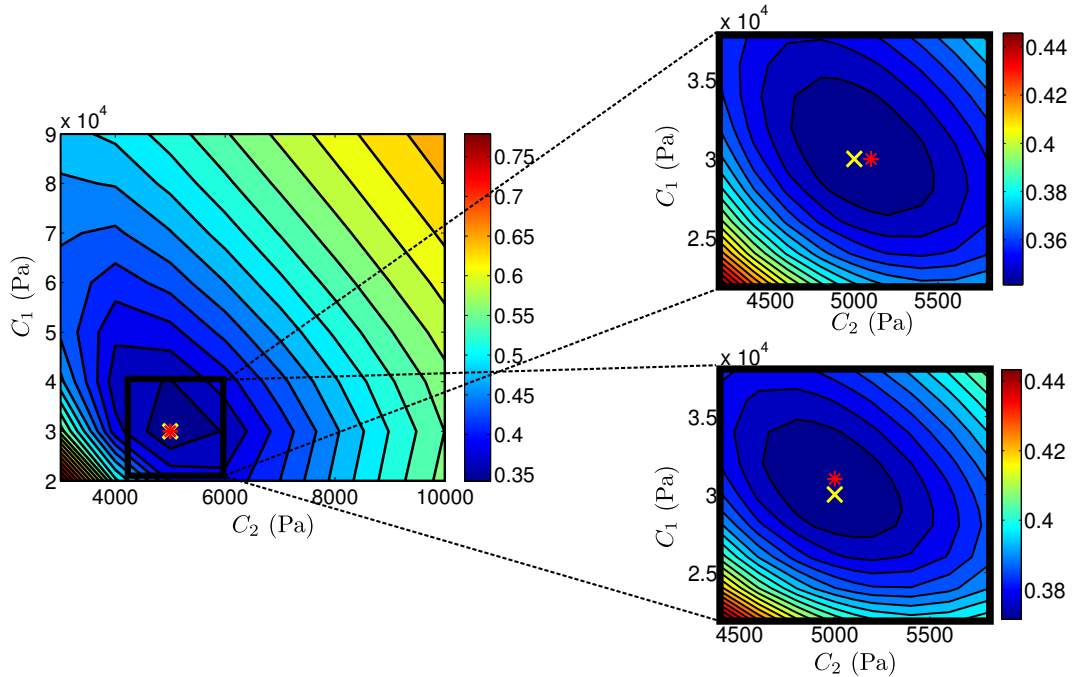
Figure 4.5 Landscape of objective function $\mathcal{J}$ of neo-fibre ($a = 1$) over parameter space. The actual parameters ($C_1 = 30kPa$, $C_2 = 5kPa$) used in the simulation are shown by a yellow cross and estimated parameters by a red star. Figures on the right show a "zoom-in" near the estimated values, where a denser grid of parameters was used. 20% Gaussian noise was added in the data, in the bottom right figure. 11×11 simulations were performed for each parameter sweep, with an average computational time of 51.120 s.

Figures 4.5 and 4.6 illustrate the behaviour of the objective function $\mathcal{J}$ over the parameter space of the neo-fibre law, for $a = 1$ and $a = 2$, respectively. As can be deduced from Fig. 4.5, the neo-fibre law ($a = 1$) maintains the practical identifiability

of the neo-Hookean law (distinct minimum) and provides accurate parameter estimates. Even in the case of noisy data, the landscape of $\mathcal{J}$ remains similar and maintains a clear distinct minimum, with a small error (6.7%) only in the fibre parameter.
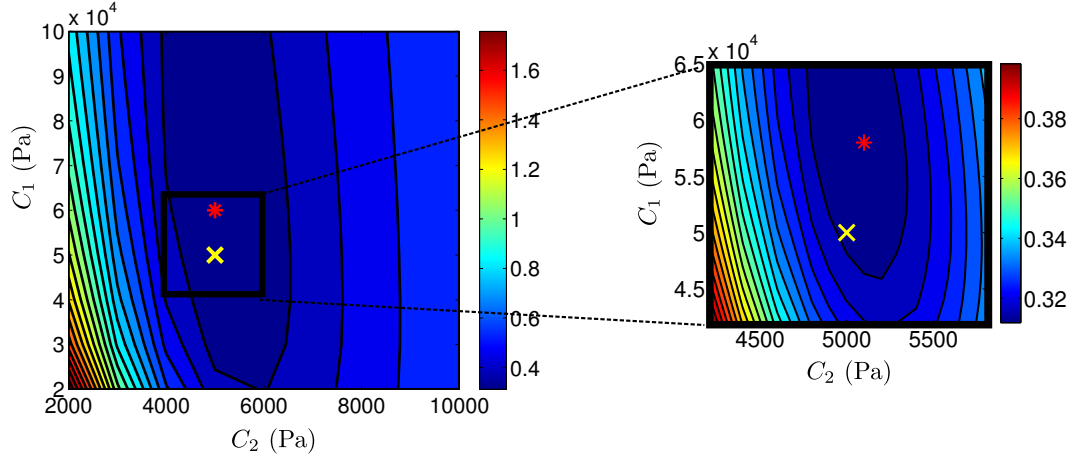
Figure 4.6 Landscape of objective function $\mathcal{J}$ of neo-fibre ($a = 2$) over parameter space. The actual parameters ($C_1 = 50kPa$, $C_2 = 5kPa$) used in the simulation are shown by a yellow cross and estimated parameters by a red star. Figure on the right shows a "zoom-in" near the estimated values, where a denser grid of parameters was used. 10×10 simulations were performed for each parameter sweep, with an average computational time of 60.546 s.

When the exponent, a, is increased to 2 (Fig. 4.6), however, the practical identifiability of the neo-fibre law is compromised (presence of valley) and the error between actual and estimated parameters increases significantly (2% and 16% for the isotropic and fibre parameters respectively). Note that, as no noise is added in this case, this error is created during the tagging process, due to the combination of limited resolution of the tags and higher non-linearity of the law.

(a)   **(b)**
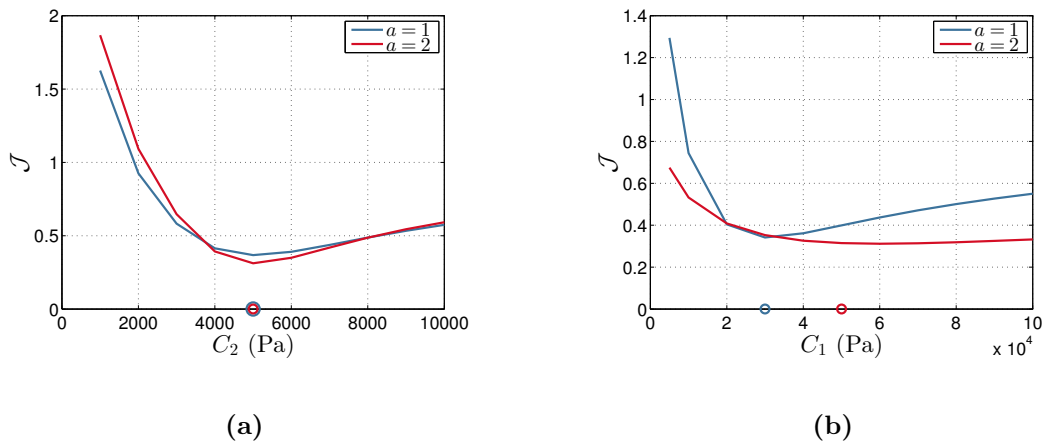
Figure 4.7 Neo-fibre $\mathcal{J}$ over **(a)** the isotropic parameter C_2 and **(b)** fibre-parameter C_1, for $a = 1$ and $a = 2$.

Furthermore, Fig. 4.7 examines the behaviour of $\mathcal{J}$ over a range of values for each parameter separately. The steeper slope of $\mathcal{J}$ around the minimum value in the case of parameter C_2 suggests that the isotropic parameter has better identifiability than the fibre-parameter. This issue is even more prominent in the $a = 2$ case, due to the increased nonlinearity in the fibre dependence. Based on Theorem 2, the neo-fibre law is structurally identifiable due to its linear parameter dependence, suggesting that the deterioration of the identifiability of the fibre parameter is due to insufficient deformation in the data. In fact, even though not presented here, when the end-diastolic pressure was increased to $3kPa$ instead of $1.5kPa$, the error in the fibre parameter decreased from 16% to 12%.

4.2.1.3 $\mathcal{J}$ characterisation of the reduced Holzapfel-Ogden Law

The practical identifiability of the reduced Holzapfel-Ogden model (see definition in 4.5) was tested on a simulaton where the values of the exponents ($b = 5$ and $b_f = 5$) were set to provide a physiological EDPVR (see section 4.2.3 and Fig. 4.13). Fig. 4.8 presents the landscape of the objective function $\mathcal{J}$ over the parameter space, indicating a clear and unique minimum for the objective function. Even though the fibre parameter a_f presents deteriorated identifiability characteristics compared to the isotropic parameter a (as also observed in the neo-fibre case), the parameter values were retrieved with small relative errors (4% and 2% for the isotropic and fibre parameters, respectively).
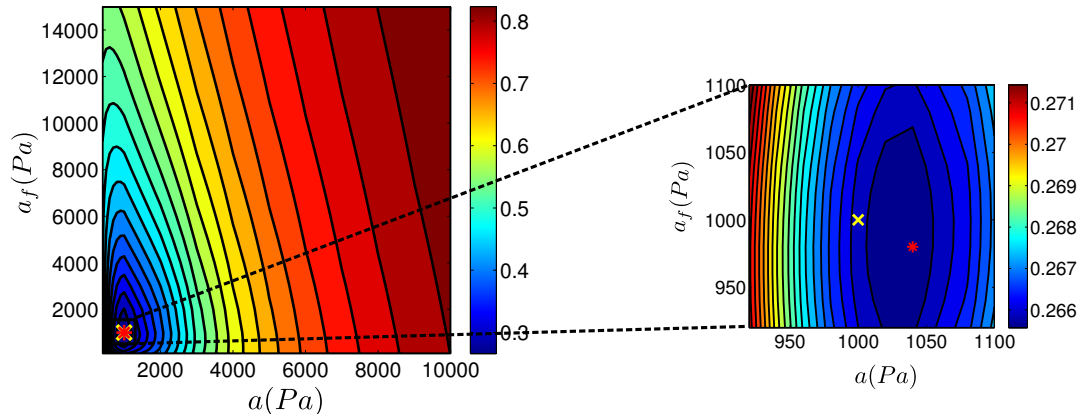
Figure 4.8 Landscape of objective function $\mathcal{J}$ of reduced Holzapfel-Ogden law over parameter space. The actual parameters ($\alpha = 1kPa$, $\alpha_f = 1kPa$) used in the simulation are shown by a yellow cross and estimated parameters by a red star. Figure on the right shows a "zoom-in" near the estimated values, where a denser grid of parameters was used. 12×14 simulations were performed for each parameter sweep, with an average computational time of 56.705 s.
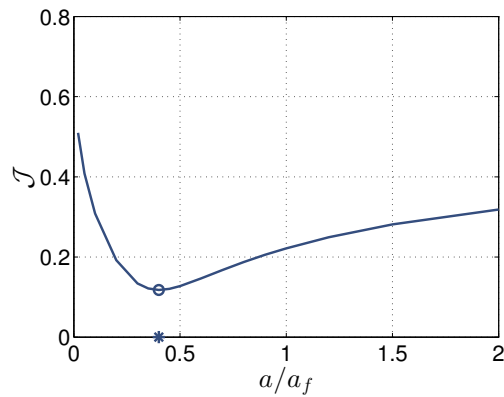
Figure 4.9 $\mathcal{J}$ over parameter ratio a/a_f for the reduced Holzapfel-Ogden law. The actual ratio is marked by a circle.

Additionally, to assist comparisons with *in vivo* models in chapter 6, Fig. 4.9 illustrates $\mathcal{J}$ over the parameter ratio a/a_f for varying a, for a volume-driven simulation. In this case, the volume constraint was enforced weakly through a Lagrange multiplier (as will be discussed in section 5.3.3.1). Fig. 4.9 indicates the presence of a unique distinct minimum at the actual parameter, suggesting that the reduced Holzapfel-Ogden law presents good identifiability characteristics in this setting as well.

4.2.1.4 $\mathcal{J}$ characterisation of the Guccione Law

The practical identifiability of the transversely isotropic Guccione law was tested using a simulation where, the parameters were chosen to fit an empirical end-diastolic pressure-volume relation (EDPVR), proposed by Klotz *et al.*[122] (see Figure 4.13). In order to assess the effect of noise in the data, 5% Gaussian error was added in the simulation results, prior to *in silico* tagging.

Table 4.1 presents the 5 parameter combinations with the smallest $\mathcal{J}$ values, with and without 5% Gaussian noise in the data. These combinations vary significantly, suggesting the presence of multiple minima. Indeed, the presence of 5% noise in the data results in a different estimate of parameters, compared to the non-noisy data. Note that this estimate, which has a larger difference from the actual simulation parameters, compensates for the increase in C with a decrease in b_f, suggesting an inter-parameter dependence.

In order to examine this issue, the Guccione law was reformulated as suggested by Xi *et al.*[276]:

$$b_f = \alpha r_1, \ b_t = \alpha r_2, \ b_{fs} = \alpha r_3, \quad r_1 + r_2 + r_3 = 1,$$

where parameter α denotes the sum of b_f, b_t, b_{fs}. Parameter sweeps were performed over parameters C and α while keeping the ratios between b_f, b_t, b_{fs} and α constant

	C	b_f	b_t	b_{fs}
Actual	**180**	**27.75**	**5.37**	**2.445**
No Gaussian noise				
	150	35	6	3
	250	25	4	3
	250	25	4	5
	200	35	4	3
	300	25	4	2
5% Gaussian noise				
	250	25	4	3
	150	35	6	3
	250	25	4	5
	200	35	4	3
	300	25	4	2

Table 4.1 Actual (in bold) and estimated parameters (in red) for the Guccione law. Furthermore, Guccione parameter combinations with 5 smallest error values are presented, with and without 5% noise in the data. Parameter sweeps were performed over 6 different values for each of the four parameters, resulting to 1296 parameter combinations.

($r_1 = 0.5$, $r_2 = 0.3$, $r_3 = 0.2$). Fig. 4.10 illustrates the behaviour of the objective function $\mathcal{J}$ over a range of the parameters C and α. The exponential shape of the blue valley representing model parameters resulting in small $\mathcal{J}$ values, verifies coupling between C and α as previously reported by Xi *et al.*[276,277]. The presence of inter-parameter dependence is also demonstrated in table 4.3, which shows a significantly larger coupling ratio R (as discussed in section 4.1.3.3) for the Guccione law. Coupling may significantly deteriorate the parameter estimation process, as any noise in the data is likely to result in a large error in the estimated parameters (in this case 5.6% for both α and C). The coupling in the Guccione law therefore suggests that we can not guarantee unique and reliable parameter estimates using 3D tags.

4.2.1.4.1 Identifiability of fibre angle

The fibre distribution is an important determinant of cardiac function, and as a result, incorporating an accurate fibre field into a cardiac model is of great significance. In an attempt to estimate the fibre angle along with the Guccione parameters of table 4.1, the fibre angle was added as an additional unknown parameter in the estimation process. (In this test, the fibre angle θ represents the maximum and minimum angle of the fibre distribution, *i.e.* a fibre angle of $\theta = 40°$ describes a fibre field varying linearly between $-40°$ on the epicardium and $40°$ on the endocardium).
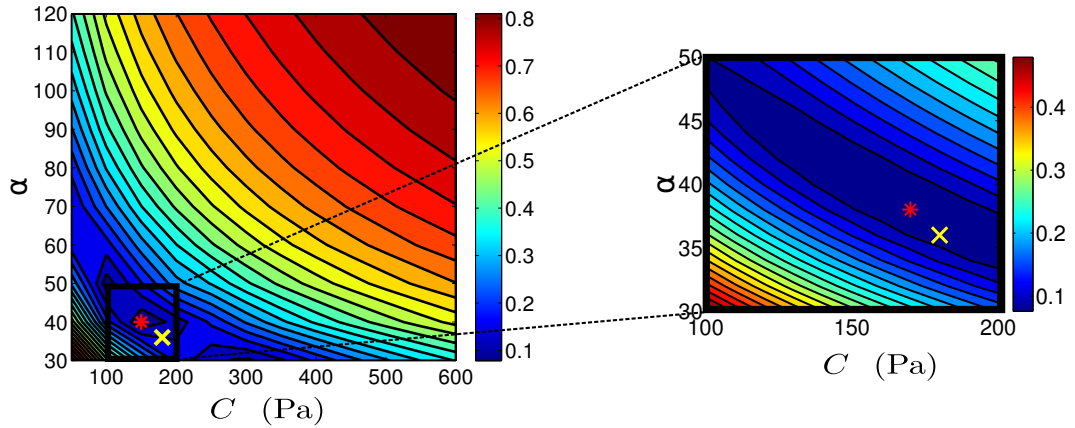
Figure 4.10 $\mathcal{J}$ over Guccione parameters C and α. The actual parameters ($\alpha = 38$, $C = 180Pa$) used in the simulation are shown by a yellow cross and estimated parameters by a red star. Figure on the right shows a "zoom-in" near the estimated values, where a denser grid of parameters was used. 12×12 simulations were performed for each parameter sweep, with an average computational time of 66.158 s.
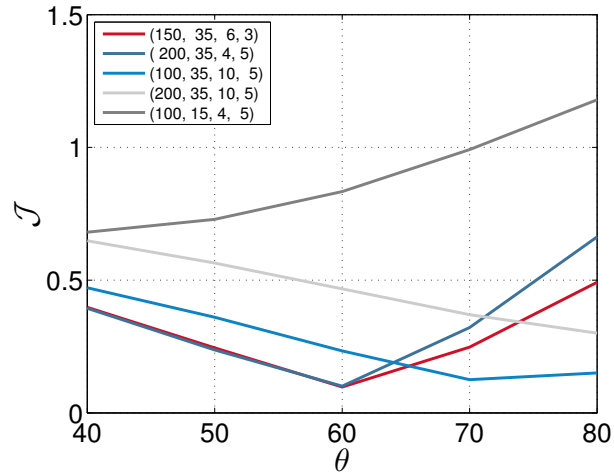

Figure 4.11 $\mathcal{J}$ over the fibre angle θ for 5 (C, b_f, b_{fs}, b_t) parameter combinations of the Guccione law.

Based on Fig. 4.11, which shows the behaviour of $\mathcal{J}$ over the fibre angle for different parameter combinations, the presence of a parameter-fibre angle coupling can be deduced. The estimated fibre angle is dependent on the parameter combination assumed, as a change in fibre angle can be compensated by a shift in the parameters. This coupling is most likely present in the other fibre-dependent constitutive laws as well, suggesting that the fibre angle can not be retrieved through this process. This issue will be discussed in further detail in the *in vivo* models in chapters 5 and 6.

4.2.1.5 Effect of noise in the 3D tagged data

The practical identifiability of the constitutive laws considered may be significantly compromised by the presence of noise in the data. In order to assess this effect, noisy data were considered, where unbiased Gaussian noise was added in the simulation results prior to *in silico* tagging. Due to the limited resolution of the data, the addition of noise is expected to deteriorate the behaviour of $\mathcal{J}$, especially for parameters with very low sensitivity. The presence of noise resulted in increased $\mathcal{J}$ values (see Fig. 4.4a and 4.5) and larger errors in the parameter estimates as indicated in tables 4.1 and 4.2. However, the landscape of $\mathcal{J}$ was not significantly altered due to the uniform noise used, as indicated by the representative case of neo-fibre $a = 1$ in Fig. 4.5. Nonetheless, unbiased noise caused a minor change to the topology of the objective function in the parameter space, as can be deduced by the increase in the coupling ratio in table 4.3.

	neo-Hookean	neo-fibre $a = 1$	neo-fibre $a = 2$	r. HO	Guccione
P.E	$0 \pm 10\%$	$0 \pm 3.33\%$	$16 \pm 2\%$	$4 \pm 2\%$	$5.56 \pm 5.56\%$
		$2 \pm 2\%$	$2 \pm 2\%$	$2 \pm 2\%$	$5.56 \pm 5.56\%$
P.E (20 % noise)	$0 \pm 10\%$	$3.33 \pm 3.33\%$	$16 \pm 2\%$	$4 \pm 2\%$	$5.56 \pm 5.56\%$
		$0 \pm 2\%$	$0 \pm 2\%$	$6 \pm 2\%$	$0 \pm 5.56\%$

Table 4.2 Percentage error (P.E.) between actual and estimated parameters for each law. The interval used in each parameter sweep is used as the uncertainty in each case. The first row corresponds to the error of the first parameter for each law.

	neo-Hookean	neo-fibre $a = 1$	neo-fibre $a = 2$	r. HO	Guccione
Gradient	-1.2516e-05	-2.6958e-07	4.8918e-08	-5.7794e-06	-2.7133e-04
		-2.4444e-06	7.7456e-06	-8.8705e-07	-2.2966e-03
R		1.3962	1.1848	1.0041	16.596
R (20 % noise)		1.4006	1.2019	1.1201	20.883
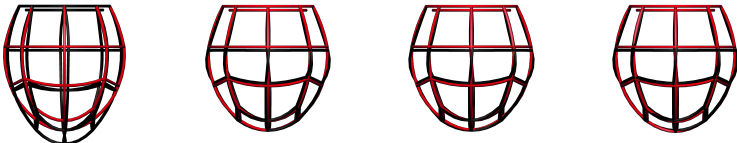
Table 4.3 Gradients at the obtained minima, for the considered constitutive laws. The first row corresponds to the gradient with respect to the first parameter for each law. Coupling ratios R are also presented, for data with and without 20% unbiased noise.

4.2.2 Comparison of models' fidelity

Keeping in mind that the choice of an appropriate constitutive law should balance between parameter identifiability and model fidelity, the constitutive laws described in section 4.1.2.2 were also tested with respect to their ability to represent physiological cardiac deformation. Furthermore, the behaviour of the objective function for any constitutive law is also influenced by model fidelity (as discussed in section 4.1.3.2), as a model which can not provide a good approximation to data can lead to unreliable

parameters. It is worth noting that, even though model fidelity does not affect the *in silico* tests in section 4.2.1, where the same constitutive law is used for generated data and simulations, it is an issue for *in vivo* cases, where the model should represent cardiac deformation.

For the purposes of this comparison, Guccione deformations were considered as the ground truth for physiological cardiac deformation. In order to cover a range of possible deformation modes during the cardiac cycle, 18 widely varying parameter combinations were used. For each of these combinations, a parameter sweep was performed for each law to provide the parameter that minimised the difference between simulations and the ground truth cardiac deformation. The comparison was performed on simulations with the same end-diastolic volume through volume-prescribed loading to reduce the parameter space by 1.

	neo-Hookean	neo-fibre $a = 1$	neofibre $a = 2$	r. Holzapfel-Ogden
Minimum error	0.089	0.063	0.084	0.054
Maximum error	0.625	0.261	0.251	0.259
Average error	0.503	0.197	0.152	0.122

Figure 4.12 Neo-Hookean, neo-fibre ($a = 1$ and $a = 2$) and reduced Holzapfel-Ogden laws are compared in terms of their ability to approximate physiological cardiac deformation. 18 Guccione parameter combinations are used as ground truth. Deformed meshes denote ground truth cardiac deformation in black and model deformation in red, for the ground truth deformation that presented the maximum difference from the model response. The table presents minimum, maximum and average $\mathcal{J}$ values over the 18 Guccione combinations for the various laws.

Fig. 4.12 compares the minimum, maximum and average errors between the various laws considered and ground truth deformation. The neo-Hookean law exhibits a significant variation compared to ground truth deformation. This is mainly due to the inability of the neo-Hookean law to produce adequate elongation and twist, which are important characteristics in cardiac deformation. On the other hand, the added fibre-dependence in the neo-fibre law allows for a more accurate approximation to physiological cardiac motion, as the lower average and maximum errors indicate that the neo-fibre can, on average, reproduce most of the deformation modes considered. The approximation to cardiac motion is further improved as the exponent α increases. Finally, the reduced form of the Holzapfel-Ogden law presents the smallest average and minimum errors between the deformations produced using a given constitutive law and the Guccione law, confirming that the values used for the exponents b and b_f are ap-

propriate and allow for physiological cardiac deformation. These observations can also be made qualitatively, using the meshes in Fig. 4.12, which present the maximum difference from Guccione combinations. For the neo-fibre and reduced Holzapfel-Ogden models, even the maximum difference from the ground truth is small, as indicated by the close match between model and ground truth cardiac deformation.

4.2.3 Comparison of models' EDPVRs

End-diastolic pressure-volume relation (EDPVR) is an important determinant of cardiac function, therefore the considered constitutive laws were compared with respect to their ability to reproduce a physiological EDPVR. For this comparison, the empirical EDPVR proposed by Klotz *et al.* was chosen as the ground truth physiological EDPVR, as it is considered capable to represent healthy and diseased cases. The EDPVR is derived from a single set of end-diastolic pressure (EDP) and volume (EDV) measurements, which, for the *in silico* tests, were chosen as EDP= 11mmHg and EDV= 140ml.
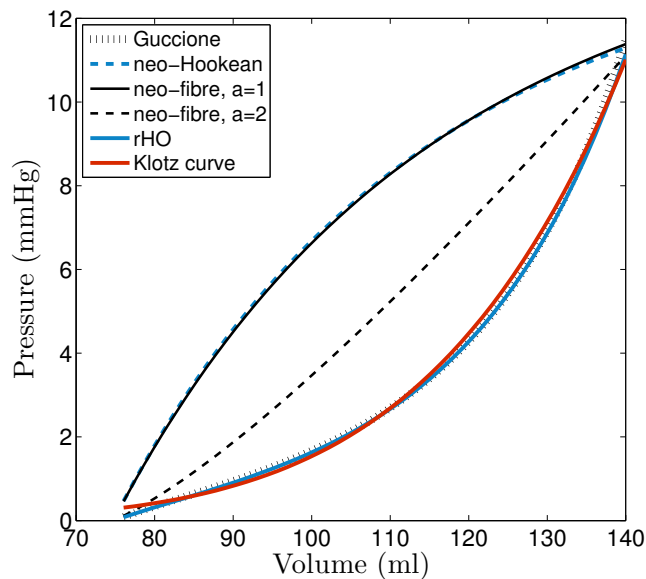
Figure 4.13 Typical end-diastolic pressure-volume curves for the constitutive laws considered and ground truth Klotz curve. While the reduced Holzapfel-Ogden and Guccione laws are able to reproduce the Klotz curve, the neo-Hookean and neo-fibre laws can not produce a physiological pressure-volume response.

Figure 4.13 illustrates typical EDPVRs for the various constitutive laws considered. As indicated by the curve, the neo-Hookean and neo-fibre laws were not able to reproduce a physiological EDPVR, even though case $a = 2$ gives a better approximation for the neo-fibre law. On the contrary, the exponential Guccione and the reduced Holzapfel-Ogden laws were able to provide a physiological EDPVR as indicated by the close

match to the Klotz curve.

4.2.4 Additional tests using the reduced Holzapfel-Ogden law

Based on the results described above, the reduced Holzapfel-Ogden law combines good identifiability characteristics with a sufficiently accurate representation of the heart function. As such, it comprises a suitable choice for a cardiac constitutive law, therefore additional tests were performed employing this model as the constitutive law, to elucidate the effect of important modelling considerations.

4.2.4.1 Effect of mesh resolution on $\mathcal{J}$ behaviour

A relatively coarse, lower order mesh was used for the *in silico* examples in section 4.2.1.3. This choice was based on the small computational time per simulation, which allowed for the large number of simulations performed to provide the landscape of the objective function over the parameter space. Nevertheless, this section examines whether the mesh resolution used was sufficient to examine parameter identifiability characteristics in the *in silico* models considered.

To investigate this aspect, the *in silico* characterisation of the reduced Holzapfel-Ogden law presented in section 4.2.1.3 was repeated on a uniformly refined mesh (448 elements, instead of 56 elements used in the initial test). As can be deduced by the similarity in both the landscape of $\mathcal{J}$ and the estimated values between Fig. 4.8 and 4.14, the coarser mesh used for the *in silico* tests is able to characterise the identifiability of the considered constitutive laws.
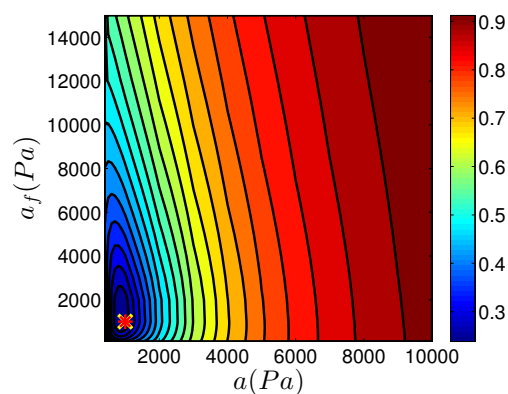
Figure 4.14 Landscape of objective function $\mathcal{J}$ of reduced Holzapfel-Ogden law over parameter space, when a finer mesh consisting of 448 elements is used.

4.2.4.2 Effect of reference configuration on $\mathcal{J}$ behaviour

A common approach in *in vivo* cardiac mechanics models is to assume that the reference configuration is known and corresponds to a specific frame of diastole. This section investigates the effect of choosing a different diastolic frame as a reference configuration on the behaviour of the objective function. Specifically, an *in silico* test was used to examine the effect of the reference configuration on the identifiability of the parameter ratio of the reduced Holzapfel-Ogden law, in a volume-prescribed diastolic filling simulation. Five different reference configurations were considered for the simulations performed over parameter sweeps: the initial reference mesh and meshes corresponding to loading steps 10, 20, 30 and 40 of the simulation used for the creation of the synthetic tags. In each case, the number of loading steps and thus observations was adjusted, so that each observation would correspond to 5 loading steps.
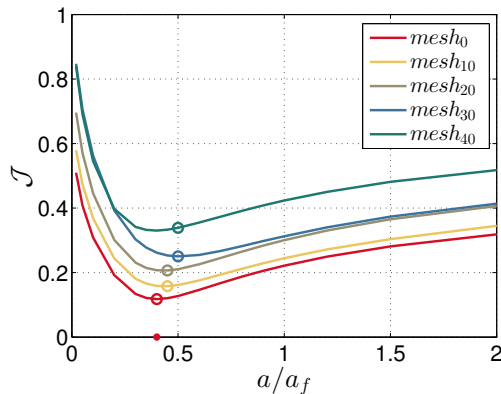
Figure 4.15 $\mathcal{J}$ over the parameter ratio a/a_f for the reduced Holzapfel-Ogden law. Five different reference configurations are used, corresponding to different diastolic phases.

Fig. 4.15 compares the behaviour of the objective function $\mathcal{J}$ when different diastolic phases are used as the reference configuration. Based on the similar behaviour of the curves, the identifiability of the parameter ratio is not sensitive to the assumed reference configuration. Interestingly, the parameter ratio is relatively consistent (20% maximum error between actual and estimated ratio), irrespective of the reference domain. It should be noted however, that this might be an artefact of the idealised geometry used or other simplifications inherent in the model produced data.

4.2.4.3 Effect of *in silico* tagging and tracking on $\mathcal{J}$ behaviour

The process of synthetic tags' generation and the tracking algorithm are likely to introduce a biased influence into the parameter estimates and the landscape of the objective

function. To investigate this effect, simulations with parameter sweeps were compared with the original simulation results, before any processing had been applied.
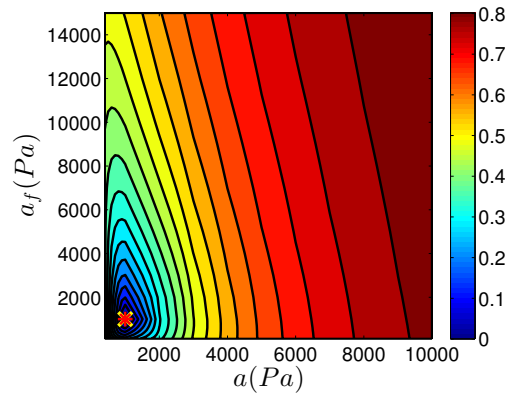
Figure 4.16 Landscape of objective function $\mathcal{J}$ of reduced Holzapfel-Ogden law over parameter space, when the simulations are compared to the unprocessed data.

Based on Fig. 4.16, the processing steps do not seem to incorporate significant bias as the landscape of the objective function is similar to Fig. 4.8. As anticipated, the error at the estimates is much smaller (0), and in general the minimum is more localised (sharper variation around the minimum). In general, the tagging and tracking process does not seem to significantly alter the topology of the objective function over the parameter space, although the identifiability behaviour moderately deteriorates.

4.2.5 Study limitations

Even though the effect of unbiased noise was examined, some aspects of the process or the data that may introduce a biased influence on the study outcomes, have not been examined. For instance, the resolution and number of tagged lines in the data are likely to incorporate consistent error in the parameter estimation process. The boundary conditions used in the simulations are also likely to influence the identifiability and model fidelity results. Understanding these attributes is important for patient-specific personalisation, therefore further work may be useful in clarifying the influence of these factors on the landscape of the objective function and the estimation process in general.

Furthermore, only one objective function has been considered, even though other objective functions may be able to elucidate other characteristics of the behaviour of the various laws. Other objective functions have not been considered here, as such a study would require proving that a potential objective function is discerning. If non-discerning, proving that unique parameter identification is achievable becomes challenging, as it must then rely on the observations exposing uniqueness of the objective

function. Nevertheless, the chosen $\mathcal{J}$ uses an $\boldsymbol{L}^2$ norm on the displacements, which is generally considered as a robust criterion and should be able to provide adequate information and accurately describe the identifiability characteristics of each law.

Finally, only *in silico* tests have been considered in the present chapter, thus further work is needed to examine effects *in vivo*, such as noisy or low resolution data, or diseased cases where the cardiac deformation is likely to differ significantly and data quality is likely to be compromised. Furthermore, model fidelity is not an issue in these *in silico* tests, but would likely affect identifiability in *in vivo* models, where matching between the model and the data will always be imperfect. However, the *in silico* tests performed provide a standard, representing the "best case scenario" which can be anticipated when using real data. Moreover, parameter identifiability and model fidelity in *in vivo* applications will be examined and discussed in detail in the following chapters (chapters 5 and 6).

4.3 Summary

In this chapter, the practical identifiability and model fidelity of a range of cardiac constitutive laws using 3D tagged MRI as the available data was examined. In order to investigate the practical identifiability of the laws considered and examine the potential of using 3D tags in parameter estimation applications, synthetic 3D tags were generated directly from simulation results, and the behaviour of the objective function over the parameter space was assessed through parameter sweeps. The laws considered were also compared with respect to their ability to represent physiological cardiac motion and EDPVR, elucidating the primary components that should guide the choice of an appropriate cardiac constitutive law – namely reliable parameters and adequate representation of cardiac deformation and function.

The results presented in the present chapter verify the reported coupling of the transversely isotropic Guccione law, suggesting the need for a law with better identifiability characteristics that would allow for reliable parameter estimates. The neo-Hookean law is shown to have good identifiability characteristics, due to linear parameter dependence. The stiffness parameter is identifiable, provided adequate deformation is present in the available data. However, due to its isotropy, neo-Hookean deformation misses key characteristic deformation modes, mainly long-axis elongation and twist. Furthermore, it can not reproduce physiological pressure-volume response.

Building on the neo-Hookean model, the neo-fibre law maintains the good identifiability characteristics, while reproducing physiological cardiac deformation. Both parameters are identifiable, even though sufficient deformation is required to allow identifiability of the fibre parameter, due to the structure of the constitutive law. However, use of the

neo-fibre law leads to an inaccurate pressure-volume response, which can not match the empirical Klotz curve.

On the other hand, the reduced Holzapfel-Ogden law, combines all important attributes considered, offering a balance between practical identifiability and adequate representation of cardiac deformation and EDPVR. Additional tests in which good identifiability characteristics are maintained, support the conclusion that the reduced Holzapfel-Ogden law offers a suitable choice in patient-specific applications with 3D tagged MRI data.

Part II

Application to personalised models

5 Development of personalised diastolic models

In order for personalised cardiac models to be a viable clinical tool, they need to provide an accurate representation of individual hearts, producing reliable metrics suitable for clinical interpretation. Optimal use of the available data in model personalisation is a crucial step in model accuracy, thus a lot of current efforts in the cardiac mechanics community are focused on bridging the gap between imaging data and developed mathematical models.

Developing accurate personalissd models is a challenging task, strictly dependent on – and limited by – the available clinical data. The accuracy of the personalised geometry and architecture, for example, is determined, among others, by the imaging modalities available, while passive material laws need to be selected to ensure parameter identifiability using the data at hand. At the same time, essential image processing steps need to be followed to reduce inconsistencies between different imaging modalities and allow for translation from the qualitative characteristics observed in images to quantitative information that can be used by mathematical models.

Boundary conditions, although often given little attention, can be used for incorporating data into the model thus improving model fidelity. The choice of boundary conditions is also important in personalised models, as a naive choice might lead to non-physiological model outcomes or over-constraining of the problem. Nevertheless, specific boundary conditions can be selected which regulate the level of adherence to the data, reducing non-physiological model deformations due to strict enforcement of the constraint or incomplete / low resolution data.

This chapter presents the pipeline followed in this thesis for the development of personalised models for the study of DCM. Emphasis is largely on optimising the use of the available data to improve model accuracy while ensuring reliable estimation of passive parameters. Based on novel boundary conditions, a computational model and parametrisation paradigm are presented, which are using strictly non-invasive data.

Initially, the clinical project and available data are presented (section 5.1), followed

by essential image processing steps aiming at limiting data inconsistencies (section 5.2). Modelling considerations studied through *in silico* tests in previous chapters are now extended to personalised *in vivo* models (section 5.3) incorporating patient-specific geometries. Furthermore, the boundary conditions employed enable driving the diastolic LV filling simulations with cavity volumes from imaging data – overcoming the need for invasive pressure measurements – and incorporate data-derived motion into the model. Finally, passive parameters are estimated using data-derived displacements and an end-diastolic pressure clinical surrogate (section 5.4). The proposed pipeline provides the framework for investigating important aspects such as model accuracy and parameter identifiability which will be discussed in chapter 6. This analysis is an essential step, enabling reliable comparisons between DCM patients and healthy volunteers.

5.1 BHF Integrated mathematical modelling and imaging study

A significant portion of the work presented in this thesis is part of the BHF funded project, *"BHF Integrated mathematical modelling and imaging study"*. The main aim of the project is to integrate comprehensive imaging data into mathematical models of heart function to develop personalised cardiac models for the study of dilated cardiomyopathy (DCM).

During this project, imaging data from two cohorts was collected. Specifically, 20 healthy volunteers with normal heart function and 16 DCM patients were recruited, aged 25-65. DCM patients recruited for the study were selected to have moderate DCM-related heart failure (defined as NYHA class I/II). Both male and female volunteers / patients were recruited.

All participants had MRI scans during which a series of images, ECG recordings, heart rate and non-invasive blood pressure measurements were acquired. Each data-set was then collected and anonymised, before being used for the construction of personalised mathematical models. Data collection was performed by myself and research and clinical collaborators, at Guys hospital, London.

5.1.1 Description of available data

A range of imaging data was acquired for each participant to allow for a detailed personalisation of the cardiac models. Each imaging modality has a different scope elucidating particular aspects of cardiac function and contributing to a complete picture

of heart kinematics. Cardiac MRI scans were performed on a 1.5T Philips Achieva system. Below, the data acquired for each participant are discussed.

5.1.1.1 Cine MRI

Cine bSSFP (balanced steady-state free precession) sequences were acquired using retrospective ECG gating, with a reconstructed spatial resolution of $1.5 \times 1.5 \times 8$ mm and a temporal resolution of 40 time frames per cardiac cycle. The acquisition was performed in respiratory navigated breath-holds. The left and right ventricles were covered by a short-axis cine stack (Fig. 5.1a), while the long axis views of the LV were also captured in standard 2-, 3- and 4-chamber views (Fig. 5.1b, 5.1c and 5.1d, respectively). An MRI breathing navigator was used for the short-axis scan to reduce artefacts due to non-reproducible breath-holds.

(a)	**(b)**	**(c)**	**(d)**
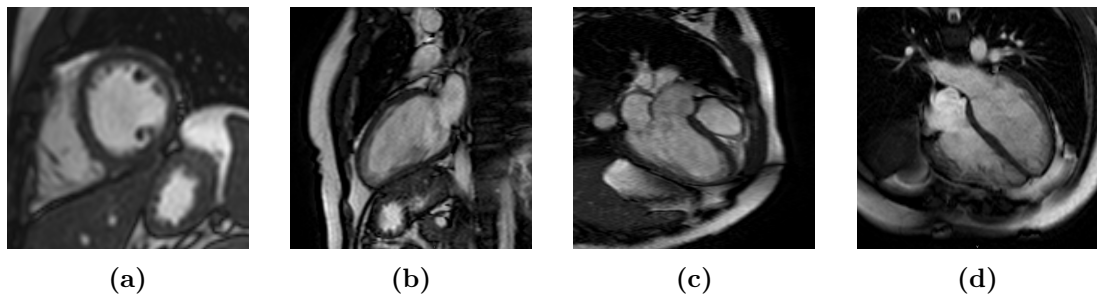
Figure 5.1 Cine MRI in **(a)** short-axis, **(b)** 2-chamber, **(c)** 3-chamber and **(d)** 4-chamber long-axis views at end diastole.

Cine MRI images provide detailed morphological characteristics of the heart and are therefore commonly used for construction of personalised model geometries[278,9]. Further, existing tracking algorithms can quantify the motion of myocardial surfaces through the cardiac cycle, which can also be used for parameter estimation[30,73].

Within the model personalisation process considered in this chapter, cine images provided the personalised geometry (section 5.2.2).

5.1.1.2 3D tagged MRI

3D tagged MRI covering mainly the LV was acquired in three breath-holds, with prospective ECG triggering using the sequence presented in Rutz *et al*[211]. The acquired spatial resolution was $3.4 \times 7.7 \times 7.7$ mm for the three components of the tag planes. These were then reconstructed on the Philips scanner to a final 3D tagged image (Fig. 5.8) of resulting spatial resolution of $1 \times 1 \times 1$ mm and approximate temporal resolution of ~ 30 ms, providing approximately 20-25 time frames per cardiac cycle.
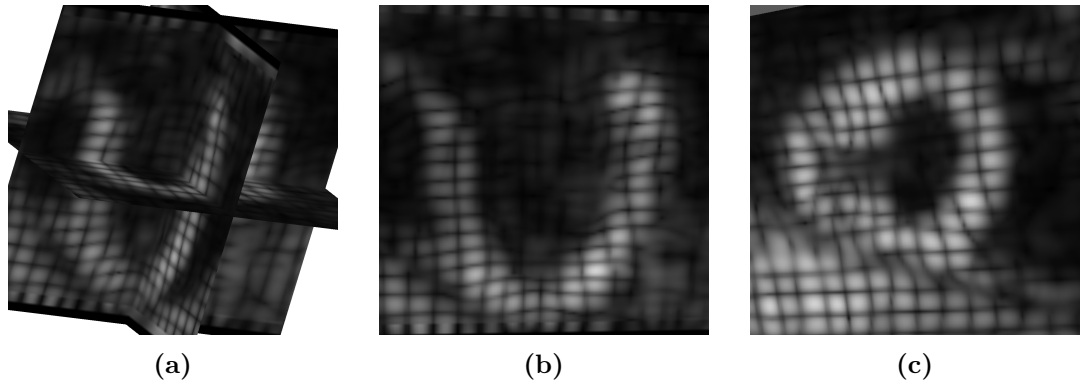
Figure 5.2 (a) Reconstructed 3D tagged MRI in **(b)** long-axis and **(c)** short-axis views at end systole.

3D tagged MRI provide a detailed quantification of regional myocardial deformation, as well as through wall motion, torsion and shear. Offering a 3D whole-heart deformation field, 3D tagged MRI has been used in parameter estimation applications[278,266]. The extracted motion can also provide data-derived boundary conditions[278] as well as loading constraints for personalised models[9].

Within the presented pipeline, motion extracted from 3D tagged MRI provides cavity volumes for driving simulations as well as deformations used for boundary conditions and parametrisation.

5.1.1.3 4D PCMRI
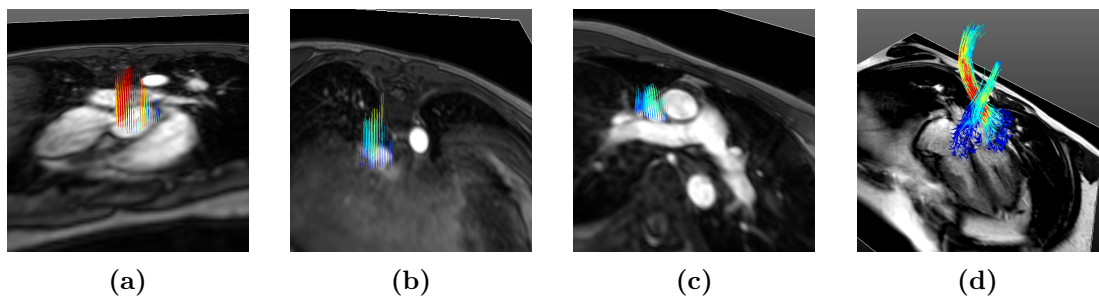
Figure 5.3 Snapshots of 2D PCMRI through **(a)** the aortic valve, **(b)** inferior vena cava, **(c)** superior vena cava. **(d)** Snapshot of 4D PCMRI image on a 4-chamber long-axis view. Coloured lines depict the direction and magnitude of flow.

4D Phase Contrast MRI data (also refered to as 4D PCMRI or 4D flow) was acquired using prospective ECG triggering (Fig. 5.3d). The acquisition was performed during free breathing using an MRI breathing navigator to restrict artefacts due to respiratory motion. The images had a spatial resolution of $2.3 \times 2.3 \times 2.3$ mm and 24 time-frames per cycle were acquired. Data acquisition was accelerated using a nominal spatio-temporal

acceleration factor of 8 and the resulting data were reconstructed using the kt PCA technique[196].

4D PCMRI images provide a detailed characterisation of blood flow, thus identifying potential abnormalities. Further, combined with modelling, they can be used for estimation of cavity pressure gradients[125].

In this work, 4D PCMRI was used for an approximation of peak early diastolic flow velocity, which can be used for an estimate of end-diastolic pressure (section 5.4)

5.1.1.4 2D PCMRI

2D PCMRI data was acquired at planes orthogonal to the blood flow at the aortic valve, inferior vena cava and superior vena cava (Fig. 5.3a-5.3c). These images had a spatial resolution of 1.5×1.5 mm and 40 frames per cycle were acquired.

2D PCMRI images enable a quick characterisation of unidimensional flow through mitral and aortic valves and main vessels. This information can also be used within Windkessel models or to provide boundary conditions in 3D models.

5.1.1.5 3D SSFP

Detailed anatomical 3D SSFP images were acquired at diastole and systole, with a reconstructed spatial resolution of $1 \times 1 \times 1$ mm. Acquisition was performed during free-breathing, using a breathing navigator.

Due to their high resolution, 3D SSFP can be used for the construction of detailed personalised geometries. In order to avoid misalignment issues – due to the fact that 3D SSPF was acquired during free-breathing as opposed to 3D tagged MRI – 3D SSFP images were not used for the creation of personalised meshes.

5.1.1.6 Pressure measurements

Throughout the acquisition of the above-mentioned images, cuff measurements of blood pressure were recorded using a Centron cBP301 device*. Through this non-invasive process, central pressure was computed by applying a transformation on the acquired brachial cuff pressure waveform[83,24]. This step involved an empirically derived generalised transfer function (based on a fast Fourier transform in the frequency domain[83]) which was calibrated using mean and diastolic peripheral pressure. This technique was shown to estimate the peak systolic central pressure with satisfactory accuracy[24].

---

*http://www.suntechmed.com/centron-cbp301

Peak systolic central pressure provides an estimate of peak systolic cavity pressure, it can therefore be used as a loading constraint and as an observation in parameter estimation applications. This data was not used within the diastolic personalised models, as central pressure is irrelevant to diastole, unless a full-cycle curve is assumed.

5.1.1.7 Outline of data used in model personalisation

The wealth of available clinical data offer the opportunity for the creation of different types of personalised cardiac models including mechanics, fluid-solid interaction and Windkessel models. For the specific requirements of the personalised diastolic mechanics models considered throughout this work, cine images, 3D tagged MRI and 4D PCMRI data were used. A summary of the available data used in model personalisation is presented below:

Non-invasive dataset

For every participant considered, the data required for developing and simulating a personalised cardiac mechanics model include:

1. Short-axis, 2-, 3- and 4-chamber long axis cine images used for creating computational mesh

2. 3D tagged MRI, providing :

   - cavity volumes $(V_{lv}(t))$ through the cycle used to drive the model

   - reference geometry (Ω_0) at end systole

   - base plane displacements for basal boundary condition

   - epicardial displacements at the RV attachment region for epicardial boundary condition

   - base plane displacements for estimating early diastolic velocity at the mitral valve (E_a)

   - diastolic displacements $(\boldsymbol{u}_d)$ for estimation of passive parameters

3. 4D PCMRI for estimating peak early diastolic flow velocity through the mitral plane (E)

5.2 Outline of proposed personalisation pipeline

A summary of the process followed in this work for incorporating the available data into personalised models is presented in this section. The pipeline is also summarised in Fig. 5.4, where each step is linked to the relevant section in the text. Initially, the various images were registered spatially and temporally to enable accurate use of data in model development. End-diastolic cine images were used to create a mesh, on which motion extracted from tagged MRI was propagated through the cardiac cycle. Personalised models were driven by the cavity volume trace extracted from this data. Data-derived boundary conditions were also applied, making the models a more accurate representation of the data. Finally, parameter estimates were acquired by matching simulated deformations with motion extracted from 3D tagged MRI, providing a basis for comparisons between DCM patients and normals. Each step of the pipeline is presented in more detail in the following sections.
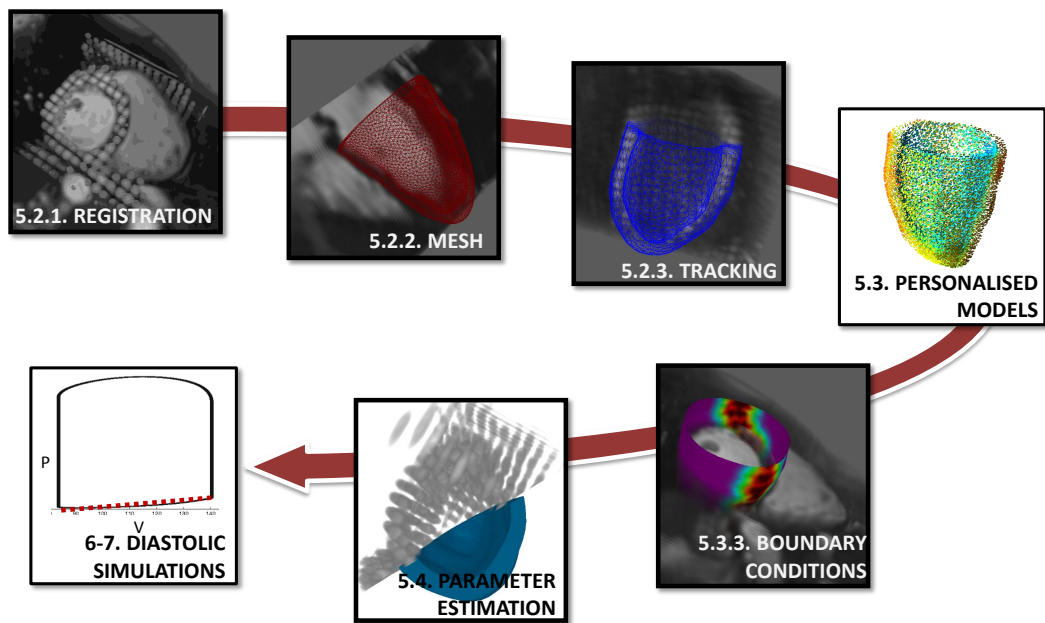
Figure 5.4 Worflow followed for the development and analysis of personalised diastolic heart models.

5.2.1 Image registration

An essential step in order to enable the use of the available data and optimise the personalisation of the patient-specific models is the spatial registration of the available images. The considered sequences (sections 5.1.1.1 and 5.1.1.2) were acquired at different phases in the cardiac cycle. Additionally, the volunteer or patient scanned was likely to change position during the acquisition of different sequences, resulting in

misaligned images. Moreover, some of the sequences were acquired under breath-holds whilst others were free-breathing, which introduced misalignment between the images. Misalignment was likely accentuated by artefacts due to respiratory motion.

These issues were resolved through appropriate image registration and selection of images (focusing on breath-hold images). Initially, the short-axis cine stack was registered to a 3D template image – in this case the 3D tagged MRI image – through rigid registration using Image Registration Toolkit [†], as described for synthetic 3D tags in section 4.1.1.3. This step also corrected potential slices' misalignment which could be caused due to non-reproducible breath-holds – even though this misalignment was limited due to the use of a breathing navigator during acquisition of short-axis cine stack. This registration step also required a mask of the myocardial wall and cavity, created using ITK-SNAP [‡288]. The resulting registered short-axis image (Fig. 5.5a) was used for the registration of 2-, 3-, 4-chamber views and 4D PCMRI data, using the same rigid registration algorithm (Fig. 5.5b and 5.5c).

(a)   (b)   (c)
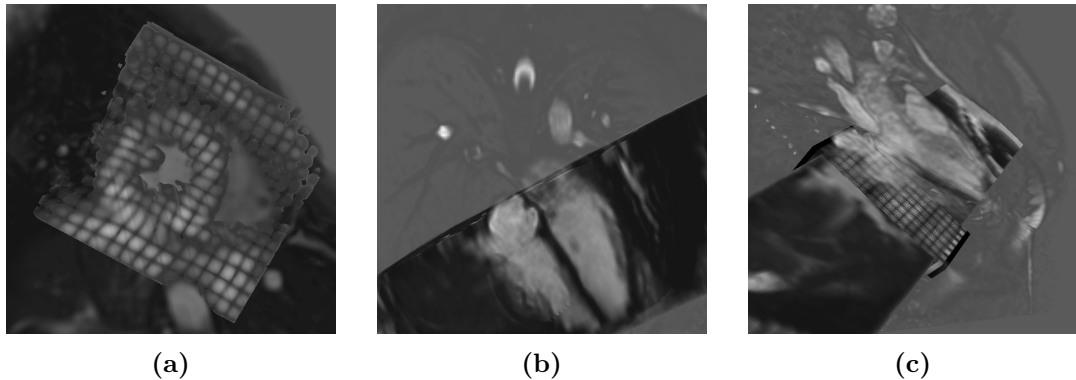
Figure 5.5 (a) Registration of short-axis cine stack to 3D tagged MRI. **(b)** Registration of 4-chamber long-axis view to the registered short-axis image **(c)** All cine images and tagged MRI are registered.

5.2.2 Construction of personalised mesh

A personalised geometry is a very important component of patient-specific applications as wall thickness and curvature have a significant influence on heart behaviour. For the cases considered, LV meshes were created using segmentations of end-diastolic cine images. End-diastolic frames are commonly used for the creation of personalised geometries as the myocardial wall and cavity are better distinguishable compared to systolic frames where papillary muscles complicate segmentations. Myocardial wall and cavity segmentations of short-axis (Fig. 5.6a) as well as 2-, 3- and 4-chamber (Fig. 5.6b) long axis images were created using ITK-SNAP. These segmentations were then merged into one mask which was further refined and smoothed. The resulting mask was compared

[†]https://www.doc.ic.ac.uk/~dr/software
[‡]www.itksnap.org

to cine images, in order to test its proper alignment to images. A template surface mesh[*] based on a statistical atlas[99] was then fit to this mask and truncated at the base. Subsequently, a personalised linear tetrahedral mesh was created (Fig. 5.6c and 5.6d), using Cubit meshing software[†].

| (a) | (b) | (c) | (d) |
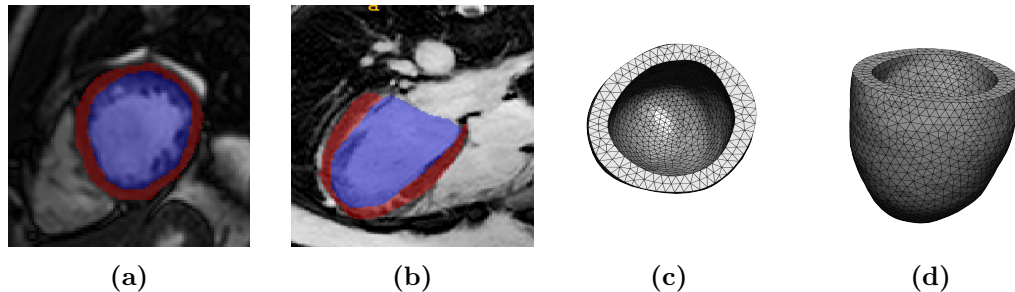
Figure 5.6 Segmentation of **(a)** short-axis and **(b)** 4-chamber cine images, used for the creation of personalised mesh presented here in **(c)** short-axis and **(d)** long-axis views.

5.2.3 3D tagged MRI motion tracking

Myocardial wall motion was extracted from 3D tagged MRI images using IRTK motion tracking described in section 4.1.1.3. The extracted motion was then propagated on the end-diastolic personalised mesh, resulting in a set of deformed meshes following the heart motion throughout the cardiac cycle.

Preliminary 3D tagged MRI tracking tests resulted in non-physiological deformations with sharp variations throughout the myocardial wall, especially around the base of the LV mesh. The use of a myocardial wall mask during motion tracking proved beneficial for the deformed meshes. By restricting the field of interest, the use of a mask reduced the effect of the surrounding tissues and organs in the extracted motion, resulting in qualitatively accurate deformation fields (comparing to tagged and cine MRI), while previously observed non-physiological deformation was restricted.

Furthermore, strict adherence to the 3D tagged data often resulted in sharp corners in the deformed domain due to noisy data. Therefore, a weaker adherence to the data was employed by modifying an appropriate penalty parameter within the registration algorithm. The described setting was used for motion tracking for all cases considered.

---

[*]http://www.cistib.upf.edu/cistib/index.php/downloads
[†]https://cubit.sandia.gov/

5.2.3.1 Extracted motion processing

Through preliminary analysis of the extracted motion, large variation in myocardial wall volume was observed over the cardiac cycle. According to experimental results, the wall volume is expected to vary by no more than 10% as discussed in section 1.3.1.4. In the considered cases, however, the wall volume was reduced by as much as 30% between end diastole and systole, as illustrated in a representative example of wall volume through the cycle in Fig. 5.7a. Such a significant variation in wall volume cannot be considered physiological, and was likely an artefact of either 3D tagged MRI data itself, or – more likely – the tracking algorithm used to extract motion (which does not ensure deformations are volume conserving). Based on direct comparisons between the data and the extracted motion, higher accuracy in long-axis motion compared to short-axis motion was observed. It is hypothesised that this was due to insufficient number of transverse tag lines covering the myocardial wall compared to the longitudinal lines. It is thus likely that wall thickening was not captured to its full extent by 3D tags and motion tracking, leading to inordinate decrease in wall volumes over systole.

(a)   (b)
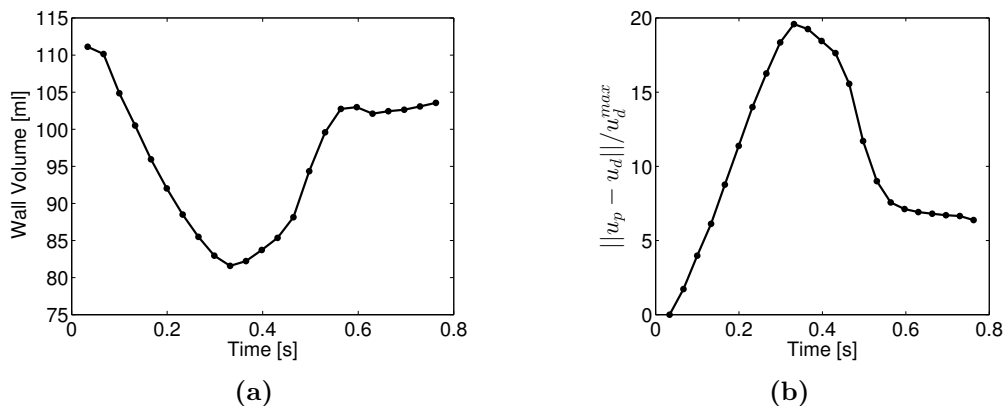
Figure 5.7 (a) Wall volume of the unprocessed data through the cycle. **(b)** Percentage difference between projected and unprocessed data.

Acknowledging this as a limitation of the motion tracked data at hand, an additional processing step was introduced to ensure physiological outcomes. As assuming a potential compressibility degree would be arbitrary, the processed data were instead assumed to be incompressible. Specifically, the motion tracked deformation field was modified to ensure that wall volumes were kept constant throughout the cycle and equal to the wall volume at end diastole. In order to ensure a close match to the original data, at each time-step the processed deformation field ($\boldsymbol{u}_p$) was obtained through an H^1 projection of the original tracking data ($\boldsymbol{u}_d$) on the space of incompressible deformations. In this process, the endocardial boundary was kept weakly the same, ensuring that important metrics such as stroke volume and ejection fraction were maintained, and a relaxed boundary condition was introduced on the base boundary (see section 5.3.3.2). The

volume-preserving deformation field $\boldsymbol{u}_p$ was obtained by the solution of the following saddle-point problem:

$$\Pi(\boldsymbol{u}_p, \lambda, \boldsymbol{\lambda}_\ell, \boldsymbol{\lambda}_b) = \inf_{\boldsymbol{v} \in \boldsymbol{U}} \sup_{q \in W} \sup_{\boldsymbol{\mu}_\ell \in \gamma_\ell \boldsymbol{U}} \sup_{\boldsymbol{\mu}_b \in \gamma_b \boldsymbol{U}} \Pi(\boldsymbol{v}, q, \boldsymbol{\mu}_\ell, \boldsymbol{\mu}_b), \quad (5.1)$$

where subscripts ℓ and b refer to the lumen and basal boundaries. The boundary conditions are enforced through Lagrange multipliers $\boldsymbol{\lambda}_\ell$ and $\boldsymbol{\lambda}_b$, as discussed in section 5.3.3.2. The volume constraint is enforced through Lagrange multiplier λ as described in 3.10. Moreover, displacement and multipliers solutions are sought in function spaces $\boldsymbol{U}$, W, $\gamma_\ell \boldsymbol{U}$ and $\gamma_b \boldsymbol{U}$, introduced in section 5.3.3.2. The functional Π at any point in time is given by:

$$\Pi(\boldsymbol{u}_p, \lambda, \boldsymbol{\lambda}_\ell, \boldsymbol{\lambda}_b) = \int_{\Omega_{ED}} |\boldsymbol{u}_p - \boldsymbol{u}_d|^2 + \alpha |\nabla(\boldsymbol{u}_p - \boldsymbol{u}_d)|^2 dV + \int_{\Gamma_{ED}^\ell} \boldsymbol{\lambda}_\ell \cdot (\boldsymbol{u}_p - \boldsymbol{u}_d) \, dA$$
$$+ \int_{\Gamma_{ED}^b} \boldsymbol{\lambda}_b \cdot \left(\boldsymbol{u}_p - \boldsymbol{u}_d - \frac{1}{2}\epsilon_b \boldsymbol{\lambda}_b\right) dA + \int_{\Omega_{ED}} \lambda(J_p - 1) \, dV.$$
$$(5.2)$$

The first integral term deals with the data projection, and $\alpha = 100$ was selected to provide equal weighting between the L^2 norm and H^1 semi-norm terms. The second and third terms are enforcing the original data motion on endocardial and basal boundaries, respectively. The final term is enforcing the incompressible deformation, where J_p is the determinant of the deformation gradient related to the projected displacement $\boldsymbol{u}_p$. Here, Ω_{ED} is the myocardial wall domain at end diastole, and Γ_{ED}^ℓ and Γ_{ED}^b denote the endocardial and basal boundary domains at end diastole, respectively. Details on the boundary condition terms can be found in section 5.3.3.2.

The resulting deformed meshes (referred to as data in the following sections) were used as the main data source for the remaining steps of model development. Fig. 5.7b illustrates the difference between the data before and after processing, computed as $\frac{||\boldsymbol{u}_p - \boldsymbol{u}_d||}{u_d^{max}}$, where $u_d^{max} = ||\boldsymbol{u}_d||_{L^\infty(I, L^2(\Omega_{ED}))}$ is the maximum data-derived displacement over the cardiac cycle. The relatively large difference (20%) is indicative of the error that could be anticipated if the unprocessed (non volume-preserving) data where used in the personalisation of incompressible models.

5.3 Personalised models

5.3.1 Reference geometry

The reference geometry is a significant component of mechanics models, yet a non-trivial process for patient-specific cardiac models. As no undeformed, unstressed state

is encountered during the cardiac cycle, the reference geometry needs to be either assumed or computed by solving an inverse problem. Estimating the reference geometry, however, is a challenging task, as it is inherently dependent on the constitutive law chosen as well as the unknown passive parameters, which in turn require the reference geometry in order to be estimated. Furthermore, the inverse approach must also deal with boundary conditions uncertainties. This approach was therefore not attempted in this work, but instead the reference configuration was assumed to be known and corresponded to a specific data frame. This is a common approach also used in other studies, for example by Wang et al[266], Gao *et al.*[73] and Xi et al[276].

In this study, the end-systolic frame of the data was chosen as the reference configuration. Using the cavity volume trace from the tagged MRI motion tracking, the end-systolic frame was chosen as the point of minimal cavity volume (red circle in Fig. 5.8a). The effect of assuming the specific data frame as the reference domain on parameter identifiability, parameter estimates and model fidelity is discussed in section 6.3.

(a)   **(b)**   **(c)**
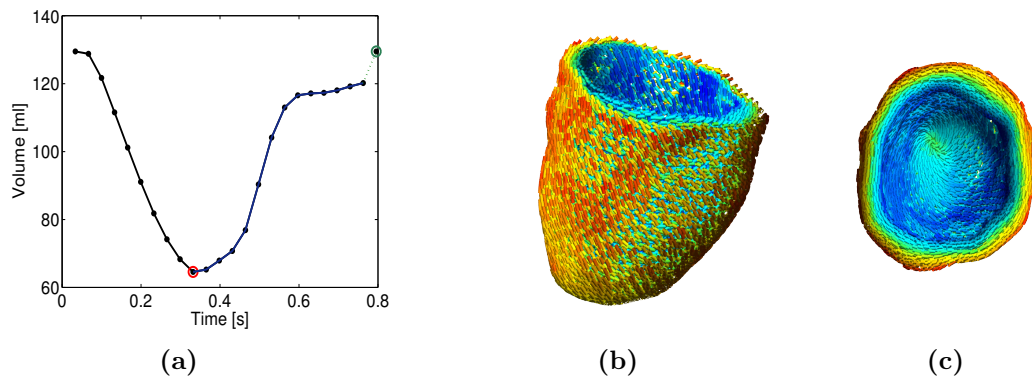
Figure 5.8 (a) Cavity volume over a cardiac cycle, starting at end diastole. The end-diastolic frame is added after the last frame to complete the cycle (green circle), as the atrial kick is often missing in 3D tagged MRI. The red circle denotes the end-systolic frame, used as the reference geometry. Blue curve denotes the frames through the cycle identified as diastolic **(b)** Long-axis and **(c)** short-axis view of the reference geometry at end systole. Streamlines through the fibre field in the model left ventricle are presented, where colour indicates fibre angle, ranging from red $(-60°)$ to blue $(60°)$.

5.3.1.1   Fibre distribution

Due to the absence of DTI data on the fibre architecture of each participant's heart, a rule-based fibre distribution was applied for all cases. As described in section 2.4.2, a fibre coordinate system needs to be defined to allow for the employment of fibre-dependent constitutive laws. Therefore, the fibre, sheet and sheet-normal directions were defined throughout the myocardial wall and were interpolated using linear piecewise discontinuous elements. The fibre distribution was created by first determining

the long-axis direction and defining a trasmular coordinate, varying between 0 on the endocardial boundary and 1 on the epicardial boundary. At each transmural position, the fibre angle was then obtained as a function of the transmural coordinate and the maximum angle magnitude, which was prescribed. The fibre direction at each point, was then determined as the tangent vector to the surface that formed an angle of the prescribed magnitude with the long-axis.

The fibre direction was assumed to vary linearly transmurally, with an angle of $60° \rightarrow -60°$ from endocardium to epicardium (Fig. 5.8b and 5.8c). Although this is the default distribution usually employed for heart mechanics models, other distributions were also considered (sections 6.1 and 6.1.3).

5.3.2 Cardiac mechanics model

In the patient-specific models under consideration, the myocardial tissue was modelled as a hyperelastic incompressible material. The incompressibility assumption was employed in accordance with several experimental and modelling studies as discussed in section 1.3.1.4. The Lagrange multiplier approach presented in Eq. 3.10 was employed. This was mainly to avoid the estimation of the penalty parameter which is present in the PL and weakly penalised formulations introduced in chapter 3, which would require an estimate of wall volume change through the cycle. As mentioned before, this kind of information could not be accurately retrieved from the available data. Further, the problems solved were not large enough to gain significant benefit by the use of the displacement-only weakly penalised approach.

The mechanics of the personalised models considered were solved using the principle of stationary potential energy, where the deformation and Lagrange multipliers solutions were found as the critical point of the elastic potential energy of the body. Following the potential energy functional in section 2.5, the potential energy Π of the myocardium can be expressed as a sum of its internal and external energy, $\Pi = \Pi_{int} + \Pi_{ext}$.

The internal energy of the myocardium is given as a function of the hyperelastic deviatoric strain energy modelling the passive constitutive behaviour. The reduced Holzapfel-Ogden law (Eq. 4.5) was chosen to model the passive myocardium in the personalised models considered. This choice was dictated by one of the basic aims of this project, namely accurate parameter estimation, which would enable reliable comparisons and conclusions about DCM. Obtaining reliable parameter estimates is dependent both on the identifiability characteristics of the constitutive law, as well as on its ability to accurately represent the available data. Based on the *in silico* tests presented in sections 4.2.1 - 4.2.3, the reduced Holzapfel-Ogden law combines good identifiability characteristics with the ability to adequately capture passive heart function. This model was identified as a suitable choice for patient-specific applications

where the main observation source is 3D tagged MRI, and was therefore employed in the *in vivo* models presented.

The external potential energy is comprised of the sum of external boundary-based energies. Boundary conditions are commonly applied on the endocardial, epicardial and basal boundaries of the mesh. Boundary conditions are introduced through the use of Lagrange multipliers resulting in the following form for the external energy,

$$\Pi_{ext}(\boldsymbol{u}, \boldsymbol{\lambda}) = \sum_{k \in (b, \ell, e)} \Pi_{ext}^{k}(\boldsymbol{u}, \boldsymbol{\lambda}_k), \tag{5.3}$$

where $\boldsymbol{\lambda}_k$ denote the Lagrange multipliers introduced on the base (b), lumen or endocardial (ℓ) and epicardial (e) boundaries. Each boundary condition will be discussed in detail in the following sections.

5.3.3 Personalised boundary conditions

5.3.3.1 Volume-driven simulation

A common approach in cardiac mechanics models is to drive diastolic simulations using cavity pressure, which is considered to dominate all other forces exerted on the endocardial boundary (for example due to papillary muscles tension). Assuming a homogeneous distribution for the cavity blood pressure P_{lv}, the diastolic filling is driven by prescribing pressure as a surface traction on the endocardial boundary, *i.e.*

$$\Pi_{ext}^{\ell}(\boldsymbol{u}) = -P_{lv} \int_{\Gamma_\ell} \boldsymbol{u} \cdot \boldsymbol{n} \, da, \tag{5.4}$$

where Γ_ℓ denotes the endocardial boundary in the deformed domain and $\boldsymbol{n}$ is the deformed normal unit vector. This boundary condition has been used extensively in cardiac mechanics models[278,266,47], owing to its straightforward nature. However, this constraint relies on knowledge of the pressure through diastole, and thus requires invasive measurements.

On the contrary, cavity volumes can be easily extracted from routinely acquired images, providing a non-invasive means of driving simulations. To this end, in this work diastolic simulations were driven by cavity volumes extracted directly from imaging data. Specifically, the cavity volume trace computed from the extracted tagged MRI motion, was used to inflate end-systolic meshes to the measured end-diastolic volume. This can be achieved by ensuring that the lumen volume matches the data-derived cavity volume at every time step, using a Lagrange multiplier-based boundary condition on

the endocardial surface, *i.e.*

$$\Pi^{\ell}_{ext}(\boldsymbol{u}, \lambda_{\ell}) = \lambda_{\ell}\big(V(\boldsymbol{u}) - V_{lv}\big), \tag{5.5}$$

where the Lagrange multiplier $\lambda_{\ell} \in \mathbb{R}$ is identified as the cavity pressure required to inflate the LV to the desired volume. Here $V(\boldsymbol{u})$ is the mesh cavity volume and V_{lv} is the cavity volume computed from the data. In order to avoid the construction of a cavity mesh, the cavity volume $V(\boldsymbol{u})$ can be conveniently calculated on the endocardial boundary of the LV mesh using Gauss theorem and choosing a function $\boldsymbol{f}$ such that its divergence is 1 on the LV cavity domain Ω_{lv}. Specifically,

$$V(\boldsymbol{u}) = \int_{\Omega_{lv}} 1 \, dv = \int_{\Omega_{lv}} \nabla \cdot \boldsymbol{f} \, dv = \int_{\Gamma_{lv}} \boldsymbol{f} \cdot \boldsymbol{n} \, da, \tag{5.6}$$

where $\Gamma_{lv} = \Gamma_{\ell} \cup \Gamma_t$ is the boundary of the cavity in the deformed domain (Γ_t is the cavity top) and $\boldsymbol{n}$ is the normal vector. A typical choice for the function $\boldsymbol{f}$ is $\boldsymbol{f} = \frac{\boldsymbol{x}}{3}$, leading to the following form for the volume calculation:

$$V(\boldsymbol{u}) = \frac{1}{3} \left(\int_{\Gamma_{\ell}} \boldsymbol{x} \cdot \boldsymbol{n} \, da + \int_{\Gamma_t} \boldsymbol{x} \cdot \boldsymbol{n}_b \, da \right), \tag{5.7}$$

where $\boldsymbol{n}_b$ is the normal vector to the base plane. A difficulty, however, arises from the fact that the top of the cavity Γ_t is not part of the LV mesh. The related integral term is often neglected, assuming that the base motion is comparatively small. This effect can also be reduced by re-orienting the base plane with the $z = 0$ plane and aligning the normal vector with $z-$ unit vector. This formulation, however, is likely to introduce significant error in the volume computation in case of substantial base motion. Moreover, simulations using this formulation require re-orientation of the mesh and additional mapping of the displacements which are incorporated through boundary conditions.

An alternative approach is to constraint the rate of change of volume instead to match the data-derived rate of volume change $\frac{\partial V_{lv}}{\partial t}$. In order to derive an expression for the rate of change of volume, it is convenient to consider a mapping $\phi : \Omega_0^{lv} \to \Omega_{lv}$, between the reference and deformed cavity domains. The mapping is required to satisfy:

$$\phi(\boldsymbol{X}) = \boldsymbol{u}(\boldsymbol{X}) + \boldsymbol{X}, \quad \forall \boldsymbol{X} \in \Gamma_0^{\ell}, \tag{5.8}$$

maintaining the motion of the mesh on the endocardial boundary, and J_{ϕ} corresponds to the Jacobian of this mapping. The rate of change of volume is then computed using

the space conservation law ($\frac{\partial J_\phi}{\partial t} = J_\phi \nabla \cdot \frac{\partial \boldsymbol{u}}{\partial t}$), as

$$
\begin{aligned}
\frac{\partial V}{\partial t} =& \frac{\partial}{\partial t} \int_{\Omega_{lv}} dv = \frac{\partial}{\partial t} \int_{\Omega_0^{lv}} J_\phi \ dV = \int_{\Omega_0^{lv}} J_\phi \nabla \cdot \frac{\partial \boldsymbol{u}}{\partial t} \ dV = \int_{\Omega_{lv}} \nabla \cdot \frac{\partial \boldsymbol{u}}{\partial t} \ dv = \\
& \int_{\Gamma_\ell} \frac{\partial \boldsymbol{u}}{\partial t} \cdot \boldsymbol{n} \ da + \int_{\Gamma_t} \frac{\partial \boldsymbol{u}_b}{\partial t} \cdot \boldsymbol{n}_b \ da,
\end{aligned}
\tag{5.9}
$$

where $\frac{\partial \boldsymbol{u}_b}{\partial t}$ denotes the velocity of the base plane and Ω_0^{lv} is the reference cavity domain. Similarly to the previous approach, the base motion is typically considered small so the base plane velocity is assumed to be zero.

The endocardial boundary energy can in this case be expressed as

$$
\Pi_{ext}^\ell(\boldsymbol{u}, \lambda_\ell) = \lambda_\ell \left(\int_{\Gamma_\ell} \frac{\partial \boldsymbol{u}}{\partial t} \cdot \boldsymbol{n} \ da - \frac{\partial V_{lv}}{\partial t} \right),
\tag{5.10}
$$

at every time step through the cycle.

The introduced volume calculation techniques in Eq. 5.7 and 5.10 are accurate and used equivalently for problems with negligible base motion. However, as will be shown in subsequent sections, they are bound to introduce a bias in patient-specific applications where the base plane moves significantly throughout the cardiac cycle, leading to an over-estimation of the enforced volume during diastole. In order to account for the substantial base motion, the function $\boldsymbol{f}$ can instead be selected so that long axis motion of the base plane is properly incorporated following Asner *et al*[9]. The choice

$$
\boldsymbol{f} = \boldsymbol{I}_b \boldsymbol{x}, \quad \boldsymbol{I}_b = \frac{1}{2} (\boldsymbol{I} - \boldsymbol{n}_b \otimes \boldsymbol{n}_b),
\tag{5.11}
$$

where $\boldsymbol{n}_b$ is the normal vector to the base plane, ensures that

$$
\int_{\Gamma_t} \boldsymbol{f} \cdot \boldsymbol{n}_b \ da = 0.
\tag{5.12}
$$

The cavity volume can now be accurately calculated on the endocardial boundary Γ_ℓ as:

$$
V(\boldsymbol{u}) = \int_{\Gamma_\ell} \boldsymbol{I}_b \boldsymbol{x} \cdot \boldsymbol{n} \ da.
\tag{5.13}
$$

5.3.3.1.1 Accuracy of endocardial boundary conditions

Section 5.3.3.1 presented different approaches for driving simulations with data-derived cavity volumes. To facilitate the selection of an appropriate method, the considered techniques were compared in terms of their accuracy against the gold standard pressure-inflation approach, which has been employed extensively in cardiac mechanics.

Specifically, the following boundary conditions were compared:

- Pressure inflation (**PI**): The LV cavity is inflated to an end-diastolic pressure by setting the endocardial traction equal to the intraventricular pressure applied in the normal to the surface direction, as described in Eq. 5.4.

- Simplified volume inflation (**SVI**): The LV is inflated to an end-diastolic volume by prescribing the cavity volume, as presented in Eq. 5.7. This boundary condition assumes that the base motion has a negligible effect on the volume and requires the base plane to be aligned with the $z = 0$ plane.

- Volume rate inflation (**VRI**): The cavity is inflated by prescribing the rate of change of volume as presented in Eq. 5.10. This approach also assumes negligible effect of the base motion on the volume calculation.

- Volume inflation (**VI**): The LV is inflated by prescribing the cavity volume, as described in Eq. 5.13. This boundary condition is constructed such that the volume calculation accounts for the base motion.
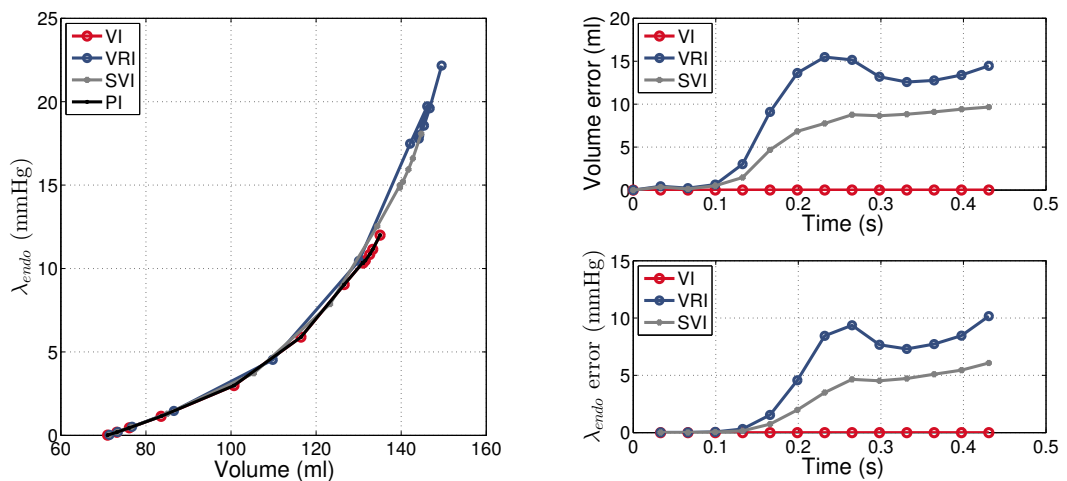
Figure 5.9 Comparison of the endocardial boundary conditions in an *in vivo* case. **(a)** Pressure-volume plots of the simplified volume inflation (SVI), volume rate inflation (VRI), volume inflation (VI) and pressure inflation (PI) simulations. **(b)** Error between data-derived volume and volume of the SVI, VRI and VI simulations over time. **(c)** Error in pressure between ground truth PI values and the SVI, VRI and VI simulations' λ_ℓ over time.

These methods were employed on diastolic filling simulations of a personalised mesh. For their comparison, both cavity volume and pressure traces were assumed to be known throughout the cycle. The base motion was prescribed directly from the extracted myocardial deformation as a Dirichlet boundary condition. For each simulation the volume of the inflated ventricular cavity was computed, while the Lagrange multiplier λ_ℓ provided the intraventricular pressure. The accuracy of the SVI, VRI and VI boundary conditions was assessed by comparing their volume and pressure outcomes, with the ground truth results of the pressure inflation (PI) case.

The application of the techniques under consideration in diastolic simulations drew interesting conclusions concerning their accuracy as volume constraints, but also their effect on intraventricular pressures (Fig. 5.9). Clearly, the base motion has a significant effect on the cavity volume computation, leading the SVI and VRI boundary conditions – which consider this effect to be negligible – to large volume errors (maximum percentage error 7.2% and 12.2%, respectively). The approaches consistently overestimate volumes as the base plane tends to move away from the apex and elongate during diastole. Interestingly, this bias is also propagated in the intraventricular pressure, with even more pronounced errors (errors of the order of magnitude of ground truth values). Both volume and pressure errors might in turn cause significant errors in parameter estimates, when used in personalised applications.

Nevertheless, the VI approach presents equivalent results with the gold standard PI method, with errors less than $10^{-4}\%$ in both volume and pressure (errors are not 0 due to the tolerances set). Due to its accurate incorporation of base motion, the VI volume computation technique leads to accurate volume and pressure outcomes, and was therefore selected for the considered patient-specific cardiac models.

5.3.3.2 Basal boundary condition

Due to the truncation of the myocardial model at the base plane, a boundary condition on the basal boundary was essential to allow for physiological motion and outcome of the LV models. In order to optimise model fidelity, motion of the base plane was prescribed directly from the data. As will be discussed in chapter 6, strict enforcement of displacements through Dirichlet boundary conditions is known to cause pressure and stress peaks. Therefore, a different approach was employed following Asner *et al*[9], where the basal boundary energy is expressed as

$$\Pi_{ext}^b(\boldsymbol{u}, \boldsymbol{\lambda}_b) = \int_{\Gamma_0^b} \boldsymbol{\lambda}_b \cdot \left(\boldsymbol{u} - \boldsymbol{u}_d - \frac{1}{2}\boldsymbol{K}_b\boldsymbol{\lambda}_b\right) dA. \tag{5.14}$$

Here $\boldsymbol{u}_d$ is the data-extracted displacement, Γ_0^b is the reference basal boundary domain and $\boldsymbol{\lambda}_b \in \gamma_b\boldsymbol{U}$ is an introduced Lagrange multiplier on the base boundary ($\gamma_b\boldsymbol{U}$ is the trace space of $\boldsymbol{U}$ on Γ_0^b). In this formulation, $\boldsymbol{K}_b$ is a relaxation matrix, defined as

$$\boldsymbol{K}_b = \epsilon_b(\boldsymbol{I} - \boldsymbol{n}_b \otimes \boldsymbol{n}_b). \tag{5.15}$$

The relaxation matrix $\boldsymbol{K}_b$ ensures that displacements in the long-axis direction are exact, while it allows relaxed enforcement of the short-axis motion. The important benefit of this approach is that it allows us to regulate the degree of adherence of the model to the data, based on how accurate we consider the data we are prescribing to be. For instance, in the case of noisy data, artefacts in the model such as non-physiological

motion, pressures or stresses can be reduced by selecting a large value for the parameter ϵ_b (*e.g.* $\epsilon_b = 10^{-4}$). A relaxed adherence to the data also improves convergence of simulations, as preliminary tests requiring strict adherence to data suffering from tracking errors, caused simulations to fail. Likewise, in the case of high quality data where strict adherence to the data would be desirable, small ϵ_b can be selected, e.g. $\epsilon_b = 10^{-10}$.

In practice, a relaxation parameter $\epsilon_b \sim 10^{-7}$ enables sufficient model fidelity, while avoiding non-physiological motion, as will be illustrated and discussed in section 6.2.1.

5.3.3.3 Epicardial boundary condition

In preliminary tests, the external energy at the epicardial energy was set to zero, *i.e.* $\Pi_{ext}^e = 0$. This is a common practice in cardiac patient-specific applications, stemming from the simplifying assumption that the epicardial boundary energy is negligible compared to the endocardial energy which provides the main driving force for the simulations. Furthermore, lack of experimental results leads to uncertainties as to the forces acting on the epicardial boundary of the LV.

However, preliminary tests using a zero-traction condition on the epicardial boundary, exhibited significant errors between models and data. Naturally, as the LV is not isolated, surrounding tissues and organs – mainly the pericardium, the diaphragm and the RV – are bound to have an influence on the external energy of the epicardial boundary. The RV in particular must exert a substantial force on the septal wall of the LV, due to stresses concentrated at the region of attachment to the RV wall. Further, typical RV diastolic cavity pressures of the order of magnitude of their LV counterpart are expected to have a significant effect on the entire LV.

To account for the influence of the stresses due to RV attachment, a different boundary condition was enforced on the epicardium. Introducing a Lagrange multiplier on the epicardial boundary and following the relaxation approach used for the basal boundary (section 5.3.3.2), the region of attachment to the RV was set to deform following the data. The region of attachment to the RV was initially defined using an ITK-SNAP segmentation. The segmentation was then used to create a spatial field H on the personalised mesh, varying smoothly between 0 and 1, marking the RV attachment points (1). The following form was used for the epicardial boundary energy,

$$\Pi_{ext}^e(\boldsymbol{u}, \boldsymbol{\lambda}_e) = \int_{\Gamma_0^e} \boldsymbol{\lambda}_e \cdot \left((\boldsymbol{u} - \boldsymbol{u}_d)H - \frac{1}{2}\epsilon_e \boldsymbol{\lambda}_e \right) \, dA, \tag{5.16}$$

where Γ_0^e is the undeformed epicardial boundary domain, $\boldsymbol{u}_d$ is the data displacement and $\boldsymbol{\lambda}_e \in \gamma_e \boldsymbol{U}$ is the introduced Lagrange multiplier on the epicardial boundary ($\gamma_e \boldsymbol{U}$

denotes the trace space of $\boldsymbol{U}$ on Γ_0^e). The relaxation parameter ϵ_e regulates the level of adherence to the data, allowing either strict adherence for high quality data or weak adherence for noisy or low resolution data. For the data at hand, a relaxation parameter of $\epsilon_e = 5 \times 10^{-6}$ was shown to improve model fidelity without over-constraining the model and causing deterioration of parameter identifiability (section 6.2.2). As will be discussed in following chapters (sections 6.1, 6.1.2), the use of the RV-epicardial condition results in substantial reductions in model error.

5.3.4 Numerical solution

5.3.4.1 Weak form of cardiac mechanics models

Taking into account the mechanics and boundary conditions described in sections 5.3.2-5.3.3.3, the state variables introduced can be obtained through the solution of the saddle-point problem,

$$\Pi(\boldsymbol{u}, p, \lambda_\ell, \boldsymbol{\lambda}_b, \boldsymbol{\lambda}_e) = \inf_{\boldsymbol{v} \in \boldsymbol{U}} \sup_{\lambda \in W} \sup_{\mu_\ell \in \mathbb{R}} \sup_{\boldsymbol{\mu}_b \in \gamma_b \boldsymbol{U}} \sup_{\boldsymbol{\mu}_e \in \gamma_e \boldsymbol{U}} \Pi(\boldsymbol{v}, \lambda, \mu_\ell, \boldsymbol{\mu}_b, \boldsymbol{\mu}_e), \tag{5.17}$$

where the total potential energy Π can now be written as a sum of the internal energy and the individual external boundary energies:

$$\begin{aligned}
\Pi(\boldsymbol{u}, p, \lambda_\ell, \boldsymbol{\lambda}_b, \boldsymbol{\lambda}_e) = &\int_{\Omega_0} \Psi_d(\boldsymbol{u}) + p(J-1) \, dV + \lambda_\ell \left(\int_{\Gamma_\ell} \boldsymbol{I}_b \boldsymbol{x} \cdot \boldsymbol{n} \, da - V_{lv} \right) \\
&+ \int_{\Gamma_0^b} \boldsymbol{\lambda}_b \cdot \left(\boldsymbol{u} - \boldsymbol{u}_d - \frac{1}{2} \boldsymbol{K}_b \boldsymbol{\lambda}_b \right) dA + \int_{\Gamma_0^e} \boldsymbol{\lambda}_e \cdot \left((\boldsymbol{u} - \boldsymbol{u}_d) H - \frac{1}{2} \epsilon_e \boldsymbol{\lambda}_e \right) dA
\end{aligned} \tag{5.18}$$

The weak form of this formulation can then be derived by taking the directional derivatives with respect to the state variables $\boldsymbol{u}$, p, λ_ℓ, $\boldsymbol{\lambda}_b$ and $\boldsymbol{\lambda}_e$, leading to the following form for the saddle-point problem:

$$\begin{aligned}
D_{\boldsymbol{u}}\Pi[\delta\boldsymbol{u}] + D_p\Pi[\delta p] + D_{\lambda_\ell}\Pi[\delta\lambda_\ell] + D_{\boldsymbol{\lambda}_b}\Pi[\delta\boldsymbol{\lambda}_b] + D_{\boldsymbol{\lambda}_e}\Pi[\delta\boldsymbol{\lambda}_e] = 0, \\
\forall (\delta\boldsymbol{u}, \delta p, \delta\lambda_\ell, \delta\boldsymbol{\lambda}_b, \delta\boldsymbol{\lambda}_e) \in (\boldsymbol{U}, W, \mathbb{R}, \gamma_b\boldsymbol{U}, \gamma_e\boldsymbol{U}).
\end{aligned} \tag{5.19}$$

Briefly,

$$
\begin{aligned}
D_{\boldsymbol{u}}\Pi[\delta\boldsymbol{u}] = &\int_{\Omega_0}(\boldsymbol{P}+pJ\boldsymbol{F}^{-T}):\nabla_{\boldsymbol{X}}\delta\boldsymbol{u}\ dV + \int_{\Gamma_0^b}\boldsymbol{\lambda}_b\cdot\delta\boldsymbol{u}\ dA + \int_{\Gamma_0^e}H\boldsymbol{\lambda}_e\cdot\delta\boldsymbol{u}\ dA \\
&+\lambda_\ell\int_{\Gamma_\ell}\delta\boldsymbol{u}\cdot\boldsymbol{n}\ da \\
D_p\Pi_{int}[\delta p] = &\int_{\Omega_0}\delta p(J-1)\ dV, \\
D_{\lambda_\ell}\Pi_{ext}^\ell[\delta\lambda_\ell] = &\delta\lambda_\ell\left(\int_{\Gamma_\ell}\boldsymbol{I}_b\boldsymbol{x}\cdot\boldsymbol{n}\ da - V_{lv}\right), \\
D_{\boldsymbol{\lambda}_b}\Pi_{ext}^b[\delta\boldsymbol{\lambda}_b] = &\int_{\Gamma_0^b}\delta\boldsymbol{\lambda}_b\cdot\left(\boldsymbol{u}-\boldsymbol{u}_d-\boldsymbol{K}_b\boldsymbol{\lambda}_b\right)\ dA, \\
D_{\boldsymbol{\lambda}_e}\Pi_{ext}^e[\delta\boldsymbol{\lambda}_e] = &\int_{\Gamma_0^e}\delta\boldsymbol{\lambda}_e\cdot\left((\boldsymbol{u}-\boldsymbol{u}_d)H-\epsilon_e\boldsymbol{\lambda}_e\right)\ dA,
\end{aligned}
\tag{5.20}
$$

where the contribution of $D_{\boldsymbol{u}}\Pi_{ext}^\ell[\delta\boldsymbol{u}]$ can be expressed using the definition of the endocardial energy in Eq. 5.5, as follows:

$$
\begin{aligned}
D_{\boldsymbol{u}}\Pi_{ext}^\ell[\delta\boldsymbol{u}] = &\lambda_\ell D_{\boldsymbol{u}}V(\boldsymbol{u})[\delta\boldsymbol{u}] = \lambda_\ell D_{\boldsymbol{u}}\int_{\Omega_0^{lv}}J_\phi\ dV[\delta\boldsymbol{u}] = \\
&\lambda_\ell\int_{\Omega_0^{lv}}D_{\boldsymbol{u}}J_\phi[\delta\boldsymbol{u}]\ dV = \lambda_\ell\int_{\Omega_0^{lv}}J_\phi\nabla\cdot\left[D_{\boldsymbol{u}}\phi[\delta\boldsymbol{u}]\right]\ dV = \\
&\lambda_\ell\int_{\Omega_{lv}}\nabla\cdot\left[D_{\boldsymbol{u}}\phi[\delta\boldsymbol{u}]\right]\ dv = \lambda_\ell\int_{\Omega_{lv}}\nabla\cdot\delta\boldsymbol{u}\ dv = \\
&\lambda_\ell\left(\int_{\Gamma_\ell}\delta\boldsymbol{u}\cdot\boldsymbol{n}\ da + \int_{\Gamma_t}\delta\boldsymbol{u}\cdot\boldsymbol{n}_b\ da\right) = \lambda_\ell\int_{\Gamma_\ell}\delta\boldsymbol{u}\cdot\boldsymbol{n}\ da,
\end{aligned}
\tag{5.21}
$$

where ϕ is the mapping between reference and deformed cavity domains, introduced in Eq. 5.8. Here, $\delta\boldsymbol{u}\cdot\boldsymbol{n}_b = 0$, due to implicit Dirichlet conditions in the normal to base direction. Additionally, the directional derivative of J_ϕ with respect to $\boldsymbol{u}$ was used ($D_{\boldsymbol{u}}J_\phi[\delta\boldsymbol{u}] = J_\phi\boldsymbol{F}_\phi^{-T}:\nabla_{\boldsymbol{X}}\delta\boldsymbol{u} = J_\phi\nabla\cdot\delta\boldsymbol{u}$[21]).

The weak formulation of the system can then be written as:

$$
\begin{aligned}
&\int_{\Omega_0}(\boldsymbol{P}+pJ\boldsymbol{F}^{-T}):\nabla_{\boldsymbol{X}}\delta\boldsymbol{u}+\delta p(J-1)\ dV + \lambda_\ell\int_{\Gamma_\ell}\delta\boldsymbol{u}\cdot\boldsymbol{n}\ da \\
&+\delta\lambda_\ell\left(\int_{\Gamma_\ell}\boldsymbol{I}_b\boldsymbol{x}\cdot\boldsymbol{n}\ da - V_{lv}\right) + \int_{\Gamma_0^b}\boldsymbol{\lambda}_b\cdot\delta\boldsymbol{u}+\delta\boldsymbol{\lambda}_b\cdot\left(\boldsymbol{u}-\boldsymbol{u}_d-\boldsymbol{K}_b\boldsymbol{\lambda}_b\right)\ dA \\
&+\int_{\Gamma_0^e}H\boldsymbol{\lambda}_e\cdot\delta\boldsymbol{u}+\delta\boldsymbol{\lambda}_e\cdot\left((\boldsymbol{u}-\boldsymbol{u}_d)H-\epsilon_e\boldsymbol{\lambda}_e\right)\ dA = 0 \\
&\forall(\delta\boldsymbol{u},\delta p,\delta\lambda_\ell,\delta\boldsymbol{\lambda}_b,\delta\boldsymbol{\lambda}_e)\in(\boldsymbol{U},W,\mathbb{R},\gamma_b\boldsymbol{U},\gamma_e\boldsymbol{U}).
\end{aligned}
\tag{5.22}
$$

5.3.4.2 Finite element solution of personalised models

The solution to this weak formulation was approximated using the finite element method. Specifically, in all personalised models considered in this thesis, a quadratic-linear interpolation scheme was employed for the displacement and pressure variables (quadratic and linear tetrahedral elements, respectively). The base and epicardial multipliers ($\boldsymbol{\lambda}_b$ and $\boldsymbol{\lambda}_e$) were approximated with quadratic triangular elements, and the endocardial multiplier was a scalar.

Basic characteristics of the meshes used for each case are presented in table 5.1, while Fig. 5.10 presents the distribution of mesh size over a representative mesh. Considering that tetrahedral meshes require a refined discretisation compared to hexahedral meshes to achieve similar levels of accuracy[15], the number of elements used in each discretisation (12148 in average) was sufficiently large when compared with convergence analysis results in Asner *et al.* on hexahedral meshes[9].
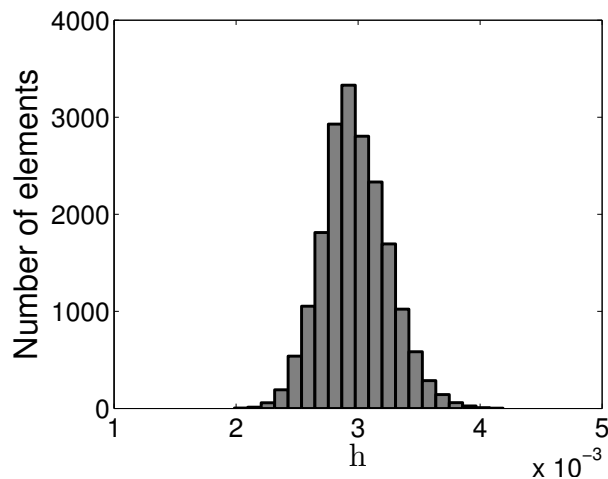
Figure 5.10 Histogram of a typical mesh used for personalised simulations. The mesh size, given in meters, was computed as $h = \det(\boldsymbol{F})^{1/3}$, $\boldsymbol{F}$ being the mapping between elements in mesh and the unit master element.

Moreover, the typical mesh size used was sufficiently small to allow for accurate parameter estimation. Asner *et al.* examined parameter error between a coarse hexahedral mesh and two uniform refinements of it ($h = 12$mm, $h = 6$mm, $h = 3$mm, respectively) and reported less than 2% parameter error between the two finer discretisations[9]. The typical mesh size used within the personalised simulations presented in this chapter ($h = 3.7$mm) was closer to the finest discretisation, suggesting that the meshes are of adequate resolution to enable reliable parameter estimation. Additionally, the typical mesh size used for the personalised models enabled the large number of simulations required to provide a characterisation of parameter identifiability (see section 6.1).

All the patient-specific simulations were carried out using $\mathcal{C}$**Heart** (section 2.7), on

Personalised meshes								
Case	**V1**	**V2**	**V3**	**V4**	**V5**	**P1**	**P2**	**P3**
Elements	17153	18896	8038	6787	7795	10740	17047	10731
LNodes	4048	4375	2327	2050	2088	2747	4173	2986
QNodes	27589	30068	14580	12657	13499	18104	28012	19025
h **(mm)**	3.33	2.98	4.43	3.88	4.34	3.90	3.47	3.45
STD(h) (mm)	0.53	0.27	1.09	0.82	0.34	0.56	0.53	0.67

Table 5.1 Basic characteristics of the personalised meshes used. Elements: number of elements, LNodes: number of linear nodes, QNodes: number of quadratic nodes, h: mesh size in mm, STD(h): standard deviation of mesh size in mm.

a quad-core (Intel® 4th Generation Core™ i7-4790 CPU @ 3.60GHz), on an 2.1GHz AMD Opteron™ Interlagos 32 processor and on an SGI with 640 2.67GHz processors (Intel® Xeon® CPU E7- 8837). The error tolerance for all simulations was set to 1×10^{-9}.

Computational time per diastolic simulation varied notably depending on the case, number of diastolic frames, mesh size and passive parameter values. Nevertheless, the average computational time per simulation on 8 processors, was under 20 minutes.

5.4 Passive parameter estimation

The next essential step in the model personalisation process is the estimation of passive parameters. The objective is to obtain the parameter set (a, a_f) of the reduced Holzapfel-Ogden law (Eq. 4.5) that produces the best match between the model and the available data. In this work, the main data-source used in the estimation process was 3D tagged MRI, as they provide a detailed 3D deformation field, creating an ideal setting for parameter estimation.

The estimation of passive parameters was performed through minimisation of the objective function $\mathcal{J}$, a metric of error between model-predicted and data-derived displacements. The objective function introduced for the *in silico* tests in Eq. 4.10 was employed, based on the $L^2(\Omega_0)$ norm of the error through time,

$$\mathcal{J} = \left(\frac{\sum_{n=1}^{N+1} ||\boldsymbol{u}_n - \boldsymbol{u}_n^d||^2}{\sum_{n=1}^{N+1} ||\boldsymbol{u}_n^d||^2} \right)^{1/2}, \tag{5.23}$$

where N is the number of diastolic frames identified in the available 3D tagged MRI data (e.g. where the cavity volume is increasing). As tagged MRI data does not cover the whole cycle, the end-diastolic mesh created from cine segmentation was included in the diastolic observations (frame $N + 1$) enriching the observation space.

In volume-driven simulations, estimation of both a and a_f parameters is not possible using displacement observations only. This is due to the linear nature of the reduced Holzapfel-Ogden model, employed as the constitutive law. Specifically, due to the linear parameter dependence, scaling of the passive parameters leads to the same scaling in cavity pressure λ_ℓ (and other multipliers), without affecting the displacements outcome. This implies that parameter combinations with the same ratio a/a_f would produce the same deformation outcome, and also scale multipliers by the same amount. Essentially, passive parameters and multipliers are unique to a constant. Taking advantage of this linear relationship between parameters and pressure, we can restrict the parameter space to only one unknown, the parameter ratio $\gamma = a/a_f$. The actual parameter values can then be recovered using a known cavity pressure value at a specific time frame, in our case cavity pressure at end diastole (EDP$^{\text{est}}$).

Specifically, γ was estimated through parameter sweeps, which – even though computationally costly – provide a characterisation of the identifiability of the material law employed. It should be noted, that when identifiability has been established, computational efficiency can be achieved using data assimilation techniques such as the reduced-order unscented Kalman filter[30,163,276]. The objective function in Eq. 5.23 was used in the parameter sweeps to assess the error between simulated and data-derived deformation. 23 values were considered for the ratio $\gamma = a/a_f$, ranging between 0.3 and 2. The parameter sweeps were performed by keeping the fibre parameter a_f constant ($a_f^{sim} = 1000Pa$) while the isotropic parameter a varied between 30 and 2000. The choice of varying a instead of a_f was based on the improved identifiability characteristics of the isotropic parameter compared to a_f, as observed in Fig. 4.8 in section 4.2.1.3. To retrieve the absolute values of the estimates, both parameter estimates (a_f^{sim}, a^{sim}) and pressure (λ_{ED}^ℓ) were multiplied by the ratio of experimentally derived and simulated end-diastolic pressures (EDP$^{\text{est}}/\lambda_{ED}^\ell$).

The end-diastolic pressure was estimated based on the E/E_a ratio (EDP$^{\text{est}} = 1.9 + 1.24\ E/E_a$) as proposed by Nagueh *et al.*[167]. Here E denotes the peak early diastolic flow velocity through the mitral valve, which was measured from 4D PCMRI data, using GyroTools GTFlow software[‡]. E_a denotes the early diastolic velocity of the mitral valve measured on the lateral basal site which was computed using the motion extracted from 3D tagged MRI.

[‡]http://www.gyrotools.com/products/gt-flow.html

5.5   Summary

This chapter presented the pipeline followed in this work for the development of personalised cardiac mechanics models, using strictly non-invasive data. The developed approach was focused on dealing with two core challenges: data integration and model parametrisation. The proposed approach for bridging the gap between imaging and modelling was outlined, mainly comprised of essential image processing steps aiming at accurate use of the data, along with carefully chosen boundary conditions. Boundary conditions were selected to enable optimal use of the available data for model personalisation while avoiding artefacts due to noisy data. A summary of the proposed pipeline is presented below.

Workflow summary

For every volunteer / patient considered, the main steps followed for the creation of personalised cardiac mechanics model include:

1. Image registration

2. Construction of anatomical mesh at end diastole

3. 3D tagged MRI motion extraction and propagation on mesh through the cycle

4. Processing deformed mesh states to ensure incompressibility

5. Estimation of end-diastolic pressure using E/E_a

6. Generation of rule-based fibre distribution on reference geometry at end systole

7. Parameter sweeps to estimate γ

8. Scaling of passive parameters and pressures to their correct absolute values

9. Simulation with correct absolute parameter values to recover all primary variables

---

The proposed workflow for personalisation of diastolic models of LV mechanics is analysed in the following chapters. With a clear emphasis on enhancing model fidelity while maintaining practical identifiability and unique parametrisation, the outlined approach

is tested in several volunteers and patients. Through the inclusion of diseased and healthy cases the effectiveness and robustness of the pipeline is assessed, and pipeline aspects that need to be refined are elucidated.

6 Investigation of *in vivo* models

A core objective of this thesis is ensuring unique parametrisation for the developed personalised heart models. As discussed in section 4.1.3, parameter identifiability depends on the model, the available data and the objective function used within the parametrisation process. Briefly, to allow for parameter identifiability the cardiac model needs to be a sufficiently accurate representation of the data at hand (*model fidelity*). Furthermore, the available data should be of adequate quality and capture important modes of deformation able to characterise model material parameters. The final requirement is for a discerning objective function, able to stratify deformations from different material parameters.

With the objective of unique parametrisation in mind, the reduced Holzapfel-Ogden law was employed for each of the patient-specific models, based on the *in silico* results in chapter 4, which illustrate that the law combines adequate model fidelity with identifiable parameters using 3D tagged MRI. However, the idealised *in silico* framework employed in section 4.2.1, provided the best-case scenario which can be anticipated. With data originating from simulations, model fidelity issues were alleviated allowing for accurate analysis of the identifiability behaviour of each law. At the same time, the synthetic data created were not compromised by motion artefacts and effects of surrounding tissues which are typically present in real 3D tagged MRI images, likely causing tracking artefacts.

In an *in vivo* environment, however, such an analysis is significantly hindered by both data artefacts and model fidelity issues. Contrary to the *in silico* tests, important modelling aspects such as the fibre distribution or the reference geometry are unknown in *in vivo* applications. Additional modelling assumptions – concerning for instance the material law and suitable boundary conditions – have to be made, leading to a model which would not necessarily be able to reproduce the available data. This issue is likely accentuated by significant variations in data quality and amount of deformation, between cases.

With these concerns in mind, the sections that follow investigate the effect of important modelling assumptions on the parameter identifiability and model accuracy and look for ways to improve on these. Focus is largely on the effect of the assumed fibre

distribution, which as an important determinant of cardiac behaviour, is expected to be a key factor in model accuracy. Different boundary conditions are examined as well, as a means of incorporating data into the model and improving model fidelity. Additionally, the effect of data processing assumptions is assessed.

Due to large variability in heart behaviour and data quality between cases, a systematic analysis of these aspects on several cases was considered essential. Through application of the pipeline proposed in chapter 5 on several volunteers and patients, the robustness of the approach, suitability of modelling assumptions and quality of data are investigated.

Initially, parameter identifiability and model accuracy are compared in personalised simulations with different fibre distributions and epicardial boundary conditions, identifying a combination of fibre field and boundary conditions that provides improved characteristics (section 6.1). Subsequently, the employed basal and epicardial boundary conditions are investigated (section 6.2). Furthermore, the influence of the data frame assumed as the reference domain on model fidelity and parameter identifiability is discussed and analysed in section 6.3. Finally, the effect of data processing assumptions is examined in section 6.4. Throughout this analysis potential limitations of the pipeline are identified and these are discussed in section 6.5.

6.1 *In vivo* identifiability and model accuracy

The personalised heart models within this thesis were developed following the model personalisation pipeline presented in chapter 5. The main aim of the current chapter is to test and evaluate the proposed pipeline, focusing on model fidelity and parameter identifiability *in vivo*. These concepts can be examined through characterisation of the behaviour of an objective function over the parameter space.

Specifically, the pipeline employs the reduced Holzapfel-Ogden law (Eq. 4.5) for diastolic simulations which are driven by cavity volume (Eq. 5.13). Following section 5.4, due to the linear dependence of the employed law on the passive parameters (a and a_f) and the volume-driven simulation used, it is not possible to estimate both parameters solely from deformations. Instead, the parameter ratio $\gamma = a/a_f$ can be estimated (as suggested by *in silico* tests in Fig. 4.9), while the absolute parameter values can be obtained using an estimate of end-diastolic pressure.

Taking the above-mentioned into account, model fidelity and parameter identifiability can be investigated through parameter sweeps over the parameter ratio γ. Model accuracy (or model error) can be assessed through the values of the objective function $\mathcal{J}$ (Eq. 5.23), which was chosen as a strict metric over deformation, to provide detailed information and enable identifiability.

6.1.1 Numerical results

Personalised models of five volunteers (V1 -V5) and three DCM patients (P1-P3) were developed and analysed. Basic metrics, potentially relevant to parameter identifiability are presented in table 6.1 to assist later analysis. Important clinical metrics are presented, namely end-diastolic and end-systolic LV cavity volume, stroke volume and ejection fraction (highlighted in the table). Of interest are also the number of diastolic frames used in the parameter estimation process as well as metrics of deformation between end systole and end diastole. Complementary information concerning the participants is presented in table 7.1.

Participants' general information							
Case	**EDV(ml)**	**ESV(ml)**	**SV(ml)**	**EF**	$\|\|\|\boldsymbol{u}^d\|\|\| \times 10^3$	**T/s**	$\|\|\boldsymbol{u}_{ED}^d\|\| \times 10^3$
V1	129.50	64.57	64.93	**0.50**	0.234	14	0.089
V2	100.85	47.67	53.18	**0.54**	0.226	14	0.083
V3	152.55	67.43	85.12	**0.56**	0.411	16	0.136
V4	93.19	45.99	47.20	**0.51**	0.202	12	0.085
V5	120.36	53.51	66.85	**0.56**	0.244	15	0.094
P1	141.12	81.91	59.21	**0.42**	0.241	15	0.088
P2	179.26	95.15	84.11	**0.47**	0.259	16	0.098
P3	136.19	79.88	56.31	**0.41**	0.178	16	0.072

Table 6.1 Participants' information relevant to parameter identifiability for the volunteers and patients considered, are presented. Clinical metrics (EDV: end-diastolic volume, ESV: end-systolic volume, SV: stroke volume, EF: ejection fraction) and other diastolic motion characteristics ($\|\|\|\boldsymbol{u}^d\|\|\|$: L^2 norm of the deformation summed over time, T/s: number of diastolic timesteps, $\|\|\boldsymbol{u}_{ED}^d\|\|$: L^2 norm of end-diastolic deformation) are shown.

For all cases, parameter identifiability and model accuracy were examined using parameter sweeps, for three fibre distributions, which varied linearly between $(-50°,\ 50°)$, $(-60°,\ 60°)$ and $(-70°,\ 70°)$ from epicardium to endocardium. Two different epicardial boundary conditions were considered through these tests, a zero traction condition (*"Zero-traction epicardial BC"*) and the boundary condition described in Eq. 5.16, where at the region of attachment to the RV wall, the motion is prescribed directly from the data (*"RV-epicardial BC"*).

Figures 6.1a - 6.8a illustrate the behaviour of the objective function $\mathcal{J}$ over the parameter ratio γ, for the 5 volunteers and 3 patients considered, respectively. For all cases, the behaviour of $\mathcal{J}$ was characterised for the three different fibre distributions and the two epicardial boundary conditions employed. Accordingly, each data-point within these graphs represents a specific diastolic simulation assuming a unique combination of parameter ratio, epicardial boundary condition and fibre distribution. Additionally,

table 6.2 summarises the parameter ratio (γ) estimates for all cases, for different fibre distributions and epicardial boundary conditions. Table 6.3 presents the second derivative of $\mathcal{J}$ at the estimated ratios, providing a measure of the local behaviour of $\mathcal{J}$.

This systematic investigation of local and global identifiability behaviour enables the deconvolution of the effects of individual modelling components and data-derived metrics, on parameter estimates and identifiability. These effects will be discussed in sections 6.1.2, 6.1.3 and 6.1.4, while the actual parameter estimates will be discussed in detail in chapter 7, section 7.2.

An initial observation is that for every case there is at least one fibre distribution that presents a unique and distinct minimum. Combined with the monotonic objective function for the cases where the lowest error is observed in the lowest ratio, this suggests that the parameter identifiability of the reduced Holzapfel-Ogden law is maintained *in vivo*. To investigate this observation further and delineate the factors that contribute to it, additional tests are required and performed in the remainder of this chapter.

Volunteer 1 (V1)

(a)

(b)   (c)

Figure 6.1 (**a**) $\mathcal{J}$ over the parameter ratio γ, for V1, for three fibre distributions and two epicardial boundary conditions. Also presented are data-derived and simulated deformation at end diastole using the estimated γ for fibres with a maximum angle of 50°, (**b**) with zero-traction and (**c**) RV-epicardial boundary conditions. Lines show data-derived deformation, while the solid mesh presents simulated end diastole, and is coloured based on the magnitude of the error between the simulated and data-derived displacements, given in metres.

Volunteer 2 (V2)

Zero–traction epicardial BC

RV–epicardial BC

(a)

(b)

(c)

Figure 6.2 (**a**) $\mathcal{J}$ over the parameter ratio γ, for V2, for three fibre distributions and two epicardial boundary conditions. Also presented are data-derived and simulated deformation at end diastole using the estimated γ for fibres with a maximum angle of 50°, (**b**) with zero-traction and (**c**) RV-epicardial boundary conditions. Lines show data-derived deformation, while the solid mesh presents simulated end diastole, and is coloured based on the magnitude of the error between the simulated and data-derived displacements, given in metres.

Volunteer 3 (V3)

(a)

(b)

(c)
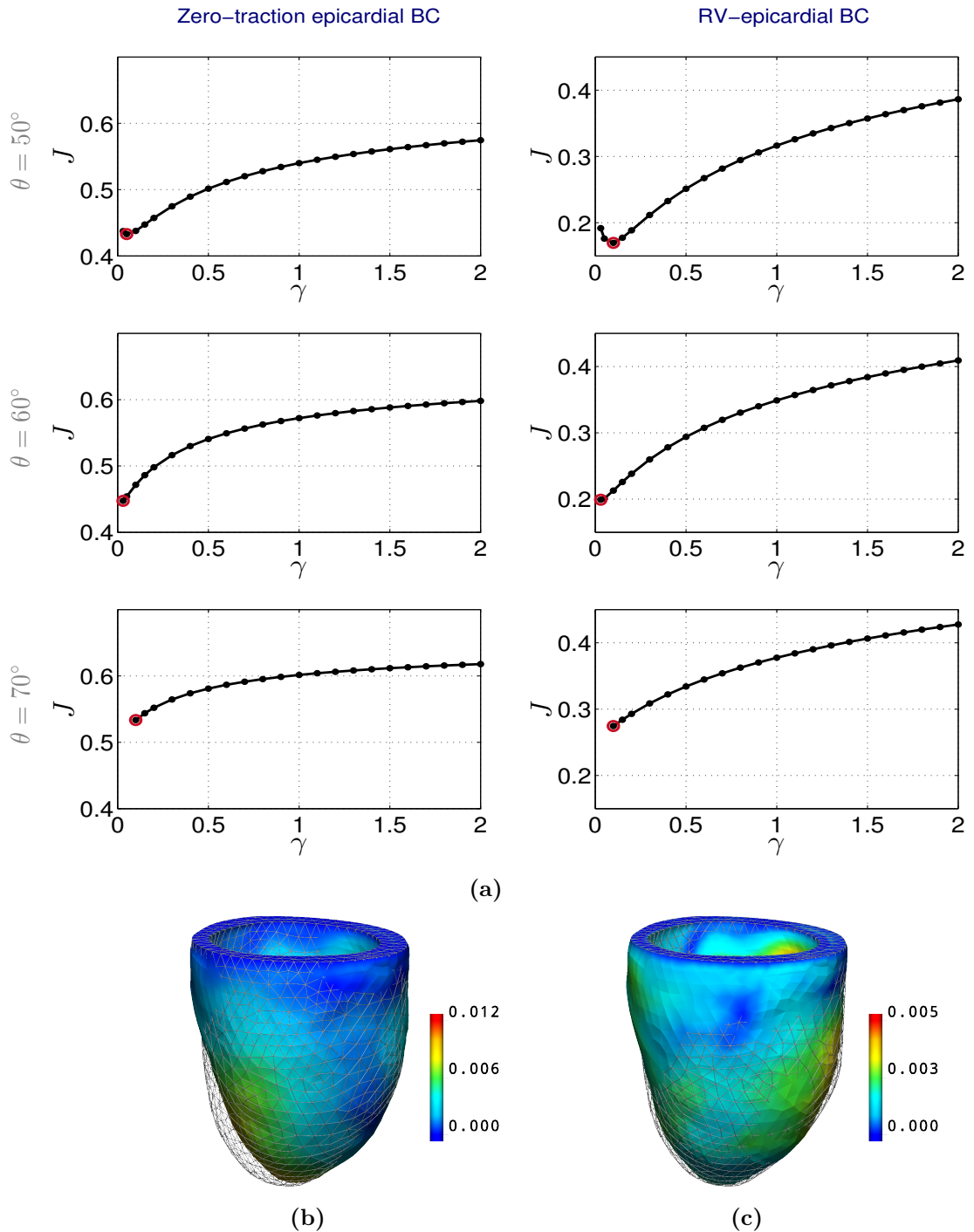
Figure 6.3 (**a**) $\mathcal{J}$ over the parameter ratio γ, for V3, for three fibre distributions and two epicardial boundary conditions. Also presented are data-derived and simulated deformation at end diastole using the estimated γ for fibres with a maximum angle of 50°, (**b**) with zero-traction and (**c**) RV-epicardial boundary conditions. Lines show data-derived deformation, while the solid mesh presents simulated end diastole, and is coloured based on the magnitude of the error between the simulated and data-derived displacements, given in metres.

Volunteer 4 (V4)

(a)

(b)

(c)
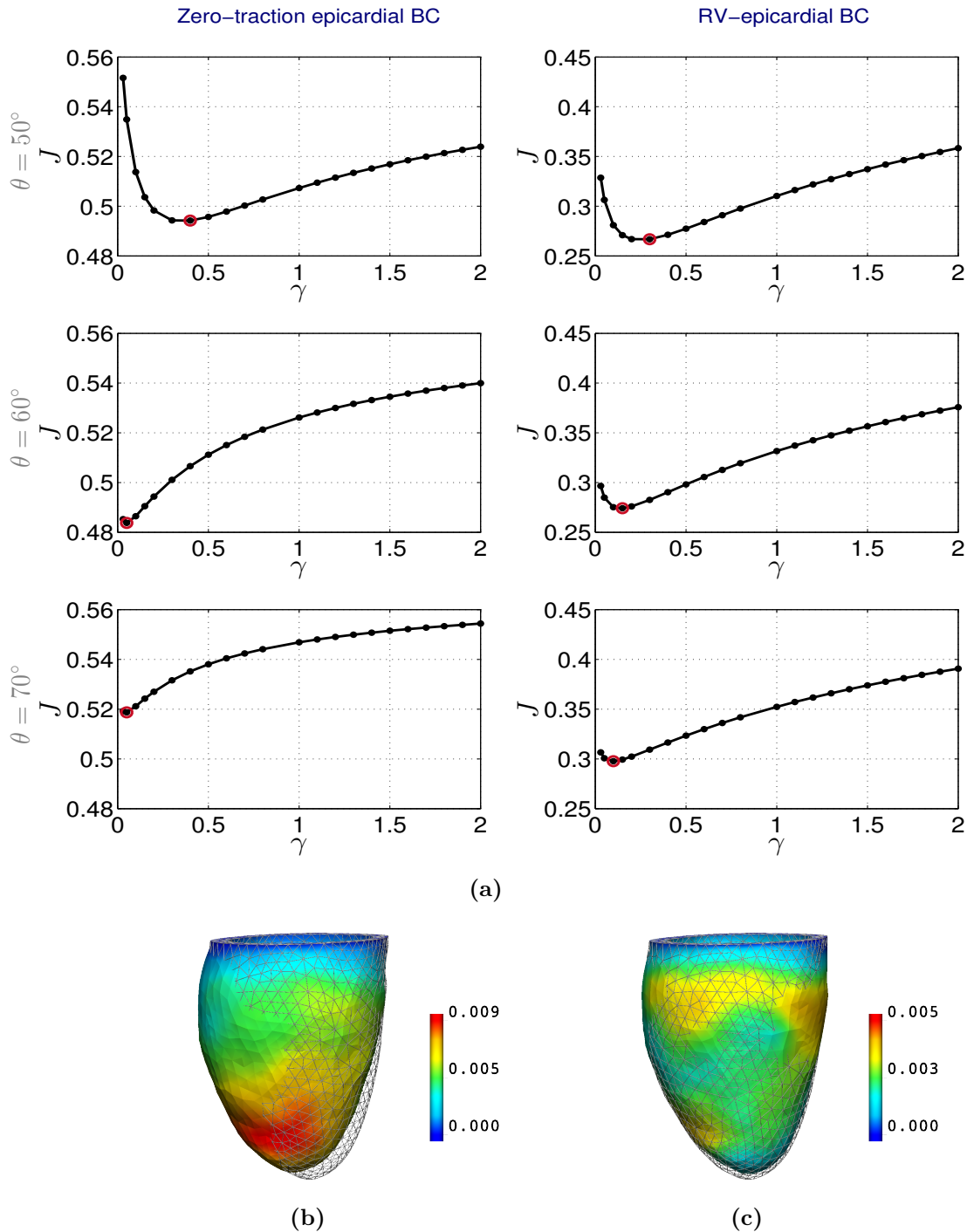
Figure 6.4 (a) $\mathcal{J}$ over the parameter ratio γ, for V4, for three fibre distributions and two epicardial boundary conditions. Also presented are data-derived and simulated deformation at end diastole using the estimated γ for fibres with a maximum angle of 50°, **(b)** with zero-traction and **(c)** RV-epicardial boundary conditions. Lines show data-derived deformation, while the solid mesh presents simulated end diastole, and is coloured based on the magnitude of the error between the simulated and data-derived displacements, given in metres.

Volunteer 5 (V5)

(a)

(b)   (c)
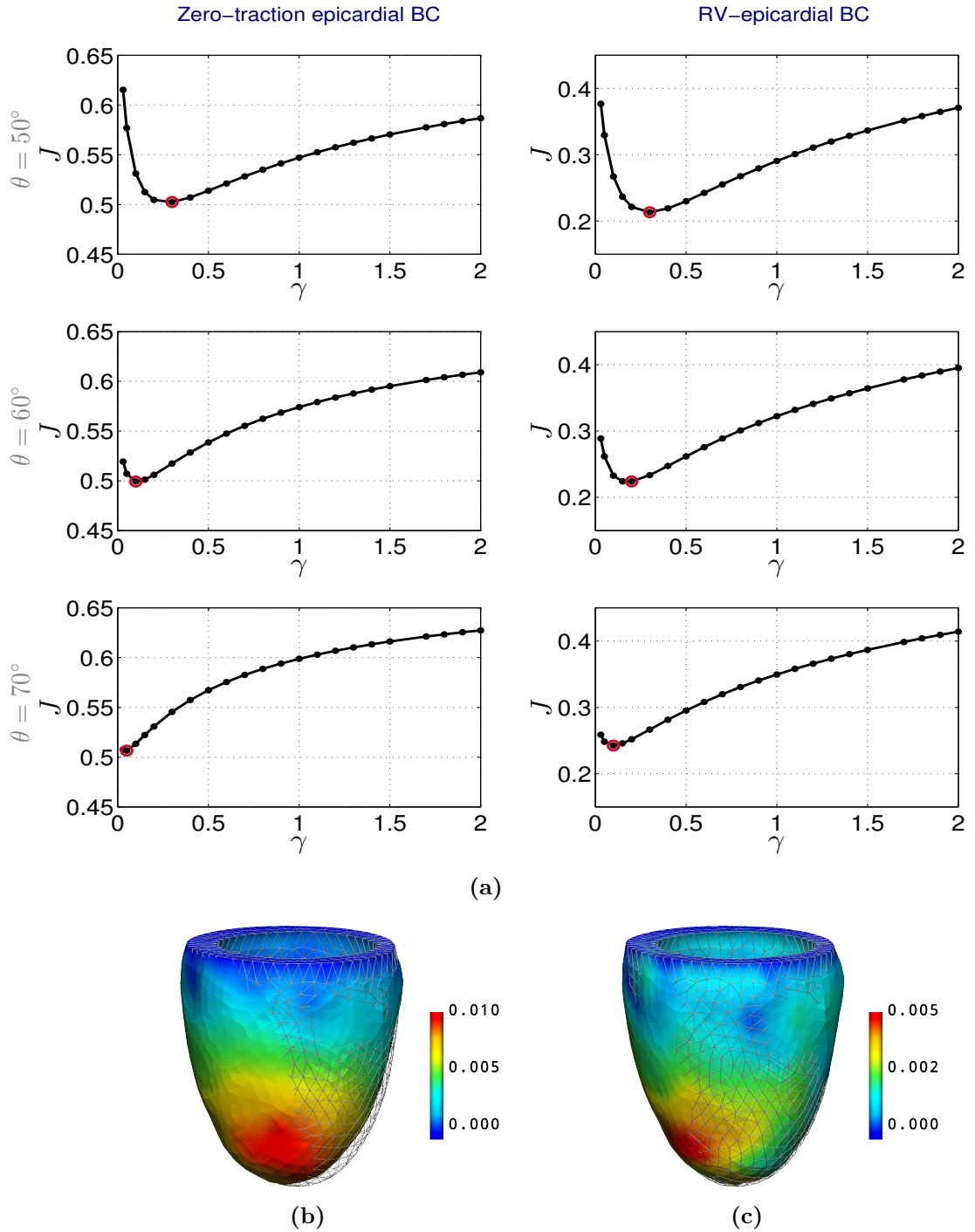
Figure 6.5 (a) $\mathcal{J}$ over the parameter ratio γ, for V5, for three fibre distributions and two epicardial boundary conditions. Also presented are data-derived and simulated deformation at end diastole using the estimated γ for fibres with a maximum angle of 50°, **(b)** with zero-traction and **(c)** RV-epicardial boundary conditions. Lines show data-derived deformation, while the solid mesh presents simulated end diastole, and is coloured based on the magnitude of the error between the simulated and data-derived displacements, given in metres.
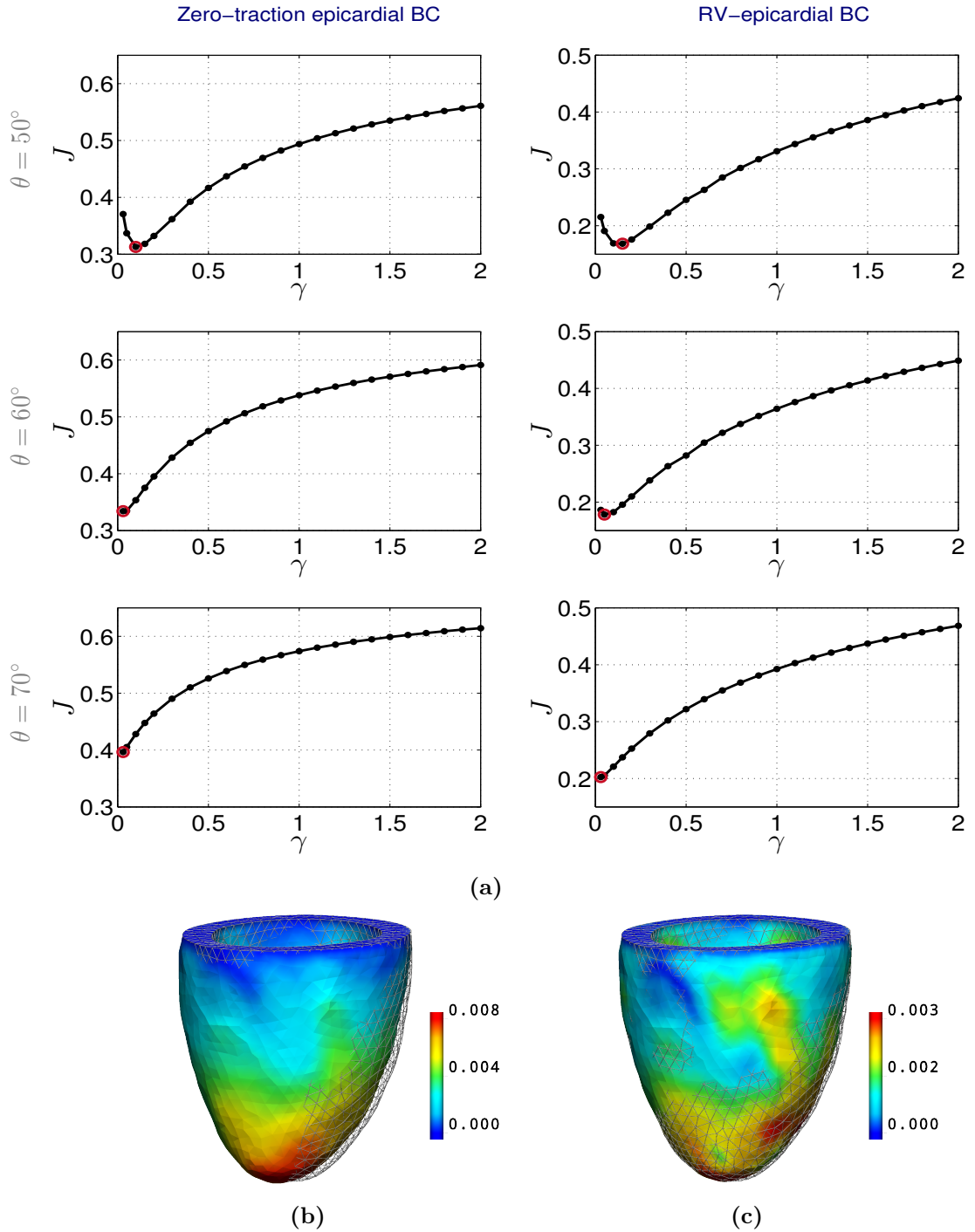
Patient 1 (P1)

(a)

(b)

(c)
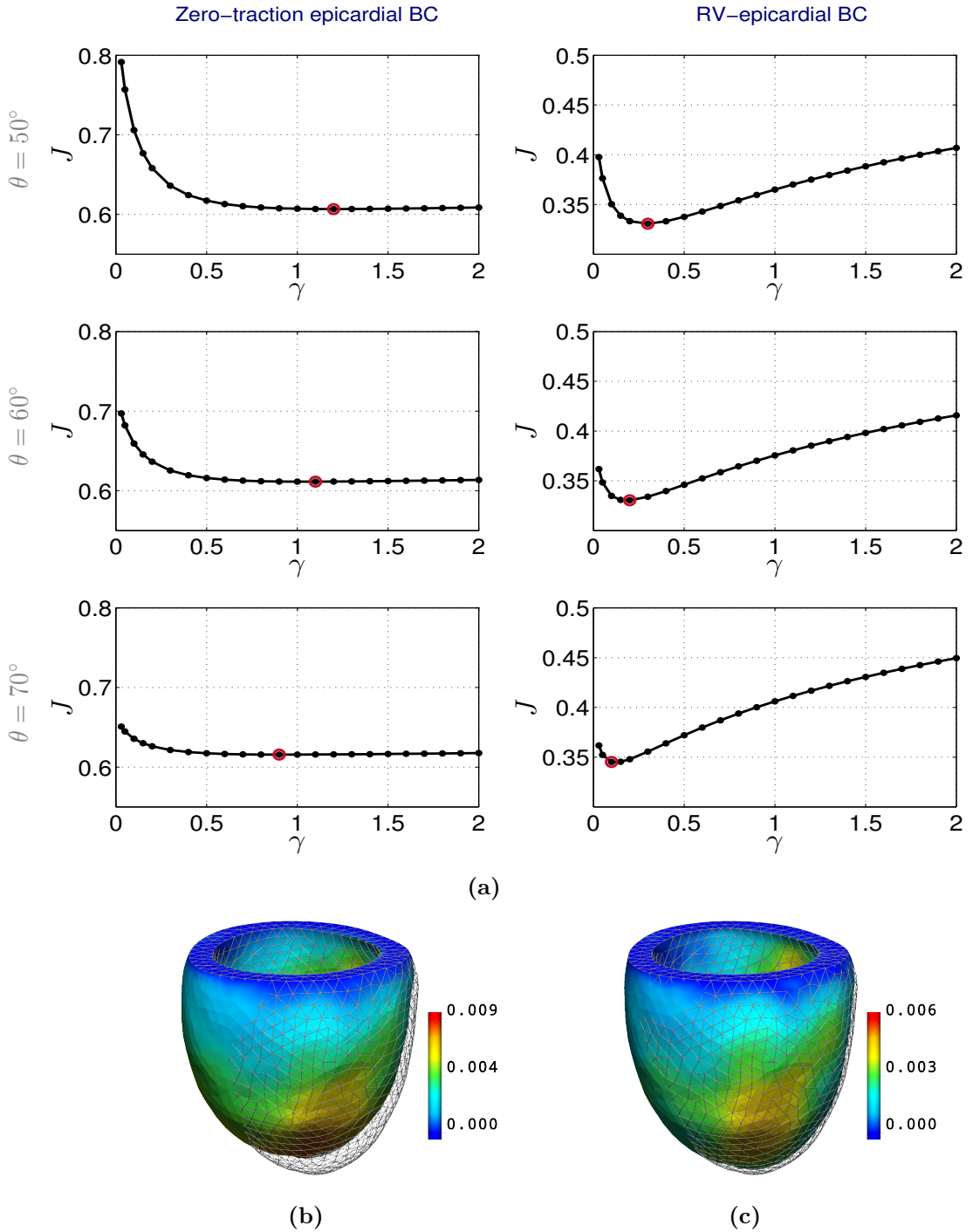
Figure 6.6 (**a**) $\mathcal{J}$ over the parameter ratio γ, for P1, for three fibre distributions and two epicardial boundary conditions. Also presented are data-derived and simulated deformation at end diastole using the estimated γ for fibres with a maximum angle of 50°, (**b**) with zero-traction and (**c**) RV-epicardial boundary conditions. Lines show data-derived deformation, while the solid mesh presents simulated end diastole, and is coloured based on the magnitude of the error between the simulated and data-derived displacements, given in metres.

Patient 2 (P2)

(a)

(b)   (c)
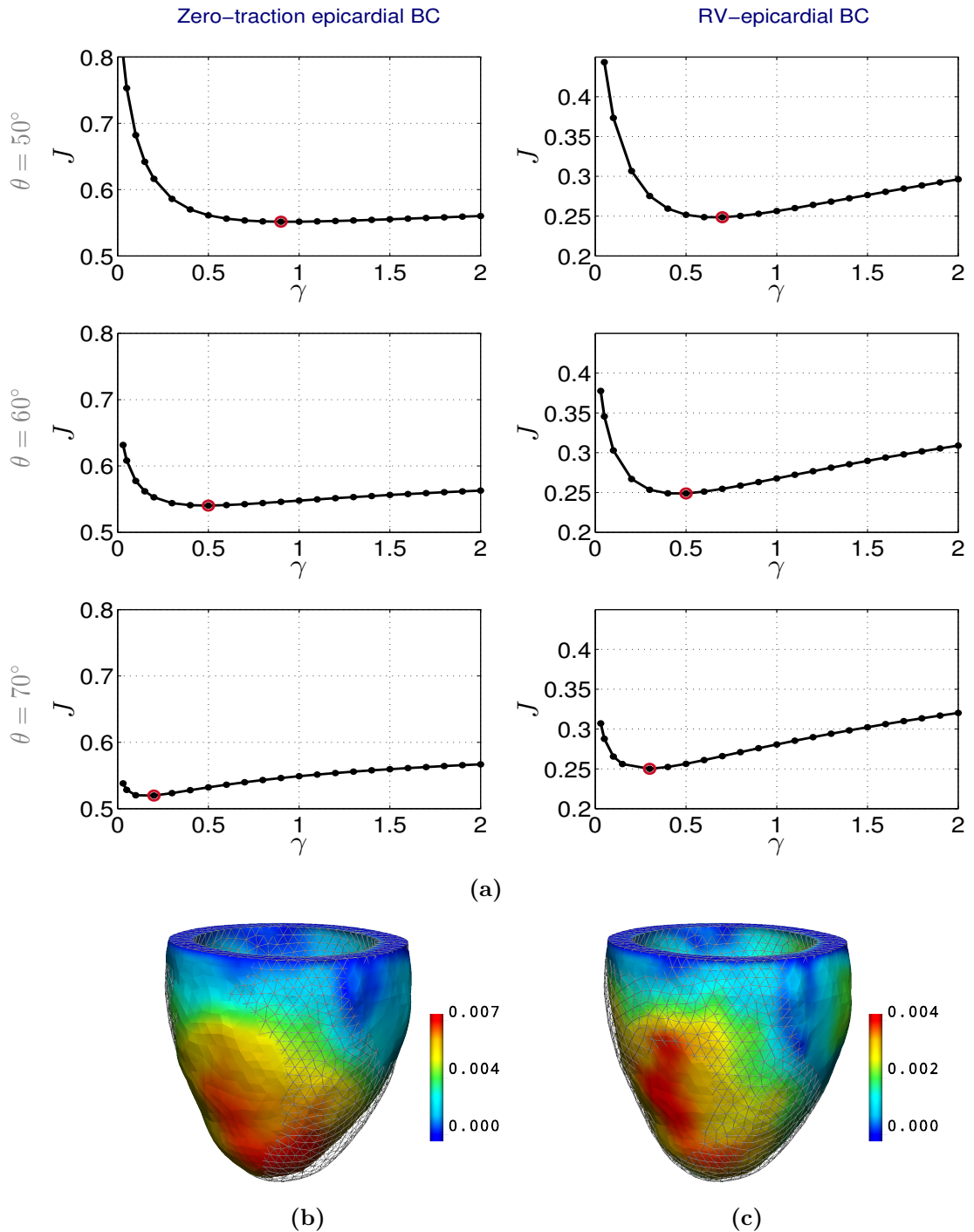
Figure 6.7 (**a**) $\mathcal{J}$ over the parameter ratio γ, for P2, for three fibre distributions and two epicardial boundary conditions. Also presented are data-derived and simulated deformation at end diastole using the estimated γ for fibres with a maximum angle of 50°, (**b**) with zero-traction and (**c**) RV-epicardial boundary conditions. Lines show data-derived deformation, while the solid mesh presents simulated end diastole, and is coloured based on the magnitude of the error between the simulated and data-derived displacements, given in metres.
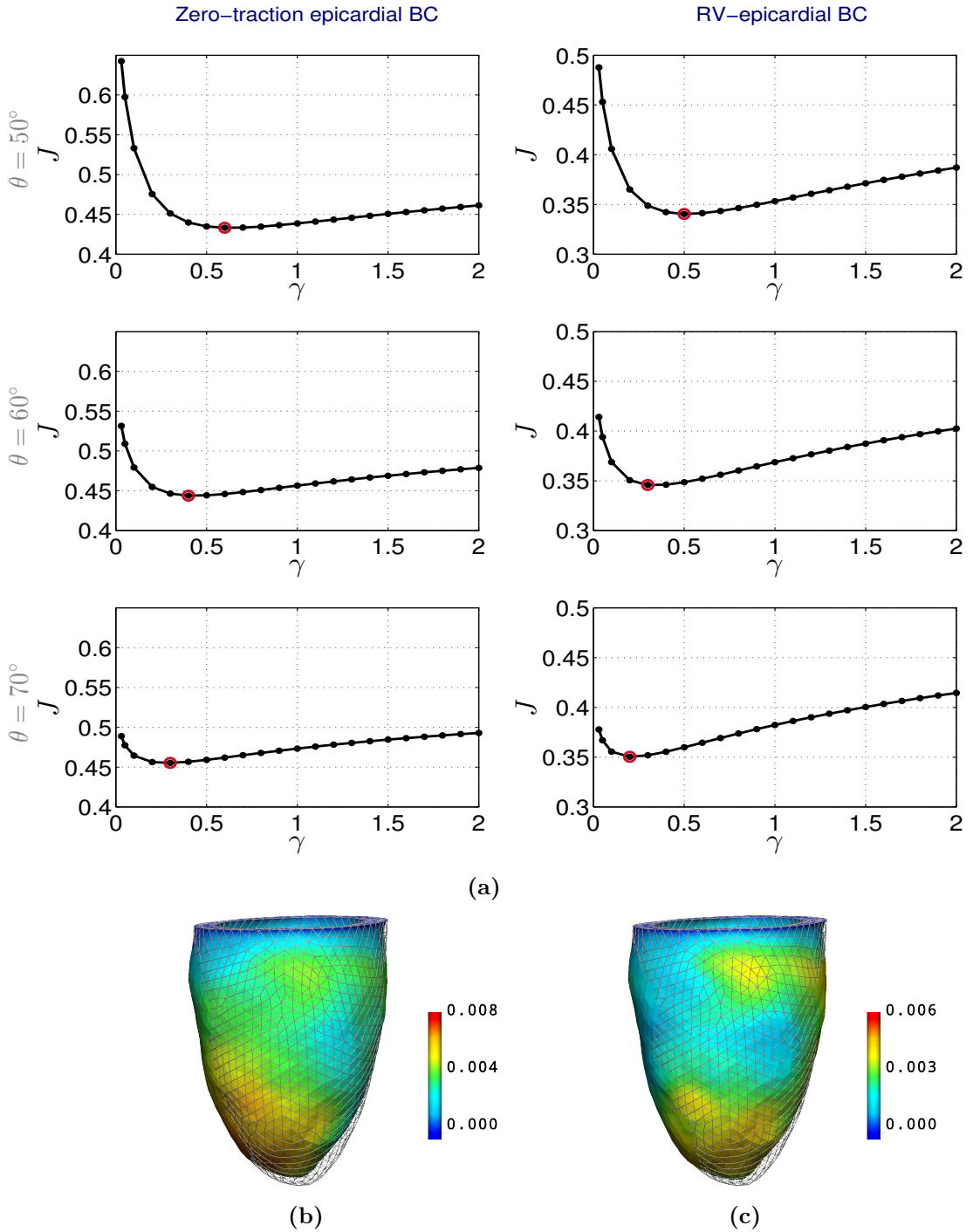
Patient 3 (P3)

(a)

(b)

(c)
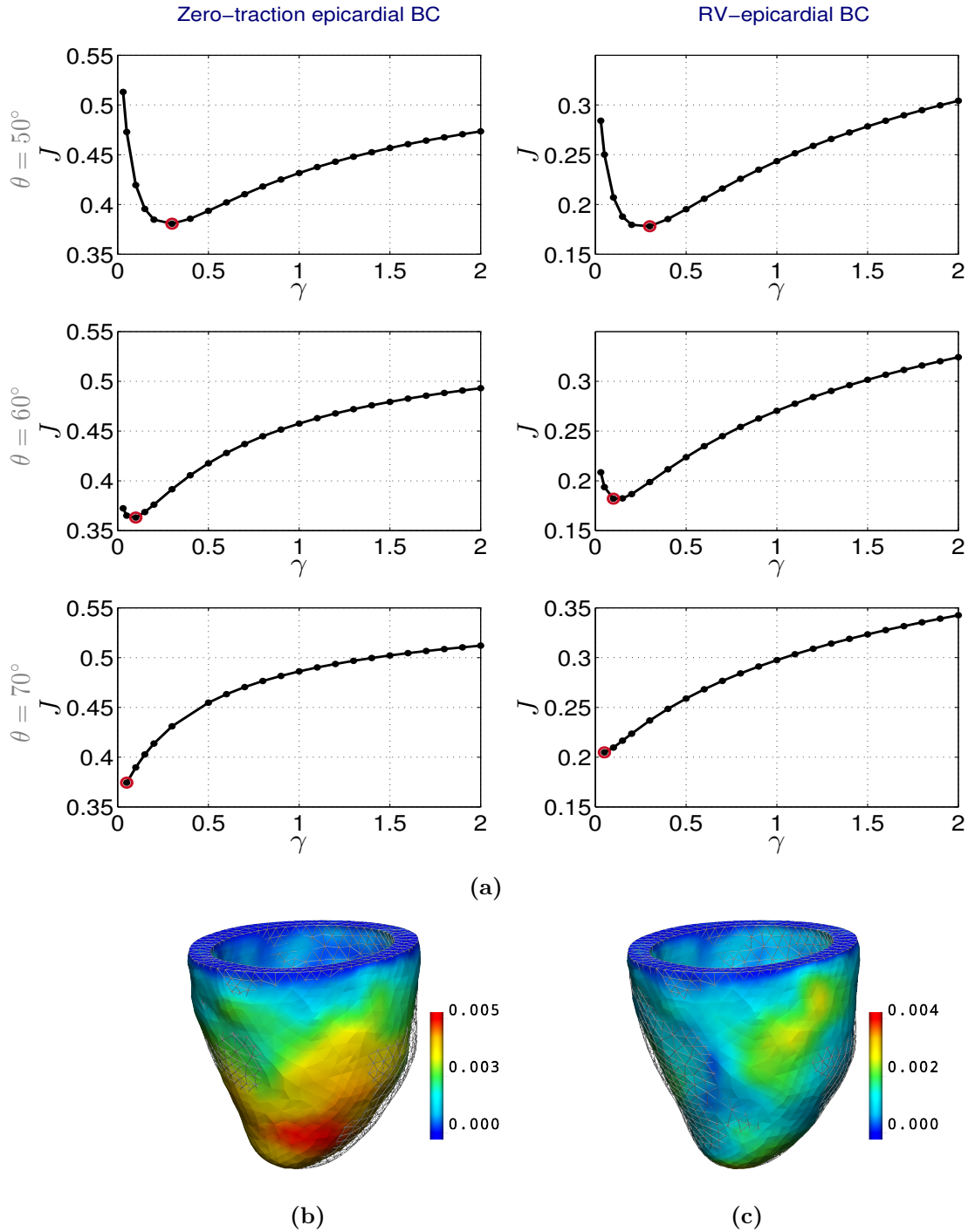
Figure 6.8 (**a**) $\mathcal{J}$ over the parameter ratio γ, for P3, for three fibre distributions and two epicardial boundary conditions. Also presented are data-derived and simulated deformation at end diastole using the estimated γ for fibres with a maximum angle of 50°, (**b**) with zero-traction and (**c**) RV-epicardial boundary conditions. Lines show data-derived deformation, while the solid mesh presents simulated end diastole, and is coloured based on the magnitude of the error between the simulated and data-derived displacements, given in metres.

|	$\theta = 50°$		$\theta = 60°$		$\theta = 70°$	
Case	NT BC	RV BC	NT BC	RV BC	NT BC	RV BC
V1	0.1	0.15	*	0.05	*	*
V2	0.6	0.5	0.4	0.3	0.3	0.2
V3	0.05	0.1	*	*	*	*
V4	0.4	0.3	0.05	0.15	0.05	0.1
V5	0.3	0.3	0.1	0.2	*	0.1
P1	1.2	0.3	1.1	0.2	0.9	0.15
P2	0.9	0.7	0.5	0.5	0.2	0.3
P3	0.3	0.3	0.1	0.1	*	*

Table 6.2 Parameter ratio γ estimates for the volunteer and patient cases. Three different fibre distributions were considered, with a maximum angle of $\theta = 50°$, $\theta = 60°$ and $\theta = 70°$. Two epicardial boundary conditions were analysed, a no-traction (*NT BC*) and an RV-epicardial (*RV BC*) boundary condition. Stars (*) denote cases where the lowest error was observed in the lowest ratio tested.

	$\mathcal{J}$ Second derivative							
Case	**V1**	**V2**	**V3**	**V4**	**V5**	**P1**	**P2**	**P3**
$\theta = 50°$	3.2E-06	2.5E-07	5.6E-06	4.5E-07	1.4E-06	5.0E-07	1.8E-07	8.6E-07
$\theta = 60°$	1.0E-05	4.9E-07	*	1.1E-06	1.7E-06	7.0E-07	2.3E-07	4.8E-06
$\theta = 70°$	*	6.6E-07	*	1.9E-06	3.6E-06	2.9E-06	5.3E-07	*

Table 6.3 Second derivatives of $\mathcal{J}$ at the estimated ratio, when the RV-epicardial boundary condition was employed. Three fibre distributions were considered. Stars (*) denote cases where the lowest value of $\mathcal{J}$ was observed at the lowest ratio considered.

6.1.2 Epicardial boundary condition

Two different epicardial conditions were examined, namely a zero-traction condition and an RV-epicardial condition, accounting for the stresses exerted on the region of attachment of the LV model to the RV wall. Observing the behaviour of the objective function over the parameter ratio γ in Fig. 6.1a- 6.8a, the application of the data-derived motion on the region of attachment to the RV, proved superior compared to the simplified zero-traction epicardial boundary condition. For all cases and all fibre distributions, the minimum $\mathcal{J}$ error was significantly lower when the RV-epicardial boundary condition was employed, compared to the zero-traction boundary condition. Specifically, the average error in $\mathcal{J}$ reduced from approximately $\sim 45\%$ to $\sim 25\%$ and from $\sim 51\%$ to $\sim 26\%$, in the volunteer and patient groups, respectively. The reduction in the error in deformation between the data and the model is also qualitatively illustrated in figures 6.1(b, c) - 6.8(b, c).

This significant reduction in error (the error was nearly half of the no-traction case), combined with the very high error values for the zero-traction case, suggest that the enforcement of this constraint is important for the accuracy of the personalised models. Based on direct comparisons of simulated results with both epicardial conditions on actual images, it appears that the zero-traction condition could not sufficiently restrict the deformation, causing a slight shift of the geometry which might lead to the LV wall crossing the RV wall or other tissues (see for example Fig. 6.9). If, instead, the RV motion was taken into account through the RV-epicardial boundary condition, the simulated deformation was restricted on a more anatomically accurate position in space, leading to significantly more accurate outcomes.

(a) (b)
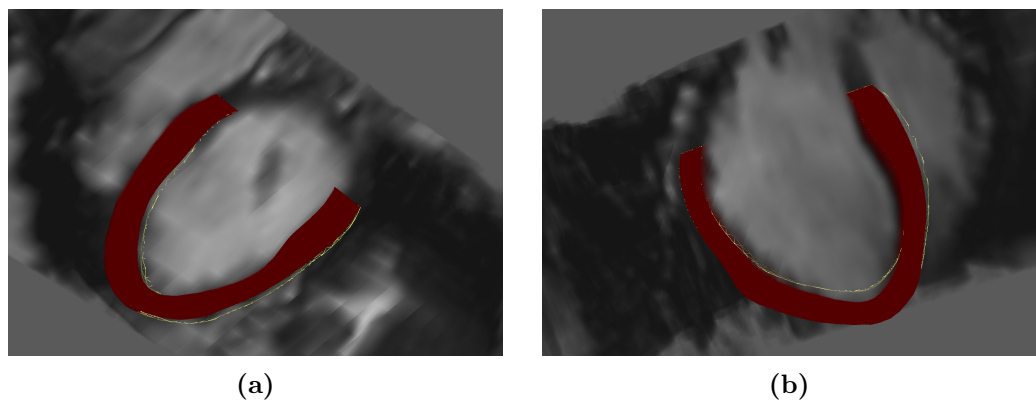
Figure 6.9 Simulated end-diastolic deformation with zero-traction epicardial boundary condition (yellow mesh lines) and RV-epicardial boundary condition (red solid mesh), for **(a)** V1 and **(b)** P1.

An equally important benefit of using the RV-epicardial condition is the improved parameter identifiability characteristics, presented in the majority of cases. Specifically, the variation in $\mathcal{J}$ (difference between maximum and minimum $\mathcal{J}$ values), increased when the RV-epicardial condition was applied, especially as the maximum fibre angle increased. The improvement in $\mathcal{J}$ behaviour stems from the fact that sufficient model fidelity is a requirement for parameter identifiability. This is clearly illustrated in P1 and P2 (Fig. 6.6a and 6.7a, respectively), where $\mathcal{J}$ is practically constant for a wide range of ratios when the zero-traction condition is used. This deteriorated identifiability does not imply that the model is not sensitive to γ, but rather that model fidelity is insufficient (errors up to 60%), with essentially a wide range of ratios leading to equally large errors. However, accounting for the effect of the RV through the application of the RV-epicardial boundary condition, allowed for sufficient model accuracy enabling significantly improved identifiability.

6.1.3 Fibre distribution

The fibre architecture is known to be an important determinant of cardiac function, and as such, it is a key factor in model accuracy. Due to the absence of personalised fibre distributions, a standard fibre field was employed, with the fibre angle varying linearly from endocardium to epicardium (maximum angles of $\theta = 50°$, $\theta = 60°$ and $\theta = 70°$ were used). As expected, the three fibre distributions employed lead to notable variation in model behaviour and parameter estimates.

Based on the parameter ratio estimates presented in table 6.2, γ estimates are strongly coupled to the assumed fibre distribution. Briefly, for the same epicardial boundary condition, an increase in fibre angle θ resulted in a decrease in the parameter ratio γ. This can be justified by noting that an increase in fibre angle leads to less elongation in deformation (the stiffer direction is now closer to the long-axis direction). Additionally, a decrease in the parameter ratio causes increased elongation and more anisotropic deformation. Therefore, as θ increases, the parameter ratio is forced to a smaller value to allow for more elongation and better matching to the data. Interestingly, the tendency for a decrease in γ with larger fibre angles led to cases with the lowest error appearing at the lowest ratio examined. In these cases, $\mathcal{J}$ was monotonic suggesting a potential minimum at a lower value, yet ratios lower than 0.03 were considered non-physiological and therefore not examined.
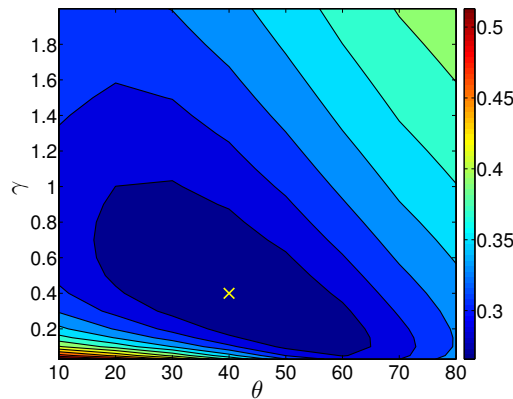
Figure 6.10 Landscape of $\mathcal{J}$ over parameter ratio γ and fibre angle θ. Yellow cross denotes the combination presenting the minimum error.

This coupling between γ and θ can also be observed in Fig. 6.10, where notably different combinations of fibre angles and parameter ratios resulted in similar error values. The presence of a wide valley with small error values suggests that the fibre angle could not be identified through this process, as already suggested through the *in silico* test in section 4.2.1.4.1, when the Guccione law was employed. The graph also confirms the tendency for an increase in the parameter ratio for smaller fibre angles. Although

the minimum here was observed for $\theta = 40°$, the difference in error from the $\theta = 50°$ case was negligible. As a maximum fibre angle of $\theta = 40°$ varies substantially from the standard distribution of $\theta = 60°$ that is commonly employed in cardiac mechanics, this fibre distribution was not analysed further.

Interestingly, the fibre distribution used, appears to also affect parameter identifiability, as can be deduced by Fig. 6.10 and 6.1a - 6.8a. While global $\mathcal{J}$ variation (difference in maximum and minimum values) appeared to increase for smaller θ, local variation in $\mathcal{J}$ was deteriorated, *i.e.* a wider neighbourhood about the minimum presented similar errors. Deterioration in local identifiability with decreased θ can also be deduced by the second derivative of $\mathcal{J}$ at the parameter estimates for the cases under consideration, in table 6.3. Nevertheless, the actual effect of this issue might be less pronounced if percentage parameter errors are considered, taking into account that estimated γ is larger for smaller fibre angles.

Another interesting finding stems from the observation that in the majority of cases employing the RV-epicardial boundary condition, the lowest error was obtained with a fibre angle of $\theta = 50°$. This observation holds for all volunteer cases with a mean decrease in $\mathcal{J}$ of 4.2% and 1.3% when $\theta = 50°$ was assumed, compared to $\theta = 70°$ and $\theta = 60°$, respectively. This observation was less pronounced for DCM patients, where the relevant mean decrease in error between $\theta = 50°$ and $\theta = 70°$ was 1.4%. Furthermore, P1 presented a marginally lower error for $\theta = 60°$.

Although as discussed, θ could not be estimated using the available data, a specific fibre distribution had to be selected to allow for consistent comparisons between cases. The presence of a consistently lower error when $\theta = 50°$ was assumed, combined with the large $\mathcal{J}$ variation observed, led to the use of the specific fibre distribution for the personalised models analysed in the remainder of this chapter, and chapter 7.

6.1.4   Parameter identifiability

This section focuses on parameter identifiability for the volunteer and patient cases analysed. Despite the small number of cases and the complex inter-related factors contributing to parameter identifiability (model fidelity, data quality and quantity), an attempt was made to decipher the identifiability behaviour and contributing factors. The analysis that follows focuses on models employing the RV-epicardial boundary condition and a fibre distribution of $\theta = 50°$ – a combination shown to reduce modelling error – to enable easier comparisons of other aspects.

Observing Fig. 6.1a - 6.8a which present the behaviour of the objective function over the parameter ratio, we can deduce that for the majority of cases good identifiability characteristics were presented. Specifically, for all volunteers and patients, $\mathcal{J}$ varied

smoothly over the parameter space and had a unique and distinct minimum. The presence of a clear minimum, combined with reasonable model errors (range of error at the estimated ratio was $(0.17 - 0.34)$ and $(0.18 - 0.33)$ for volunteers' and patients' groups, respectively) suggest that at the personalised models considered, the reduced Holzapfel-Ogden law maintained the good identifiability characteristics observed in *in silico* tests. This implies that the model assumptions made enabled sufficient model accuracy, without which parameter identifiability would not had been possible. Furthermore, it suggests that the data used for model personalisation were of sufficient quality.

Despite the generally satisfactory identifiability behaviour of $\mathcal{J}$, certain aspects of it differed between cases. For instance, the variation between the minimum and maximum $\mathcal{J}$ value was notably different from case to case. $\mathcal{J}$ variation can be thought of as a measure of identifiability, as a large $\mathcal{J}$ variation between parameters that differ significantly makes a large error in the parameter estimate less likely. Combining observations from $\mathcal{J}$ for the different cases and information from table 6.1, $\mathcal{J}$ variation appeared to mainly depend on the magnitude of the deformation, whether at end diastole ($||\boldsymbol{u}^d_{ED}||$) or summed over time ($|||\boldsymbol{u}^d|||$). This dependence is attributed to the fact that substantial deformation is required for parameter identifiability. Accordingly, on average, patients presented reduced $\mathcal{J}$ variation (mean variation 0.13 in patients over 0.18 in volunteers) compared to normals, as the heart is known to be hypokinetic in DCM[89]. Similarly, V4 who presented the smallest deformation amongst volunteers, also presented the lowest $\mathcal{J}$ variation.

Differences can also be observed in the local $\mathcal{J}$ behaviour. The behaviour of $\mathcal{J}$ in a neighbourhood about the estimate is another measure for identifiability. Specifically, a sharp variation about the minimum provides confidence in the parameter estimate, contrary to the presence of a valley with similar $\mathcal{J}$ values. The local behaviour can be observed in $\mathcal{J}$ plots for the different cases, as well as in table 6.3, showing the second derivative of $\mathcal{J}$ at the estimate. The second derivative can be related to the sensitivity of $\mathcal{J}$ to the passive parameter ratio, thus the larger the value of the second derivative, the better the parameter identifiability. With these ideas in mind, DCM patients saw deteriorated local identifiability compared to normals. Similar to $\mathcal{J}$ variation, this could again be attributed to reduced deformation which is common in DCM. Likewise, the deteriorated local identifiability of V2 could be justified by the fact the V2 presented the lowest $||\boldsymbol{u}^d_{ED}||$ among volunteers.

It is worth noting, that based on these findings, identifiability was not markedly affected by bulk functional heart metrics such as ejection fraction and stroke volume, but was mostly influenced by the degree of deformation present in the data. Furthermore, due to the dependence of $\mathcal{J}$ on the deformation (Eq. 5.23), cases with small deformation were also related to larger model errors.

6.2 Investigation of employed boundary conditions

The sections that follow examine the suitability of the boundary conditions employed within the proposed pipeline, and investigate their effect on parameter identifiability and model accuracy.

6.2.1 Investigation of basal boundary condition

As discussed in section 5.3.3.2, the basal boundary condition employed (Eq. 5.14) was selected mainly to reduce artefacts introduced because of strict enforcement of motion through a Dirichlet boundary condition. Specifically, strict enforcement of deformation constraints is known to cause non-physiological pressure peaks. The aim of this section is to verify – via a representative example – that the relaxed basal boundary condition reduces pressure peaks associated with Dirichlet boundary conditions, while allowing for sufficient model accuracy and parameter identifiability.
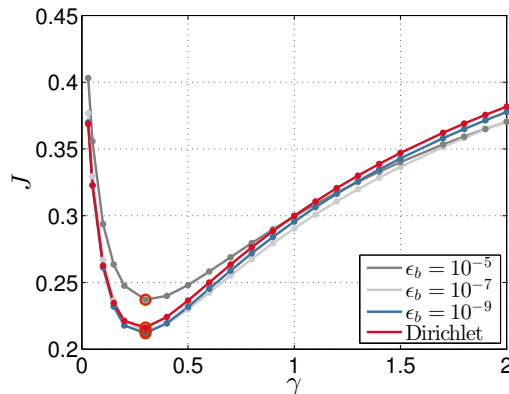
Figure 6.11 Landscape of $\mathcal{J}$ over parameter ratio γ for V5, for different values of the relaxation parameter in the basal boundary condition. A Dirichlet basal boundary condition is considered as well.

Fig. 6.11 compares the behaviour of $\mathcal{J}$ over γ for three values of the relaxation parameter ϵ_b in Eq. 5.14. For all cases, identifiability was maintained while the ratio retrieved was the same. As expected, the highest ϵ_b, at which relaxation of the constraint was substantial, resulted in the largest error (Fig. 6.11 and 6.12d). Interestingly, the application of the Dirichlet boundary condition did not result in the lowest error, as the strict enforcement of the constraint caused not only local pressure peaks but also non-physiological deformation near the base (Fig. 6.12a). These artefacts in both pressure and deformations were reduced as the constraint was progressively relaxed (Fig. 6.12b, 6.12c and 6.12d). The value $\epsilon_b = 10^{-7}$ used for the personalised simulations in section 6.1 provided an adequate model accuracy – consequently allowing for parameter identifiability – while in parallel restricting regional pressure peaks.
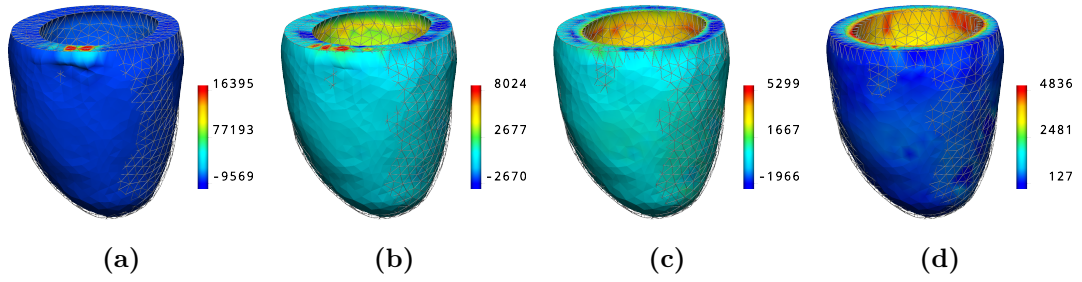
Figure 6.12 Simulated end-diastolic deformation for V5, with **(a)** Dirichlet basal boundary condition and relaxed basal boundary condition, with a relaxation parameter of **(b)** $\epsilon_b = 10^{-9}$, **(c)** $\epsilon_b = 10^{-7}$ and **(d)** $\epsilon_b = 10^{-5}$. Mesh lines show the data-derived deformation, while the coloured solid mesh presents the wall pressure (Pa).

6.2.2 Investigation of RV-epicardial boundary condition

The application of the RV-epicardial boundary condition was shown to be critical for both model accuracy and parameter identifiability. Both aspects however, are dependent on the value chosen for the relaxation parameter ϵ_e in Eq. 5.16. These attributes were investigated via a representative example (application on V5) presented in this section.
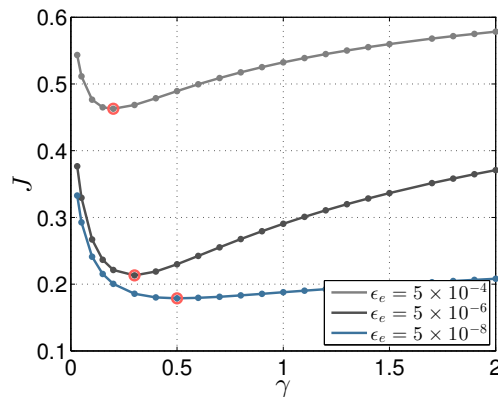
Figure 6.13 Landscape of $\mathcal{J}$ over parameter ratio γ for V5, for different values of the relaxation parameter in the RV-epicardial boundary conditions.

As anticipated, a lower value for ϵ_e, requiring a strict enforcement of the constraint, reduced model error remarkably (Fig. 6.13 and 6.14). However, a strict condition might in parallel lead to over-constraining of the parameter estimation problem, causing deterioration of identifiability. This is obvious in Fig. 6.13, where the strict enforcement of motion for the lowest value of ϵ_e forced a wide range of parameter ratios to produce very similar deformation – and hence error – and in this way diminished parameter identifiability. Instead, $\epsilon_e = 5 \times 10^{-6}$ (as selected for the considered personalised models in section 6.1) provided a balance between model accuracy and parameter identifiabil-

ity.

(a)   (b)   (c)
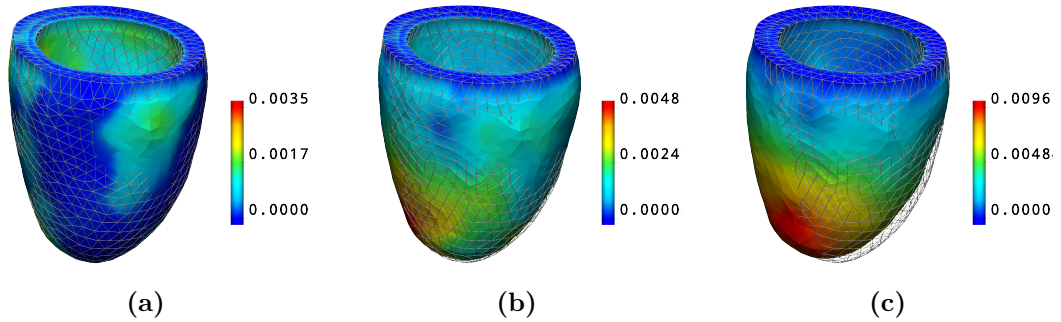
Figure 6.14 Simulated end-diastolic deformation for V5, with a relaxation parameter of **(a)** $\epsilon_e = 5 \times 10^{-8}$, **(b)** $\epsilon_e = 5 \times 10^{-6}$ and **(c)** $\epsilon_e = 5 \times 10^{-4}$ for the RV-epicardial boundary condition. Mesh lines show the data-derived deformation, while the coloured solid mesh presents the error between model and data (m).

6.3   Effect of reference configuration

Estimation of the reference / undeformed geometry is undoubtedly one of the biggest challenges in cardiac mechanics. As no such state exists in the cardiac cycle, a common approach is to use one of the available data frames as the reference configuration. Within this work, the end-systolic frame was employed as the reference configuration for all personalised models considered. The aim of this section is to assess the effect of this assumption on model accuracy and parameter identifiability / estimates. However, as the reference geometry is unknown, this effect cannot be directly assessed. Instead, this section considers different diastolic frames as the reference configuration and investigates the effect of this assumption on the behaviour of the objective function.

(a)   (b)
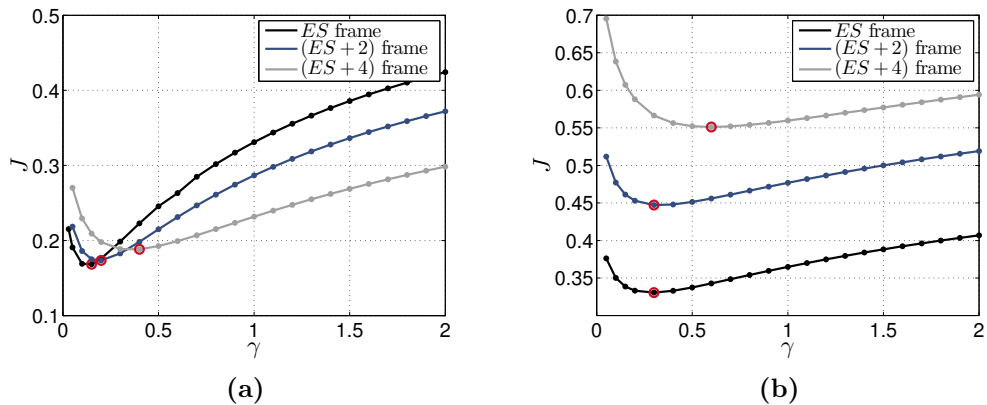
Figure 6.15 Objective function $\mathcal{J}$ over the parameter ratio γ, with three different data frames (end-systolic (ES), the second and fourth after ES) assumed as the reference geometry, for **(a)** V1 and **(b)** P1.

Fig. 6.15 compares the behaviour of $\mathcal{J}$ when different diastolic frames (end-systolic, second and fourth after end-systolic) were used as the reference geometry, for a volunteer and a patient case. In both cases, $\mathcal{J}$ presented a unique, distinct minimum for all assumed reference configurations, suggesting that γ identifiability is feasible, independent of the diastolic frame used as reference. The error between model and data increased when later diastolic frames were used as reference domains, an effect that could be accredited to the smaller deformation observed between reference and end-diastolic frames. Unlike the *in silico* test in section 4.2.4.2 where γ estimates were relatively consistent, there is a notable difference between γ estimates using the end-systolic and fourth after end-systolic frames. Nevertheless, based on the consistency in behaviour in the two cases (γ appeared to increase when later diastolic frames were employed as the reference), we can deduce that the choice of a different diastolic frame introduces a consistent bias in the results, maintaining the ability for reliable comparisons between cases.

6.4 Effect of extracted motion processing

Based on preliminary tests with motion extracted from 3D tagged MRI data, the wall volume appeared to change significantly over the cardiac cycle. Regarding this volume change as non-physiological, an additional processing step was considered essential as discussed in section 5.2.3.1, over which the extracted motion was processed to maintain constant wall volume through the cycle. The processed or projected data were constructed to ensure a close match to unprocessed data, maintaining important metrics such as stroke volume and ejection fraction and restricting the processing effect mainly to wall volume.
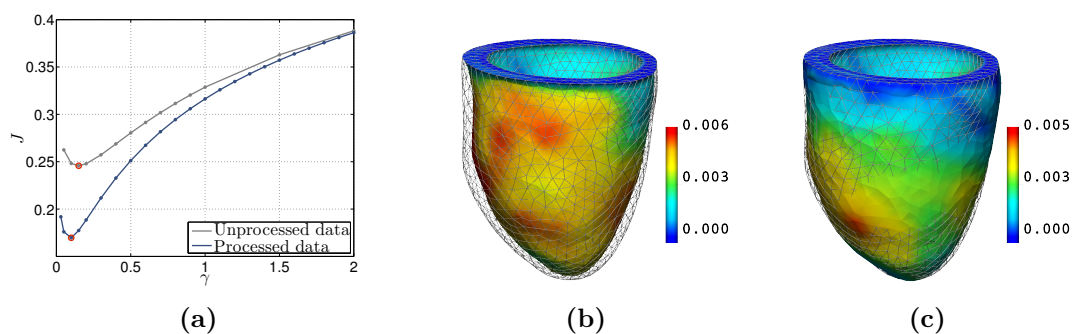
Figure 6.16 (a) Landscape of $\mathcal{J}$ over parameter ratio γ for V3, when unprocessed and processed data are used. Models assume a fibre distribution with $\theta = 50°$ and employ the RV-epicardial condition. **(b)** Simulated end-diastolic deformation for V3, with unprocessed and **(c)** processed data. Mesh lines show the data-derived deformation, while the coloured solid mesh presents the error between model and data (m).

Even though the processed data are close to the original data and maintain impor-

tant characteristics, acknowledging that this processing assumption might alter the outcomes and introduce a bias into our model, this section aims to shed some light onto the effect of this post-processing step. To this end, model accuracy and parameter identifiability / estimates were investigated using both unprocessed and processed data. Here, an example of a healthy volunteer is presented.

Firstly, as illustrated in Fig. 6.16a and 6.16c, data projection enabled lower model errors, as also observed in the majority of cases analysed. This is mainly attributed to the inability of incompressible models to match data whose volume changes dramatically over the diastolic part of the cycle (Fig. 6.16b). Furthermore, parameter identifiability was maintained and – in several cases – improved, possibly due to the smaller difference between model and processed data. Based on table 6.4, parameter estimates did not change dramatically, with the exception of cases V2 and P2, which however presented deteriorated identifiability throughout the tests. Nevertheless, based on reduced $\mathcal{J}$ values, the parameter estimates retrieved from the processed data are likely to be more accurate.

Parameter ratio estimated with unprocessed and processed data								
Case	**V1**	**V2**	**V3**	**V4**	**V5**	**P1**	**P2**	**P3**
Unprocessed data	0.15	0.8	0.15	0.4	0.4	0.4	0.9	0.2
Processed data	0.15	0.5	0.1	0.3	0.3	0.3	0.7	0.3

Table 6.4 Parameter ratio (γ) estimates, when unprocessed and processed data are used. Models assume a fibre distribution with $\theta = 50°$ and employ the RV-epicardial condition.

6.5   Study limitations

The systematic analysis followed in this chapter elucidated modelling aspects, contributing to, and improving model accuracy and parameter identifiability for the considered personalised models. The findings of this analysis, which to the best of our knowledge have not been examined before, could be of use to similar patient-specific applications. As illustrated, exploiting these modelling attributes led in significant improvement in results, with errors of $17 - 34\%$, which are within satisfactory levels, considering the strict metric used for $\mathcal{J}$. Nevertheless, the presence of non-negligible errors suggests the need for further investigation of modelling and data processing aspects.

Perhaps the most obvious source of error might stem from the choice of material law. Even though a more complex orthotropic law might be able to better capture cardiac deformation and reduce modelling error, the simplified version of the reduced Holzapfel-

Ogden law used, was selected to allow for parameter identifiability. The presence of a unique and distinct $\mathcal{J}$ minimum for all cases considered suggests that the constitutive law selected was a suitable choice, although additional patient cases should be analysed to confirm that this choice is appropriate for DCM cases.

Furthermore, based on the results presented, for certain cases and fibre distributions the lowest error was observed at the lowest ratio examined. This issue might indicate that the employed fibre distribution was not appropriate for the specific cases, not only in terms of fibre angle but mainly in terms of spatial variability. In the absence of personalised fibres though, a consistent fibre distribution had to be assumed to enable comparisons.

As previously discussed, the reference geometry was assumed to be known and correspond to the end-systolic data frame. This assumption was partially investigated by analysing the effect of choosing a different diastolic data frame as the reference configuration. A much more elaborate approach must be employed in order to estimate the actual reference state and thus assess the effect of this assumption. In fact, based on Asner *et al.*, including the reference domain as an unknown in the estimation process, resulted in deteriorated identifiability in the passive parameters, due to their coupling with the reference configuration[8]. Nevertheless, here it is hypothesised that potential bias in the parameter estimates introduced by this assumption, would be consistent, thus enabling comparisons between cases.

In the presented analysis, the objective function was computed over all data frames (including end-diastolic frame) after end systole. The number of diastolic image frames used in other studies is variable with authors considering all or part of diastole. This variability is due to assumptions on residual active tension, the presence of which is confirmed by decreasing cavity pressures even after the opening of the mitral valve, as discussed in Pasipoularides *et al*[195]. As a result, it is possible that early diastolic frames (including the end-systolic frames used as refence geometry) do not contain purely passive tissue behaviour, but also contain residual active stress. This effect was neglected during the passive parameter estimation, mainly because of the inability of accurately determining the presence of active tension in the data. However, parameter identifiability should be robust to this effect, an assumption also supported by the fact that active tension undergoes exponential decay through early stages of diastole, limiting its impact on the motion. Nevertheless, this hypothesis can be corrected for, by subsequent estimation of the active tension. Passive estimation can then be adjusted based on the frames identified as purely passive by the estimation results during this period, as discussed in Asner *et al*[8].

Additionally, the data itself or the data processing might also be responsible for the modelling error observed. Even though the use of a mask during the motion extraction process significantly reduced non-physiological tracking outcomes, the extracted

169

deformation was not quite smooth, an effect which the considered models would not be able to – and should not – reproduce. Yet, when compared against cine images, the extracted deformation was physiological through the cycle.

Despite the limitations of the pipeline discussed here, the resulting modelling error is actually within satisfactory levels, if the simplicity of the model employed is contrasted with the complexity of the human heart. Considering the main scope of this work for personalised models balancing accuracy with parameter identifiability, the current findings suggest that the proposed pipeline has been successful with respect to the objectives set.

6.6 Summary

This chapter presented tests and evaluations of the pipeline proposed in chapter 5 for the development of personalised passive cardiac mechanics models. Emphasis was largely on investigating parameter identifiability of the reduced Holzapfel-Ogden law in an *in vivo* setting. Of interest were modelling aspects that can improve model fidelity and parameter identifiability, namely fibre distribution and boundary conditions. Additional assumptions (reference domain, data processing) were analysed with respect to their effect on the results.

The thorough analysis performed over a number of volunteer and patient cases enabled safe conclusions on the factors contributing to model fidelity and parameter identifiability. Specifically, both model accuracy and parameter identifiability were significantly improved when the effect of the RV was taken into account through an appropriate epicardial boundary condition. Additionally, based on the available data and the material law employed, the fibre angle could not be retrieved, yet a fibre distribution of $\theta = 50°$ was shown to consistently present the lowest error, compared to $\theta = 60°$ and $\theta = 70°$ distributions. This fibre angle is similar to values reported in *ex vivo*[208,65] and *in vivo*[251,237] human DTMRI studies, although the studies report variation in angle magnitude between endocardium and epicardium, and between basal and apical regions. Through systematic investigations of the fibre distribution, boundary conditions and additional aspects on several cases, important modelling assumptions can now be replaced by informed decisions, optimising the model's accuracy and parameter identifiability.

Additionally, variations in identifiability behaviour and model fidelity between cases highlighted their dependence on the available data. Specifically, in cases with larger diastolic deformation, identifiability was improved as the rich deformation field allowed for better stratification of parameters outcomes. This observation highlights the importance of adequate deformation and sufficient data quality for unique parametri-

sation.

Throughout all the volunteers and patients cases considered, the objective function presented a unique and distinct minimum confirming that parameter identifiability for the reduced version of the Holzapfel-Ogden law is maintained *in vivo*. Combined with errors within acceptable levels for all cases, these findings suggest that the employed material law is suitable for the personalised models considered. Further, the consistency in results with respect to both model fidelity and parameter identifiability demonstrate a robust and reliable pipeline, while the large number of cases – and sub-cases – analysed confirms its efficiency. In summary, the systematic analysis presented ensures a reliable and efficient pipeline for model personalisation, setting the foundation for case-by-case comparisons, considered in chapter 7.

7 Comparative analysis of *in vivo* cases

Dilated cardiomyopathy (DCM) is a progressive cardiac disorder associated with enlarged ventricles[128,52], and an overall deterioration of the heart's contractile function characterised by reduced ejection fraction and contractility[166,89] (section 1.2). Studies have suggested that significant LV remodelling is observed in DCM, including changes in LV size and shape[128,87], as well as tissue composition[16,39], architecture[16,190] and stiffness[47,190]. This adverse remodelling affects not only contractile, but also diastolic cardiac performance, rendering diastolic function a key determinant in the development of DCM. Despite significant research interest into the disease, little is understood about the mechanisms contributing to it and particularly the role of diastolic dysfunction.

The personalised models developed through the pipeline proposed in chapter 5, provide a framework for comparisons between DCM patients and healthy volunteers with the ultimate goal of assisting in a better understanding of the disease. The systematic evaluation in chapter 6, indicated a robust pipeline enabling sufficient model accuracy and unique parametrisation. This observation suggests that the developed patient-specific models can be used as a reliable tool for a preliminary assessment of the disease.

The aim of the this chapter is to present some preliminary comparisons between DCM patients and healthy volunteers, leading the way for thorough analyses of the mechanisms underpinning DCM. Initially, important clinical metrics are derived directly from the available imaging data, providing valuable information on structural and functional differences between DCM patients and normals (section 7.1). Subsequently, comparisons are extended to personalised models developed through the proposed pipeline, which provide information, inaccessible solely through clinical data. Comparisons focus on passive parameters estimates – a key component and indicator of diastolic function – and the factors influencing the estimates (section 7.2). Additional information about DCM characteristics is obtained through comparisons of regional strain distributions (section 7.3). Further, data-to-model strain comparisons provide an additional means for testing the proposed pipeline and modelling assumptions, strengthening the preliminary findings discussed (sections 7.4 and 7.5).

7.1 Analysis of data-derived information

The wealth of clinical data available as part of the present study provides valuable insights into individual hearts' anatomy and kinematics. Following the data processing pipeline in section 5.2, quantified information was extracted, allowing for of comparisons of basic clinical metrics between DCM and normals. Clinical metrics derived from the available data and used throughout the model personalisation process are presented in table 7.1 along with basic information on the volunteers and patients.

Case	Age	G	HR	EDV	ESV	SV	EF	t_{ED}	t_{ES}	$\frac{LA}{SA}$	$\frac{LA_{ED}-LA_{ES}}{LA_{ED}}$	EDP$^{\text{est}}$
	(yrs)	-	(bpm)	(ml)	(ml)	(ml)	-	(mm)	(mm)	-	-	(mmHg)
						Volunteers						
V1	28	M	66	129.50	64.57	64.93	0.50	8.03	10.61	1.35	0.13	10.46
V2	29	F	73	100.85	47.67	53.18	0.53	7.09	9.07	1.59	0.14	16.09
V3	48	M	62	152.55	67.43	85.12	0.56	8.73	12.1	1.40	0.15	10.23
V4	35	F	77	93.19	45.99	47.20	0.51	6.58	8.74	1.59	0.13	8.76
V5	41	M	64	120.36	53.51	66.85	0.56	8.38	11.38	1.33	0.14	11.35
Mean	36.2	-	68.4	119.29	55.84	63.46	0.53	7.76	10.34	1.45	0.14	11.38
SD	8.4	-	6.35	23.63	9.74	14.60	0.03	0.90	1.45	0.13	0.01	2.79
						DCM Patients						
P1	28	F	60	141.12	81.91	59.21	0.42	7.92	10.11	1.23	0.12	16.27
P2	55	M	63	179.26	95.15	84.11	0.47	7.94	10.33	1.21	0.10	17.57
P3	43	F	64	136.19	79.88	56.31	0.41	6.54	8.24	1.24	0.10	11.55
Mean	42	-	62.3	152.19	85.65	66.54	0.43	7.46	9.56	1.22	0.11	15.13
SD	13.5	-	2.08	23.57	8.29	15.28	0.03	0.80	1.15	0.18	0.01	3.17

Table 7.1 Participant's general information are considered (age and gender (G)). Clinical metrics derived from the available data are presented as well (HR: heart rate (beats per minute), EDV: end-diastolic volume, ESV: end-systolic volume, SV: stroke volume, EF: ejection fraction, t_{ED} and t_{ES}: wall thickness at end diastole and end systole, LA/SA: ratio of long-axis to short-axis dimensions at end diastole, $\frac{LA_{ED}-LA_{ES}}{LA_{ED}}$: long-axis shortening, EDP$^{\text{est}}$: end-diastolic pressure estimate).

The reported heart rate was measured during the acquisition of the tagged MRI sequence. End-diastolic and end-systolic volumes were computed from the deformed meshes which followed the 3D tagged MRI motion, using the approach described in section 5.3.3.1 and Eq. 5.13. Stroke volume and ejection fraction were directly computed from the cavity volumes ($SV = EDV - ESV$, $EF = \frac{EDV - ESV}{EDV}$). It should be noted that the reported volumes differ from standard clinical volume metrics, due to the truncation of the LV mesh at a plane lower than the valve plane.

Wall thickness at end diastole and end systole was approximated by the ratio of the wall volume over the mean surface area of encocardial and epicardial surfaces. The long-axis length was computed as the maximum distance of an epicardial node to the

centre point of the base. The short-axis dimension was computed as twice the mean distance of each epicardial node to the long-axis. The end-diastolic cavity pressure was estimated using a surrogate measure based on the E/E_a ratio[167], as described in section 5.4.
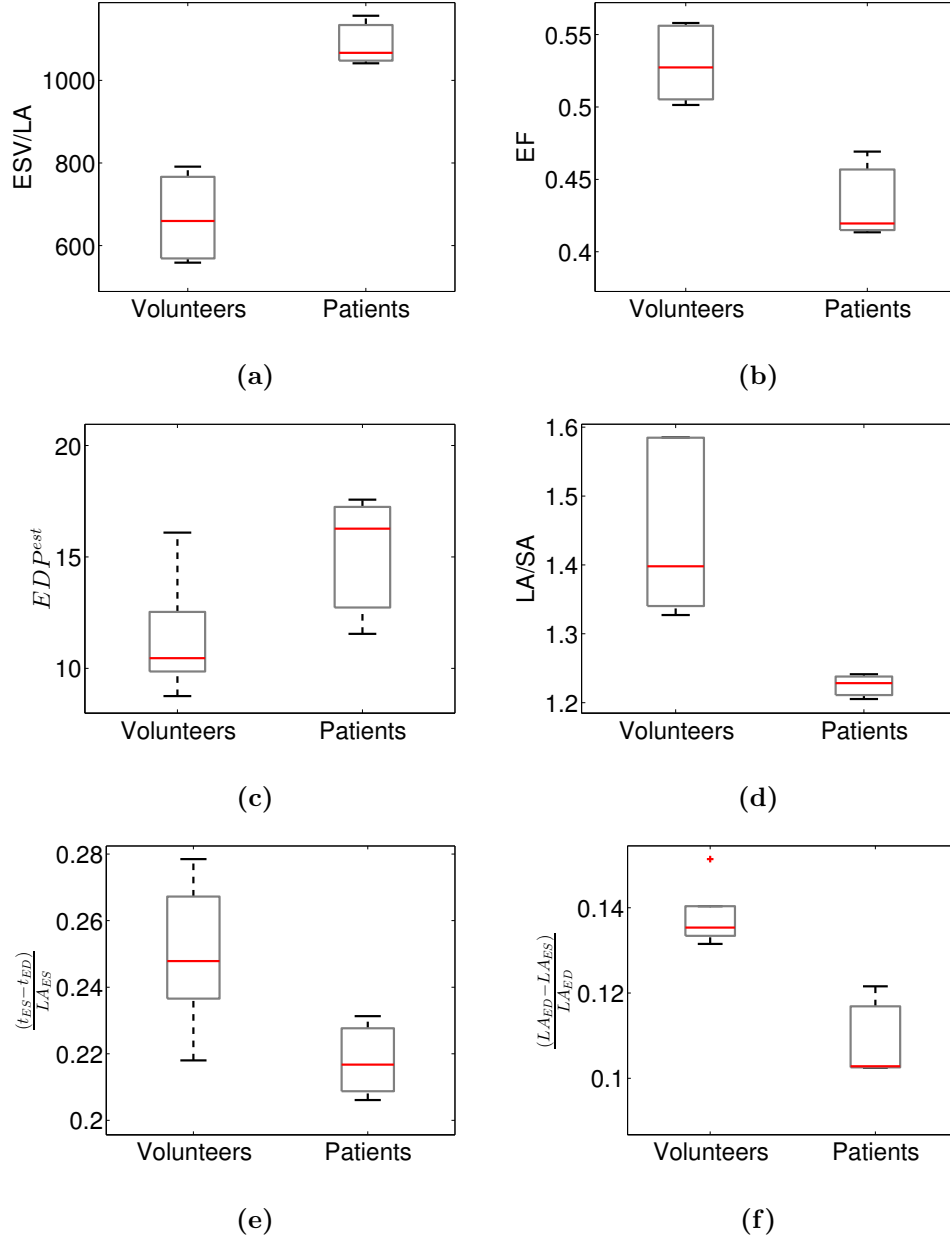
Figure 7.1 Comparison of **(a)** end-systolic volume normalised over long-axis length at end diastole, **(b)** ejection fraction, **(c)** end-diastolic pressure estimate, **(d)** ratio of long-axis to short-axis dimensions at end diastole, **(e)** wall thickening over end-systolic thickness **(f)** long-axis shortening over long-axis length at end diastole, between the volunteer and patient groups. Red lines show the median, the boxes' edges denote 25th and 75th percentiles, while black lines show extreme data points.

Differences in the presented quantities between healthy volunteers and DCM patients

were assessed through comparisons of the mean and standard deviation of each group, also presented in table 7.1. Additionally, unpaired $t-$tests were performed to assess the statistical significance of these differences, although in certain cases the sample size was too small to allow for statistical significance. For ease of presentation, this information is also presented graphically per group in Fig. 7.1, allowing for easier comparisons between DCM patients and healthy volunteers.

Despite the small number of volunteers and patients, distinct differences were identified within the two groups (table 7.1 and Fig. 7.1). Pronounced increases were observed in end-diastolic and end-systolic cavity volumes in DCM hearts (table 7.1), as extensively reported in literature[5,284,128]. To avoid biased comparisons due to cavity volumes computed after mesh truncation, comparisons were also performed over the end-diastolic and end-systolic volumes, normalised by the end-diastolic long-axis length. Normalised end-diastolic volumes were notably higher in the patient group compared to the volunteer group (1930.5 ± 215.4 ml/m vs. 1425.5 ± 246.7 ml/m, $p = 0.03$), due to the ventricular dilation which is a key characteristic of DCM. Even more pronounced was the difference in normalised end-systolic volumes (Fig. 7.1a) which were significantly higher for DCM patients compared to normals (1088.2 ± 60.5 ml/m vs. 668.0 ± 105.5 ml/m, $p \leq 0.001$). Stroke volume did not present strong differences as anticipated, based on the increase in both end-diastolic and end-systolic volumes. Nevertheless, ejection fraction (Fig. 7.1b) was markedly lower in the patient group (0.43 ± 0.03 vs. 0.53 ± 0.03, $p \leq 0.005$), marking the deteriorated contractile and diastolic filling function typically associated with DCM.

Additional geometrical differences between normals and DCM patients can be observed through the ratio of long-axis to short-axis dimensions. The decrease in ratio (Fig. 7.1d) for DCM hearts (1.22 ± 0.18 vs. 1.45 ± 0.13, $p = 0.03$) is characteristic of the change in shape from elliptical to spherical observed in DCM[128,87]. Moreover, wall thickness was moderately decreased in DCM patients compared to normals both at end diastole and end systole – though this difference was not statistically significant – as also reported by other studies[190,42]. Nevertheless, a more evident trend ($p = 0.07$) was observed in the wall thickening ratio $(t_{ES} - t_{ED})/t_{ES}$, with the ratio decreasing in the DCM group (Fig. 7.1e). Similar findings have been reported in the literature[42,284,279], indicating reduced wall thickening during contraction and thus impaired contractile function in the presence of DCM. Similarly, normalised long-axis shortening (Fig. 7.1f) was significantly decreased in the DCM group ($p \leq 0.005$)

Another key distinction was observed in the estimated end-diastolic pressure (EDP[est]). In accordance with previous studies[128,5,89] and despite outliers, EDP[est] was notably higher in the DCM group (15.15 ± 3.17 mmHg) compared to normals (11.34 ± 2.79 mmHg), although this difference did not reach statistical significance ($p = 0.13$).

7.2 Passive parameter estimation

This section extends the comparisons between DCM and normals to metrics derived from personalised diastolic models. Building on the findings of chapter 6, the RV-epicardial boundary condition and a fibre distribution of $\theta = 50°$ were employed for the creation of the personalised models considered in this chapter. The models employ the reduced Holzapfel-Ogden law (Eq. 4.5), shown to provide adequate model fidelity and parameter identifiability *in vivo* (section 6.1.4). To allow for more accurate parameter estimates, parameter sweeps were repeated considering values closer to the γ estimates obtained in the parameter identifiability study in section 6.1 and presented in table 6.2 ($\gamma = a/a_f$). The absolute values of the parameters a and a_f were retrieved through scaling by the ratio between the estimated (EDP$^{\text{est}}$) and the simulated (λ_ℓ^{ED}) end-diastolic cavity pressure, as described in section 5.4. Parameter estimates and quantities relevant for the parameter estimation process are presented in table 7.2

Case	γ	λ_ℓ^{ED}	EDP$^{\text{est}}$/λ_ℓ^{ED}	EF	a	a_f
	-	(mmHg)	-	-	(Pa)	(Pa)
Volunteers						
V1	0.13	4.73	2.21	0.50	278.91	2214.73
V2	0.51	13.49	1.19	0.53	608.31	1192.78
V3	0.09	7.55	1.36	0.56	121.98	1355.35
V4	0.25	6.87	1.28	0.51	318.98	1275.90
V5	0.29	13.68	0.83	0.56	240.71	830.02
Mean	0.26	9.27	1.38	0.53	315.58	1373.75
SD	0.17	4.08	0.51	0.03	179.97	511.26
DCM Patients						
P1	0.29	3.71	4.39	0.42	1273.21	4390.41
P2	0.65	8.65	2.03	0.47	1320.83	2032.05
P3	0.26	2.59	4.46	0.41	1160.59	4463.80
Mean	0.40	4.99	3.63	0.43	1251.55	3628.75
SD	0.22	3.22	1.38	0.03	82.29	1383.27

Table 7.2 Parameter ratio γ estimates for the volunteers and patients under consideration. The simulated LV end-diastolic pressure (λ_ℓ^{ED}) and the ratio between measured and simulated end-diastolic pressure (EDP$^{\text{est}}$/ λ_ℓ^{ED}) are presented as well, providing the absolute values for the parameters a and a_f. Ejection fraction (EF) is presented again, to assist comparisons.

Based on table 7.2, the values of the parameter ratio $\gamma = a/a_f$ are in all cases strictly lower than 1, indicating that the isotropic parameter a is consistently lower than the

fibre parameter a_f. Noting the equal values for the exponents b and b_f in Eq. 4.5, this suggests that the tissue is stiffer in the fibre direction, for all cases considered. This observation is in agreement with various experimental[188,57] and modelling[82,266] studies reporting that the cardiac tissue is stiffer in the fibre direction.

However, the values of the parameter ratio γ show notable variation, ranging between $(0.09 - 0.65)$. Moreover, no significant difference in γ can be noted between the volunteer and patient groups. Although the mean ratio is higher for the patient group, the large variation within groups does not allow for statistical significance and definite conclusions. These observations indicate that γ, a measure of the degree of anisotropy, is not a constant / consistent quantity between cases. More importantly, it is possible to suggest based on these findings, that the degree of anisotropy is not markedly affected by the significant ventricular remodelling occurring in the DCM hearts. Nevertheless, a larger sample might accentuate the differences between the groups, ultimately suggesting a change in the degree of anisotropy with DCM.

The estimation of the actual values of a and a_f though, provides more distinct differences allowing for more reliable conclusions (table 7.2, Fig. 7.2). Specifically, the isotropic parameter a is distinctly higher in the DCM group compared to normals $(1251.55 \pm 82.29$ Pa vs. 315.58 ± 179.97 Pa, $p = 0.0002)$. A similar strong trend is also observed in the fibre parameter a_f $(3628.75 \pm 1383.27$ Pa vs. 1373.75 ± 511.26 Pa, $p = 0.014)$. With both isotropic and fibre parameters significantly higher in the DCM group, it is suggested that the cardiac tissue becomes stiffer in DCM models.
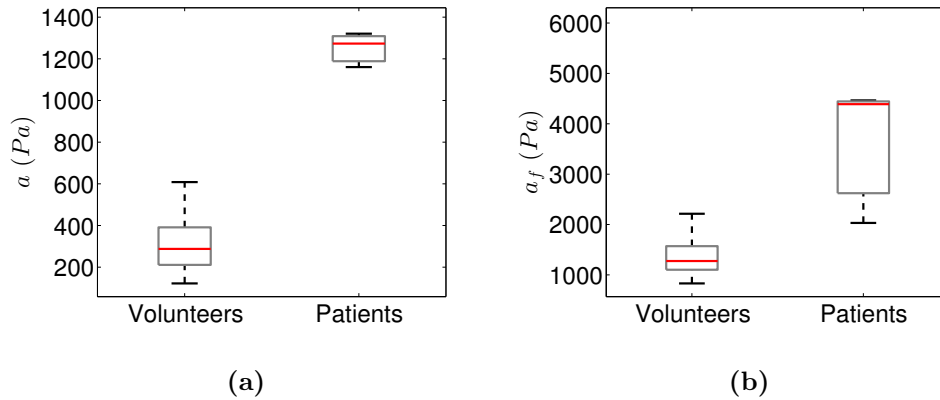
Figure 7.2 Comparison of (a) isotropic parameter a and (b) fibre parameter a_f between the volunteers' and patients' groups. Red lines show the median, the boxes' edges denote 25th and 75th percentiles, while black lines show extreme data points.

Analysing this observation further, we can consider the estimation of the absolute values of the parameters a and a_f as described in section 5.4, with $a_f^{sim} = 1000$Pa, which can

be summarised as,

$$a = 1000\gamma \frac{EDP^{est}}{\lambda_\ell^{ED}}, \qquad a_f = 1000 \frac{EDP^{est}}{\lambda_\ell^{ED}}. \tag{7.1}$$

These relations suggest that the parameters are affected by several possibly inter-related factors. Taking advantage of the clearly outlined pipeline and modelling assumptions used, an interpretation of the increased stiffening in DCM models was attempted.

Firstly, with only a directly dependent on the estimated ratio γ, the increase in both parameters should be mainly attributed to the ratio of estimated to simulated cavity pressures ($EDP^{est}/\lambda_\ell^{ED}$), which based on table 7.2 was found to be significantly higher in DCM (3.63 ± 1.38 vs. 1.38 ± 0.51, $p = 0.014$). This dependence is again two-fold: the parameters are directly related to the measured EDP^{est} and inversely proportional to the simulated λ_ℓ^{ED}. As EDP^{est} is higher in DCM (although this observation did not reach statistical significance), this factor can be considered partially responsible for the increase in parameter values.

The second dependence stems from the simulated cavity pressure (λ_ℓ^{ED}), which is notably lower in the DCM group (even though this difference was not statistically significance with $p = 0.17$). This factor appears to be strongly dependent on the ejection fraction ($p = 0.03$), yielding higher λ_ℓ^{ED} for higher ejection fractions. This relation can be attributed to the fact that increased cavity pressure is required for a more pronounced LV inflation. The inverse relation between parameters and ejection fraction can justify the higher parameter estimates for DCM hearts, where ejection fraction is significantly lower. Similarly, V1 who presented the lowest ejection fraction amongst volunteers, also had a notably higher a_f. Finally, λ_ℓ^{ED} is also affected by the parameter ratio, since for a constant a_f, a larger a would yield a stiffer heart thus requiring a higher pressure for inflation to the same end-diastolic volume. The dependence of λ_ℓ^{ED} on the ratio is mainly affecting a_f, since in the estimation of a this effect is counteracted by scaling by γ whose influence appears to be stronger. The inverse relation between a_f and γ justifies the fact that P2 who presented the highest parameter ratio between patients also had the lowest a_f.

Taking the results discussed above into account, the absolute values of the passive parameters a and a_f are affected by several factors of the proposed pipeline, the most important being the measured end-diastolic pressure, the ejection fraction and the parameter ratio estimate γ. The higher end-diastolic pressure, low ejection fraction and increased parameter ratio γ observed in the DCM cases all contribute to the increased a and a_f values. The factors hypothesised to contribute in a and a_f values are summarised in table 7.3.

	γ	EF	EDP$^{\text{est}}$	λ_ℓ^{ED}
a	$\Uparrow$	$\Downarrow$	$\Uparrow$	$\Downarrow$
a_f	$\Downarrow$	$\Downarrow$	$\Uparrow$	$\Downarrow$
λ_ℓ^{ED}	$\Uparrow$	$\Uparrow$	-	$\Uparrow$

Table 7.3 Schematic representation of factors possibly contributing in the estimation of passive parameters a and a_f. Upward arrows in each row indicate an increase in the a, a_f and λ_ℓ^{ED} with an increase in γ, ejection fraction, EDP$^{\text{est}}$ and λ_ℓ^{ED}. Similarly, downward arrows denote decrease in row-quantities with increase in column-quantities.

7.3 Preliminary analysis of strain distributions

The analysis of data- and model-derived information presented so far has provided important insights in global characteristics of motion and behaviour. In order to allow for assessment of regional cardiac behaviour in both normals and DCM, this section focuses on the estimation of regional strain distributions. Analysis of regional behaviour might elucidate important information, inaccessible from global metrics. Further, comparing strain distributions between data and model will provide a means for assessing model accuracy.

Each personalised geometry was divided in 16 regions according to the American Heart Association (AHA) recommendations[29] as illustrated in Fig. 7.3. The apex was not included as a separate 17$^{\text{th}}$ region due to the inability of accurately identifying its location. Strains were therefore computed on the first 16 AHA regions, for both data and model, for all volunteers and patients considered.

1. basal anterior
2. basal anteroseptal
3. basal inferoseptal
4. basal inferior
5. basal inferolateral
6. basal anterolateral
- - - - - - - - - - - - - - - - - -
7. mid anterior
8. mid anteroseptal
9. mid inferoseptal
10. mid inferior
11. mid inferolateral
12. mid anterolateral
- - - - - - - - - - - - - - - - - -
13. apical anterior
14. apical septal
15. apical inferior
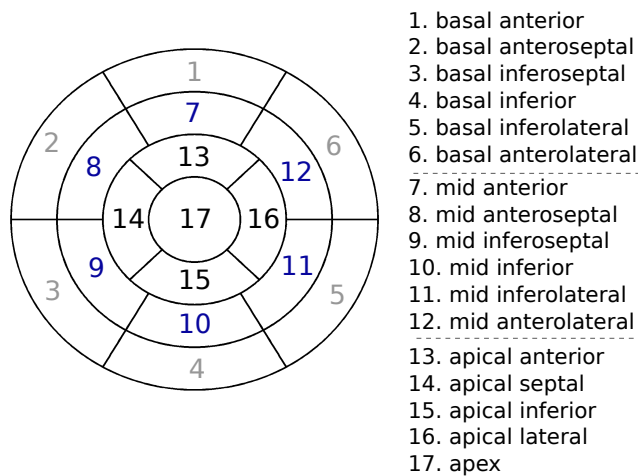16. apical lateral
17. apex

Figure 7.3 Display of the name and location of the 17 *AHA* segments of the LV[29]. Regions marked with grey, blue and black colour correspond to the basal, mid-ventricle and apical regions, respectively.

Based on the Lagrange-Green definition of strain ($\boldsymbol{E} = \frac{1}{2}(\boldsymbol{C} - \boldsymbol{I})$), strain is dependent on spatial derivatives of data-derived displacement, which is very sensitive to noise. Taking into account the potential local non-smooth deformations extracted from 3D tagged MRI, this noise sensitivity could have a severe impact on strain distributions. In order to avoid this sensitivity to noise and possibly non-physiological outcomes, an alternative way of computing strain was employed.

Considering the fundamental definition of the deformation gradient ($d\boldsymbol{x} = \boldsymbol{F}d\boldsymbol{X}$), $\boldsymbol{F}$ maps infinitesimal vectors $d\boldsymbol{X}$ in the undeformed domain to their corresponding vectors $d\boldsymbol{x}$ in the deformed domain. Instead of computing $\boldsymbol{F}$ at every node in the geometry, an approximate value $\bar{\boldsymbol{F}}$ per AHA region was estimated. Specifically, for each mesh node of the AHA region, the "infinitesimal" vectors $d\bar{\boldsymbol{x}}$ and $d\bar{\boldsymbol{X}}$ were computed with respect to the centroid of the region in the deformed and undeformed domain, respectively. $\bar{\boldsymbol{F}}$ for every AHA region was then computed as the tensor that satisfied $d\bar{\boldsymbol{x}} = \bar{\boldsymbol{F}}d\bar{\boldsymbol{X}}$ for all nodes k in the region, in a least-squares sense:

$$\bar{\boldsymbol{F}} = \min_{\boldsymbol{A} \in \mathbb{R}^{3\times3}} \sum_k ||d\bar{\boldsymbol{x}}_k - \boldsymbol{A}d\bar{\boldsymbol{X}}_k||^2. \tag{7.2}$$

Strain was subsequently computed using the approximated deformation gradient per region as

$$\boldsymbol{E} = \frac{1}{2}(\bar{\boldsymbol{F}}^T \bar{\boldsymbol{F}} - \boldsymbol{I}). \tag{7.3}$$

The use of definition 7.3 for strain avoids bias introduced by noise-sensitive derivative estimates. Combined with the use of mean quantities per AHA region, this strain definition should reduce noise sensitivity, providing physiological strains.

7.3.1 Characterisation of average data-derived strain

Strains were approximated using the above-mentioned definition (Eq. 7.3) for each AHA region for all volunteers and patients. For all cases, the reported values correspond to strains at end diastole with respect to end systole. Strain in the radial ($E_{rr} = \boldsymbol{Er} \cdot \boldsymbol{r}$), longitudinal ($E_{ll} = \boldsymbol{El} \cdot \boldsymbol{l}$) and circumferential ($E_{\theta\theta} = \boldsymbol{E\theta} \cdot \boldsymbol{\theta}$) directions were computed for each region, with $\boldsymbol{r}$, $\boldsymbol{l}$ and $\boldsymbol{\theta}$ the unit vectors in the radial, long-axis and circumferential directions, respectively. The spectral norm of the strain tensor was computed as well ($||\boldsymbol{E}||_2 = \sqrt{\lambda_{max}(\boldsymbol{EE})}$), providing a global strain estimate.

Average values of strain metrics over all regions were considered, to provide overall deformation characteristics (table 7.4). Average radial strain at end diastole was negative for all cases, due to wall thinning while active tension gradually decays over diastole. In contrast, average longitudinal and circumferential strains were positive for all cases, indicative of LV lengthening and dilation observed during diastole. The average strain values obtained for the volunteers' group (-0.14 ± 0.02, 0.18 ± 0.05, 0.18 ± 0.02, for E_{rr},

E_{ll} and $E_{\theta\theta}$, respectively) are in agreement with values reported by Young *et al.* for healthy volunteers (0.15 ± 0.07, -0.17 ± 0.02, -0.2 ± 0.02, for E_{rr}, E_{ll} and $E_{\theta\theta}$, respectively), where strains were reported at end systole with respect to end diastole [286].

The average strain metrics reported enable direct comparisons between the volunteer and patient groups. As indicated by the decrease in $||\boldsymbol{E}||_2$ in the DCM group (0.29 ± 0.03 vs. 0.24 ± 0.003, $p = 0.02$), strain was decreased in DCM hearts. In fact, strain in radial and circumferential directions was notably reduced in the patients' group ($p < 0.1$ for both E_{rr} and $E_{\theta\theta}$). Decrease was also observed in longitudinal strain, even though not statistically significant.

Case	E_{rr}	E_{ll}	$E_{\theta\theta}$	$||\boldsymbol{E}||_2$
Volunteers				
V1	-0.13	0.19	0.17	0.27
V2	-0.13	0.13	0.19	0.28
V3	-0.18	0.26	0.18	0.34
V4	-0.14	0.14	0.17	0.30
V5	-0.15	0.19	0.19	0.29
Mean	-0.14	0.18	0.18	0.29
SD	0.02	0.05	0.01	0.03
DCM Patients				
P1	-0.13	0.16	0.14	0.24
P2	-0.12	0.15	0.17	0.25
P3	-0.12	0.14	0.15	0.24
Mean	-0.12	0.15	0.15	0.24
SD	0.006	0.01	0.01	0.003

Table 7.4 Average data strain at end diastole with respect to end systole for all volunteers and patients under consideration. Strain in the radial (E_{rr}), longitudinal (E_{ll}) and circumferential ($E_{\theta\theta}$) directions along with strain norm ($||\boldsymbol{E}||_2$) are presented.

7.3.2   Regional strain characterisation

In order to provide an assessment of regional myocardial behaviour, strain per AHA region was computed from data for all volunteers and patients considered. Figures of radial, longitudinal and circumferential strain per AHA region for all cases are presented in Appendix E. Notable variations in both regional distribution and magnitude were observed between the cases considered, hindering the identification of consistencies between cases or differences between groups.

Nevertheless, certain observations appear to be consistent in the majority of cases and

are also validated by Fig. 7.4 which displays strains per AHA region, averaged over the volunteers and patients groups. Specifically, for most cases considered, the maximum (in magnitude) radial strains were observed in the equatorial region, as also indicated in the average distribution in Fig. 7.4a. This observation has also been reported in the literature in healthy volunteers[286] as well as DCM cases[42,60]. Additionally, in the majority of cases, minimum longitudinal strain was observed in the basal-septal region, while maximum circumferential strain was observed in the basal-lateral region of the LV. These observations are in agreement with average quantities in Fig. 7.4b and 7.4c, respectively.
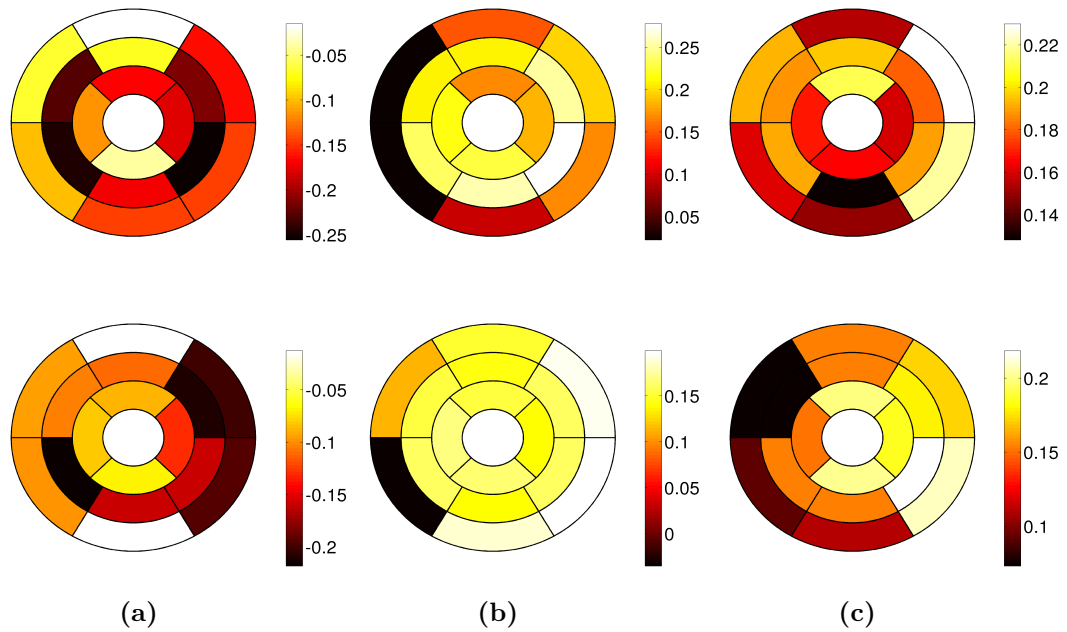
Figure 7.4 Average strain values per AHA region over all volunteers (top row) and patients (bottom row) considered in **(a)** radial, **(b)** longitudinal and **(c)** circumferential directions.

7.3.2.1 Data-model strain comparisons

Strain per AHA region was also computed for the personalised models created, to enable qualitative regional comparisons between data and model. Data and model strains per AHA region were computed for all volunteers and patients and are presented in Appendix E. Representative examples of one volunteer (V5) and one patient (P3) cases are presented in Fig 7.5 and 7.6, respectively.

Based on Fig. 7.5 and 7.6 and Appendix E, notable similarities can be observed between spatial distributions of data and model strains. Despite differences in magnitude, the regions of maximum and minimum strains are – in most cases – consistent between model and data. The similarity in strain distributions between data and model sug-

gests that the personalised models developed, reasonably reflect the true data-derived strains.

Interestingly, the most notable differences between data and model occur at regions of sharp variations in data-derived strain. Due to the global passive parameters and homogeneous endocardial boundary condition used, along with the continuum mechanics framework employed, model-deformation would most likely be more smooth than data-derived deformation. To this end, models are not likely to replicate sharp variations present in data, while maximum and minimum strain values are mediated in the model compared to data.

Another interesting observation stems from the longitudinal strain of V2 and V4 (Fig. E.2c, E.4c, respectively). In only these two cases, longitudinal strain was negative in the basal region, suggesting that this part of the LV was shortening instead of lengthening over diastole. This issue was possibly due to data / motion tracking artefacts. Interestingly, as the model is not set up to reproduce such a behaviour, this could be a reason for higher modelling errors and deteriorated identifiability observed for these two volunteers in chapter 6. In fact, V2 and V4 also presented the largest errors in E_{rr} and E_{ll} between model and data.

Volunteer 5 (V5)

Volunteer 5 (V5)

Figure 7.5 Strain for V5 at end diastole per *AHA* region in **(a, b)** radial, **(c, d)** longitudinal and **(e, f)** circumferential directions. Strain is computed for **(a, c, e)** data and **(b, d, f)** model with respect to end systole.

Patient 3 (P3)

Patient 3 (P3)

Figure 7.6 Strain for P3 at end diastole per *AHA* region in **(a, b)** radial, **(c, d)** longitudinal and **(e, f)** circumferential directions. Strain is computed for **(a, c, e)** data and **(b, d, f)** model with respect to end systole.

7.4 Discussion and study limitations

7.4.1 Parameter estimation

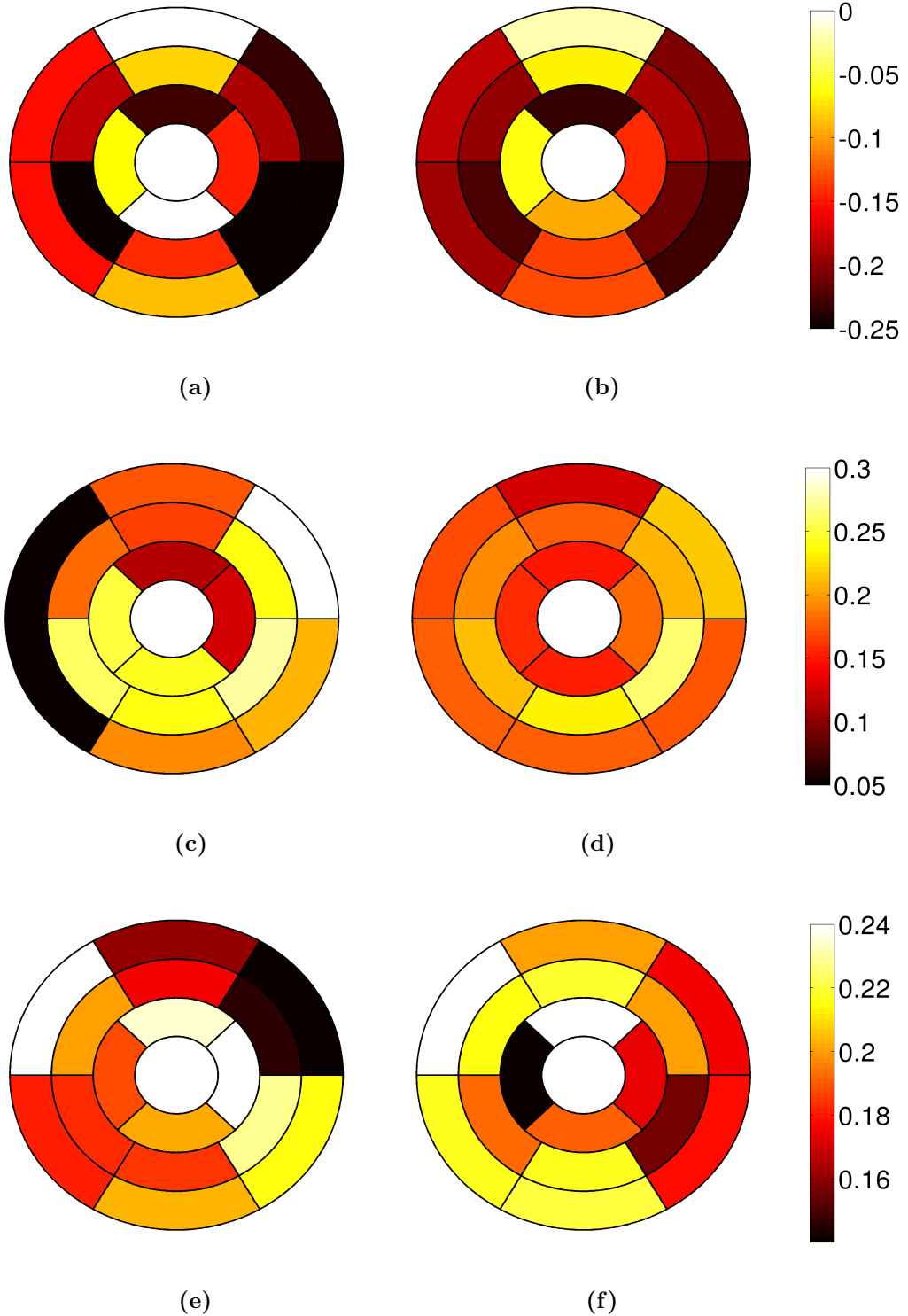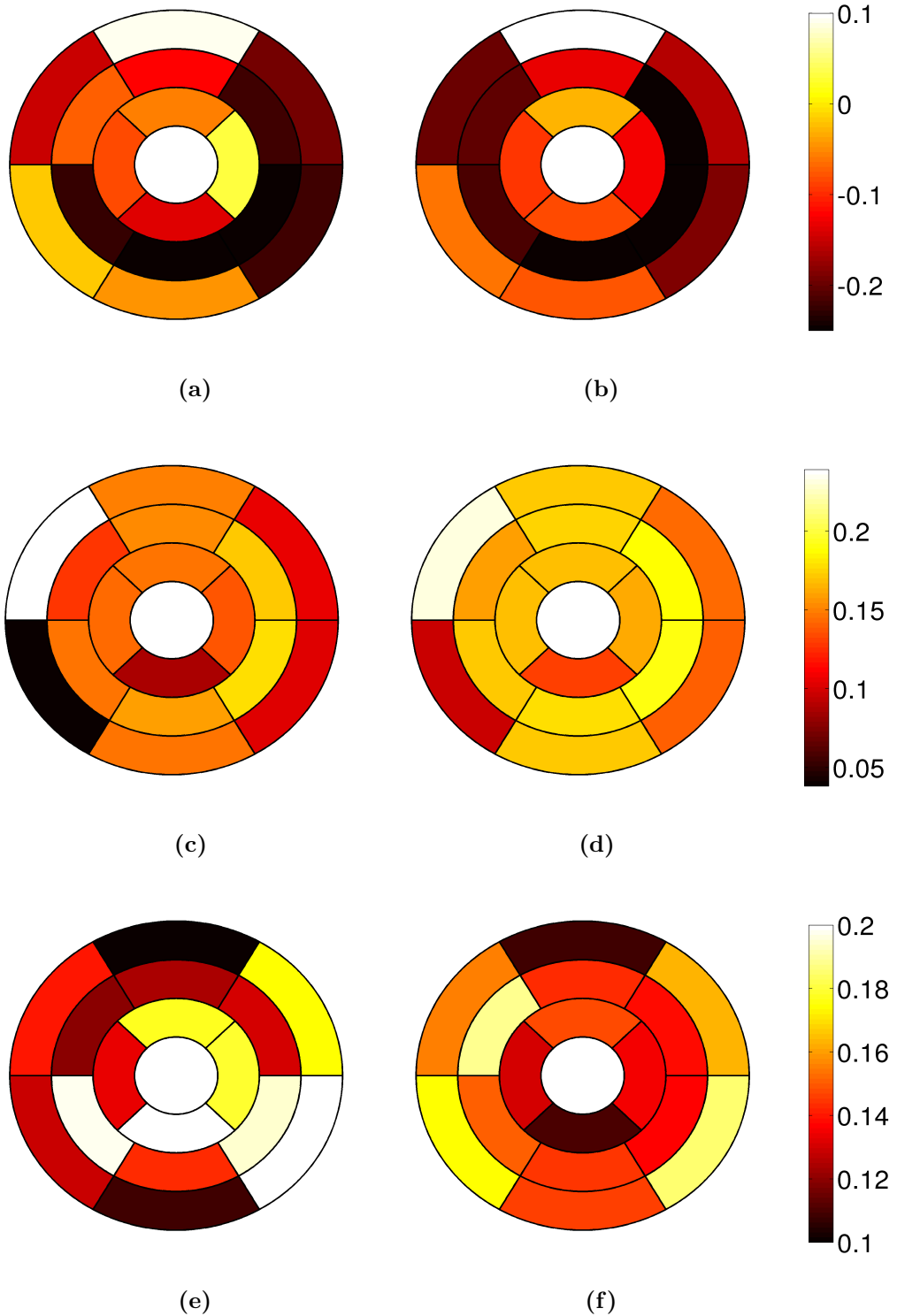The increase in stiffness observed for the DCM models analysed in this chapter, has also been reported for mice[190,47]. Omens *et al.* deduced increased stiffness based on pressure-volume analysis, as well as by an increase in the Guccione[82] scaling parameter, required to match simulated and measured epicardial strains[190]. Similarly, using the same DCM model for genetically engineered mice, Costandi *et al.* estimated the Guccione scaling parameter based on pressure-volume data, reporting progressively increased values for later stages of the disease[47]. The observed increased stiffness which is consistent with increased collagen, is thought to be linked to structural changes in cellular and tissue level which contribute to the disease's progression[190]. Further, Costandi *et al.* have proposed that the elevated stiffness in early stages of DCM acts as a compensatory mechanism, temporarily improving systolic function. Based on this result, increased stiffness is thought to be a key determinant in the development of DCM[190,138,47].

The personalised models analysed in this chapter extend the observation of increased stiffness in humans and provide a framework for further research and understanding of this aspect. For instance, exploiting the outlined model personalisation process, factors contributing to the elevated parameter values were identified. More importantly, the observation of increased stiffness was based on a carefully selected model personalisation process focusing on unique parameterisation, which provides confidence in the parameter estimates and conclusions.

Nevertheless, the parameter estimates can only suggest increased stiffness within the modelling framework employed. As the modelling assumptions are likely to introduce a bias into the parameter estimates, parameter identifiability does not necessarily imply parameter accuracy. An important model assumption, for instance, is the employed fibre distribution which even though selected based on model fidelity and parameter identifiability arguments (section 6.1.3), might differ notably from the actual fibre architecture. This variation is likely to be more pronounced in DCM, with studies reporting structural changes affecting fibre architecture[92,190] and observing larger fibre angles for DCM hearts[65].

Exploiting the clearly outlined modelling framework which enabled an assessment of the effect of modelling assumptions, we can hypothesise the impact of a different fibre distribution on the parameter estimates. Accordingly, assuming a larger fibre angle for DCM models would lead to a decrease in γ estimate (section 6.1.3), which based on table 7.3 would, in turn, result in an increase in a_f. With the effect of γ on a being less pronounced, assuming a fibre distribution of a larger fibre angle for DCM models

would still suggest increased stiffness compared to normals.

Finally, parameter estimates are also dependent on the end-diastolic pressure. In the absence of invasive pressure measurements, a surrogate measure was used based on the ratio E/E_a. Even thought the parameter estimates are sensitive to this approximation, the use of this ratio as an estimate of end-diastolic pressure has been verified over a range of healthy volunteers and patients, including DCM cases[167].

7.4.2 Strain characterisation

Comparisons of different average strain metrics in section 7.3.1 have suggested reduced strains for DCM patients compared to normals. The observation of a hypokinetic LV wall in DCM has often been reported in the literature in the form of both reduced ejection fraction as well as decreased strains. Several studies have reported reduced radial strains, focusing on the deteriorated contractile function indicated by the reduced wall thickening[284,190,42]. Omens *et al.* also reported reduction in longitudinal strains[190] compared to normals, while Duan et al. observed significant reductions in longitudinal, radial and circumferential strains[60].

Even though average strains measures provided a clear distinction between normals and patients, characterisation of regional strain distributions was more challenging. Significant variations in strain patterns were observed between cases, hindering the identification of consistent behaviours. Although some regional strain similarities were discussed in section 7.3.2, more volunteers and patients need to be considered to allow for a thorough analysis of strain regional distribution. Nevertheless, it is likely that motion might vary significantly between individuals, hampering a generic strain distribution. Perhaps, normalisation of strains to account for differences in wall thickness and curvature might elucidate a more consistent strain pattern.

7.5 Summary

This chapter has presented some preliminary analysis of the developed personalised models, enabling comparisons between normals and DCM patients. Notable discrepancies between patients and volunteers were identified directly from available data including increased end-diastolic and end-systolic cavity volumes and a change of shape from elliptical to spherical, all characteristic attributes of the disease. Further, reduced ejection fraction and wall thickening were observed in DCM, indicating deteriorated efficiency in DCM hearts, both in contractile and diastolic function. Diastolic dysfunction was also suggested by elevated estimated end-diastolic pressure in DCM patients.

Building on the valuable observations from clinical data, personalised models can provide important information on tissue stiffness, through the estimation of passive parameters. The presented analysis suggested higher stiffness for DCM hearts – previously shown on a mice model[47,190] – based on significant increase in both passive parameters. Taking advantage of the fact that models enable a clearer interpretation of individual effects, an attempt was made to delineate the effect and correlations of different attributes resulting in increased stiffness. To this end, end-diastolic pressure, ejection fraction and anisotropy were identified as having a synergistic effect leading to increased stiffness in DCM models. Moreover, the thorough analysis and validation of the personalisation pipeline in chapter 6 ensures that the obtained parameter estimates are unique. Having confidence in the parameter values, we can then draw conclusions on stiffness' difference between DCM patients and normals.

Additional information distinguishing healthy volunteers and DCM patients was obtained through comparison of regional strain. Radial, longitudinal and circumferential strains were reduced in DCM hearts compared to normals, in accordance with studies reporting hypokinetic LV wall in the presence of DCM. Furthermore, estimation of strains per AHA segment revealed regional data abnormalities, not distinguishable from global metrics. Finally, data-to-model strain comparisons showed notable consistencies in regional strain distributions, providing an additional validation of the personalised models.

In summary, this chapter provided a preliminary analysis of the considered personalised models, identifying significant variations between DCM patients and normals. The increased stiffness observed in DCM models combined with elevated end-diastolic pressures are likely to be key determinants in the onset and progression of the disease, and as such future research needs to be directed towards understanding their interaction along with their effect on the development of DCM. Finally, the development and analysis of more personalised models for both healthy volunteers and patients is required to enable a careful statistical analysis and allow for safe conclusions.

8 Conclusions and future directions

The primary aim of the work presented in this thesis was the development of patient-specific diastolic models for the study of DCM. Due to the large number of volunteer and patient models that had to be created, the development of a consistent, robust and efficient pipeline was considered essential to allow for fair comparisons and safe conclusions. Emphasis was largely placed on achieving optimal use of the available data, to assist in model personalisation and enable reliable model outcomes. Therefore, with the potential and limitations of the available data in mind, significant part of the work was devoted to investigating important modelling aspects of the pipeline, initially using *in silico* studies and subsequently *in vivo* tests.

Initially, the choice of a numerical scheme for approximating incompressibility or near incompressibility was examined. Owing to the controversial degree of myocardial compressibility along with numerical issues hindering solution approaches, various numerical schemes are used throughout the cardiac mechanics literature. In order to identify a suitable solution approach, depending on the scope of the specific application, commonly used numerical methods were compared in terms of their accuracy and efficiency. Particularly, the well-known penalty and Lagrange multiplier (LM and PL) methods were compared with a modified displacement-only weakly penalised formulation, structured to avoid locking phenomena associated with the penalty approach. Numerical comparisons highlighted the fact that – although often used equivalently – penalty and Lagrange formulations might result in markedly different outcomes due to over-constraining of the solution space in the case of the penalty formulation. Furthermore, due to its simple structure as a single field approach, the weakly-penalised formulation provides an accurate alternative to the LM method in the case of large systems. The systematic comparison of the considered formulations elucidates the strengths and weaknesses of each approach, facilitating the selection of an appropriate solution method based on the needs of the specific application.

Another modelling aspect of critical import is the material law chosen to represent passive myocardial behaviour. With a range of available constitutive laws varying in structure and complexity, this choice is also based on the objectives of the individual applications. Naturally, a fundamental requirement for a constitutive law is the ability

to capture and reproduce the main characteristics of heart behaviour, in order to allow for an accurate assessment of cardiac function. An additional condition posed within this work, is the unique identifiability of the constitutive law's parameters, based on the available data. Particularly, passive parameters are speculated to be key determinants of function in DCM, due to the significant ventricular remodelling and diastolic dysfunction associated with this condition. Therefore, there is a strong need for ensuring unique and accurate passive parameter estimates, which would enable valid comparisons between healthy volunteers and DCM patients.

Accordingly, to assist the choice of an appropriate constitutive law when the available data is 3D tagged MRI – the main data source for parametrisation within this work – the practical identifiability and model fidelity of commonly used passive material laws were investigated. The practical identifiability of each law was examined by generating synthetic 3D tags from *in silico* simulations, enabling mapping of the objective function over the parameter space as well as assessment of the error in parameter estimates. Keeping in mind the need for an adequate representation of the cardiac behaviour, model fidelity was tested by comparing the models considered with the extensively used Guccione law and by characterising their passive end-diastolic pressure-volume relation. These *in silico* tests identified a reduced version of the Holzapfel-Ogden law as the suitable choice for our requirements, providing the best balance between identifiability and model fidelity across the tests considered.

In a clinical setting however, parameter identifiability is significantly hindered by both data quality and model fidelity issues. Contrary to the presented *in silico* tests where data originated from simulations, important modelling aspects such as the suitability of the constitutive law, the fibre distribution and the loading and boundary conditions are unknown in *in vivo* models. With these concerns in mind, parameter identifiability for the reduced Holzapfel-Ogden law was investigated in an *in vivo* setting. Important modelling attributes such as fibre distribution, boundary conditions and reference configurations were investigated, with the objective of improving model accuracy and parameter identifiability. A systematic analysis of these aspects on several cases highlighted the importance of accounting for the RV effect and indicated that a maximum fibre angle of $\theta = 50°$ produced a consistently lower model error. More importantly, the application on both volunteers and patients where unique parametrisation was combined with acceptable levels of model error, suggested that the employed modelling assumptions were a suitable choice for the considered personalised models.

The systematic investigation of the above-mentioned modelling attributes has also enabled testing and evaluation of the proposed pipeline, which focuses on two core challenges in patient-specific applications: data integration and parameter identifiability. The novel boundary conditions used enabled selective relaxation or strengthening of data integration constraints, thus avoiding non-physiological outcomes due to errors in

data processing. Combined with processing steps reducing data inconsistencies, they have enabled a successful application of the pipeline on several cases, with data varying in quality and consistency. Furthermore, unique passive parameters were obtained for all cases using strictly non-invasive data. Moreover, the consistency in results with respect to both model fidelity and parameter identifiability demonstrated a robust, efficient and reliable pipeline, suitable for case-to-case comparisons.

Naturally, the proposed pipeline was then employed for comparisons between DCM patients and volunteers with healthy heart function. Initially, important clinical metrics derived from the available data illustrated notable differences between patients and normals, including discrepancies in cavity volumes, ejection fraction, ventricular shape and estimated end-diastolic pressure. Personalised models were then analysed, producing marked increase in both passive parameters in DCM patients compared to normals. Within the modelling framework, factors contributing or related to the increased stiffness were identified, an analysis that would not be possible solely through clinical data. Further, the careful testing of the model personalisation pipeline provides confidence in the parameter estimates, thus supporting the validity of the increased stiffness finding in DCM hearts within the employed modelling framework.

8.1 Future directions

The work presented has provided insights into important attributes of patient-specific modelling, while in parallel indicating clear directions for further investigation. These are mainly identified in a more thorough investigation of DCM hearts, and improvements in the personalised models.

8.1.1 Future research for DCM assessment

Firstly, keeping in mind the key objective for a thorough study of DCM through personalised cardiac mechanics models, there is a clear need for processing of additional volunteers and patients. The development and analysis of patient-specific models for the 20 volunteers and 16 patients cases available will strengthen the statistical significance of the metrics considered in previous chapters, and might elucidate significant discrepancies that have not been identified through the models analysed.

Although the focus of the presented work was the diastolic part of the cycle, significant variations – reduced contractility, intra-ventricular conduction delay – are reported in DCM hearts over systole. The systolic component of the considered personalised models has been developed in parallel with this work by our group[8]. *In silico* and *in vivo* tests[8] have verified unique parametrisation of the active tension through the

191

cycle, allowing for comparison between cases, over both diastole and systole. Therefore, comparisons related to contractile function of normals and DCM patients are a readily available addition, potentially elucidating significant variations in DCM.

Further, the increased stiffness combined with elevated end-diastolic pressures observed in the DCM cases analysed, are considered key determinants of diastolic function and as such are likely to have a significant influence on the onset and progression of the disease. Costandi *et al.* suggested that in early disease stages, dilation, end-diastolic pressure and stiffness act together as compensatory mechanisms, initially improving systolic function[47]. Based on experiments on genetically engineered mice, they observed that in later stages of DCM the end-diastolic pressure decreased approaching normal values, while increased stiffness was observed throughout the disease's progression. Therefore, analysis of additional patient cases with varying levels of severity or progression of the disease, might assist deciphering whether these attributes are responsible for DCM development, or ramifications of it.

Passive parameters and ratio could also be investigated with respect to potential correlation to ventricular twist and torsion. The increased ratio and absolute values might be related to the decreased torsion observed in DCM hearts[42,184]. Hence further investigation of these aspects might provide important information on LV torsion and its potential relation to diastolic dysfunction and impaired filling efficiency of the heart.

Additional information on DCM can be provided through the investigation of changes introduced in cardiac behaviour after administration of beta blockers. The clinical protocol described in section 5.1, was repeated after administration with esmolol, a beta blocker with a short duration of action. The rationale for these scans was that, the development of personalised models before and after esmolol administration, will assist into a better understanding of the clinically reported benefits of lowering heart rates in DCM patients. Differences in tissue stiffness and contractility after esmolol administration might suggest a possible reverse remodelling resulting in the reported improvement of the condition. In fact, based on these data, Chabiniok *et al.* have reported reduction in contractility under esmolol infusion[31]. Furthermore, important information can potentially be obtained through investigation of cardiac energetics, which are hypothesised to be key determinants in DCM. Systematic comparisons could show that lower heart rates result in an improved energy dissipation in DCM and elucidate the underlying mechanisms responsible.

An ultimate goal of patient-specific models such as the ones presented, is their translation to the clinic. This is, however, a long and challenging process, firstly due to the difficulties associated with data-model integration, as discussed throughout the thesis. Additionally, personalised models must be able to translate their mathematical outcomes into clinically relevant metrics, providing critical information that could not had been predicted through existing techniques. Once these requirements are met, the

model-derived metrics need to be tested and validated through extensive clinical trials. As significant progress needs to be achieved before usage of personalised models in the clinic is possible, there is a growing number of patient-specific cardiac applications contributing towards this goal.

8.1.2 Future research in model development

Future work could also be directed towards improving model accuracy. Even though the systematic investigations of several modelling attributes led to a marked decrease in modelling error, modifications to the modelling pipeline could result in further error reductions. Model accuracy could for instance be improved by allowing for spatially varying parameters. Considering heterogeneous passive parameters might also provide a justification for the particularly deteriorated function observed on the septal wall in DCM[284,114].

Furthermore, a rule-based fibre distribution was employed throughout the developed personalised models, which is likely to vary significantly from the true individual fibre architectures. Variation is likely to be more pronounced in DCM hearts, with structural changes reported for DCM patients[92,65]. Therefore, consideration of different fibre distributions, varying in both magnitude and distribution, might enable improved model fidelity and more physiologically accurate model outcomes.

A very interesting, yet challenging, future direction would be towards the validation of the proposed personalised models. Despite the wealth of information from the available imaging data, strict model validation is not possible for the study presented, as a number of modelling assumptions had to be made, which are likely to introduce significant bias in model results. The validity or effect of the modelling assumptions made – such as reference domain and fibre distribution – could, however, be tested through *ex vivo* and *in vivo* animal experiments. For example, an animal study providing both *in vivo* clinical data (cine MRI, 3D tagged MRI, DTMRI, LV pressure) and *ex vivo* data including biaxial / shear tests would provide an ideal setting for the development and validation of personalised models. Within this environment, the effect of model assumptions could be directly assessed, as the actual fibre distribution, for instance, would be known. Moreover, model parameters fit to experimental data could be compared with estimated values, evaluating the accuracy of the parameter estimates.

Finally, owing to a broad applicability of the methodology proposed in this work (tested on volunteers and patients, and to data of different quality), the pipeline can be extended to the study of other cardiac conditions as well. As a result, the work presented provides a small step towards physiologically accurate personalised models of cardiac mechanics. Such models have the potential of evolving into a valuable clinical tool, assisting in both improved understanding and treatment of cardiac conditions.

Appendices

A Discrete weak forms / Jacobian matrices for the penalty, PL and LM methods

The aim of this section is to provide the discrete weak forms of the formulations implemented and used in this work. A detailed derivation of the weak forms of the penalty, LM and PL methods is provided in various textbooks[21,97]. Specifically, the weak form for the penalty method is acquired by requiring that the directional derivative of the penalty functional Π_k vanishes for all arbitrary directions $\delta\boldsymbol{u}^h$ in the homogeneous zero Dirichlet space $\boldsymbol{X_0}^h$, *i.e.*

$$D\Pi_k(\boldsymbol{u}^h)[\delta\boldsymbol{u}^h] = 0, \quad \forall \delta\boldsymbol{u}^h \in \boldsymbol{X_0}^h. \tag{A.1}$$

Similarly, the PL method requires that,

$$D\Pi_\lambda(\boldsymbol{u}^h, \lambda^h)[\delta\boldsymbol{u}^h, \delta q^h] = 0, \tag{A.2}$$

for every $(\delta\boldsymbol{u}^h, \delta q^h) \in \boldsymbol{X_0}^h \times W^h$. The discrete weak forms for the penalty,PL and LM systems can also be written in operator notation as,

$$A(\boldsymbol{u}^h, \delta\boldsymbol{u}^h) + P(\boldsymbol{u}^h, \delta\boldsymbol{u}^h) = F(\delta\boldsymbol{u}^h), \tag{A.3}$$

$$A(\boldsymbol{u}^h, \delta\boldsymbol{u}^h) + B(p^h, \boldsymbol{u}^h, \delta\boldsymbol{u}^h) + \hat{B}(\boldsymbol{u}^h, \delta p^h) - \frac{1}{k}M(p^h, \delta p^h) = F(\delta\boldsymbol{u}^h), \tag{A.4}$$

$$A(\boldsymbol{u}^h, \delta\boldsymbol{u}^h) + B(p^h, \boldsymbol{u}^h, \delta\boldsymbol{u}^h) + \hat{B}(\boldsymbol{u}^h, \delta p^h) = F(\delta\boldsymbol{u}^h), \tag{A.5}$$

where the operators A, P, F, B, $\hat{B}$, M, and C are defined as,

$$A(\boldsymbol{u}^h, \delta\boldsymbol{u}^h) = \int_{\Omega_0} \boldsymbol{F}_h \boldsymbol{S}_h : \nabla_{\boldsymbol{X}} \delta\boldsymbol{u}^h dV,$$

$$P(\boldsymbol{u}^h, \delta\boldsymbol{u}^h) = \int_{\Omega_0} k J_h (J_h - 1) \boldsymbol{F}_h^{-T} : \nabla_{\boldsymbol{X}} \delta\boldsymbol{u}^h dV,$$

$$F(\delta\boldsymbol{u}^h) = \int_{\Omega_0} \boldsymbol{f} \cdot \delta\boldsymbol{u}^h dV + \int_{\partial\Omega_0} \boldsymbol{t} \cdot \delta\boldsymbol{u}^h dA,$$

$$B(\lambda^h, \boldsymbol{u}^h, \delta\boldsymbol{u}^h) = \int_{\Omega_0} \lambda^h J_h \boldsymbol{F}_h^{-T} : \nabla_{\boldsymbol{X}} \delta\boldsymbol{u}^h dV,$$

$$\hat{B}(\boldsymbol{u}^h, \delta q^h) = \int_{\Omega_0} \delta q^h (J_h - 1) dV,$$

$$M(\lambda^h, \delta q^h) = \int_{\Omega_0} \lambda^h \delta q^h dV,$$

where $\boldsymbol{F}_h = \nabla\boldsymbol{u}^h + \boldsymbol{I}$ and $\boldsymbol{S}_h$ represent the discrete deformation gradient and second Piola stress tensors, respectively.

The Jacobian of these formulations is then derived by taking the directional derivative of the discrete weak forms with respect to displacement (and pressure). For the penalty method, the Jacobian can not be derived analytically due to the nonlinearity of hyperelastic laws and is usually estimated by the finite difference approximation of the gradient of the operators A, P and F:

$$\boldsymbol{J}_k = \boldsymbol{A} + \boldsymbol{P}, \tag{A.6}$$

$$
\begin{aligned}
[\boldsymbol{A}]_{ij} = \ & \frac{1}{\epsilon}\big(A(\boldsymbol{u}^h + \epsilon\boldsymbol{\phi}_u^j, \boldsymbol{\phi}_i) - F(\boldsymbol{u}^h + \epsilon\boldsymbol{\phi}_u^j, \boldsymbol{\phi}_i) \\
& - A(\boldsymbol{u}^h - \epsilon\boldsymbol{\phi}_u^j, \boldsymbol{\phi}_i) + F(\boldsymbol{u}^h - \epsilon\boldsymbol{\phi}_u^j, \boldsymbol{\phi}_i)\big),
\end{aligned}
$$

$$[\boldsymbol{P}]_{ij} = \frac{1}{\epsilon}(P(\boldsymbol{u}^h + \epsilon\boldsymbol{\phi}_u^j, \boldsymbol{\phi}_i) - P(\boldsymbol{u}^h - \epsilon\boldsymbol{\phi}_u^j, \boldsymbol{\phi}_i)) \tag{A.7}$$

where the operator F is included in the Jacobian estimation as it often depends on $\boldsymbol{u}$.

The Jacobian of the PL method is written in matrix form as

$$\boldsymbol{J}_{PL} = \begin{pmatrix} \boldsymbol{A} & \boldsymbol{B} \\ \hat{\boldsymbol{B}} & \frac{-1}{k}\boldsymbol{M} \end{pmatrix}, \tag{A.8}$$

where the block matrices $\boldsymbol{A}$ $\boldsymbol{B}$ and $\hat{\boldsymbol{B}}$ are defined as

$$
\begin{aligned}
[\boldsymbol{A}]_{ij} = \ & \frac{1}{\epsilon}\big(A(\boldsymbol{u}^h + \epsilon\boldsymbol{\phi}_u^j, \boldsymbol{\phi}_i) + B(\lambda^h, \boldsymbol{u}^h + \epsilon\boldsymbol{\phi}_u^j, \boldsymbol{\phi}_i) - F(\boldsymbol{u}^h + \epsilon\boldsymbol{\phi}_u^j, \boldsymbol{\phi}_i) \\
& - A(\boldsymbol{u}^h - \epsilon\boldsymbol{\phi}_u^j, \boldsymbol{\phi}_i) - B(\lambda^h, \boldsymbol{u}^h - \epsilon\boldsymbol{\phi}_u^j, \boldsymbol{\phi}_i) + F(\boldsymbol{u}^h - \epsilon\boldsymbol{\phi}_u^j, \boldsymbol{\phi}_i)\big),
\end{aligned}
$$

$$[\boldsymbol{B}]_{ij} = B(\phi_w^j, \boldsymbol{u}^h, \boldsymbol{\phi}_u^i) \tag{A.9}$$

$$[\hat{\boldsymbol{B}}]_{ij} = B(\phi_w^i, \boldsymbol{u}^h, \boldsymbol{\phi}_u^j) \tag{A.10}$$

The block matrix $\boldsymbol{M}$ is the mass matrix defined in Eq. 3.19.

The Jacobian matrix of the LM formulation can be derived from the Jacobian of the PL formulation by assuming $k \to \infty$, as

$$\boldsymbol{J}_\lambda = \begin{pmatrix} \boldsymbol{A} & \boldsymbol{B} \\ \hat{\boldsymbol{B}} & \boldsymbol{0} \end{pmatrix}, \tag{A.11}$$

where the $\boldsymbol{0}$ block matrix results in a non-positive definite Jacobian matrix which may cause numerical difficulties.

B Stress derivation for Guccione and neo-fibre laws

Following Nordsletten[179], the stress tensors for the Guccione law can be conveniently derived by considering the deviatoric second Piola-Kirchhoff in the fibre coordinate system $\boldsymbol{S}_F^d$:

$$\boldsymbol{S}_F^d(\boldsymbol{E}_F) = \frac{1}{2}\left(\frac{\partial \Psi_d}{\partial \boldsymbol{E}_F} + \frac{\partial \Psi_d}{\partial \boldsymbol{E}_F^T}\right), \tag{B.1}$$

where Ψ_d is the deviatoric strain energy function in Eq. 2.33. Following the definition of Ψ_d and the chain rule:

$$\begin{aligned}
\boldsymbol{S}_F^d =& \frac{C}{4}e^{Q(\boldsymbol{E}_F)}\left(\frac{\partial Q}{\partial \boldsymbol{E}_F} + \frac{\partial Q}{\partial \boldsymbol{E}_F^T}\right) \\
=& Ce^{Q(\boldsymbol{E}_F)}\begin{pmatrix} b_f E_{ff} & b_{fs}E_{fs} & b_{fs}E_{fn} \\ b_{fs}E_{sf} & b_t E_{ss} & b_t E_{sn} \\ b_{fs}E_{nf} & b_t E_{ns} & b_t E_{nn} \end{pmatrix}.
\end{aligned} \tag{B.2}$$

Using Eq. 2.19 and the rotation matrix $\boldsymbol{Q}$, the Cauchy stress tensor with respect to the reference coordinate system can be derived:

$$\boldsymbol{\sigma}_d = \frac{Ce^{Q(\boldsymbol{E}_F)}}{J}\boldsymbol{F}\boldsymbol{Q}\begin{pmatrix} b_f E_{ff} & b_{fs}E_{fs} & b_{fs}E_{fn} \\ b_{fs}E_{sf} & b_t E_{ss} & b_t E_{sn} \\ b_{fs}E_{nf} & b_t E_{ns} & b_t E_{nn} \end{pmatrix}\boldsymbol{Q}^T\boldsymbol{F}^T. \tag{B.3}$$

The deviatoric Cauchy stress tensor for the neo-fibre law, defined by Eq. 2.37, can be derived following the approach of Nordsletten et $al.$[180] for constitutive laws which are functions of invariants. For the case of the neo-fibre law, $\Psi_d(I_{\hat{C}}, I_{\hat{C}_f})$, so using the chain rule and formulas in[180], the second Piola-Kirchhoff stress tensor can be expressed as:

$$\boldsymbol{S}_d = 2\left(\frac{\partial \Psi_d}{\partial I_{\hat{C}}}\frac{\partial I_{\hat{C}}}{\partial \hat{\boldsymbol{C}}} : \frac{\partial \hat{\boldsymbol{C}}}{\partial \boldsymbol{C}} + \frac{\partial \Psi_d}{\partial I_{\hat{C}_f}}\frac{\partial I_{\hat{C}_f}}{\partial \hat{\boldsymbol{C}}} : \frac{\partial \hat{\boldsymbol{C}}}{\partial \boldsymbol{C}}\right). \tag{B.4}$$

Considering each contribution separately:

$$\frac{\partial \Psi_d}{\partial I_{\hat{C}}} \frac{\partial I_{\hat{C}}}{\partial \hat{\boldsymbol{C}}} : \frac{\partial \hat{\boldsymbol{C}}}{\partial \boldsymbol{C}} = \frac{\partial \Psi_d}{\partial I_{\hat{C}}} \frac{1}{III_C^{1/3}} \left(\boldsymbol{I} - \frac{I_C}{3} \hat{\boldsymbol{C}}^{-1} \right) = \frac{C_2}{2J^{2/3}} (\boldsymbol{I} - \frac{I_{\hat{C}}}{3} \hat{\boldsymbol{C}}^{-1}), \qquad \text{(B.5)}$$

$$\begin{aligned}
\frac{\partial \Psi_d}{\partial I_{\hat{C}_f}} \frac{\partial I_{\hat{C}_f}}{\partial \hat{\boldsymbol{C}}} : \frac{\partial \hat{\boldsymbol{C}}}{\partial \boldsymbol{C}} =& \frac{\partial \Psi_d}{\partial I_{\hat{C}_f}} \frac{1}{III_C^{1/3}} \left(\mathbf{f_0} \otimes \mathbf{f_0} - \frac{I_{C_f}}{3} \boldsymbol{C}^{-1} \right) = \\
& \frac{(C_1 - C_2)}{J^{2/3}} (I_{\hat{C}_f} - 1)^a \left(\mathbf{f_0} \otimes \mathbf{f_0} - \frac{I_{\hat{C}_f}}{3} \hat{\boldsymbol{C}}^{-1} \right).
\end{aligned} \qquad \text{(B.6)}$$

The deviatoric Cauchy stress tensor can then by expresed using $\boldsymbol{\sigma}_d = \frac{1}{J} \boldsymbol{F} \boldsymbol{S}_d \boldsymbol{F}^T$ and Eq. B.4, as:

$$\begin{aligned}
\boldsymbol{\sigma}_d =& J^{-\frac{5}{3}} \Big[C_2 \boldsymbol{B} - \frac{1}{3} C_2 I_C \boldsymbol{I} + (C_1 - C_2)(I_{\hat{C}_f} - 1)^a \boldsymbol{F} \mathbf{f_0} \otimes \mathbf{f_0} \boldsymbol{F}^T \\
& - \frac{1}{3}(C_1 - C_2)(I_{\hat{C}_f} - 1)^a I_{\hat{C}_f} \boldsymbol{I} \Big],
\end{aligned}$$

leading to the formulation in Eq. 2.39:

$$\boldsymbol{\sigma}_d = J^{-\frac{5}{3}} \Big[C_2 \boldsymbol{B} + (C_1 - C_2)(I_{\hat{C}_f} - 1)^a \mathbf{f} \otimes \mathbf{f} - \frac{1}{3} \big(C_2 I_C + (C_1 - C_2)(I_{\hat{C}_f} - 1)^a I_{\hat{C}_f} \big) \boldsymbol{I} \Big].$$

C Derivation of the residual modifications

As mentioned in chapter 3, the weakly penalised formulation is a generalisation of the PL method, and as such should be able to present similar nonlinear behaviour. To this end, the residual of the weakly penalised approach in sections 3.1.4.2 and 3.1.4.3 is modified based on the residual derived from the PL method, in order to achieve the same nonlinear convergence. The static condensation used in the weakly penalised system follows the linear algebra used in this section in order to eliminate the pressure variable from the PL formulation. We can therefore use the PL formulation in order to study and understand the sources of poor nonlinear convergence for the weakly penalised formulation.

For later comparison, we first present the linearised system for the weakly penalised formulation, when the SNR scheme is applied, without the modifications introduced in this work. Based on equation 2.69, the update $\delta \boldsymbol{U}^n$ for the n-th iteration of the weakly penalised formulation is given by

$$\boldsymbol{J}(\boldsymbol{U}^\beta)\delta\boldsymbol{U}^n = -\boldsymbol{R}(\boldsymbol{U}^n), \tag{C.1}$$

where the Jacobian is computed at a previous iteration β (the parameter α^n will be added in later through the minimisation step). Using Eq. 3.34, the linearised system for the weakly penalised formulation can be written as

$$(\boldsymbol{A}^\beta + k[\boldsymbol{B}^\beta]^T\boldsymbol{M}^{-1}\boldsymbol{B}^\beta)\delta\boldsymbol{U}^n = -\boldsymbol{R}_A(\boldsymbol{U}^n) + k[\boldsymbol{B}^n]^T\boldsymbol{M}^{-1}\boldsymbol{R}_J^n = -\boldsymbol{R}_A^n - \boldsymbol{R}_P^n, \quad (C.2)$$

The linearised system for the $(n+1) - th$ iteration of the PL method when the SNR scheme (section 2.6.3.2) is applied, can be expressed as

$$\begin{pmatrix} \boldsymbol{A}^\beta & [\boldsymbol{B}^\beta]^T \\ \boldsymbol{B}^\beta & \frac{-1}{k}\boldsymbol{M} \end{pmatrix} \begin{pmatrix} \delta\boldsymbol{U}^n \\ \delta p^n \end{pmatrix} = \begin{pmatrix} -\boldsymbol{R}_A^n - [\boldsymbol{B}^n]^T p^n \\ -\boldsymbol{R}_J^n + \frac{1}{k}\boldsymbol{M}p^n \end{pmatrix}, \tag{C.3}$$

where we use the Jacobian matrix of the PL system (equation A.8) computed at a previous iteration β in the SNR iterative process. The updates for the displacement

and pressure at the $(n) - th$ iteration are given by vectors $\delta \boldsymbol{U}^n$ and δp^n. The right hand side of the matrix equation C.3 denotes the residual at the n-th iteration, where $\boldsymbol{R}_A^n$ denotes the residual used in equation 3.35 and $\boldsymbol{R}_J^n$ refers to the residual defined in equation 3.20.

The matrix equation C.3 the matrix Eq. C.3 can be decomposed into the following equations:

$$\boldsymbol{A}^\beta \delta \boldsymbol{U}^n + [\boldsymbol{B}^\beta]^T \delta p^n = -\boldsymbol{R}_A^n - [\boldsymbol{B}^n]^T p^n, \tag{C.4}$$

$$\delta p^n = k \boldsymbol{M}^{-1} \boldsymbol{B}^\beta \delta \boldsymbol{U}^n + k \boldsymbol{M}^{-1} \boldsymbol{R}_J^n - p^n. \tag{C.5}$$

Combining the two equations we obtain

$$(\boldsymbol{A}^\beta + k[\boldsymbol{B}^\beta]^T \boldsymbol{M}^{-1} \boldsymbol{B}^\beta) \delta \boldsymbol{U}^{n+1} = -\boldsymbol{R}_A^n + [\boldsymbol{B}^\beta]^T p^n - k[\boldsymbol{B}^\beta]^T \boldsymbol{M}^{-1} \boldsymbol{R}_J^n - [\boldsymbol{B}^n]^T p^n. \tag{C.6}$$

Note that if $\beta = n$ always, this equation matches equation C.2 of the weakly penalised approach thus the convergence behaviour of the two formulations should be the same.

Taking into account Eq. C.5, we can see that $p^n = p^{n-1} + \delta p^{n-1} = k \boldsymbol{M}^{-1}(\boldsymbol{B}^\beta \delta \boldsymbol{U}^{n-1} + \boldsymbol{R}_J^{n-1})$, which represents the linearised estimate for $\boldsymbol{R}_J^n$. Using this estimate,

$$(\boldsymbol{A}^\beta + k[\boldsymbol{B}^\beta]^T \boldsymbol{M}^{-1} \boldsymbol{B}^\beta) \delta \boldsymbol{U}^{n+1} = -\boldsymbol{R}_A^n - k[\boldsymbol{B}^n]^T \boldsymbol{M}^{-1}(\boldsymbol{B}^\beta \delta \boldsymbol{U}^{n-1} + \boldsymbol{R}_J^{n-1})$$
$$+ k[\boldsymbol{B}^\beta]^T \boldsymbol{M}^{-1}(\boldsymbol{R}_J^{n-1} + \boldsymbol{B}^\beta \delta \boldsymbol{U}^{n-1} - \boldsymbol{R}_J^n), \tag{C.7}$$

where for later comparison we introduce $\boldsymbol{R}_{P*}^\beta$ and $\boldsymbol{R}_e^\beta$

$$(\boldsymbol{A}^\beta + k[\boldsymbol{B}^\beta]^T \boldsymbol{M}^{-1} \boldsymbol{B}^\beta) \delta \boldsymbol{U}^{n+1} = -\boldsymbol{R}_A^n - \boldsymbol{R}_{P*}^\beta - k[\boldsymbol{B}^\beta]^T \boldsymbol{R}_e^\beta. \tag{C.8}$$

The last formulation can be used for a better understanding of the poor nonlinear convergence behaviour of the weakly penalised formulation.

D Structural identifiability of cardiac constitutive laws

In this section we examine an application of Theorem 2, where we study the structural identifiability of the constitutive laws considered in chapter 4. Specifically, we consider a block of tissue (Fig. D.1), and show that for the neo-Hookean, neo-fibre and reduced Holzapfel-Ogden laws which have a linear dependence on their parameters, a single pure tension experiment is sufficient to prove the bijectivity of their φ mapping, thus ensuring their structural identifiability.

We can consider a block of incompressible tissue (Fig. D.1), under pure tension in one of the three directions. The body is fully constrained at $(0, 0, 0)$ and is under the influence of zero traction on the side boundaries.

For the case of the neohookean law, due to its isotropy, pure tension in any of the three directions is sufficient to ensure structural identifiability. Specifically, for elongation in the X direction the deformation gradient $\boldsymbol{F}$ and left Cauchy-Green deformation tensor can be expressed as

$$
\boldsymbol{F} = \begin{bmatrix} \lambda & 0 & 0 \\ 0 & \frac{1}{\sqrt{\lambda}} & 0 \\ 0 & 0 & \frac{1}{\sqrt{\lambda}} \end{bmatrix}, \quad \boldsymbol{B} = \begin{bmatrix} \lambda^2 & 0 & 0 \\ 0 & \frac{1}{\lambda} & 0 \\ 0 & 0 & \frac{1}{\lambda} \end{bmatrix} \tag{D.1}
$$

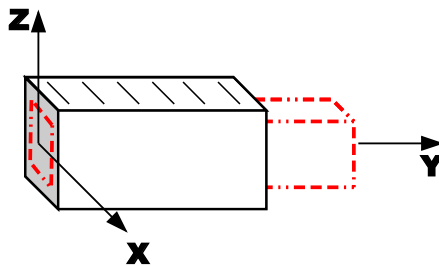where λ denotes the stretch of the body in the X direction, and the deformation in the

Figure D.1 The block of tissue under consideration. The red lines show the deformed configuration

Y and Z components is derived from the symmetry and incompressibility of the body. As the neo-Hookean law has only one parameter, expression 4.8 becomes $\boldsymbol{\sigma} = \mu\boldsymbol{\sigma}_1$, where using definition 2.29 and $J = 1$,

$$\boldsymbol{\sigma}_1 = (\lambda^2 - \frac{1}{\lambda}) \begin{bmatrix} \frac{2}{3} & 0 & 0 \\ 0 & -\frac{1}{3} & 0 \\ 0 & 0 & -\frac{1}{3} \end{bmatrix}. \tag{D.2}$$

If we choose the test function $\boldsymbol{v} = \left[\frac{1}{2}\boldsymbol{x}, -\frac{1}{4}\boldsymbol{y}, -\frac{1}{4}\boldsymbol{z}\right]$, $\boldsymbol{A}$ in Theorem 2 is now a non-zero scalar $\left(\boldsymbol{A} = \frac{1}{2}(\lambda^2 - \frac{1}{\lambda})\right)$, for any non-zero elongation ($\lambda \neq 1$). This ensures that ϕ is bijective, suggesting structural identifiability of the neo-Hookean law.

The neo-fibre and reduced Holzapfel-Ogden law can also be shown to be structurally identifiable through a pure tension experiment, where the elongation is exerted in the cross-fibre direction $Y = 0$ (Note that for elongation in the fibre direction, the matrix $\boldsymbol{A}$ becomes singular for any choice of test functions $\boldsymbol{v} \in \boldsymbol{W}^u_{0,Div}$). The deformation gradient and left Cauchy-Green tensor in this case are described by

$$\boldsymbol{F} = \begin{bmatrix} \frac{1}{\sqrt{\lambda}} & 0 & 0 \\ 0 & \lambda & 0 \\ 0 & 0 & \frac{1}{\sqrt{\lambda}} \end{bmatrix}, \quad \boldsymbol{B} = \begin{bmatrix} \frac{1}{\lambda} & 0 & 0 \\ 0 & \lambda^2 & 0 \\ 0 & 0 & \frac{1}{\lambda} \end{bmatrix} \tag{D.3}$$

where λ represents stretch in the cross-fibre direction, and $\mathbf{f_0} = [1\ 0\ 0]$. According to 4.8, the stress tensors for the neo-fibre and reduced Holzapfel-Ogden law can be written as $\boldsymbol{\sigma} = C_2\boldsymbol{\sigma}_1 + C_1'\boldsymbol{\sigma}_2$ and $\boldsymbol{\sigma} = \alpha\boldsymbol{\sigma}_1 + 2\alpha_f\boldsymbol{\sigma}_2$ respectively, where for simplicity $C_1' = C_1 - C_2$. Taking the specific deformation mode into account, $\mathbf{f} = [\frac{1}{\sqrt{\lambda}}\ 0\ 0]$, $I_{\hat{C}_f} = \frac{1}{\lambda}$ and the two stress components for the neo-fibre law are

$$\boldsymbol{\sigma}_1 = (\lambda^2 - \frac{1}{\lambda}) \begin{bmatrix} -\frac{1}{3} & 0 & 0 \\ 0 & \frac{2}{3} & 0 \\ 0 & 0 & -\frac{1}{3} \end{bmatrix} \tag{D.4}$$

$$\boldsymbol{\sigma}_2 = \frac{1}{\lambda}(\frac{1}{\lambda} - 1)^\alpha \begin{bmatrix} \frac{2}{3} & 0 & 0 \\ 0 & -\frac{1}{3} & 0 \\ 0 & 0 & -\frac{1}{3} \end{bmatrix}. \tag{D.5}$$

Similarly, the two stress component for the reduced Holzapfel-Ogden law can be expressed as

$$\boldsymbol{\sigma}_1 = \exp[5(\lambda^2 + \frac{2}{\lambda} - 3)](\lambda^2 - \frac{1}{\lambda}) \begin{bmatrix} -\frac{1}{3} & 0 & 0 \\ 0 & \frac{2}{3} & 0 \\ 0 & 0 & -\frac{1}{3} \end{bmatrix} \tag{D.6}$$

$$\boldsymbol{\sigma}_2 = \exp[5(\frac{1}{\lambda} - 1)^2]\frac{1}{\lambda}(\frac{1}{\lambda} - 1)\begin{bmatrix} \frac{2}{3} & 0 & 0 \\ 0 & -\frac{1}{3} & 0 \\ 0 & 0 & -\frac{1}{3} \end{bmatrix}. \tag{D.7}$$

Clearly, the two components of the neo-fibre and reduced Holzapfel-Ogden law have the same matrix structure which can be represented as

$$\boldsymbol{\sigma}_1 = \begin{bmatrix} \alpha_1 & 0 & 0 \\ 0 & \beta_1 & 0 \\ 0 & 0 & \alpha_1 \end{bmatrix}, \quad \boldsymbol{\sigma}_2 = \begin{bmatrix} \alpha_2 & 0 & 0 \\ 0 & \beta_2 & 0 \\ 0 & 0 & \beta_2 \end{bmatrix} \tag{D.8}$$

If we then choose our test functions to be $\boldsymbol{v_1} = \left[\frac{1}{2}\boldsymbol{x}, -\frac{1}{4}\boldsymbol{y}, -\frac{1}{4}\boldsymbol{z}\right]$ and $\boldsymbol{v_2} = \left[-\frac{1}{4}\boldsymbol{x}, \frac{1}{2}\boldsymbol{y}, -\frac{1}{4}\boldsymbol{z}\right]$, matrix $\boldsymbol{A}$ in Theorem 2 becomes

$$\boldsymbol{A} = \begin{bmatrix} \frac{1}{4}(\alpha_1 - \beta_1) & \frac{1}{2}(\alpha_2 - \beta_2) \\ \frac{1}{2}(\beta_1 - \alpha_1) & \frac{1}{4}(\beta_2 - \alpha_2) \end{bmatrix}, \tag{D.9}$$

whose determinant $|\boldsymbol{A}| = \frac{3}{16}(\alpha_1 - \beta_1)(\alpha_2 - \beta_2)$ is non-zero due to the structure of $\boldsymbol{\sigma}_1$ and $\boldsymbol{\sigma}_2$. Based on Theorem 2, the invertibility of $\boldsymbol{A}$ ensures the bijectivity of φ for the neo-fibre and reduced Holzapfel-Ogden laws, proving that they are structurally identifiable.

E   *In vivo* data and model strains

This section presents strain distributions per AHA region, computed using the strain definition in 7.3. Strain was computed for both data and models, elucidating regional differences. The presented model strain was computed on models with a fibre distribution of a maximum angle of $\theta = 50°$, employing the RV-epicardial condition and using the estimated parameters. Strain is presented in radial, longitudinal and circumferential directions.

Volunteer 1 (V1)

Figure E.1 Strain for V1 at end-diastole per *AHA* region in **(a, b)** radial, **(c, d)** longitudinal and **(e, f)** circumferential directions. Strain is computed for **(a, c, e)** data and **(b, d, f)** model with respect to end-systole. Region 1 was not part of the volumetric mesh and therefore not presented here.

Volunteer 2 (V2)

(a)

(b)

(c)

(d)

(e)

(f)

Figure E.2 Strain for V2 at end-diastole per *AHA* region in **(a, b)** radial, **(c, d)** longitudinal and **(e, f)** circumferential directions. Strain is computed for **(a, c, e)** data and **(b, d, f)** model with respect to end-systole.

Volunteer 3 (V3)

(a)

(b)

(c)

(d)

(e)

(f)

Figure E.3 Strain for V3 at end-diastole per *AHA* region in **(a, b)** radial, **(c, d)** longitudinal and **(e, f)** circumferential directions. Strain is computed for **(a, c, e)** data and **(b, d, f)** model with respect to end-systole.

Volunteer 4 (V4)
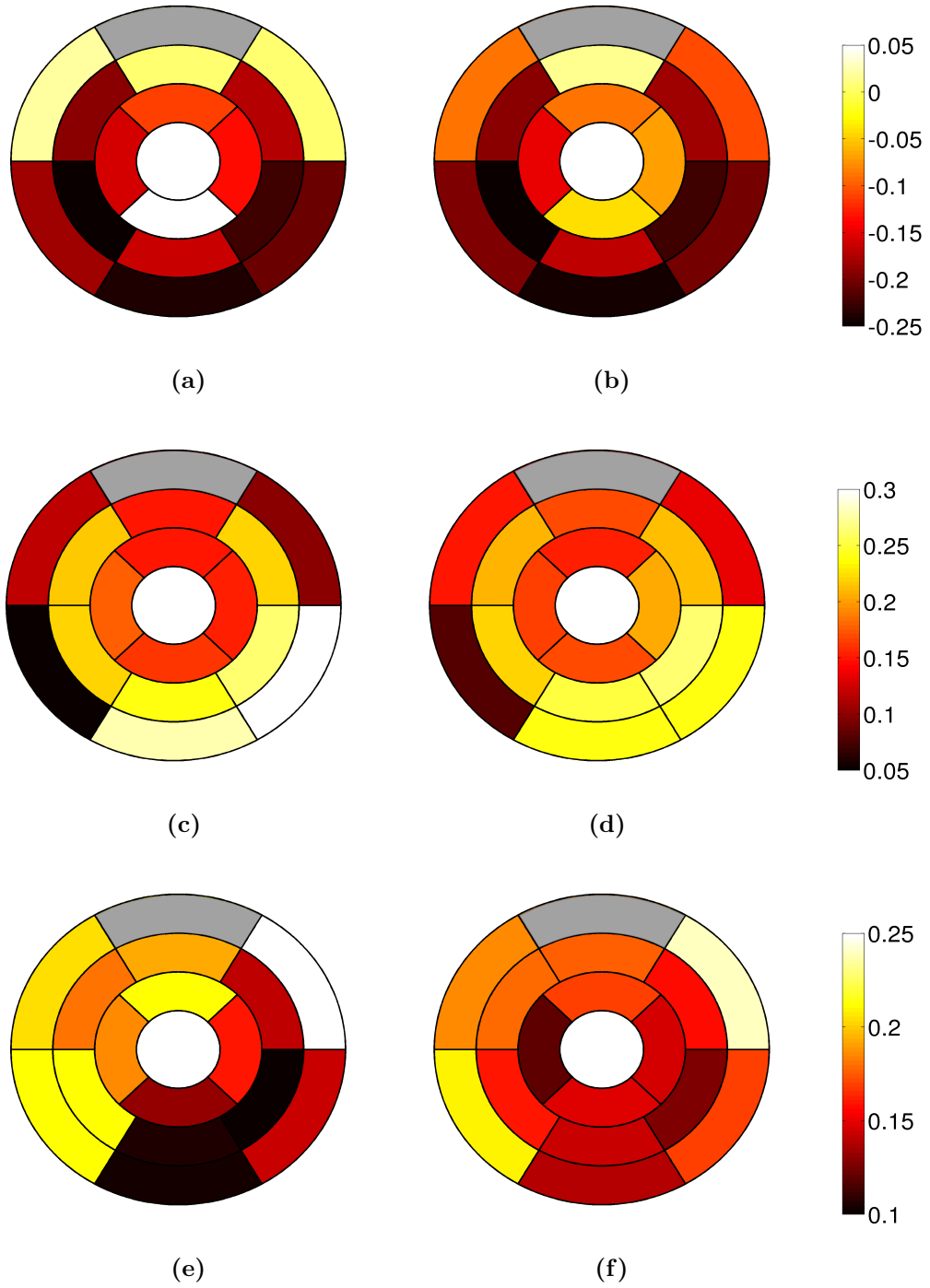

(a)

(b)

(c)

(d)

(e)

(f)

Figure E.4 Strain for V4 at end-diastole per *AHA* region in **(a, b)** radial, **(c, d)** longitudinal and **(e, f)** circumferential directions. Strain is computed for **(a, c, e)** data and **(b, d, f)** model with respect to end-systole.

Patient 1 (P1)

(a)

(b)

(c)

(d)

(e)

(f)

Figure E.5 Strain for P1 at end-diastole per *AHA* region in **(a, b)** radial, **(c, d)** longitudinal and **(e, f)** circumferential directions. Strain is computed for **(a, c, e)** data and **(b, d, f)** model with respect to end-systole.

Patient 2 (P2)

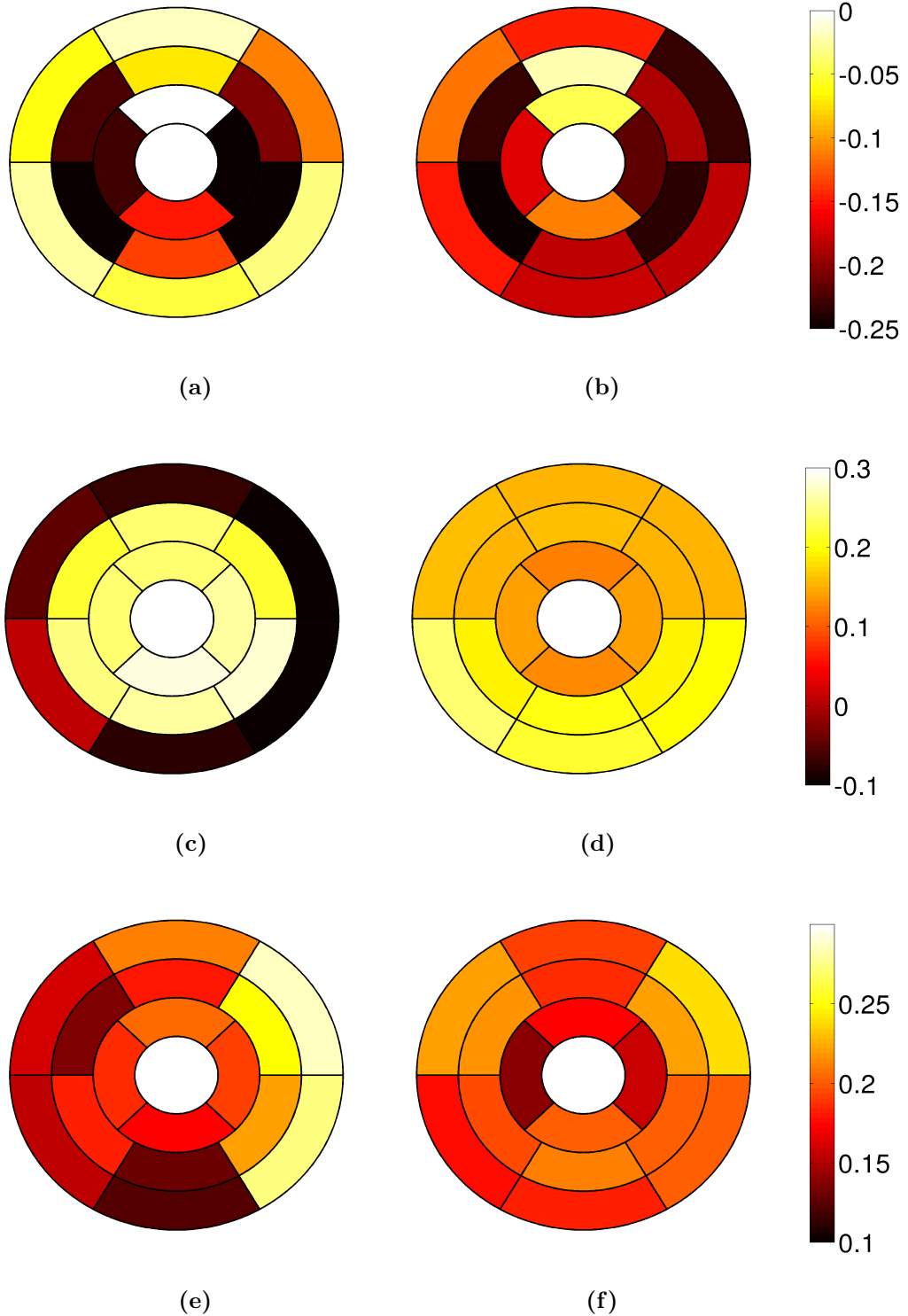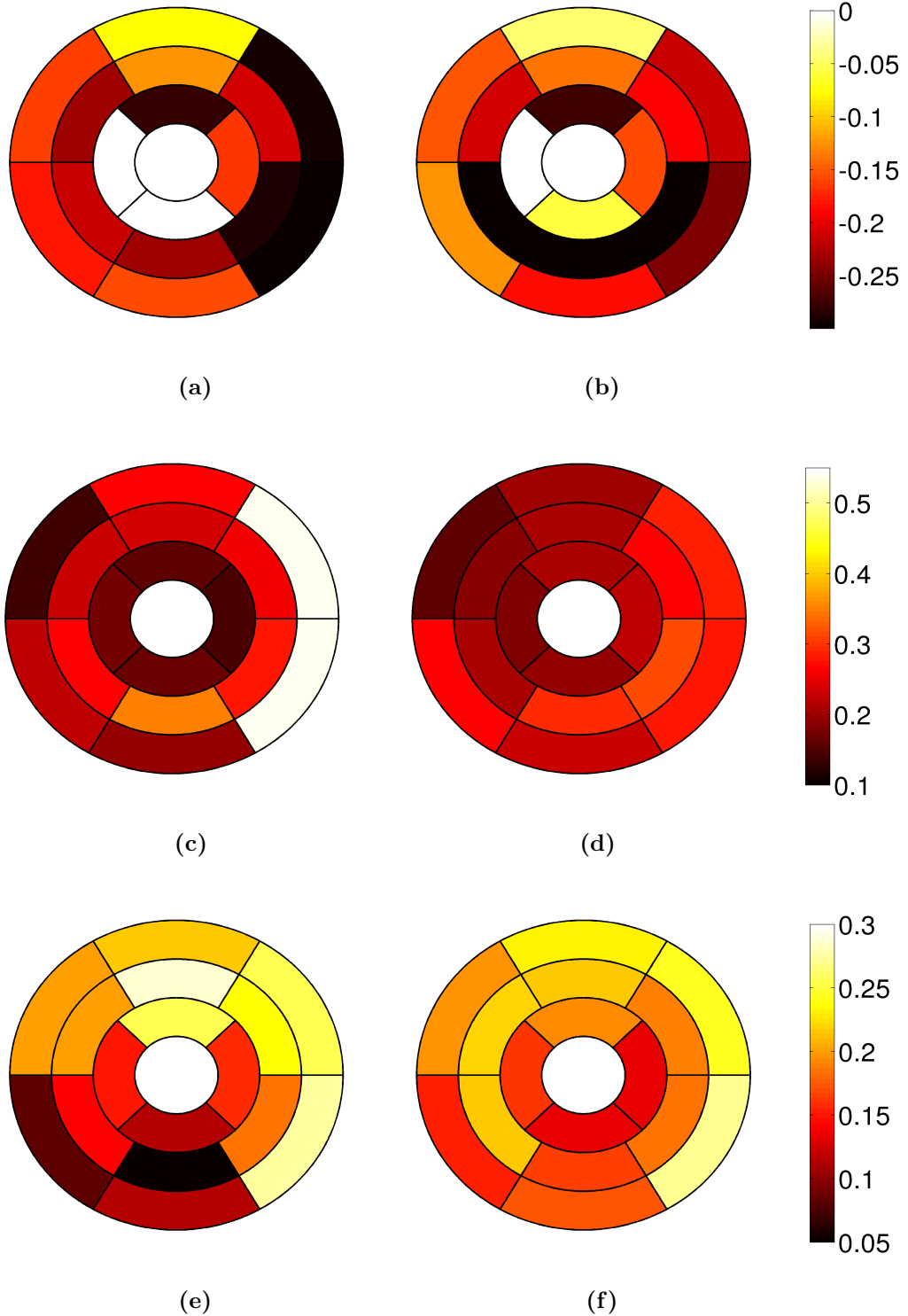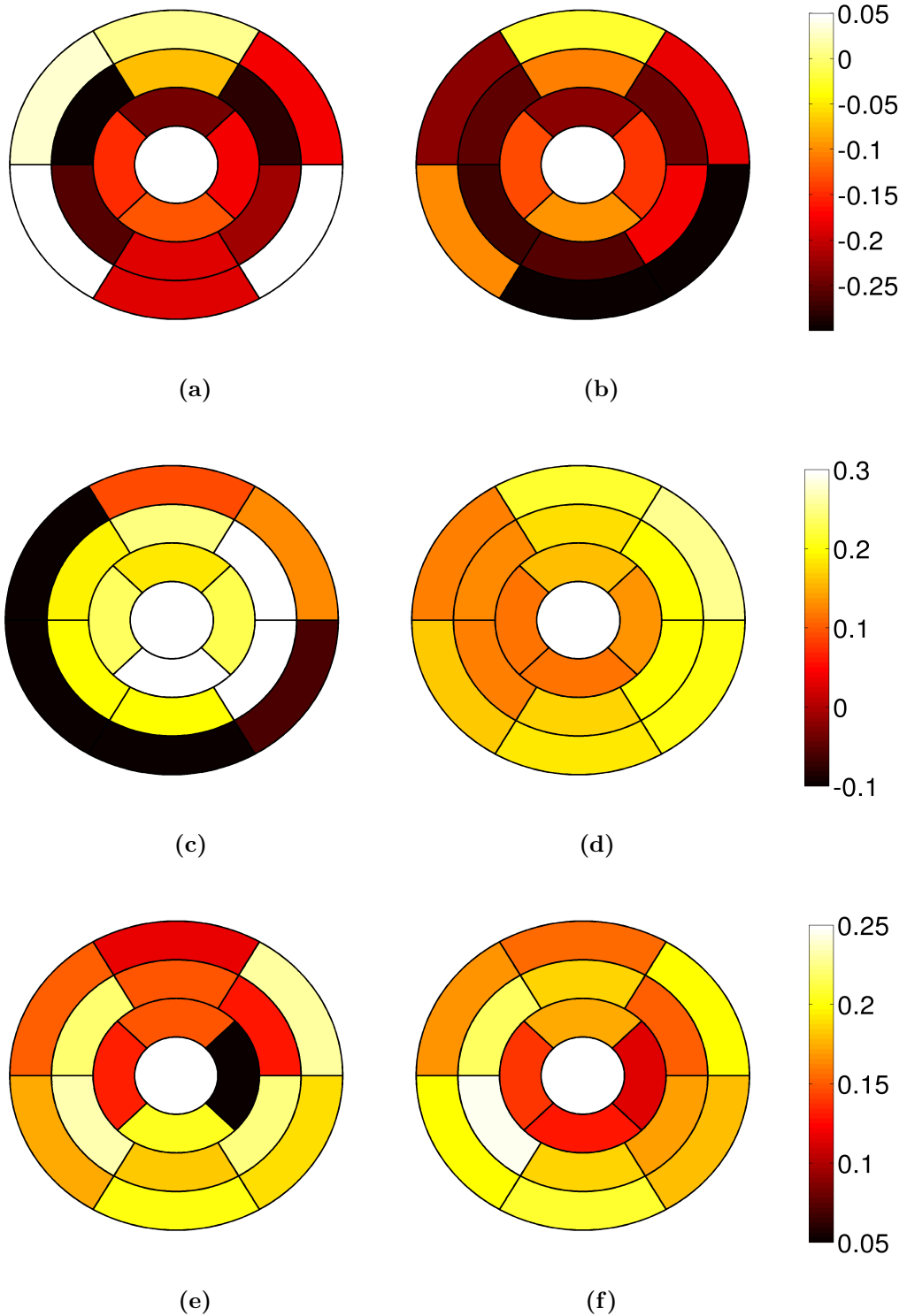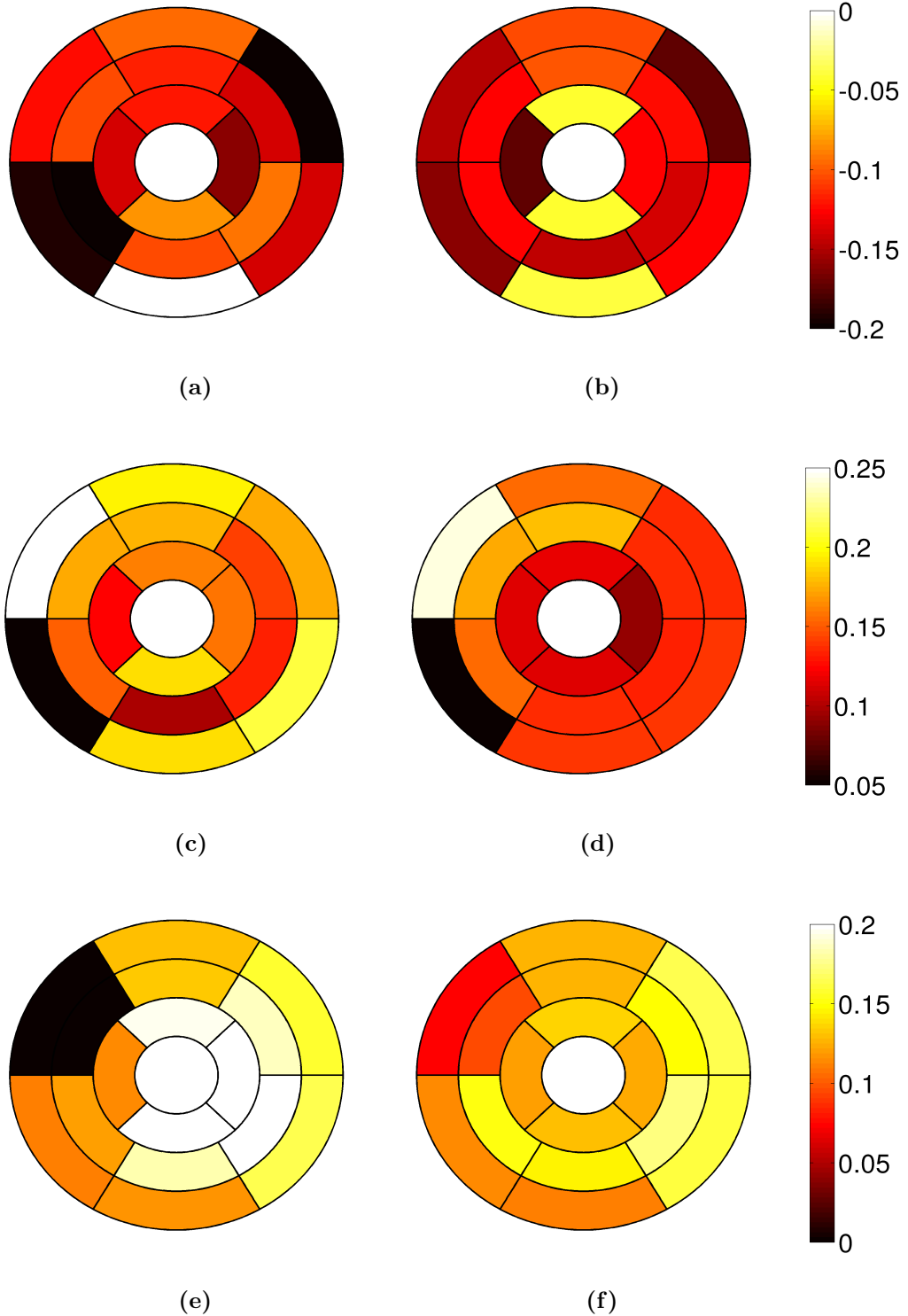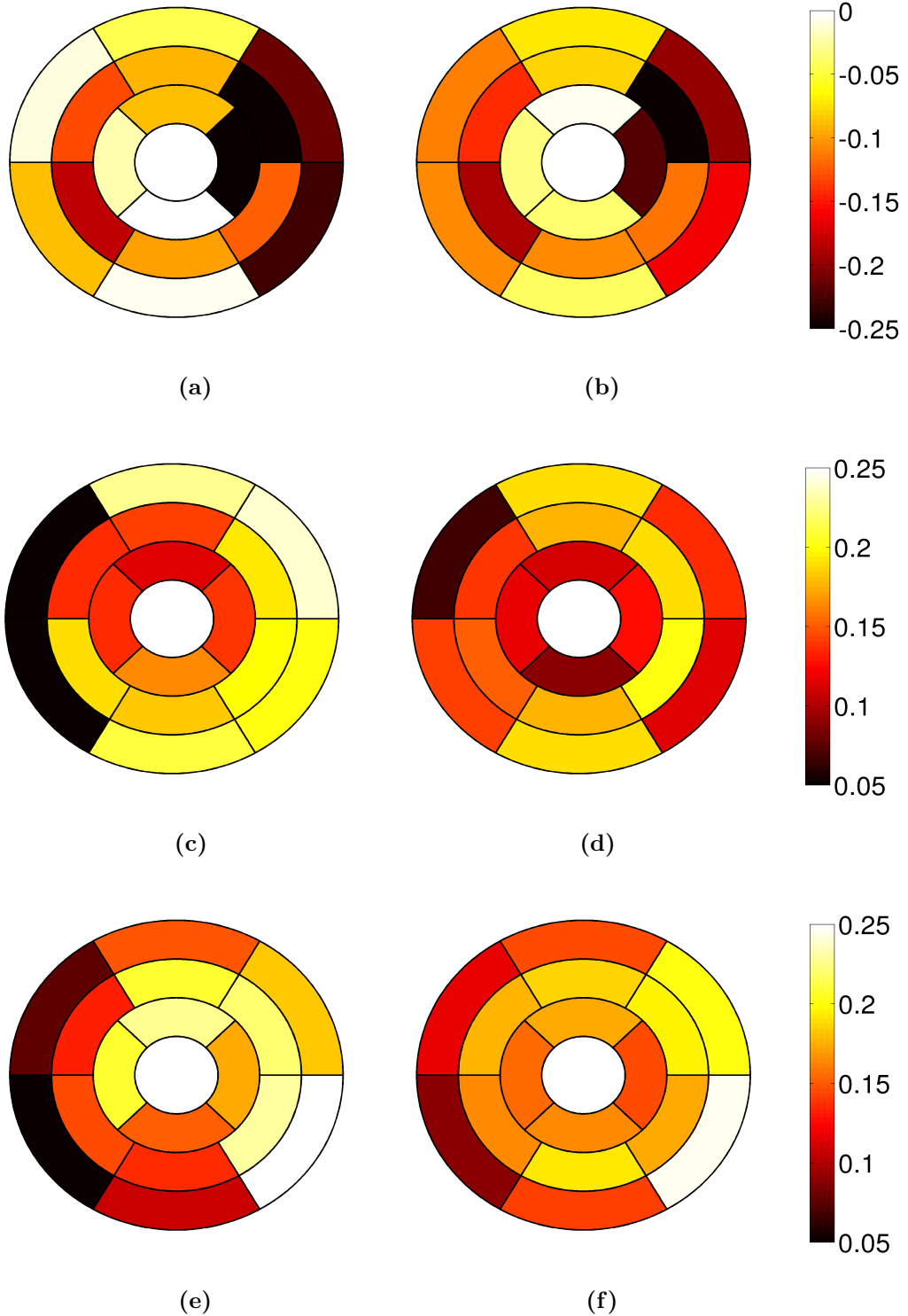(a)

(b)

(c)

(d)

(e)

(f)

Figure E.6 Strain for P2 at end-diastole per *AHA* region in **(a, b)** radial, **(c, d)** longitudinal and **(e, f)** circumferential directions. Strain is computed for **(a, c, e)** data and **(b, d, f)** model with respect to end-systole.

Bibliography

[1] Aguado-Sierra, J., Krishnamurthy, A., Villongco, C., Chuang, J., Howard, E., Gonzales, M. J., Omens, J., Krummen, D. E., Narayan, S., Kerckhoffs, R. C. P., and McCulloch, A. D. (2011). Patient-specific modeling of dyssynchronous heart failure: A case study. *Progress in Biophysics and Molecular Biology*, 107(1):147–155.

[2] Aguado-Sierra, J., Santiago, A., Rivero, M., Lpez-Yunta, M., Soto-Iglesias, D., Dux-Santoy, L., Camara, O., and Vazquez, M. (2015). Fully-Coupled Electromechanical Simulations of the LV Dog Anatomy Using HPC: Model Testing and Verification. In Camara, O., Mansi, T., Pop, M., Rhode, K., Sermesant, M., and Young, A., editors, *Statistical Atlases and Computational Models of the Heart - Imaging and Modelling Challenges*, volume 8896 of *Lecture Notes in Computer Science*, pages 114–122. Springer International Publishing.

[3] Akar, F. G., Spragg, D. D., Tunin, R. S., Kass, D., and Tomaselli, G. F. (2004). Mechanisms underlying conduction slowing and arrhythmogenesis in nonischemic dilated cardiomyopathy. *Circulation Research*, 95:717–725.

[4] Alexander, L. K., Small, J. D., Edwards, S., and Baric, R. S. (1992). An experimental model for dilated cardiomyopathy after rabbit coronavirus infection. *The Journal of infectious diseases*, 166(5):978–985.

[5] Alter, P., Rupp, H., Rominger, M. B., Klose, K. J., and Maisch, B. (2008). A new methodological approach to assess cardiac work by pressure-volume and stress-length relations in patients with aortic valve stenosis and dilated cardiomyopathy. *Pflugers Archiv European Journal of Physiology*, 455:627–636.

[6] Arts, T., Costa, K. D., Covell, J. W., and McCulloch, A. D. (2001). Relating myocardial laminar architecture to shear strain and muscle fiber orientation. *American journal of physiology. Heart and circulatory physiology*, 280:H2222–H2229.

[7] Arts, T., Prinzen, F. W., Delhaas, T., Milles, J. R., Rossi, A. C., and Clarysse, P. (2010). Mapping Displacement and Deformation of the Heart With Local Sine-Wave Modeling. *IEEE T Med Imaging*, 29:1114–1123.

[8] Asner, L., Hadjicharalambous, M., Chabiniok, R., Peresutti, D., Sammut, E., Wong, J., Chowienczyk, P., Lee, J., King, A., Smith, N., Razavi, R., and Nordsletten, D. (In print). Estimation of passive and active properties in the human heart using 3D tagged MRI. *Biomechanics and Modeling in Mechanobiology*.

[9] Asner, L., Hadjicharalambous, M., Lee, J., and Nordsletten, D. (2015). Stacom challenge: Simulating left ventricular mechanics in the canine heart. In Camara, O., Mansi, T., Pop, M., Rhode, K., Sermesant, M., and Young, A., editors, *Statistical Atlases and Computational Models of the Heart - Imaging and Modelling Challenges*, volume 8896 of *Lecture Notes in Computer Science*, pages 123–134. Springer International Publishing.

[10] Augenstein, K. F., Cowan, B. R., LeGrice, I. J., Nielsen, P. M. F., and Young, A. A. (2005). Method and Apparatus for Soft Tissue Material Parameter Estimation Using Tissue Tagged Magnetic Resonance Imaging. *J Biomech Eng-T Asme*, 127(1):148–157.

[11] Axel, L. and Dougherty, L. (1989). MR imaging of motion with spatial modulation of magnetization. *Radiology*, 171:841–845.

[12] Babuška, I. (1973). The finite element method with Lagrangian multipliers. *Numerische Mathematik*, 20(3):179–192.

[13] Baccani, B., Domenichini, F., Pedrizzetti, G., and Tonti, G. (2002). Fluid dynamics of the left ventricular filling in dilated cardiomyopathy. *Journal of Biomechanics*, 35(5):665–671.

[14] Baltes, C., Kozerke, S., Hansen, M. S., Pruessmann, K. P., Tsao, J., and Boesiger, P. (2005). Accelerating cine phase-contrast flow measurements using k-t BLAST and k-t SENSE. *Magnetic Resonance in Medicine*, 54:1430–1438.

[15] Bathe, K. J. (1996). *Finite Element Procedures*. Prentice Hall.

[16] Beltrami, C., Finato, N., Rocco, M., Feruglio, G., Puricelli, C., Cigola, E., Sonnenblick, E. H., Olivetti, G.,

and Anversa, P. (1995). The cellular basis of dilated cardiomyopathy in humans. *Journal of molecular and cellular cardiology*, 27(1):291–305.

[17] Benzi, M., Golub, G. H., and Liesen, J. (2005). Numerical solution of saddle point problems. *Acta Numerica*, 14(April 2005):1–137.

[18] Bercovier, M. (1978). Perturbation of mixed variational problems. Application to mixed finite element methods. *RAIRO Anal. Numer.*, 3:211–236.

[19] Bermejo, J., Benito, Y., Alhama, M., Yotti, R., Martínez-Legazpi, P., Pérez Del Villar, C., Pérez-David, E., González-Mansilla, A., Santa-Marta, C., Barrio, A., Fernández-Avilés, F., and Del Alamo, J. C. (2014). Intraventricular vortex properties in non-ischemic dilated cardiomyopathy. *American journal of physiology. Heart and circulatory physiology*, pages 718–729.

[20] Boland, J. M. and Nicolaides, R. A. (1983). Stability of finite elements under divergence constraints. *SIAM Journal on Numerical Analysis*, 20(4):722–731.

[21] Bonet, J. and Wood, R. (2008). *Nonlinear Continuum Mechanics for Finite Element Analysis*. Cambridge University Press.

[22] Bovendeerd, P., Arts, T., Huyghe, J., van Campen, D., and Reneman, R. (1992). Dependence of local left ventricular wall mechanics: a model study.

[23] Bozkurt, B. and Mann, D. L. (2007). Dilated Cardiomyopathy. In *Cardiovascular Medicine*, pages 1233–1259.

[24] Brett, S. E., Guilcher, A., Clapp, B., and Chowienczyk, P. (2012). Estimating central systolic blood pressure during oscillometric determination of blood pressure. *Blood Pressure Monitoring*, 17(3):132–136.

[25] Brezzi, F. and Fortin, M. (1991). *Mixed and Hybrid Finite Element Methods*. Springer Series in Computational Mathematics.

[26] Brink, U. and Stein, E. (1996). On some mixed finite element methods for incompressible and nearly incompressible finite elasticity. *Computational Mechanics*, 19(1):105–119.

[27] Burch, G. E., Ray, C. T., and Cronvich, J. (1952). Certain mechanical peculiarities of the human cardiac pump in normal and diseased states. *Circulation*, 5(April 1952):504–513.

[28] Caruel, M., Chabiniok, R., Moireau, P., Lecarpentier, Y., and Chapelle, D. (2014). Dimensional reductions of a cardiac model for effective validation and calibration. *Biomech Model Mechan*, 13:897–914.

[29] Cerqueira, M. D., Weissman, N. J., Dilsizian, V., Jacobs, A. K., Kaul, S., Laskey, W. K., Pennell, D. J., Rumberger, J., Ryan, T. J., and Verani, M. S. (2002). Standardized Myocardial Segmentation and Nomenclature for Tomographic Imaging of the Heart. *Journal of Cardiovascular Magnetic Resonance*, 4(2):203–210.

[30] Chabiniok, R., Moireau, P., Lesault, P.-F., Rahmouni, A., Deux, J.-F., and Chapelle, D. (2012). Estimation of tissue contractility from cardiac cine-MRI using a biomechanical heart model. *Biomech Model Mechan*, 11(5):609–30.

[31] Chabiniok, R., Sammut, E., Hadjicharalambous, M., Asner, L., Nordsletten, D., Razavi, R., and Smith, N. (2015). Steps towards quantification of the cardiological stress exam. In van Assen, H., Bovendeerd, P., and Delhaas, T., editors, *Functional Imaging and Modeling of the Heart*, volume 9126 of *Lecture Notes in Computer Science*, pages 12–20. Springer International Publishing.

[32] Chabiniok, R., Wang, V., Hadjicharalambous, M., Asner, L., Lee, J., Sermesant, M., Kuhl, E., Young, A., Moireau, P., Nash, M., Chapelle, D., and Nordsletten, D. (In review). Multiphysics and Multiscale Modeling, Data-Model Fusion and Integration of Organ Physiology in the Clinic: Cardiac Mechanics. *Interface Focus*.

[33] Chahboune, B. and Crolet, J. M. (1998). Numerical simulation of the blood-wall interaction in the human left ventricle. *The European Physical Journal Applied Physics*, 2(3):291–297.

[34] Chan, B. T., Abu Osman, N. A., Lim, E., Chee, K. H., Abdul Aziz, Y. F., Abed, A. A., Lovell, N. H., and Dokos, S. (2013). Sensitivity Analysis of Left Ventricle with Dilated Cardiomyopathy in Fluid Structure Simulation. *PLoS ONE*, 8(6):1–11.

[35] Chandrashekara, R., Mohiaddin, R. H., and Rueckert, D. (2004). Analysis of 3-D myocardial motion in tagged MR images using nonrigid image registration. *IEEE T Med Imaging*, 23(10):1245–50.

[36] Chang, T., Saleeb, A. F., and Li, G. (1991). Large strain analysis of rubber-like materials based on a perturbed Lagrangian variational principle. *Computational Mechanics*, 8(4):221–233.

[37] Chapelle, D., Gerbeau, J. F., Sainte-Marie, J., and Vignon-Clementel, I. E. (2010). A poroelastic model valid in large strains with applications to perfusion in cardiac modeling. *Computational Mechanics*, 46(1):91–101.

[38] Chen, J. S., Han, W., T, W. C., and W, D. (1997). On the perturbed Lagrangian formulation for nearly incompressible and incompressible hyperelasticity. *Computer Methods in Applied Mechanics and Engineering*, 142:335–351.

[39] Cheng, A., Langer, F., Nguyen, T. C., Malinowski, M., Ennis, D. B., Daughters, G. T., Ingels, N. B., and Miller, D. C. (2006). Transmural left ventricular shear strain alterations adjacent to and remote from infarcted myocardium. *The Journal of heart valve disease*, 15:209–218; discussion 218.

[40] Cheng, Y., Oertel, H., and Schenkel, T. (2005). Fluid-structure coupled CFD simulation of the left ventricular flow during filling phase. *Annals of Biomedical Engineering*, 33(5):567–576.

[41] Chis, O.-T., Banga, J. R., and Balsa-Canto, E. (2011). Structural identifiability of systems biology models: a critical comparison of methods. *PloS one*, 6(11):e27755.

[42] Chuang, J. S., Zemljic-Harpf, A., Ross, R. S., Frank, L. R., McCulloch, A. D., and Omens, J. H. (2010). Determination of three-dimensional ventricular strain distributions in gene-targeted mice using tagged MRI. *Magnetic Resonance in Medicine*, 64(July):1281–1288.

[43] Cookson, A., Lee, J., Michler, C., Chabiniok, R., Hyde, E., Nordsletten, D., Sinclair, M., Siebes, M., and Smith, N. (2012). A novel porous mechanical framework for modelling the interaction between coronary perfusion and myocardial mechanics. *Journal of Biomechanics*, 45(5):850–855.

[44] Costa, K. D., Holmes, J. W., and McCulloch, A. D. (2001). Modelling cardiac mechanical properties in three dimensions. *Philosophical transactions. Series A, Mathematical, physical, and engineering sciences*, 359(1783):1233–1250.

[45] Costa, K. D., May-Newman, K., Farr, D., O'Dell, W. G., McCulloch, A. D., and Omens, J. H. (1997). Three-dimensional residual strain in midanterior canine left ventricle. *The American journal of physiology*, 273(4 Pt 2):H1968–H1976.

[46] Costa, K. D., Takayama, Y., McCulloch, A. D., and Covell, J. W. (1999). Laminar fiber architecture and three-dimensional systolic mechanics in canine ventricular myocardium. *The American journal of physiology*, 276:H595–H607.

[47] Costandi, P. N., Frank, L. R., McCulloch, A. D., and Omens, J. H. (2006). Role of diastolic properties in the transition to failure in a mouse model of cardiac dilatation. *American journal of physiology. Heart and circulatory physiology*, 291(6):H2971–H2979.

[48] Craene, M. D., Piella, G., Camara, O., Duchateau, N., Silva, E., Doltra, A., Dhooge, J., Brugada, J., Sitges, M., and Frangi, A. F. (2012). Temporal diffeomorphic free-form deformation: application to motion and strain estimation from 3D echocardiography . *Med Image Anal*, 16:427–450.

[49] Criscione, J. C., Douglas, A. S., and Hunter, W. C. (2001). Physically based strain invariant set for materials exhibiting transversely isotropic behavior. *Journal of the Mechanics and Physics of Solids*, 49(4):871–897.

[50] Crouzeix, M. and Raviart, P. (1973). Conforming and nonconforming finite element methods for solving the stationary Stokes equations I. *ESAIM: Mathematical Modelling and Numerical Analysis - Modélisation Mathématique et Analyse Numérique*, 7:33–75.

[51] Dave, J. K., Halldorsdottir, V. G., Eisenbrey, J. R., Raichlen, J. S., Liu, J. B., McDonald, M. E., Dickie, K., Wang, S., Leung, C., and Forsberg, F. (2012). Noninvasive LV pressure estimation using subharmonic emissions from microbubbles. *JACC: Cardiovascular Imaging*, 5(1):87–92.

[52] De Marco, T., Chatterjee, K., Rouleau, J. L., and Parmley, W. W. (1988). Abnormal coronary hemodynamics and myocardial energetics in patients with chronic heart failure caused by ischemic heart disease and dilated cardiomyopathy. *American heart journal*, 115:809–815.

[53] De Vecchi, A., Gomez, A., Pushparajah, K., Schaeffter, T., Nordsletten, D., Simpson, J., Penney, G., and Smith, N. (2014). Towards a fast and efficient approach for modelling the patient-specific ventricular haemodynamics. *Progress in Biophysics and Molecular Biology*, 116(1):3–10.

[54] Dec, W. and Fuster, V. (1994). Idiopathic dilated cardiomyopathy. *The New England Journal of Medicine*, 331(23):1564–1575.

[55] Demer, L. L. and Yin, F. C. (1983). Passive biaxial mechanical properties of isolated canine myocardium. *The Journal of physiology*, 339:615–630.

[56] Dodge, H. T., Sandier, H., Ballew, D. W., and Lord, J. D. (1960). The use of biplane angiocardiography for the measurement of left ventricular volume in man. *American heart journal*, 60(5):762–776.

[57] Dokos, S., Smaill, B. H., Young, A., and LeGrice, I. J. (2002). Shear properties of passive ventricular myocardium. *American journal of physiology. Heart and circulatory physiology*, 283:H2650–H2659.

[58] Domenichini, F., Pedrizzetti, G., and Baccani, B. (2005). Three-dimensional filling flow into a model left ventricle. *Journal of Fluid Mechanics*, 539(-1):179.

[59] Du, C. K., Morimoto, S., Nishii, K., Minakami, R., Ohta, M., Tadano, N., Lu, Q. W., Wang, Y. Y., Zhan, D. Y., Mochizuki, M., Kita, S., Miwa, Y., Takahashi-Yanaga, F., Iwamoto, T., Ohtsuki, I., and Sasaguri, T. (2007). Knock-in mouse model of dilated cardiomyopathy caused by troponin mutation. *Circulation Research*, 101:185–194.

[60] Duan, F., Xie, M., Wang, X., Li, Y., He, L., Jiang, L., and Fu, Q. (2012). Preliminary clinical study of

left ventricular myocardial strain in patients with non-ischemic dilated cardiomyopathy by three-dimensional speckle tracking imaging. *Cardiovascular Ultrasound*, 10(1):8.

[61] Duan, Q., Moireau, P., Angelini, E., Chapelle, D., and Laine, A. (2007). Simulation of 3D ultrasound with a realistic electro-mechanical model of the heart. *Functional Imaging and Modeling of the Heart*, pages 463–473.

[62] Ebbers, T., Wigstrom, L., Bolger, A. F., Wranne, B., and Karlsson, M. (2002). Noninvasive Measurement of Relative Pressure Fields Within the Human Heart. *Journal of Biomechanical Engineering*, 124(June):288–293.

[63] Ecabert, O., Peters, J., Schramm, H., Lorenz, C., Von Berg, J., Walker, M. J., Vembar, M., Olszewski, M. E., Subramanyan, K., Lavi, G., and Weese, J. (2008). Automatic model-based segmentation of the heart in CT images. *IEEE Transactions on Medical Imaging*, 27(9):1189–1202.

[64] Edwards, C. H., Rankin, J. S., McHale, P. A., Ling, D., and Anderson, R. W. (1981). Effects of ischemia on left ventricular regional function in the conscious dog. *The American journal of physiology*, 240:H413–H420.

[65] Eggen, M., Swingen, C., and Iaizzo, P. (2009). Analysis of fiber orientation in normal and failing human hearts using diffusion tensor MRI. *2009 IEEE International Symposium on Biomedical Imaging: From Nano to Macro*, pages 642–645.

[66] Eichhorn, E. J., Heesch, C. M., Barnett, J. H., Alvarez, L. G., Fass, S. M., Grayburn, P. A., Hatfield, B. A., Marcoux, L. G., and Malloy, C. R. (1994). Effect of metoprol on myocardial function and energetics in patients with nonischemic dilated cardiomyopathy: A randomized, double-blind, placebo-controlled study. *American college of Cardiology*, 24(5):1310–1320.

[67] Eisenstat, S. C. and Walker, H. F. (1994). Globally convergent inexact Newton methods. *SIAM, Journal of Optimization*, 4(2):393–422.

[68] Fernandez-Teran, M. and Hurle, J. M. (1982). Myocardial fiber architecture of the human heart ventricles. *The Anatomical record*, 204:137–147.

[69] Fried, I. (1974). Finite element analysis of incompressible material by residual energy balancing. *International Journal of Solids and Structures*, 10(9):993–1002.

[70] Fry, D. L., Griggs, D. M., and Greenfield, J. C. (1964). Myocardial Mechanics : Tension-Velocity-Length relationships of heart muscle. *Circulation*, 14:73–86.

[71] Fung, Y. C. (1973). Biorheology of soft tissues. *Biorheology*, 10:139–155.

[72] Gao, H., Carrick, D., Berry, C., Griffith, B. E., and Luo, X. (2014). Dynamic finite-strain modelling of the human left ventricle in health and disease using an immersed boundary-finite element method. *IMA Journal of Applied Mathematics*, page hxu029.

[73] Gao, H., Li, W. G., Cai, L., Berry, C., and Luo, X. Y. (2015). Parameter estimation in a Holzapfel-Ogden law for healthy myocardium. *Journal of Engineering Mathematics*.

[74] Geselowitz, D. B. and Miller, W. T. (1983). A bidomain model for anisotropic cardiac muscle. *Annals of Biomedical Engineering*, 11(3-4):191–206.

[75] Ghista, D. N. and Sandler, H. (1969). An analytic elastic-viscoelastic model for the shape and the forces in the left ventricle. *Journal of biomechanics*, 2:33–47.

[76] Gil, D., Garcia-Barnes, J., Aris, R., Houzeaux, G., and Vaszquex, M. (2009). A Riemannian Approach to Cardiac Fiber Architecture Modelling. In *1st International Conference on Mathematical and Computational Biomedical Engineering - CMBE2009*.

[77] Glowinski, R. and Le Tallec, P. (1989). *Augmented Lagrangian and operator-splitting methods in nonlinear mechanics,*. SIAM.

[78] Göktepe, S., Acharya, S. N. S., Wong, J., and Kuhl, E. (2011). Computational modeling of passive myocardium. *International Journal for Numerical Methods in Biomedical Engineering*, 27(1):1–12.

[79] Gould, P., Ghista, D., Brombolich, L., and Mirsky, I. (1972). In vivo stresses in the human left ventricular wall: Analysis accounting for the irregural 3-dimensional geometry and comparison with idealised geometry analyses. *Journal of biomechanics*, 5:521–539.

[80] Grant, R. P. (1965). Notes on the Muscular Architecture of the Left Ventricle. *Circulation*, 32(August):301–308.

[81] Greenbaum, R., Ho, S. Y., Gibson, D. G., Becker, A. E., and Anderson, R. H. (1981). Left ventricular fibre architecture in man. *British heart journal*, 45(July 1980):248–263.

[82] Guccione, J. M., McCulloch, A. D., and Waldman, L. K. (1991). Passive material properties of intact ventricular myocardium determined from a cylindrical model. *Journal of biomechanical engineering*, 113(1):42–55.

[83] Guilcher, A., Brett, S., Munir, S., Clapp, B., and Chowienczyk, P. J. (2011). Estimating central SBP from the peripheral pulse: influence of waveform analysis and calibration error. *Journal of hypertension*, 29(7):1357–1366.

[84] Guyton, A. C. and Hall, J. E. (2006). *Textbook of medical physiology, 11th edition*. Elsevier Saunders.

[85] Hadjicharalambous, M., Chabiniok, R., Asner, L., Sammut, E., Wong, J., Carr-White, G., Lee, J., Razavi, R., Smith, N., and Nordsletten, D. (2015). Analysis of passive cardiac constitutive laws for parameter estimation using 3D tagged MRI. *Biomechanics and Modeling in Mechanobiology*, 14(4):807–828.

[86] Hadjicharalambous, M., Lee, J., Smith, N. P., and Nordsletten, D. A. (2014). A displacement-based finite element formulation for incompressible and nearly-incompressible cardiac mechanics. *Computer Methods in Applied Mechanics and Engineering*, 274:213–236.

[87] Harjai, K. J., Edupuganti, R., Nunez, E., Turgut, T., Scott, L., and Pandian, N. G. (2000). Does left ventricular shape influence clinical outcome in heart failure? *Clinical cardiology*, 23(11):813–819.

[88] Hassaballah, A. I., Hassan, M. A., Mardi, A. N., and Hamdi, M. (2013). An inverse finite element method for determining the tissue compressibility of human left ventricular wall during the cardiac cycle. *PLoS ONE*, 8(12).

[89] Hayashida, W., Kumada, T., Kohno, F., Noda, M., Ishikawa, N., Kambayashi, M., and Kawai, C. (1992). Left ventricular relaxation in dilated cardiomyopathy: relation to loading conditions and regional nonuniformity. *Journal of the American College of Cardiology*, 20(5):1082–1091.

[90] Heethaar, R. M., Pao, Y. C., and Ritman, E. L. (1977). Computer aspects of three-dimensional finite element analysis of stresses and strains in the intact heart. *Computers and Biomedical research*, 10:271–285.

[91] Heinzer, S., Krucker, T., Stampanoni, M., Abela, R., Meyer, E. P., Schuler, A., Schneider, P., and Müller, R. (2006). Hierarchical microimaging for multiscale analysis of large vascular networks. *NeuroImage*, 32(2):626–636.

[92] Helm, P., Younes, L., Beg, M. F., Ennis, D. B., Leclercq, C., Faris, O. P., McVeigh, E., Kass, D., Miller, M. I., and Winslow, R. L. (2006). Evidence of structural remodeling in the dyssynchronous failing heart. *Circulation Research*, 98(1):125–132.

[93] Herrmann, L. R. (1965). Elasticity equations for incompressible and nearly incompressible materials by a variational theorem. *AIAA Journal*, 3:1896–1900.

[94] Hill, A. V. (1938). The heat of shortening and the dynamic constants of muscle. *Proceedings of the Royal Society of London*, 126:136–195.

[95] Hirzel, H. O., Tuchschmid, C. R., Schneider, J., Krayenbuehl, H. P., and Schaub, M. C. (1985). Relationship between myosin isoenzyme composition, hemodynamics, and myocardial structure in various forms of human cardiac hypertrophy. *Circulation research*, 57(5):729–740.

[96] Hoffman, J. I. and Spaan, J. A. (1990). Pressure-flow relations in coronary circulation. *Physiological reviews*, 70(2):331–390.

[97] Holzapfel, G. (2001). *Mixed and Hybrid Finite Element Methods*. John Wiley and Sons.

[98] Holzapfel, G. A. and Ogden, R. W. (2009). Constitutive modelling of passive myocardium: a structurally based framework for material characterization. *Philosophical transactions. Series A, Mathematical, physical, and engineering sciences*, 367:3445–3475.

[99] Hoogendoorn, C., Duchateau, N., Sánchez-Quintana, D., Whitmarsh, T., Sukno, F. M., De Craene, M., Lekadir, K., and Frangi, A. F. (2013). A high-resolution atlas and statistical model of the human heart from multislice CT. *IEEE transactions on medical imaging*, 32(1):28–44.

[100] Horowitz, A., Lanir, Y., Yin, F. C., Perl, M., Sheinman, I., and Strumpf, R. K. (1988). Structural three-dimensional constitutive law for the passive myocardium. *Journal of biomechanical engineering*, 110(August 1988):200–207.

[101] Hughes, T. J. R. (1980). Generalization of selective integration procedures to anisotropic and nonlinear media. *International Journal for Numerical Methods in Engineering*, 15:1413–1418.

[102] Humphrey, J. D. (2002). *Cardiovascular solid mechanics: cells, tissues, and organs*. Springer Science + Business Media, New York.

[103] Humphrey, J. D., Strumpf, R. K., and Yin, F. C. (1990). Determination of a constitutive relation for passive myocardium: II. Parameter estimation. *Journal of biomechanical engineering*, 112(August 1990):340–346.

[104] Humphrey, J. D. and Yin, F. C. (1987). A new constitutive formulation for characterizing the mechanical behavior of soft tissues. *Biophysical journal*, 52(October):563–570.

[105] Hunter, P. J., McCulloch, A. D., and ter Keurs, H. E. (1998). Modelling the mechanical properties of cardiac muscle. *Progress in biophysics and molecular biology*, 69(2-3):289–331.

[106] Hunter, P. J., Pullan, A. J., and Smaill, B. H. (2003). Modeling total heart function. *Annual review of biomedical engineering*, 5:147–177.

[107] Huo, Y. and Kassab, G. S. (2007). A hybrid one-dimensional Womersley model of pulsatile blood flow in the entire coronary arterial tree. *American journal of physiology. Heart and circulatory physiology*, 46202:2623–2633.

216

[108] Huxley, A. F. (1957). Muscle structure and theories of contraction. *Progress in biophysics and biophysical chemistry*, 7:255–318.

[109] Huyghe, J. M., Arts, T., van Campen, D. H., and Reneman, R. S. (1992). Porous medium finite element model of the beating left ventricle. *The American journal of physiology*, 262(4 Pt 2):H1256–H1267.

[110] Iwasaki, T., Sinak, L. J., Hoffman, E. A., Robb, R. A., Harris, L. D., Bahn, R. C., and Ritman, E. L. (1984). Mass of left ventricular myocardium estimated with dynamic spatial reconstructor. *The American journal of physiology*, 246:H138–H142.

[111] Janz, R. F. and Grimm, A. F. (1972). Finite-element model for the mechanical behavior of the left ventricle. Prediction of deformation in the potassium-arrested rat heart. *Circulation research*, 30:244–252.

[112] Janz, R. F. and Grimm, A. F. (1973). Deformation of the diastolic left ventricle. I. Nonlinear elastic effects. *Biophysical journal*, 13:689–704.

[113] Janz, R. F., Kubert, B. R., Moriarty, T. F., and Grimm, A. F. (1974). Deformation of the diastolic left ventricle-II. Nonlinear geometric effects. *Journal of biomechanics*, 7:509–516.

[114] Joseph, S., Moazami, N., Cupps, B. P., Howells, A., Craddock, H., Ewald, G., Rogers, J., and Pasque, M. K. (2009). Magnetic Resonance Imaging-based Multiparametric Systolic Strain Analysis and Regional Contractile Heterogeneity in Patients With Dilated Cardiomyopathy. *Journal of Heart and Lung Transplantation*, 28(4):388–394.

[115] Judd, R. M. and Levy, B. I. (1991). Effects of barium-induced cardiac contraction on large- and small-vessel intramyocardial blood volume. *Circulation research*, 68:217–225.

[116] Juillière, Y., Marie, P. Y., Danchin, N., Gillet, C., Paille, F., Karcher, G., Bertrand, A., and Cherrier, F. (1993). Radionuclide assessment of regional differences in left ventricular wall motion and myocardial perfusion in idiopathic dilated cardiomyopathy. *European heart journal*, 14(February):1163–1169.

[117] Karamanoglu, M., O'Rourke, M. F., Avolio, A. P., and Kelly, R. P. (1993). An analysis of the relationship between central aortic and peripheral upper limb pressure waves in man. *European heart journal*, 14(2):160–167.

[118] Kass, D. A., Chen, C. H., Curry, C., Talbot, M., Berger, R., Fetics, B., and Nevo, E. (1999). Improved left ventricular mechanics from acute VDD pacing in patients with dilated cardiomyopathy and ventricular conduction delay. *Circulation*, 99(12):1567–1573.

[119] Kerckhoffs, R. C. P., Bovendeerd, P. H. M., Kotte, J. C. S., Prinzen, F. W., Smits, K., and Arts, T. (2003). Homogeneity of cardiac contraction despite physiological asynchrony of depolarization: A model study. *Annals of Biomedical Engineering*, 31:536–547.

[120] Kerckhoffs, R. C. P., Healy, S. N., Usyk, T. P., and Mcculloch, A. D. (2006). Computational methods for cardiac electromechanics. *Proceedings of the IEEE*, 94(4):769–782.

[121] Kerckhoffs, R. C. P., Neal, M. L., Gu, Q., Bassingthwaighte, J. B., Omens, J. H., and McCulloch, A. D. (2007). Coupling of a 3D finite element model of cardiac ventricular mechanics to lumped systems models of the systemic and pulmonic circulation. *Annals of Biomedical Engineering*, 35(1):1–18.

[122] Klotz, S., Hay, I., Dickstein, M. L., Yi, G.-H., Wang, J., Maurer, M. S., Kass, D. A., and Burkhoff, D. (2006). Single-beat estimation of end-diastolic pressure-volume relationship: a novel method with potential for noninvasive application. *American journal of physiology. Heart and circulatory physiology*, 291(January 2006):H403–H412.

[123] Korakianitis, T. and Shi, Y. (2006). Numerical simulation of cardiovascular dynamics with healthy and diseased heart valves. *Journal of Biomechanics*, 39:1964–1982.

[124] Krishnamurthy, A., Villongco, C. T., Chuang, J., Frank, L. R., Nigam, V., Belezzuoli, E., Stark, P., Krummen, D. E., Narayan, S., Omens, J. H., McCulloch, A. D., and Kerckhoffs, R. C. P. (2013). Patient-specific models of cardiac biomechanics. *Journal of Computational Physics*, 244:4–21.

[125] Krittian, S. B. S., Lamata, P., Michler, C., Nordsletten, D. A., Bock, J., Bradley, C. P., Pitcher, A., Kilner, P. J., Markl, M., and Smith, N. P. (2012). A finite-element approach to the direct computation of relative cardiovascular pressure from time-resolved MR velocity data. *Medical Image Analysis*, 16(5):1029–1037.

[126] Kronenberg, M. W., Cohen, G. I., Leonen, M. F., Mladsi, T. A., and Di Carli, M. F. (2006). Myocardial oxidative metabolic supply-demand relationships in patients with nonischemic dilated cardiomyopathy. *Journal of Nuclear Cardiology*, 13(4):544–553.

[127] Lamata, P., Niederer, S., Nordsletten, D., Barber, D. C., Roy, I., Hose, D. R., and Smith, N. (2011). An accurate, fast and robust method to generate patient-specific cubic Hermite meshes. *Medical Image Analysis*, 15(6):801–813.

[128] Laskey, W. K., Sutton, M. S., Zeevi, G., Hirshfeld, J. W., and Reichek, N. (1984). Left ventricular mechanics in dilated cardiomyopathy. *The American journal of cardiology*, 54(6):620–625.

[129] Lee, J., Cookson, A., Roy, I., Kerfoot, E., Asner, L., Vigueras, G., Sochi, T., Michler, C., Smith, N., and

Nordsletten, D. (In review). Multi-physics computational modeling in **C**Heart. *SIAM Journal on Scientific Computing*.

[130] Lee, J., Niederer, S., Nordsletten, D., Le Grice, I., Smaill, B., Kay, D., and Smith, N. (2009). Coupling contraction, excitation, ventricular and coronary blood flow across scale and physics in the heart. *Philosophical transactions. Series A, Mathematical, physical, and engineering sciences*, 367:2311–2331.

[131] Lee, J. and Smith, N. P. (2012). The multi-scale modelling of coronary blood flow. *Annals of Biomedical Engineering*, 40(11):2399–2413.

[132] Legrice, I., Sands, G., Hooks, D., Gerneke, D., and Smaill, B. (2004). Proceedings of the Australian Physiological and Pharmacological Society Symposium : Functional Imaging MICROSCOPIC IMAGING OF EXTENDED TISSUE VOLUMES. *Young*, (August):902–905.

[133] Legrice, I. J., Hunter, P. J., and Smaill, B. H. (1997). Laminar structure of the heart: a mathematical model. *The American journal of physiology*, 272:H2466–H2476.

[134] LeGrice, I. J., Smaill, B. H., Chai, L. Z., Edgar, S. G., Gavin, J. B., and Hunter, P. J. (1995). Laminar structure of the heart: ventricular myocyte arrangement and connective tissue architecture in the dog. *The American journal of physiology*, 269:H571–H582.

[135] Lemmon, J. D. and Yoganathan, A. P. (2000). Computational modeling of left heart diastolic function: examination of ventricular dysfunction. *Journal of biomechanical engineering*, 122(4):297–303.

[136] Levine, H. J. and Britman, N. A. (1964). Force-Velocity Relations in the Intact Dog Heart. *The Journal of clinical investigation*, 43(7):1383–1396.

[137] Lin, D. and Yin, F. (1998). A multiaxial constitutive law for mammalian left ventricular myocardium in steady-state barium contracture or tetanus. *Journal of biomechanical engineering*, 120(4):504–517.

[138] Little, W. C. (2005). Diastolic dysfunction beyond distensibility: Adverse effects of ventricular dilatation. *Circulation*, 112(19):2888–2890.

[139] Liu, C., Hofstetter, G., and Mang, H. (1994). 3D finite element analysis of rubber-like materials at finite strains. *Engineering computations*, 11(2):111–128.

[140] Liu, H. and Shi, P. (2009). Maximum a posteriori strategy for the simultaneous motion and material property estimation of the heart. *IEEE T Bio-Med Eng*, 56(2):378–89.

[141] Liu, Y. H., Bahn, R. C., and Ritman, E. L. (1992). Dynamic intramyocardial blood volume: evaluation with a radiological opaque marker method. *The American journal of physiology*, 263:H963–H967.

[142] Loerakker, S., Cox, L. G. E., van Heijst, G. J. F., de Mol, B. A. J. M., and van de Vosse, F. N. (2008). Influence of dilated cardiomyopathy and a left ventricular assist device on vortex dynamics in the left ventricle. *Computer methods in biomechanics and biomedical engineering*, 11(6):649–660.

[143] MacCallum, J. (1900). On the muscular architecture and growth of the ventricles of the heart. *Johns Hopkins Hospital Reports*, 9:307–335.

[144] Malkus, D. S. and Hughes, T. J. (1978). Mixed finite element methods Reduced and selective integration techniques: A unification of concepts. *Computer Methods in Applied Mechanics and Engineering*, 15(1):63–81.

[145] Mall, F. P. (1911). On the muscular architecture of the ventricles of the human heart. *American Journal of Anatomy*, 11:211–266.

[146] Malvern, L. E. (1969). *Introduction to the Mechanics of a Continuous Medium*.

[147] Mann, D. L., Kubo, S. H., Sabbah, H. N., Starling, R. C., Jessup, M., Oh, J. K., and Acker, M. A. (2012). Beneficial effects of the CorCap cardiac support device: Five-year results from the Acorn Trial. *Journal of Thoracic and Cardiovascular Surgery*, 143(5):1036–1042.

[148] Martínez-Legazpi, P., Bermejo, J., Benito, Y., Yotti, R., Pérez del Villar, C., González-Mansilla, A., Barrio, A., Villacorta, E., Sánchez, P. L., Fernández-Avilés, F., and Del Álamo, J. C. (2014). Contribution of the Diastolic Vortex Ring to Left Ventricular Filling. *Journal of the American College of Cardiology*, 64(16):1711–1721.

[149] Matitiau, A., Perez-Atayde, A., Sanders, S. P., Sluysmans, T., Parness, I. A., Spevak, P. J., and Colan, S. D. (1994). Infantile dilated cardiomyopathy. Relation of outcome to left ventricular mechanics, hemodynamics, and histology at the time of presentation. *Circulation*, 90(3):1310–1318.

[150] Maughan, D. W. (2005). Kinetics and energetics of the crossbridge cycle. *Heart Failure Reviews*, 10:175–185.

[151] May-Newman, K., Omens, J. H., Pavelec, R. S., and McCulloch, A. D. (1994). Three-dimensional transmural mechanical interaction between the coronary vasculature and passive myocardium in the dog. *Circulation research*, 74(6):1166–1178.

[152] McCormick, M., Nordsletten, D. A., Kay, D., and Smith, N. P. (2013). Simulating left ventricular fluid-solid mechanics through the cardiac cycle under LVAD support. *Journal of Computational Physics*, 244:80–96.

[153] McCulloch, A. D., Smaill, B. H., and Hunter, P. J. (1987). Left ventricular epicardial deformation in isolated arrested dog heart. *The American journal of physiology*, 252:H233–H241.

[154] McCulloch, A. D., Smaill, B. H., and Hunter, P. J. (1989). Regional left ventricular epicardial deformation in the passive dog heart. *Circulation research*, 64:721–733.

[155] McQueen, D. M. and Peskin, S. (1989). A Three-Dimensional Computational Method for Blood Flow in the Heart. II. Contractile fibers. 2899297:289–297.

[156] Merlo, M., Pyxaras, S. A., Pinamonti, B., Barbati, G., Di Lenarda, A., and Sinagra, G. (2011). Prevalence and prognostic significance of left ventricular reverse remodeling in dilated cardiomyopathy receiving tailored medical treatment. *Journal of the American College of Cardiology*, 57(13):1468–1476.

[157] Meunier, J. (1998). Tissue motion assessment from 3D echographic speckle tracking . *Phys Med Biol*, 43:12411254.

[158] Miehe, C., Stein, E., and Wagner, W. (1994). Associative multiplicative elasto-plasticity: Formulation and aspects of the numerical implementation including stability analysis. *Computers & Structures*, 52(5):969–978.

[159] Mihalef, V., Ionasec, R. I., Sharma, P., Georgescu, B., Voigt, I., Suehling, M., and Comaniciu, D. (2011). Patient-specific modelling of whole heart anatomy, dynamics and haemodynamics from four-dimensional cardiac CT images. *Interface Focus*, 1(3):286–296.

[160] Mirsky, I. (1969). Left ventricular stresses in the intact human heart. *Biophysical journal*, 9(2):189–208.

[161] Mirsky, I. (1973). Ventricular and arterial wall stresses based on large deformation analyses. *Biophysical journal*, 13(1972):1141–1159.

[162] Mirsky, I. and Parmley, W. W. (1973). Assessment of passive elastic stiffness for isolated heart muscle and the intact heart. *Circulation research*, 33:233–243.

[163] Moireau, P., Chapelle, D., and Le Tallec, P. (2008). Joint state and parameter estimation for distributed mechanical systems. *Comput Methods Appl Mech Engrg*, 197:659–677.

[164] Moireau, P., Chapelle, D., and Le Tallec, P. (2009). Filtering for distributed mechanical systems using position measurements: perspectives in medical imaging. *Inverse Probl*, 25(3):035010.

[165] Moriarty, T. F. (1980). The Law of Laplace. Its limitations as a relation for diastolic pressure, volume, or wall stress of the left ventricle. *Circulation research*, 46(3):321–331.

[166] Mu, Y., Chen, L., Tang, Q., and Ayoufu, G. (2010). Real time three-dimensional echocardiographic assessment of left ventricular regional systolic function and dyssynchrony in patients with dilated cardiomyopathy. *Echocardiography*, 27(4):415–420.

[167] Nagueh, S. F., Middleton, K. J., Kopelen, H. A., Zoghbi, W. A., and Quin, M. A. (1997). Doppler Tissue Imaging : A Noninvasive Technique for Evaluation of Left Ventricular Relaxation and Estimation of Filling Pressures. *Journal of American College of Cardiology*, 30(6):1527–1533.

[168] Nash, M. (1994). *Mechanics and Material Properties of the Heart using an Anatomically Accurate Mathematical Model*. PhD thesis.

[169] Nash, M. and Hunter, P. (2000). Computational Mechanics of the Heart- From Tissue Structure to Ventricular Function. *J Elasticity*, 61:113–141.

[170] Nash, M. P. and Hunter, P. J. (2001). Computational Mechanics of the Heart. *Journal of Elasticity*, 61:113–141.

[171] Neglia, D., De Caterina, A., Marraccini, P., Natali, A., Ciardetti, M., Vecoli, C., Gastaldelli, A., Ciociaro, D., Pellegrini, P., Testa, R., Menichetti, L., L'Abbate, A., Stanley, W. C., and Recchia, F. A. (2007). Impaired myocardial metabolic reserve and substrate selection flexibility during stress in patients with idiopathic dilated cardiomyopathy. *American journal of physiology. Heart and circulatory physiology*, 293(6):H3270–H3278.

[172] Nelson, G. S., Berger, R. D., Fetics, B. J., Talbot, M., Spinelli, J. C., Hare, J. M., and Kass, D. A. (2000). Left ventricular or biventricular pacing improves cardiac function at diminished energy cost in patients with dilated cardiomyopathy and left bundle-branch block. *Circulation*, 102:3053–3059.

[173] Nickerson, D., Smith, N., and Hunter, P. (2005). New developments in a strongly coupled cardiac electromechanical model. *Europace*, 7:118–127.

[174] Nicolaides, R. A. (1982). SIAM Journal on Numerical Analysis,. *SIAM Journal on Numerical Analysis*, 19(2):349–357.

[175] Niederer, S. A., Plank, G., Chinchapatnam, P., Ginks, M., Lamata, P., Rhode, K. S., Rinaldi, C. A., Razavi, R., and Smith, N. P. (2011). Length-dependent tension in the failing heart and the efficacy of cardiac resynchronization therapy. *Cardiovascular Research*, 89:336–343.

[176] Niederer, S. A. and Smith, N. P. (2008). An improved numerical method for strong coupling of excitation and contraction models in the heart. *Progress in Biophysics and Molecular Biology*, 96(1-3):90–111.

[177] Nielsen, P. M., Le Grice, I. J., Smaill, B. H., and Hunter, P. J. (1991). Mathematical model of geometry and fibrous structure of the heart. *The American journal of physiology*, 260:H1365–H1378.

[178] Nikolić, S., Yellin, E. L., Tamura, K., Vetter, H., Tamura, T., Meisner, J. S., and Frater, R. W. (1988). Passive properties of canine left ventricle: diastolic stiffness and restoring forces. *Circulation research*, 62(6):1210–1222.

[179] Nordsletten, D. (2009). *Fluid - Solid Coupling for the Simulation of Left Ventricular Mechanics* . PhD thesis, University of Oxford.

[180] Nordsletten, D., Hadjicharalambous, M., and Asner, L. (2013). Biomechanics in the Heart: an Introduction. Technical report.

[181] Nordsletten, D., M, M., Kilner, P. J., Hunter, P., Kay, D., and Smith, N. (2011a). Fluid-solid coupling for the investigation of diastolic and systolic human left ventricular function. *International Journal for numerical methods in biomedical engineering*, 27:10171039.

[182] Nordsletten, D. A., Niederer, S. A., Nash, M. P., Hunter, P. J., and Smith, N. P. (2011b). Coupling multi-physics models to cardiac mechanics. *Progress in Biophysics and Molecular Biology*, 104:77–88.

[183] Novak, V. P., Yin, F. C., and Humphrey, J. D. (1994). Regional mechanical properties of passive myocardium. *Journal of Biomechanics*, 27(4):403–412.

[184] Ochs, A., Schuster, A., Riffel, J., Düchting, J., Thome, S., Andre, F., Seitz, S. A., Galuschky, C., Mahrholdt, H., Bruder, O., Korosoglou, G., Katus, H. A., and Buss, S. (2015). LV rotational mechanics in patients with dilated cardiomyopathy compared to healthy individuals : Experience from the European CMR Registry. *Journal of Cardiovascular Magnetic Resonance*, 17(Suppl 1):Q69.

[185] Oden, J. T. and Key, J. E. (1970). Numerical analysis of finite axisymmetric deformations of incompressible elastic solids of revolution. *International Journal of Solids and Structures*, 6:497–518.

[186] Omens, J., MacKenna, D., and McCulloch, A. (1993a). Measurement of strain and analysis of stress in resting rat left ventricular myocardium. *J. Biomechanics*, 26.6:665–676.

[187] Omens, J. H. and Fung, Y. C. (1990). Residual strain in rat left ventricle. *Circulation research*, 66(1):37–45.

[188] Omens, J. H., MacKenna, D. A., and McCulloch, A. D. (1993b). Measurement of strain and analysis of stress in resting rat left ventricular myocardium.

[189] Omens, J. H., May, K. D., and McCulloch, A. D. (1991). Transmural distribution of three-dimensional strain in the isolated arrested canine left ventricle. *The American journal of physiology*, 261(18):H918–H928.

[190] Omens, J. H., Usyk, T. P., Li, Z., and McCulloch, A. D. (2002). Muscle LIM protein deficiency leads to alterations in passive ventricular mechanics. *American journal of physiology. Heart and circulatory physiology*, 282:H680–H687.

[191] Osman, N. F., Kerwin, W. S., McVeigh, E. R., and Prince, J. L. (1999). Cardiac Motion Tracking Using CINE Harmonic Phase (HARP) Magnetic Resonance Imaging. *Magnetic Resonance in Medicine*, 42:1048–1060.

[192] Pan, L., Prince, J. L., Lima, J. A. C., and Osman, N. F. (2005). Fast tracking of cardiac motion using 3D-HARP. *IEEE T Bio-Med Eng*, 52(8):1425–35.

[193] Panda, S. C. and Natarajan, R. (1977). Finite-element method of stress analysis in the human left ventricular layered wall structure. *Medical & biological engineering & computing*, 15(January):67–71.

[194] Pao, Y. C., Ritman, E. L., and Wood, E. H. (1974). Finite-element analysis of left ventricular myocardial stresses. *Journal of Biomechanics*, 7:467–477.

[195] Pasipoularides, A., Mirsky, I., Hess, O. M., Grimm, J., and Krayenbuehl, H. P. (1986). Myocardial relaxation and passive diastolic properties in man. *Circulation*, 74(5):991–1001.

[196] Pedersen, H., Kozerke, S., Ringgaard, S., Nehrke, K., and Won, Y. K. (2009). K-t PCA: Temporally constrained k-t BLAST reconstruction using principal component analysis. *Magnetic Resonance in Medicine*, 62(3):706–716.

[197] Pedrizzetti, G. and Domenichini, F. (2005). Nature optimizes the swirling flow in the human left ventricle. *Physical Review Letters*, 95(10):1–4.

[198] Peskin, C. S. and McQueen, D. M. (1989). A three-dimensional computational method for blood flow in the heart. I. Immersed elastic fibers in a viscous incompressible fluid. *Journal of Computational Physics*, 81(2):372–405.

[199] Peters, J., Ecabert, O., Schmitt, H., Grass, M., and Weese, J. (2009). Local cardiac wall motion estimation from retrospectively gated ct images. *Lecture Notes in Computer Science (including subseries Lecture Notes in Artificial Intelligence and Lecture Notes in Bioinformatics)*, 5528:191–200.

[200] Pinto, J. G. and Fung, Y. C. (1973). Mechanical properties of the heart muscle in the passive state. *Journal of biomechanics*, 6:597–616.

[201] Quarterman, R. L., Moonly, S., Wallace, A. W., Guccione, J., and Ratcliffe, M. B. (2002). A finite element model of left ventricular cellular transplantation in dilated cardiomyopathy. *ASAIO journal (American Society for Artificial Internal Organs : 1992)*, 48(5):508–513.

[202] Quarteroni, A. (1994). *Numerical approximation of partial differential equations.* Springer-Verlag Berlin Heidelberg.

[203] Raue, A., Kreutz, C., Maiwald, T., Bachmann, J., Schilling, M., Klingmüller, U., and Timmer, J. (2009). Structural and practical identifiability analysis of partially observed dynamical models by exploiting the profile likelihood. *Bioinformatics*, 25(15):1923–9.

[204] Raue, A., Kreutz, C., Maiwald, T., Klingmuller, U., and Timmer, J. (2011). Addressing parameter identifiability by model-based experimentation. *IET systems biology*, 5(2):120–130.

[205] Reichek, N. (1999). MRI myocardial tagging. *JMRI*, 10(5):609–16.

[206] Rihal, C. S., Nishimura, R. A., Hatle, L. K., Bailey, K. R., and Tajik, A. J. (1994). Systolic and diastolic dysfunction in patients with clinical diagnosis of dilated cardiomyopathy. Relation to symptoms and prognosis. *Circulation*, 90(6):2772–2779.

[207] Robb, J. S. and Robb, R. C. (1942). The normal heart. Anatomy and physiology of the structural units. *American Heart Journal*, 23(4):455–467.

[208] Rohmer, D., Sitek, A., and Gullberg, G. T. (2007). Reconstruction and visualization of fiber and laminar structure in the normal human heart from ex vivo diffusion tensor magnetic resonance imaging (DTMRI) data. *Investigative radiology*, 42(11):777–789.

[209] Rueckert, D., L. Sonoda, C. Hayes, D. H. M. L., and Hawkes, D. (1999). Nonrigid registration using free-form deformations: application to breast MR images. *IEEE T Med Imaging*, 18(8):712–21.

[210] Russell, K., Eriksen, M., Aaberge, L., Wilhelmsen, N., Skulstad, H., Remme, E. W., Haugaa, K. H., Opdahl, A., Fjeld, J. G., Gjesdal, O., Edvardsen, T., and Smiseth, O. (2012). A novel clinical method for quantification of regional left ventricular pressure-strain loop area: A non-invasive index of myocardial work. *European Heart Journal*, 33(6):724–733.

[211] Rutz, A., Ryf, S., Plein, S., Boesiger, P., and Kozerke, S. (2008). Accelerated whole-heart 3D CSPAMM for myocardial motion quantification. *Magn Reson Med*, 59:755–763.

[212] Saber, N. R., Gosman, A. D., Wood, N. B., Kilner, P. J., Charrier, C. L., and Firmin, D. N. (2001). Computational flow modeling of the left ventricle based on in vivo MRI data: Initial experience. *Annals of Biomedical Engineering*, 29(4):275–283.

[213] Saber, N. R., Wood, N. B., Gosman, A. D., Merrifield, R. D., Yang, G. Z., Charrier, C. L., Gatehouse, P. D., and Firmin, D. N. (2003). Progress towards patient-specific computational flow modeling of the left heart via combination of magnetic resonance imaging with computational fluid dynamics. *Annals of Biomedical Engineering*, 31(1):42–52.

[214] Saccomani, M. P. (2013). Structural vs Practical Identifiability in System Biology. *IWBBIO 2013. Proceedings*, pages 18–20.

[215] Sandler, H. and Dodge, H. T. (1963). Left Ventricular Tension and Stress in Man. *Circulation research*, 13:91–104.

[216] Sands, G. B., Gerneke, D. A., Hooks, D. A., Green, C. R., Smaill, B. H., and Legrice, I. J. (2005). Automated imaging of extended tissue volumes using confocal microscopy. *Microscopy Research and Technique*, 67(February):227–239.

[217] Scheffler, K. and Lehnhardt, S. (2003). Principles and applications of balanced SSFP techniques. *European Radiology*, 13(11):2409–2418.

[218] Schenkel, T., Malve, M., Reik, M., Markl, M., Jung, B., and Oertel, H. (2009). MRI-Based CFD analysis of flow in a human left ventricle: Methodology and application to a healthy heart. *Annals of Biomedical Engineering*, 37(3):503–515.

[219] Schmid, H., O'Callaghan, P., Nash, M. P., Lin, W., LeGrice, I. J., Smaill, B. H., Young, A. A., and Hunter, P. J. (2008). Myocardial material parameter estimation: A non-homogeneous finite element study from simple shear tests. *Biomechanics and Modeling in Mechanobiology*, 7:161–173.

[220] Schnabel, J. A., Rueckert, D., Quist, M., Blackall, J. M., Castellano-smith, A. D., Hartkens, T., Penney, G. P., Hall, W., Liu, H., Truwit, C. L., Gerritsen, F. A., Hill, D. L. G., and Hawkes, D. J. (2001). A generic framework for non-rigid registration based on non-uniform multi-level free-form deformations. *Medical Image Computing and Computer-Assited Intervention*, 2208:573–581.

[221] Sermesant, M., Delingette, H., and Ayache, N. (2006a). An Electromechanical Model of the Heart for Image Analysis and Simulation. 25(5):612–625.

[222] Sermesant, M., Forest, C., Pennec, X., Delingette, H., and Ayache, N. (2003). Deformable biomechanical models: application to 4D cardiac image analysis. *Med Image Anal*, 7(4):475–88.

[223] Sermesant, M., Moireau, P., Camara, O., Sainte-Marie, J., Andriantsimiavona, R., Cimrman, R., Hill, D. L. G., Chapelle, D., and Razavi, R. (2006b). Cardiac function estimation from MRI using a heart model and data assimilation: advances and difficulties. *Med Image Anal*, 10(4):642–56.

[224] Shamanskii, V. (1967). A modification of newton's method. *Ukrainian Mathematical Journal*, 19(1):118–122.

[225] Shi, W., Zhuang, X., Wang, H., Duckett, S., Luong, D. V. N., Tobon-Gomez, C., Tung, K., Edwards, P. J., Rhode, K. S., Razavi, R. S., Ourselin, S., and Rueckert, D. (2012). A comprehensive cardiac motion estimation framework using both untagged and 3-D tagged MR images based on nonrigid registration. 31(6):1263–75.

[226] Simo, J., Taylor, R., and Pister, K. (1985a). Variational and projection methods for the volume constraint in finite deformation elasto-plasticity. *Computer Methods in Applied Mechanics and Engineering*, 51(1-3):177–208.

[227] Simo, J. C. and Taylor, R. L. (1991). Quasi-incompressible finite elasticity in principal stretches. continuum basis and numerical algorithms. *Computer Methods in Applied Mechanics and Engineering*, 85(3):273–310.

[228] Simo, J. C., Wriggers, P., and Taylor, R. L. (1985b). A perturbed Lagrangian formulation for the finite element solution of contact problems. *Computer Methods in Applied Mechanics and Engineering*, 50(2):163–180.

[229] Smaill, B. and Hunter, P. (1991). Structure and function of the diastolic heart: material properties of passive myocardium. In *Theory of Heart*, pages 1–29. Springer.

[230] Smaill, B. H., LeGrice, I. J., Hooks, D. A., Pullan, A. J., Caldwell, B. J., and Hunter, P. J. (2004). Cardiac structure and electrical activation: Models and measurement. *Clinical and Experimental Pharmacology and Physiology*, 31(12):913–919.

[231] Smith, N., Stevens, C., and Hunter, P. (2005). Computational Modeling of Ventricular Mechanics and Energetics. *Applied Mechanics Reviews*, 58:77.

[232] Smith, N. P. (2004). A computational study of the interaction between coronary blood flow and myocardial mechanics. *Physiological measurement*, 25(4):863–877.

[233] Smith, N. P., Buist, M. L., and Pullan, A. J. (2003). Altered T wave dynamics in a contracting cardiac model. *Journal of cardiovascular electrophysiology*, 14(10 Suppl):S203–S209.

[234] Smith, N. P., Pullan, A. J., and Hunter, P. J. (2002). An anatomically based model of transient coronary blood flow in the heart. *SIAM J. Appl. Math*, 62(3):990–1018.

[235] Spaan, J. A. E., Siebes, M., ter Wee, R., Kolyva, C., van Teeffelen, J. W. G. E., Vink, H., Fokkema, D. S., Streekstra, G., and VanBavel, E. (2005). Visualisation of intramural coronary vasculature by an imaging cryomicrotome suggests compartmentalisation of myocardial perfusion areas. *Medical and Biological Engineering and Computing*, 43(4):431–435.

[236] Stevens, C., Remme, E., LeGrice, I., and Hunter, P. (2003). Ventricular mechanics in diastole: Material parameter sensitivity. *Journal of Biomechanics*, 36(November 2002):737–748.

[237] Stoeck, C. T., Kalinowska, A., von Deuster, C., Harmer, J., Chan, R. W., Niemann, M., Manka, R., Atkinson, D., Sosnovik, D. E., Mekkaoui, C., and Kozerke, S. (2014). Dual-Phase Cardiac Diffusion Tensor Imaging with Strain Correction. *PLoS ONE*, 9(9):e107159.

[238] Streeter, D. D. and Bassett, D. L. (1966). An engineering analysis of myocardial fiber orientation in pig's left ventricle in systole. *The Anatomical Record*, 155:503–511.

[239] Streeter, D. D., Spotnitz, H. M., Patel, D. P., Ross, J., and Sonnenblick, E. H. (1969). Fiber orientation in the canine left ventricle during diastole and systole. *Circulation research*, 24(8):339–347.

[240] Suga, H., Igarashi, Y., Yamada, O., and Goto, Y. (1985). Mechanical efficiency of the left ventricle as a function of preload, afterload, and contractility. *Heart and Vessels*, 1:3–8.

[241] Sun, K., Stander, N., Jhun, C.-S., Zhang, Z., Suzuki, T., Wang, G.-Y., Saeed, M., Wallace, A. W., Tseng, E. E., Baker, A. J., Saloner, D., Einstein, D. R., Ratcliffe, M. B., and Guccione, J. M. (2009). A computationally efficient formal optimization of regional myocardial contractility in a sheep with left ventricular aneurysm. *J Biomed Eng*, 131(11):111001.

[242] Suri, M. (1996). Analytical and computational assessment of locking in the hp finite element method. *Computer Methods in Applied Mechanics and Engineering*, 133(95):347–371.

[243] Sussman, T. and Bathe, K.-J. (1987). A finite element formulation for nonlinear incompressible elastic and inelastic analysis. *Computers & Structures*, 26(I):357–409.

[244] Taber, L. A., Yang, M., and Podszus, W. W. (1996). Mechanics of ventricular torsion. *Journal of Biomechanics*, 29(6):745–752.

[245] Taylor, R. L., Pister, K. S., and Herrmann, L. R. (1968). On a variational theorem for incompressible and nearly-incompressible orthotropic elasticity. *International Journal of Solids and Structures*, 4(9):875–883.

[246] Ter Keurs, H. E., Rijnsburger, W. H., van Heuningen, R., and Nagelsmit, M. J. (1980). Tension development and sarcomere length in rat cardiac trabeculae. Evidence of length-dependent activation. *Circulation research*, 46(5):703–714.

[247] Thorvaldsen, T., Osnes, H., and Sundnes, J. (2005). A mixed finite element formulation for a non-linear, transversely isotropic material model for the cardiac tissue. *Computer methods in biomechanics and biomedical engineering*, 8(April 2012):369–379.

[248] Tomlinson, K. A., Hunter, P. J., and Pullan, A. J. (2002). A Finite Element Method for an Eikonal Equation Model of Myocardial Excitation Wavefront Propagation.

[249] Torii, R., Keegan, J., Wood, N. B., Dowsey, A. W., Hughes, A. D., Yang, G. Z., Firmin, D. N., Thom, S. A. M., and Xu, X. Y. (2010). MR image-based geometric and hemodynamic investigation of the right coronary artery with dynamic vessel motion. *Annals of Biomedical Engineering*, 38(8):2606–2620.

[250] Torrent-Guasp, F., Kocica, M. J., Corno, A., Komeda, M., Cox, J., Flotats, a., Ballester-Rodes, M., and Carreras-Costa, F. (2004). Systolic ventricular filling. *European Journal of Cardio-thoracic Surgery*, 25:376–386.

[251] Toussaint, N., Sermesant, M., Stoeck, C. T., Kozerke, S., and Batchelor, P. G. (2010). In vivo human 3D cardiac fibre architecture: Reconstruction using curvilinear interpolation of diffusion tensor images. *Lecture Notes in Computer Science (including subseries Lecture Notes in Artificial Intelligence and Lecture Notes in Bioinformatics)*, 6361 LNCS(PART 1):418–425.

[252] Uribe, S., Beerbaum, P., Sø rensen, T. S., Rasmusson, A., Razavi, R., and Schaeffter, T. (2009). Four-dimensional (4D) flow of the whole heart and great vessels using real-time respiratory self-gating. *Magnetic Resonance in Medicine*, 62:984–992.

[253] Uribe, S., Muthurangu, V., Boubertakh, R., Schaeffter, T., Razavi, R., Hill, D. L. G., and Hansen, M. S. (2007). Whole-heart cine MRI using real-time respiratory self-gating. *Magnetic Resonance in Medicine*, 57(October 2006):606–613.

[254] Usyk, T. P., Mazhari, R., and Mcculloch, A. D. (2000). Effect of laminar orthotropic myofiber architecture on regional stress and strain in the canine left ventricle. *Journal of Elasticity*, 61:143–164.

[255] Usyk, T. P. and Mcculloch, A. D. (2002). Computational Methods for Soft Tissue Biomechanics. *Biomechanics of Soft Tissue in Cardiovascular Systems*, 441:273–342.

[256] Usyk, T. P. and McCulloch, A. D. (2003). Relationship between regional shortening and asynchronous electrical activation in a three-dimensional model of ventricular electromechanics. *Journal of cardiovascular electrophysiology*, 14(10 Suppl):S196–S202.

[257] Vasquez, M., Aris, R., Houzeaux, G., Aubry, R., Villar, P., Garcia-Barnes, J., Gil, D., and Carreras, F. (2011). A massively parallel computational electrophysiology model of the heart. *International Journal for Numerical Methods in Biomedical Engineering*, 27(12):1911–1929.

[258] Vendelin, M., Bovendeerd, P. H. M., Arts, T., Engelbrecht, J., and Van Campen, D. H. (2000). Cardiac mechanoenergetics replicated by cross-bridge model. *Annals of Biomedical Engineering*, 28(6):629–640.

[259] Vendelin, M., Bovendeerd, P. H. M., Engelbrecht, J., and Arts, T. (2002). Optimizing ventricular fibers: uniform strain or stress, but not ATP consumption, leads to high efficiency. *American journal of physiology. Heart and circulatory physiology*, 283:H1072–H1081.

[260] Vetter, F. J. and McCulloch, A. D. (2000). Three-dimensional stress and strain in passive rabbit left ventricle: a model study. *Annals of biomedical engineering*, 28:781–792.

[261] Waldman, L. K., Nosan, D., Villarreal, F., and Covell, J. W. (1988). Relation between transmural deformation and local myofiber direction in canine left ventricle. *Circulation research*, 63:550–562.

[262] Walker, J. C., Ratcliffe, M. B., Zhang, P., Wallace, A. W., Hsu, E. W., Saloner, D. A., and Guccione, J. M. (2008). Magnetic resonance imaging-based finite element stress analysis after linear repair of left ventricular aneurysm. *The Journal of thoracic and cardiovascular surgery*, 135(May):1094–1102, 1102.e1–e2.

[263] Wang, H. M., Luo, X. Y., Gao, H., Ogden, R. W., Griffith, B. E., Berry, C., and Wang, T. J. (2014). A modified Holzapfel-Ogden law for a residually stressed finite strain model of the human left ventricle in diastole. *Biomechanics and Modeling in Mechanobiology*, 13:99–113.

[264] Wang, J. and Nagueh, S. F. (2009). Current perspectives on cardiac function in patients with diastolic heart failure. *Circulation*, 119(8):1146–1157.

[265] Wang, V. Y., Casta, C., Croisille, P., Clarysse, P., Zhu, Y. M., Cowan, B. R., Young, A. A., and Nash, M. P. (2012). Estimation of in vivo human myocardial fibre strain by integrating diffusion tensor and tagged MRI using FE modelling. *Proceedings - International Symposium on Biomedical Imaging*, pages 46–49.

[266] Wang, V. Y., Lam, H. I., Ennis, D. B., Cowan, B. R., Young, A. A., and Nash, M. P. (2009). Modelling passive diastolic mechanics with quantitative MRI of cardiac structure and function. *Medical Image Analysis*, 13(5):773–784.

[267] Wang, V. Y., Lam, H. I., Ennis, D. B., Cowan, B. R., Young, A. A., and Nash, M. P. (2010). Cardiac active contraction parameters estimated from magnetic resonance imaging. *Lecture Notes in Computer Science (including subseries Lecture Notes in Artificial Intelligence and Lecture Notes in Bioinformatics)*, 6364 LNCS:194–203.

223

[268] Wang, V. Y., Lam, H. I., Ennis, D. B., Young, A. A., and Nash, M. P. (2008). Passive ventricular mechanics modelling using MRI of structure and function. *Lecture Notes in Computer Science (including subseries Lecture Notes in Artificial Intelligence and Lecture Notes in Bioinformatics)*, 5242 LNCS:814–821.

[269] Watanabe, H., Sugiura, S., Kafuku, H., and Hisada, T. (2004). Multiphysics simulation of left ventricular filling dynamics using fluid-structure interaction finite element method. *Biophysical journal*, 87(3):2074–2085.

[270] Weiss, J., Maker, B., and Govindjee, S. (1996). Finite element implementation of incompressible, transversely isotropic hyperelasticity. *Comput. Methods Appl. Mech. Engrg.*, 135:107–128.

[271] Wellnhofer, E., Goubergrits, L., Kertzscher, U., Affeld, K., and Fleck, E. (2009). Novel non-dimensional approach to comparison of wall shear stress distributions in coronary arteries of different groups of patients. *Atherosclerosis*, 202(2):483–490.

[272] Wenk, J. F., Ge, L., Zhang, Z., Mojsejenko, D., Potter, D. D., Tseng, E. E., Guccione, J. M., and Ratcliffe, M. B. (2013). Biventricular finite element modeling of the acorn CorCap cardiac support device on a failing heart. *Annals of Thoracic Surgery*, 95(6):2022–2027.

[273] Wong, A. Y. and Rautaharju, P. M. (1968). Stress distribution within the left ventricular wall approximated as a thick ellipsoidal shell. *American heart journal*, 75(5):649–662.

[274] Wong, K. C. L., Zhang, H., Liu, H., and Shi, P. (2007). Physiome-model-based state-space framework for cardiac deformation recovery. *Acad Radiol*, 14(11):1341–9.

[275] Woods, R. H. (1892). A few applications of a physical theorem to membranes in the human body in a state of tension. *Transactions of the Royal Academy of Medicine in Ireland*, 10:417–427.

[276] Xi, J., Lamata, P., Lee, J., Moireau, P., Chapelle, D., and Smith, N. (2011a). Myocardial transversely isotropic material parameter estimation from in-silico measurements based on a reduced-order unscented Kalman filter. *Journal of the Mechanical Behavior of Biomedical Materials*, 4(7):1090–1102.

[277] Xi, J., Lamata, P., Niederer, S., Land, S., Shi, W., Zhuang, X., Ourselin, S., Duckett, S. G., Shetty, A. K., Rinaldi, C. A., Rueckert, D., Razavi, R., and Smith, N. P. (2013). The estimation of patient-specific cardiac diastolic functions from clinical measurements. *Medical Image Analysis*, 17(2):133–146.

[278] Xi, J., Lamata, P., Shi, W., Niederer, S., Land, S., Rueckert, D., Duckett, S. G., Shetty, A. K., Rinaldi, C. A., Razavi, R., and Smith, N. (2011b). An automatic data assimilation framework for patient-specific myocardial mechanical parameter estimation. *Lecture Notes in Computer Science (including subseries Lecture Notes in Artificial Intelligence and Lecture Notes in Bioinformatics)*, 6666 LNCS(2009):392–400.

[279] Yanagida, R., Sugawara, M., Kawai, A., and Koyanagi, H. (2001). Regional differences in myocardial work of the left ventricle in patients with idiopathic dilated cardiomyopathy: Implications for the surgical technique used for left ventriculoplasty. *Journal of Thoracic and Cardiovascular Surgery*, 122(September):600–607.

[280] Yin, F. C. (1981). Ventricular wall stress. *Circulation research*, 49:829–842.

[281] Yin, F. C., Chan, C. C., and Judd, R. M. (1996). Compressibility of perfused passive myocardium. *The American journal of physiology*, 271(20):H1864–H1870.

[282] Yin, F. C., Strumpf, R. K., Chew, P. H., and Zeger, S. L. (1987). Quantification of the mechanical properties of noncontracting canine myocardium under simultaneous biaxial loading. *Journal of Biomechanics*, 20(6):577–589.

[283] Yotti, R., Bermejo, J., Antoranz, J. C., Desco, M. M., Cortina, C., Rojo-Álvarez, J. L., Allué, C., Martín, L., Moreno, M., Serrano, J. A., Muñoz, R., and García-Fernández, M. A. (2005). A noninvasive method for assessing impaired diastolic suction in patients with dilated cardiomyopathy. *Circulation*, 112(19):2921–2929.

[284] Young, A. A., Dokos, S., Powell, K. A., Sturm, B., McCulloch, A. D., Starling, R. C., McCarthy, P. M., and White, R. D. (2001). Regional heterogeneity of function in nonischemic dilated cardiomyopathy. *Cardiovascular Research*, 49:308–318.

[285] Young, A. A., Kraitchman, D. L., Dougherty, L., and Axel, L. (1995). Tracking and finite element analysis of stripe deformation in magnetic resonance tagging. *IEEE T Med Imaging*, 14(3):413–21.

[286] Young, A. A., Kramer, C. M., Ferrari, V. A., Axel, L., and Reichek, N. (1994). Three-dimensional left ventricular deformation in hypertrophic cardiomyopathy. *Circulation*, 90(2):854–867.

[287] Young, A. A., Legrice, I. J., Young, M. A., and Smaill, B. H. (1998). Extended confocal microscopy of myocardial laminae and collagen network. *Journal of Microscopy*, 192(November):139–150.

[288] Yushkevich, P. A., Piven, J., Hazlett, H. C., Smith, R. G., Ho, S., Gee, J. C., and Gerig, G. (2006). User-guided 3D active contour segmentation of anatomical structures: Significantly improved efficiency and reliability. *NeuroImage*, 31(3):1116–1128.

[289] Zerhouni, E. A., Parish, D. M., Rogers, W. J., Yang, A., and Shapiro, E. P. (1988). Human heart: tagging with MR imaging–a method for noninvasive assessment of myocardial motion. *Radiology*, (2):59–63.

[290] Zhuang, X., Rhode, K. S., Razavi, R. S., Hawkes, D. J., and Ourselin, S. (2010). A registration-based propagation framework for automatic whole heart segmentation of cardiac MRI. *IEEE Transactions on Medical Imaging*, 29(9):1612–1625.

[291] Zienkiewicz, O. C. and Taylor, R. L. (2000). *The Finite Element Method. Volume 1: The Basis.* Butterworth-Heinemann.

[292] Zienkiewicz, O. C., Taylor, R. L., and Too, J. M. (1971). Reduced integration technique in general analysis of plates and shells. *International Journal for Numerical Methods in Engineering*, 3(2):275–290.